Commissioning and Out-of-Field Dose Characterisation of the Elekta Unity MRL

Thesis submitted by

Marcus Powers BSc(Hons)

in (February) (2022)

for the degree of Doctor of Philosophy

in the School of Engineering & Physical Sciences

James Cook University

Statement of Access

I, the undersigned, the author of this thesis, understand the James Cook University will make it available for use within the University Library and, by microfilm or other means, allow access to users in other approved libraries. All users consulting with this thesis will have to sign the following statement:

> In consulting this thesis I agree not to copy or closely paraphrase it in whole or in part without the written consent of the author; and to make proper written acknowledgement for any assistance which I have obtained from it.

Beyond this, I do not wish to place any restriction on access to this thesis.

01-Feb-2022

Marcus Powers — Date

Sources Declaration

I declare that this thesis is my own work and has not been submitted in any form for another degree or diploma at any university or other institute of tertiary education. Information derived from the published and unpublished work of others has been acknowledged in the text and a list of references is given.

01-Feb-2022

Marcus Powers — Date

Statement of Contribution of Others

I gratefully acknowledge the contributions detailed below:

Funding support was provided by an Australian Government Research Training Program scholarship.

Editorial assistance was provided by Dr. John Baines for the entire thesis. Chapters 3 and 4 are based on a submitted journal article, and Chapter 5 and Appendix B are based on a published article, and editorial assistance for these chapters was provided by the listed co-authors.

Contributions to co-authored publications that form the basis of Chapters 3-5, and Appendix B, are as follows. In all cases, I performed the measurements and analysed results, with assistance by all listed co-authors. I prepared all figures and wrote the text. In Chapters 3 and 4, some data collection was performed with Jason Arts of Elekta, and the code to determine MV Isocentre size in Chapter 3 was developed by Robert Crane. In Chapter 5, the presented comparative data was acquired by the following external investigators: Sandra Fisher, Jessica Lye, Reza Alignaghi Zadeh and Rob Behan of the Olivia Newton-John Cancer Research and Wellness Centre. Chapters 6 and 7 are intended for publication, and for these I performed the data collection and analysis with some assistance from Mikala Wright of James Cook University. I prepared all figures and wrote the text, with assistance from John Baines.

Intellectual support was additionally provided by: Michael Roche of Cork University Hospital; Jason Arts, Thomas Brostrom, Ewa Juresic and Mark Smith of Elekta; and Shannon Robards of the Townsville Cancer Centre.

Use of infrastructure external to James Cook University was provided by the Townsville Cancer Centre, Townsville University Hospital, through access to the Elekta Unity MR-Linac, associated equipment, simulation software and auxiliary systems.

Abstract

The combination of Magnetic Resonance Imaging (MRI) and mega-voltage (MV) radiation therapy treatments is readily achieved through MR-Linacs (MRLs). Such a system is the 1.5 T Elekta Unity MR-Linac (Elekta, Stockholm, Sweden) which was clinically introduced to the Townsville Cancer Centre (TCC) in 2019. Research on this system has seen much development; however, there is still a need to improve clinical knowledge. Of note was the current limited scope of commissioning work regarding the linear accelerator component. Additionally, due to the presence of the magnetic field, charged particle behaviour on MRLs is altered from conventional linacs. This causes changes to out-of-field dose (OFD) characteristics, and was an area warranting further investigation. Particularly lacking was a systematic investigation of Spiralling Contaminant Electrons (SCE) and the Electron Streaming Effect (ESE), with measurements compared to simulations using the commercial Monaco Treatment Planning System (TPS). These two areas, commissioning and an assessment of OFD, were investigated in this work using the Elekta Unity MRL.

In this thesis, mechanical and safety commissioning work is discussed with emphasis on the use of MR-compatible equipment, readily available to a clinic, for performing tests. Using adaptions of vendor supplied equipment, a method was proposed for gantry angle quality assurance (QA), which indicated accurate angular position within published tolerances of $< 0.3°$, using visual inspection of images. When analysing pixel intensity profiles, the gantry angle accuracy was confirmed within 0.1°. Using an in-house method, the machine isocentre was measured as 0.38 ± 0.04 mm (dependent on equipment), comparable to values measured with commercial equipment. This indicated that other clinics can measure the MV isocentre without the use of expensive, MRL specific isocentre software. An in-bore radiation survey was performed in 0 T, and this data was provided so that other centres can compare measurements, if desired.

Commissioning work that focused on the machine dosimetry is also provided. Attenuation of the anterior imaging coil was investigated using an in-house, cylindrical phantom. The attenuation was small with an average value of approximately 0.6 %, and consistent between simulations and measurements. Due to equipment limitations, an adapted methodology was proposed to determine the $TPR_{20,10}$ beam quality metric, and was determined to be 0.705 ± 0.001, consistent with published values. $TPR_{20,10}$ was found to be insensitive to beam quality changes which significantly impacted beam characteristics, such as beam output and shape. Other Unity users report using a different depth for reference dosimetry to that used in this work. This had implications for equipment set up and correction factors. Hence in this work, a novel methodology for machine output calibration was discussed and used to result in a machine output of 1.000 ± 0.002 Gy per 100 MU, depth 5.0 cm, from gantry 90.0°. The use of published magnetic field correction factors with this method was confirmed. The interference of the MR system on linac operation was also measured, and results were negligible. Treatment plan commissioning was performed using EBT3 and EBT-XD film (Ashland ISP Advanced Materials, NJ, USA) and the PTW Octavius 1500^{MR} array (PTW, Freiburg, Germany). These dosimeters were able to highlight issues during patient plan deliveries, when appropriate gamma criteria were set. Additionally, E2E testing

of plan adaption algorithms was performed using an in-house, 3D printed phantom and EBT3 film. Both E2E and patient plan commissioning results were within published tolerances for correct machine settings, with average passes above 95.0 % (2.0 %, 2.0 mm).

OFD due to SCE was investigated with EBT3 film and Monaco TPS simulations. The Monaco TPS can accurately model this effect when appropriate calculation criteria are set. Additionally, it was demonstrated that previously published Monte Carlo data did not agree with measured values. SCE surface doses were measured to be of the order of 4.0 to 5.0 % of the D_{max} dose to water for a $10.0 \times 10.0\,\mathrm{cm}^2$ field.

A phantom study was used to investigate OFD due to ESE. Simulated and measured ESE doses were consistent for the fields investigated. ESE doses were shown to be clinically significant, and larger than those for SCE, consistent with previous works. ESE doses were measured to be up to 22.6 % of the D_{max} dose to water for a $5.0 \times 5.0\,\mathrm{cm}^2$ field. The effect was dependent on field size and the simulated density of air through which electron streams travel, similar to SCE.

Finally, ESE was investigated during irradiation of the tilted anterior MR-imaging coil. Similar to the phantom investigation, film and TPS simulations of ESE doses were compared. Different models of the anterior coil were employed in the TPS, based either on a CT of the coil or the default Elekta supplied model. The use of the latter returned simulated results which were in agreement with measured data. ESE dose from the coil was also determined to be clinically significant, both above and below the coil, and implications for this during treatments was discussed. Dose as high as 23.0 % of the D_{max} dose to water for a $10.0 \times 10.0\,\mathrm{cm}^2$ was observed, comparable to phantom investigations and that observed in previous publications.

Acknowledgements

I would like to gratefully acknowledge the contributions of my mentors and supervisors, Prof. Ron White and Dr. John Baines whose continued support, advice, guidance and knowledge were instrumental for this project. I would like to thank my mentor and friend Mr. Michael Roche for setting me on this path and for his support over the years.

I also thank my good friends Ari, Atir, Dean, Deepti, Gaby, Glen, Jess, Jia, Kirsty, Kurt, Mark, Matt, Michael S. and Shannon for ensuring that I was not over-worked. I am also grateful to Marissa and Scott of Osk Bar for helping in that endeavour. I extend my thanks to my family for supporting me on the many ups and downs along the way.

Thank you to those who contributed their knowledge and time to discuss, solve, question and overcome the problems faced along the way: Jason Arts, Thomas Brostrom, Ewa Juresic and Mark Smith of Elekta; Robert Crane, Chantelle Fisher, Stephen Gibson, Linda Marsh, Glen Newman, Bronwyn Oar, Shannon Robards, Ariadne Shoobridge, Peter Stokes, Marchant Van der Walt and Glenn de Vine of the Townsville Cancer Centre; Daniel Cox and Mikala Wright of James Cook University; Sandra Fisher and the MRL-Physics team at Olivia Newton-John Cancer Wellness and Research Centre; and Emily Simpson-Page of the Royal Brisbane and Women's Hospital.

Finally thank you to the entire Radiation Oncology Department at the Townsville Cancer Centre, who all aided in this project and work tirelessly to provide world-class care to regional cancer patients.

List of Publications and Presentations

This thesis contains content that was published in the following journal articles:

[1] Marcus Powers, John Baines, Robert Crane, Chantelle Fisher, Stephen Gibson, Linda Marsh, Bronwyn Oar, Ariadne Shoobridge, Emily Simpson, Page Marchant, and Van Der Walt Glenn. Commissioning measurements on an Elekta Unity MR-Linac. *Physical and Engineering Sciences in Medicine*, **Online** (2022). doi:10.1007/s13246-022-01113-7

[2] John Baines, Marcus Powers, and Glen Newman. Sources of out-of-field dose in MRgRT: an inter-comparison of measured and Monaco treatment planning system doses for the Elekta Unity MR-linac. *Physical and Engineering Sciences in Medicine* (2021). doi:10.1007/s13246-021-01039-6

[3] Marcus Powers and John Baines. Electron Streaming Effect Associated With the Elekta Unity Anterior Imaging. *Frontiers in Physics*, **10** (2022). doi:10.3389/fphy.2022.880121

The following articles are also intended for submission, however are still being drafted:

- Marcus Powers and John Baines. In-bore radiation survey performed on the Elekta Unity MRL. Target journal: Physical and Engineering Sciences in Medicine. *(In draft)*
- Stephen Gibson, Marcus Powers, John Baines and Glenn de Vine. Mutual Interference of the MR and MV systems on the Elekta Unity. Target journal: Journal of Medical Imaging and Radiation Oncology. (Est date of submission: May 2022). *(In draft)*
- Marcus Powers and John Baines. Sources of out-of-field dose in MRgRT: a systematic investigation of measured and calculated phantom electron streaming doses on the Elekta Unity MRL. Target journal: Physics in Medicine and Biology. (Est date of submission: March 2022). *(In draft)*

This thesis also contains content that was presented at the following:

- A dosimetric investigation of Elekta Unity based adaptive planning with Monaco 5.4. How to Develop Research/Validation Programmes when Implementing New Technology? Edition 1: MRI Linac. Marcus Powers. ESTRO, Madrid 2019.
- Treatment plan quality assurance review for the first cohort of patients treated using the Elekta Unity MR linac in Australia. John Baines, Marcus Powers, Ariadne Brodmann. Elekta Users Meeting, Noosa, 2020.

- Out of field dose due to electrons generated in-field on an Elekta Unity MR linac. John Baines, Marcus Powers. Engineers and Physical Sciences in Medicine Conference, Brisbane, 2020.
- Plan QA and Independent MU Verification at the Townsville Cancer Centre. Marcus Powers, John Baines. 15th Elekta MR-Linac Consortium Meeting, Virtual 2020.
- Physics considerations for Unity. Marcus Powers, Ariadne Shoobridge. Elekta Asia Pacific Unity User Collaborative, Virtual, December 2020.
- Measured and calculated electron streaming on the Elekta Unity MRL. Marcus Powers, John Baines. Engineers and Physical Sciences in Medicine Conference, Brisbane, 2021.
- Energy measurements on the Elekta Unity following the 2UNI2 upgrade. Marcus Powers, John Baines. 16th Elekta MR-Linac Consortium Meeting, Virtual 2021. (Poster Presentation)
- Extra-terrestrial applications of the MR-linear accelerator. Tim Squire, Marcus Powers, John Baines. 16th Elekta MR-Linac Consortium Meeting, Virtual 2021. (Poster Presentation)

Contents

List of Figures

1 Introduction

The use of directed, ionizing radiation for the provision of cancer therapy (Radiation Therapy, RT) can be achieved through Medical Linear Accelerators. Medical Linear Accelerators (linacs) were first developed in the 1950's [10–12] and have evolved into complex machines. Current designs are capable of daily imaging using low energy (kV) x-rays to enable patient positioning prior to treatment. The use of ionizing radiation for imaging can be undesirable due to increased radiation doses to patients, increasing the risk of secondary cancers [13,14]. More recently, the integration of Magnetic Resonance imaging (MRI) and Linear Accelerator systems, termed MR-Linacs or MRLs, have been discussed and introduced into clinics around the world [15, 16]. Such systems make use of non-ionizing MR imaging to produce daily patient images, without the damage to healthy tissue associated with x-ray based imaging. However, perhaps the greatest benefit of these systems is the use of MR imaging, providing superior soft-tissue visualization of internal anatomy compared to conventional kV photon imaging [17], and allowing for adaptive radiotherapy [18].

The combination of MRI with an MV (linac) system, such as that provided in the Elekta Unity MR-Linac (Elekta, Stockholm, Sweden) design, presents challenges for clinics during commissioning and ongoing quality assurance. For example, commonly used equipment for conventional (non-MR) systems, may be incompatible with MRL designs for a number of reasons, most notable being MR safety and bore size restrictions. Commercial MR safe equipment can be expensive, and specific to individual tests that a clinic may want to perform. Furthermore, given that such systems have only been recently introduced into radiotherapy clinics, there is little guidance on mechanical and dosimetric characteristics and tolerances [19–22]. Hence, the opportunity exists to improve knowledge in this area with a focus on unique commissioning

tests with commonly available MR-safe equipment. Other clinics with these systems could then repeat measurements and compare results across institutions. Published data will potentially be of benefit to governing agencies seeking to implement guidance and standards for safe operation. Therefore, a primary goal of this work was to perform and present on commissioning measurements on the linac component of the Townsville Cancer Centre's clinical 1.5 T Elekta Unity MR-Linac. Where available, 0 T data is also presented.

With the presence of the MR field, the trajectories of charged particles will be altered due to the Lorentz force. This will subsequently change dose deposition in-field and out-of-field, relative to behaviour in a non-MR system. Of note with MR systems is the significant increase in out-of-field dose (OFD) [8,9,23]. Two effects of interest have been highlighted on system designs similar to the Elekta Unity: Spiralling Contaminant Electrons (SCE) and the Electron Streaming Effect (ESE). Although doses reported from these effects are significant, there is currently little available literature specific to the Unity [2,8,9,24–26]. There is a clear need to investigate these effects on this system, with OFD in 0 T data for comparative measurements also required. Furthermore, modelling of these effects with the clinically provided simulation toolkit (Monaco®, Elekta, Stockholm, Sweden), and performing a quantitative comparison with measured data, would add significantly to the current knowledge of OFD. Characterisation of OFD for the Unity was an additional goal of this work.

The structure of this thesis is as follows. Chapter 2 introduces linear accelerator systems, providing a brief history and basics of operation. Also presented in this chapter is a simple overview of the Elekta Unity design, and the commercial Monaco Treatment Planning System (TPS), provided by Elekta for radiation transport modelling. The basic physics of altered electron trajectories in MR fields, due to the Lorentz force, is briefly discussed. A literature review is provided, highlighting research gaps for (1) commissioning tests (mechanical and dosimetric) and (2) out-of-field dose characterisation on the Elekta Unity MRL. Chapter 3 incorporates mechanical and safety commissioning tests on the system, focusing on novel tests with commonly available equipment. Measurements of the gantry angle and MV isocentre with a vendor supplied phantom are presented. An in-bore radiation survey in 0 T is also discussed. Chapter 4 focuses on dosimetric tests for the Unity. In this chapter, measurement of the angular dependent attenuation of the anterior coil using an in-house phantom is presented. Beam quality, reference dosimetry and determination of magnetic field effects on ionization chamber behaviour, and linac operation, are discussed. Lastly for this chapter, commissioning for Intensity Modulated Radiation Therapy (IMRT) and End-to-End (E2E) testing are reported. Chapter 5 discusses OFD on the Unity system, with a focus on SCE. Measurements in 0 T and 1.5 T are presented, and compared to Monaco simulations and previous investigations. Chapter 6 provides an overview of a phantom based investigation of ESE. A systematic approach for measuring this effect with simple geometries was utilised. Chapter 7 provides a thorough investigation of ESE associated with the anterior imaging coil. Such an investigation had yet

to be performed for the Elekta Unity. Chapter 8 summarises each investigation, and provides recommendations for future directions. Two appendices are provided at the end of the thesis. Appendix A provides further novel commissioning work, which is not currently under consideration for publication and was removed from the body of the thesis for brevity. Finally, Appendix B discusses clinical investigations of OFD for three patient treatments, provided to give context for phantom investigations.

2

Background and Literature Review

The following chapter starts by introducing the basic concepts of a medical linear accelerator and radiation therapy, with some key terminology discussed. Following this, the concept of an MR Linear accelerator is provided, along with the specific machine design of the Elekta Unity. The effect of the magnetic field on charged particles is then briefly shown, and the subsequent changes to dose characteristics is introduced. Following this is a literature review focused on mechanical and dosimetric commissioning of an Elekta Unity MR-Linac. Finally, a literature review of out-of-field dose effects on the Unity is given, with focus on Spiralling Contaminant Electrons and the Electron Streaming Effect.

2.1 Background

2.1.1 Conventional Linear Accelerator Systems

Linear Accelerators had long been used for scientific research before their development into medical devices [10]. Two groups were concurrently working on accelerating electrons to MeV energies using microwave generating or magnifying devices: the W. W. Hansen group at Stanford University (California, United States of America) and D. D. Fry's group at Telecommunications Research Establishment in Great Malvern (England). By as early as 1947, both groups had achieved acceleration of electrons to energies above 3.0 MeV [10]. These groups benefited greatly from microwave radar technology developed in World War II and paved the way for the first clinical linear accelerator. In the early 1950's the first clinical linear accelerator (now referred as simply a linac) was built [10,11], with the first patient treatment in August 1953 [10,12]. This

linac produced an ionizing, 8.0 MV, x-ray beam (note the omission of the "e" when referring to photon energies) with a 2.0 MW magnetron.

Conventional linacs are more complicated than their early designs, and operate at a broader ionizing energy range of approximately 4.0 to 25.0 MeV [10]. Generally, there are five key components to a linac [10]: an injection system, a Radio-Frequency (RF) system, the auxiliary system/s, a beam transport system and lastly the beam collimation and monitoring system. The injection system is the source of electrons, referred to as the electron gun, where free electrons are generated through thermionic emission from a wire filament. RF system designs vary between linac manufacturers; however, are comprised of an RF source (magnetron or klystron with RF driver), a modulator for RF and electron gun pulsing (the Thyratron in the Elekta design), a control unit, an evacuated accelerating waveguide, and a circulator to restrict RF reflection from the accelerating waveguide back to the source [10]. Whilst in the waveguide, electrons experience acceleration, due to the RF, from velocities of approximately 0.4c up to about 0.998c. Additionally, in this section of the linac, the electron beam is focused and steered using high-powered magnet coils. Two common waveguide designs are in widespread production: the standing wave design, where constructive interference of back reflected RF occurs with that entering, and; the longer, travelling wave design, where waste RF is either terminated with a load (sink) system, or recycled to enable higher accelerating potential.

As one would expect, the auxiliary system comprises crucial subsystems for continual use of the machine such as cooling, vacuum pumping, air pressure monitoring and radiation shielding, to name a few. After exiting the accelerating waveguide, the electrons enter the evacuated beam transport system. Here they can be further focused and steered toward either a target for photon irradiation, or a window for electron irradiation. Electrons striking the target will generate bremsstrahlung and characteristic x-rays, hence this component is referred to as the radiation source. Photons emanating from the target form an energy dependent, tear-drop shape (see Figure 2.1), where for higher energy electrons striking the target, a more focused (forward directed) tear-drop is generated. This broad photon beam will then pass through the collimation and monitoring system, to be shaped into the clinically useful radiation beam [10]. A simple block diagram of a conventional linear accelerator with the components listed above, is shown in Figure 2.2.

The collimating system can also vary significantly between linac vendors. For this work it is enough to say that this system, in the Elekta design, is comprised of: a primary collimator, a conical flattening filter, ionization (ion) chamber for monitoring, jaws and multileaf collimators (MLCs) and associated optical system for MLC positioning. This section of the linac, often referred to as the Beam Limiting Device (BLD), can weigh up to 500.0 kg, due in part to necessary shielding against Head Leakage and Scatter (HLS) from stray photons/electrons interacting with other BLD components. The broad, tear drop shape emanating from the target is clinically undesirable and the collimating system aids to shape this into a useful beam. The primary collimator

Figure 2.1: An image taken from Mayles *et al.* [4] showing (a) the peaked beam profile emanating from photons directly from the target and (b) the resulting profile with the presence of the flattening filter

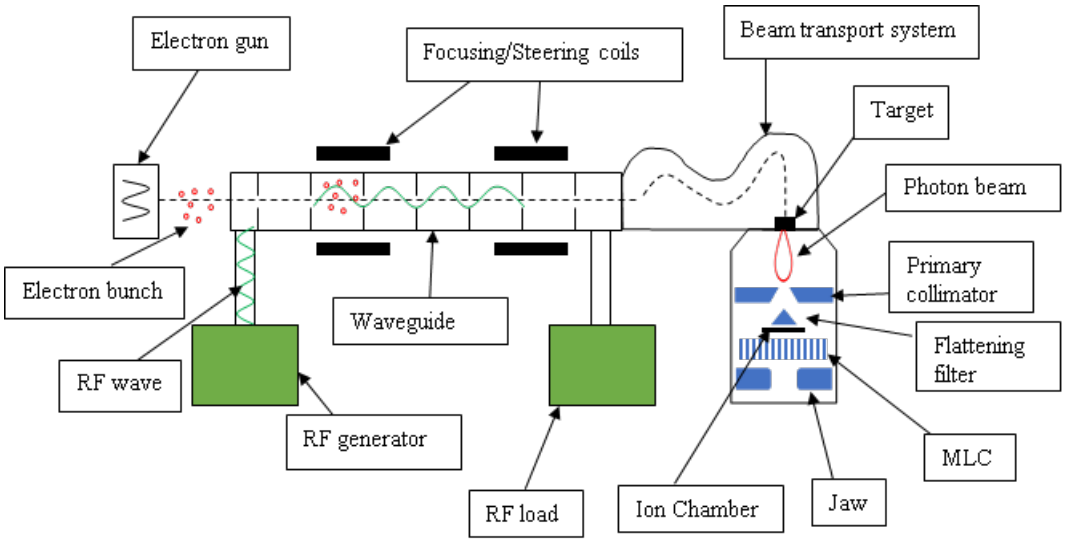

Figure 2.2: Block diagram of a conventional linear accelerator design, not to scale, for the travelling wave design. The dashed line indicates the beam line through the system

usually restricts the cross-sectional area of the beam to an approximately 50.0 cm diameter circle, at 100.0 cm from the source in a plane perpendicular to the direction of the electrons striking the target. Outside this region, international standards recommend doses be less than 0.1 % of that in the primary beam [27], where the primary beam is defined as that emanating from the BLD, from the most distal collimating system to the source. In conventional treatments, a forward peaked radiation beam can be difficult to use and as such a flattening filter is introduced to make the beam uniform in cross section, as in Figure 2.1.

This flattening filter acts an attenuating device, greatly reducing the dose-rate, and is a significant source of head scatter. Most linac designs have ability to rotate this filter out of the path of the beam, thereby generating a so-called Flattening Filter Free (FFF) beam. Without the presence of the attenuating filter dose-rates for FFF beams are significantly greater than conventionally flattened beams (cFF) [10, 28]. Whether flattened or not, the shape, dose and dose-rate of the beam is monitored by the ion chamber, which relates radiation counts to Monitor Units (MU). The calibration of this nondescript unit to a clinical relevant dose is performed by physicists, and is maintained for a specific set of reference conditions of irradiation. As an example, it is typical for 100.0 MU to correspond to a dose of 1.0 Gy for a 10.0×10.0 cm^2 field, to the depth of maximum dose within a water phantom, whose surface is at 100.0 cm from the radiation source [29]. This Source-to-Surface Distance is referred to as SSD.

With concepts such as isotoxic and inverse planning, the avoidance of Organs-at-Risk (OARs) and escalation of dose to Planning Target Volumes (PTV) needs to be achieved through the use of highly modulated (small) fields. The shaping of these, often-called beamlets, is achieved through the use of MLCs in combination with the jaws. MLC motion direction is in an axis perpendicular to the beam direction, with jaw direction orthogonal to both. Depending on the vendor and machine design, there can be up to 160.0 of these leaves (80.0 on opposing sides) with thicknesses that typically project to approximately 0.25 cm to 1.0 cm at an SSD of 100.0 cm. On an Elekta system, the MLCs are 0.5 cm at 100.0 cm SSD (for recent machine models), are capable of inter-digitization and can shape fields as small as 0.5×0.5 cm^2.

The systems above are mounted on a rotatable drum called the gantry. With such a system, radiation can be directed from multiple angles through a patient, thereby reducing the dose to healthy tissue whilst maximizing the cumulative dose to the tumour. The point about which the drum rotates is called the gantry isocentre. When treating patients, a representation of the internal anatomy is crucial, with both the geometry and electron density of importance. Given the energy range of linac operation, electron density information is required for accurate representation of Compton interactions and radiation transport through the patient material. For this reason, patient simulation occurs with Computed Tomography (CT) systems. Such systems make use of ionizing radiation, in the energy range of approximately 100.0 - 200.0 keV, for the purpose of discerning the pertinent information of patient anatomy. After simulation, the CT representation of the patient (CT dataset) is transferred to a Treatment Plan-

ning System (TPS). Given the complex physical and mathematical requirements of radiation transport, dose calculation is handled by this computerised TPS. TPS dose calculation algorithms can vary based on vendor and linear accelerator design; however, for this work the Elekta provided Monaco® TPS (Elekta, Stockholm, Sweden) is considered, which makes use of Monte Carlo based engines for dose calculation. Internal anatomical features of interest are demarcated using contours, and radiation dose limits are applied to such structures for the generation of a treatment plan. The treatment plan dictates the radiation delivery in terms of MU, dose-rate, machine geometry and MLC/jaw shaping (to name a few), based on the user input above, specific to the patient and treatment prescription. After appropriate Quality Assurance (QA) is performed on this plan, it is transferred to a Sequencer, with the Elekta supplied solution named MOSAIQ. Broadly, a sequencer acts as a communication and verification system between the TPS and the linac, for the delivery of the radiation treatment plan.

For treatment, the patient is situated on a hard, ideally radio-transparent, flat-top couch, capable of translational and rotational movements. The patient is aligned, using the couch motion, such that the intended target is in a similar position to that in the treatment plan. Given the damaging nature of the radiation, accurate and reproducible positioning of the patient relative to the intended radiation target is paramount. This alignment is achieved through an on-board kV imaging system. This ionizing radiation enables production of a new daily image of the patient, against which the reference planning image can be registered to determine required shifts for patient alignment. These shifts are affected using couch motion, and after correct alignment, the radiation plan is delivered. This common approach of patient alignment to the plan isocentre is referred to as Image Guided Radiation Therapy (IGRT).

The delivery of the entire radiation prescription, to eliminate the cancerous cells, in a single instance would likely also cause irrevocable damage to healthy tissue. To make use of the differing cell survival rates, between healthy and cancerous cells, radiation treatments are typically delivered across several days. Division of radiation doses into sessions is referred to as fractionation, and the reader is referred to other texts for more information on this process [30]. With the increasingly precise nature of linear accelerators and patient set up, greater doses per fraction are able to be delivered with reduced toxicity to healthy tissue. For lowly fractionated, high dose plans to small targets ("stereotactic" [31]), the importance of accurate machine delivery is increased [32]. Regardless of this, all aspects of the machine and TPS behaviour need to be properly characterised prior to their clinical introduction into a department. This process is referred to as commissioning, where physicists and other staff will determine mechanical, safety and dosimetric behaviour of the linac or TPS, against which routine measurements can be compared for continuous QA. Further information on the aspects of linear accelerators, QA and on the treatment process, can be found in previous publications [4, 10, 32–35]. Information regarding dose calibration and dosimetry protocols can also be found elsewhere [29, 33, 36].

2.1.2 The Elekta Unity MRL and Monaco TPS

As mentioned above, ionizing radiation is utilised in conventional IGRT treatments for patient imaging and the use of such radiation causes additional damage to patient healthy tissue. The use of Magnetic Resonance Imaging (MRI) alleviates this issue, whilst vastly improving soft tissue contrast, which is not possible with kV x-ray based systems [17]. Further to this is the combination of such imaging with the Linac treatment machine, resulting in MR-Linear Accelerators (MRLs) [17, 37–41]. In such systems, an MR is integrated with a linear accelerator to achieve irradiation in the presence of a strong magnetic field. This has implications for charged particle motion, which in turn affects dose deposition within and external to the region of the primary beam [8, 9, 20, 42–44]. In contrast to the conventional treatments, in MRL systems the patient has daily MR imaging on the treatment couch ("online") and such images are used to generate a daily radiation plan, adapted to the changing shape and location of the tumour [18]. In MR guided Radiotherapy (MRgRT), the plan is typically shifted to match the daily patient position (instead of the converse in IGRT systems), and therefore must be recalculated daily [18]. Note that some MRL systems still allow for minimal couch motion to align patients, and hence recalculation would not be required [41].

One such system is the Elekta Unity MR-Linac (Elekta, Stockholm, Sweden), whose genesis dates to as early as 2004 [44, 45]. Early work focussing on technical feasibility listed three issues: (1) magnetic interference of the MRI system and the accelerator, (2) beam transmission through the MRI and (3) the change in dose deposition due to the magnetic field [45]. To address these issues, some techniques of note were employed. First the modification of typical active magnetic shielding, from standard shield designs, enabled the formation of a toroidal volume of lower field strength through the magnet transversal mid-plane [45]. The field strength was sufficiently low enough to allow the linear accelerator to be placed and operate without significant MR-interference. To reduce the beam transmission through the magnet system, the super-conducting coil configuration was split, to allow an approximate 20.0 cm region through which the beam can pass with relatively low attenuation, again through the magnet transversal mid-plane. The gradient coils were also modified in this way. The change in dose deposition, due to the magnetic field altering electron trajectories (see below), is clearly not able to be overcome with machine design changes. Instead, this effect is modelled [44] and must be accounted for in planning system calculations [6, 46] and dosimetry protocols [5, 47, 48]. A prototype of this design depicted a static linear accelerator, mounted on a wooden table, outside the MRI system [37]. Linac rotation about the magnet clearly was not possible with this early design; nevertheless, simultaneous operation of the MR and linac systems was proven in that work [37]. The linac has evolved since this first design, with the aid of commercial partners in the program, and the current design is that which is of focus in this work.

The current design of the Unity system has been discussed by other investigators [16, 19, 21, 22, 37, 42], and the general concepts of beam generation and shaping are

similar to the conventional paradigm; however, relevant differences are highlighted. Here, it is sufficient to say the current Elekta Unity MRL is a combination of a modified Philips Ingenia 1.5 T MRI, with a split-coil superconducting magnet and a straight-through linear accelerator. The beam generation system produces a 7 MV FFF x-ray beam with an approximate depth of maximum dose of 1.3 cm. This system is mounted on an annular gantry that is free to rotate around a cylindrical cryostat containing the static-field MR coils. Two key differences from the conventional design, specific to this work, are: a lack of steering and focusing magnets around the waveguide, the presence of which would disrupt the imaging MR field, and; electron injection is no longer controlled with a switching (thyratron) system, and instead a voltage grid is set between the gun and the accelerating waveguide. When not in operation, the grid is maintained at a lower voltage (below the cathode/filament) to restrict electron flow into the waveguide. However, during beam-on the grid is pulsed to a voltage above the cathode, synchronous with the RF, and electrons accelerate into the waveguide. Additionally, with the lack of a beam steering system, the beam-line is directed orthogonal to the tungsten target and mechanical alignment of the electron gun, accelerating waveguide, tungsten target and collimating system, is paramount.

Gantry rotation axis and the central axis of the coils are coincident, with the static magnetic field (B_0) in the negative Y direction (IEC 61217) as shown in Figure 2.3. For all gantry angles, the beam passes through the cryostat and is perpendicular to B_0. The angular dependent beam transmission through the cryostat (aluminium annular structure containing liquid helium) is referred to as the cryostat characterisation and will vary between Unity systems mostly due to differences in construction of the cryostat annulus; however, a small component will be due to differences in helium fill [22]. A modified Elekta Agility® BLD shapes fields ranging from 0.8×0.5 cm^2 to 57.4×22.0 cm^2 at isocentre. MLCs in this system project to a size of approximately 7.0 mm at isocentre. At the time this work was conducted, the dose-rate at this point was 425.0 MU/min; however, recent upgrades have enabled continuously varying dose-rate. The patient positioning system (PPS) is capable of longitudinal movement only and the isocentre is 14.0 cm above the PPS, 143.5 cm from the source. A fixed EPID panel, now called the mega-voltage imager (MVI) [21], diametrically opposite the x-ray source on the gantry, is capable of MV portal imaging a maximum field size of 22.0×9.5 cm^2, for QA purposes only. For patient setup, a single sagittal laser is provided by default, to aid with patient setup. A schematic of the MR-linac is shown in Figure 2.3, along with the IEC 61217 coordinate system, courtesy of Elekta. The patient/body planes coordinate system is shown in Figure 2.4.

The Elekta Unity MRL, in conjunction with its treatment planning system, enables real-time adaptive radiotherapy planning. Adaptive radiotherapy (ART) is the process by which treatment plans are changed to optimize delivery to suit changes in patient anatomy [49,50]. Examples of these anatomical changes are tumour or organ locations, size, biology and shape [49]. Broadly, there are three time-scales over which ART can be utilised: (1) offline, between fractions; (2) online, immediately prior to a fraction,

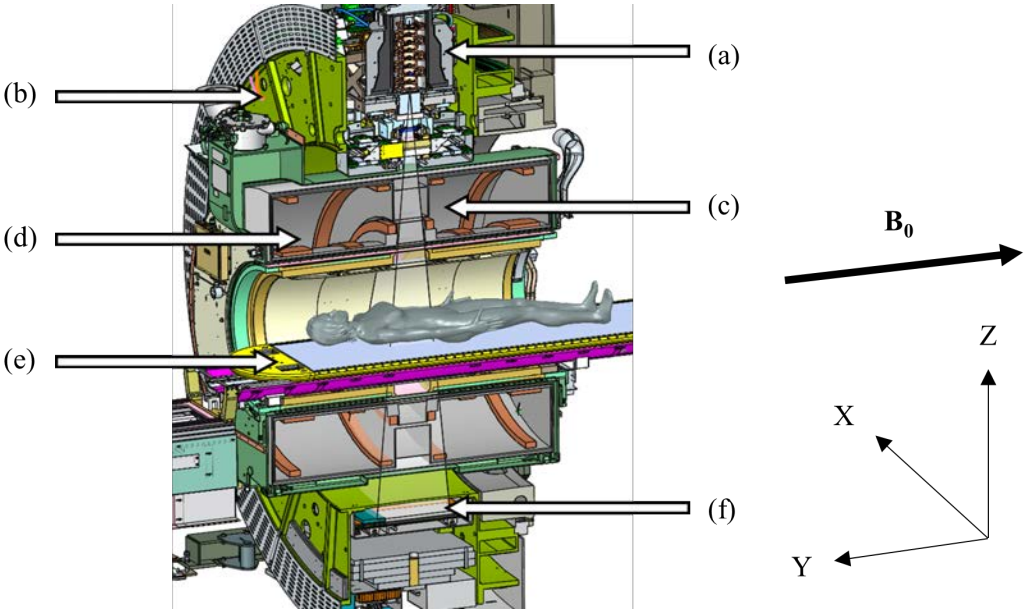

Figure 2.3: A schematic of the Elekta Unity MR-Linac, courtesy of Elekta, showing (a) the straight-through waveguide, (b) the gantry ring, (c) the primary radiation beam passing through (d) the coil system embedded in the magnet cryostat, (e) the patient positioning system and (f) the MVI for x-ray imaging. The IEC61217 coordinate system is shown, and for the head-first-supine patient orientation in the figure, B_0 is in the craniocaudal direction (negative Y)

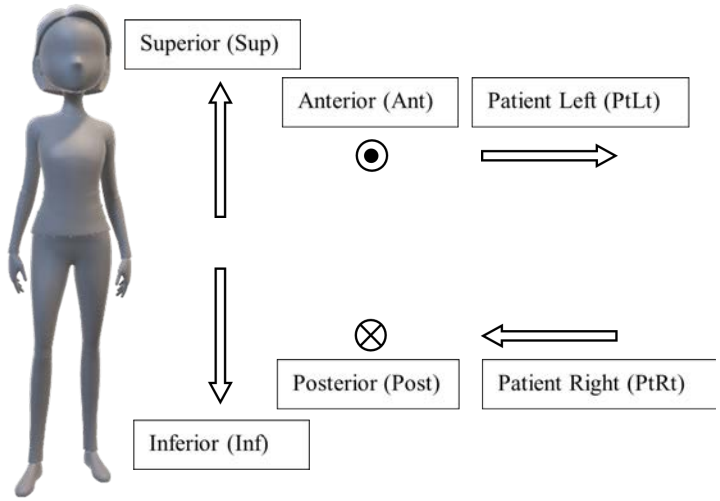

Figure 2.4: The body coordinate system. Anterior and Posterior directions are into and out of the page, respectively

and; (3) in real-time during a fraction [49]. Offline adaptions can take place without the patient present on the couch, and hence are more readily implemented by a department. Systematic changes in anatomy can be addressed, and PTV margins can be customized to suit the patient. Conversely, online and real-time adaptions occur with the patient remaining on the couch [49]. Hence, daily anatomy changes can be addressed and treatments further optimized than what is typically available for non-ART or offline ART techniques. Of course, ART does not come without its own problems, as each change or adaption can create a new plan, which ideally would undergo additional QA measurements, and a physicist's work will scale with the number of treated fractions. Plan QA, including both plan quality assessments [51] and deliverability, can be a challenge with ART (particularly with online adaptions). Further, *in vivo* patient dose assessments, including out-of-field doses (discussed later), can be difficult as the planned doses change each adaption.

The TPS used with the Elekta Unity MRL is Monaco v5.40. For clarity, there is a distinction made between Monaco types depending on whether a pre-treatment reference plan is being calculated (Offline Monaco) or whether a daily adapted plan is generated with the patient on the couch (Online Monaco). Within both, the GPU Monte Carlo dose (GPUMCD) algorithm is used for fast calculations in the presence of a static 1.5 T magnetic field [6, 46]. Dose calculations are performed on voxelized models of volumes, with relative electron density (RED) assigned per voxel based on a scanner specific, CT number-to-RED table. For calculations performed on MR datasets, RED information is assigned on a per structure basis with user specified values, since no electron density is obtained from the image. Typically, the mean RED for a structure is calculated from a reference CT scan. REDs are converted to mass densities, with the result mapped to chemical composition using Patient, Phantom or Couch material look-up tables. Users can specify a dose calculation grid resolution and statistical uncertainty to control the accuracy and duration of calculations. For plan adaptation two workflows are available, Adapt-to-Position (ATP) or Adapt-to-Shape (ATS). ATP involves repositioning of pre-treatment (reference) plan isocentre, based on the rigid registration of that plan and image dataset with a daily MR image. The pre-treatment plan can be recalculated or re-optimized on the reference dataset to reproduce or improve target dose coverage [18]. ATS allows for plan adaptation based on anatomical changes as shown on the daily MR image. Contours can be automatically deformed to match the daily anatomy, with optional user-based adjustments. The reference plan is recalculated or re-optimized using reference plan constraints [18]. For more information on the replanning options the reader is referred to other works [6, 18, 46].

2.1.3 Basic Physics of the Lorentz Force

The kinetics of charged particles in external electric and magnetic fields can be described using the widely known Lorentz Force:

$$\tilde{F} = q\tilde{E} + q(\tilde{v} \times \tilde{B}), \tag{2.1}$$

Figure 2.5: Point spread distribution change with the presence of a 1.5 T magnetic field. Image has been taken from van Asselen *et al.* [5]

where, q is the particle charge (polarity dependent), $\tilde{v}$ is the particle velocity, likened to particle energy and $\tilde{E}$ and $\tilde{B}$ are external electric and magnetic fields, respectively. On an MRL system, there is no external electric field of concern, and Equation 2.1 reduces to the simpler:

$$\tilde{F} = q(\tilde{v} \times \tilde{B}). \tag{2.2}$$

Clearly, any component of particle motion parallel to the magnetic field will not experience any force and thus will undergo no perturbation. However, for a component of motion perpendicular to $\tilde{B}$, the Lorentz force acts on the particle in a direction dictated by the right hand rule. The motion of photons is not perturbed (since they are uncharged particles); however, the electrons generated in the Compton interactions will have altered trajectories relative to a non-magnetic field (0 T) environment. For MRgRT platforms such as the 1.5 T Elekta MRL [17, 18, 37] and the 0.35 T ViewRay MRIdian linac and cobalt based systems (ViewRay, Oakwood Village, OH, USA) [38], the static magnetic field is transverse to the x-ray beam direction. Specific to the Unity design, the magnetic field is directed out of the bore and the result is that secondary electrons have deflected paths (primarily in the + X direction for deliveries from a gantry angle of 0.0°, parallel to gravity). Hence, a skew in the dose deposition kernels occurs, as shown in Figure 2.5 [5, 52]. This deflection has effects on in-field beam characteristics such as profile shape, dose deposition with depth and surface dose [20, 42, 44].

Using a simple relation of centripetal force to the Lorentz force equation in 2.2, the following can be derived:

$$r = \frac{mv^2}{qvB\sin\theta}, \tag{2.3}$$

where r describes the radius of curvature of a particle with mass m, velocity v

Figure 2.6: Profiles generated in 0 T and 1.5 T. Penumbras in 1.5 T are skewed in the same direction of the Lorentz force. Image was taken from Ahmad *et al.* [6]

and charge q, moving in a magnetic field of strength B, at an instantaneous angle θ relative to the magnetic field direction. For the Elekta Unity the maximum radius of curvature for electrons is approximately 6.0 mm. However, an average value of 2.2 mm [42] is more commonly used for the radius of curvature of secondary electrons. Figure 2.6, taken from Ahmad *et al.* [6], is an example of magnetic field effects on beam characteristics where a skew in beam penumbras is observed [6, 20]. The magnitude of this change is between 2.0 to 3.0 mm, consistent with the average electron spiral radius.

The deflection of perpendicular motion has interesting consequences on doses at beam entry and exit through phantoms, as well as for out-of-field doses (OFD). With the curved paths of electrons, it is possible after their exit from a higher density material into a lower (i.e. water to air) to spiral around and return to the exit surface, Figure 2.7 [7]. This is the so-called electron-return-effect (ERE) and has seen much investigation for MRgRT systems [7, 42, 43, 52–54]. These electrons will deposit their doses superficially at this surface, and an increase in exit dose can be observed for a percentage dose-with-depth (PDD) curve in a magnetic field, which is not observed in a 0 T environment, as shown in Figure 2.8.

Since the parallel velocity component is unperturbed by the magnetic field, a helical spiralling effect can occur whereby electrons spiral either parallel or anti-parallel to the magnetic field. Consequently, electrons generated in the air surrounding the patient/phantom will not be able to reach the latter volumes (as their motion perpendicular to the magnetic field will be perturbed), and instead will travel helically

Content has been removed due to copyright restrictions

Figure 2.7: The effect of the magnetic field on the electron paths, giving rise to ERE. For the 1.5 T case, the magnetic field is directed into the page. Image taken from Lagendijk *et al.* [7]

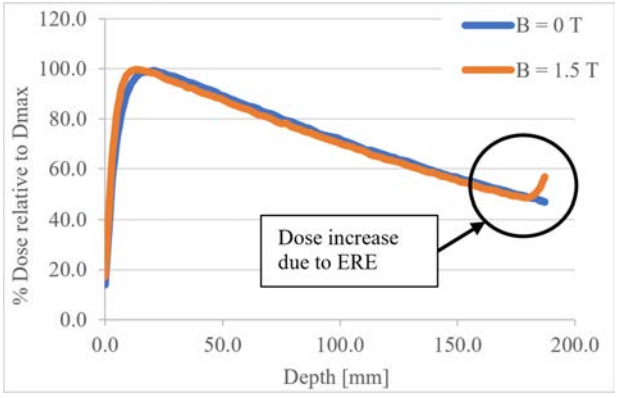

Figure 2.8: Percentage depth-doses in 0 T and 1.5 T magnetic field environments. A noticeably steep increase at the phantom exit (end of the curves) can be seen for the 1.5 T case compared to the 0 T

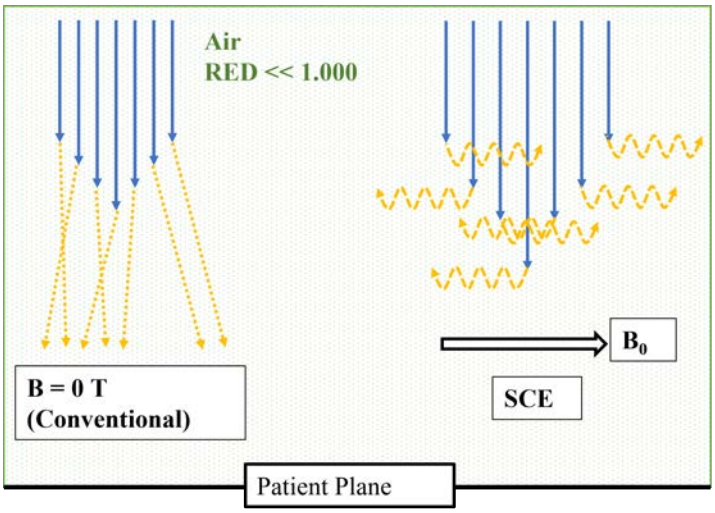

Figure 2.9: A schematic showing spiralling contaminant electrons. In 0 T, electrons (gold) generated by photons (blue) are able travel toward the patient plane. With a transverse magnetic field, the Lorentz force acts produces spiralling motion parallel and anti-parallel to B_0

around the field lines, until they reach an attenuating material. These are referred to as Spiralling Contaminant Electrons (SCE) [9], shown schematically in Figure 2.9. Additionally, it is possible that electrons generated in field from phantom and patient surfaces are able to be ejected from the beam, through either forward scatter (say, at the phantom exit) or backscatter (at the phantom entrance). In certain geometrical situations, it is possible for these forward or backward scattered electrons to spiral and miss the surface from which they were ejected, for example with a sloped surface. In this case, the electron motion parallel to $\tilde{B}$ is unperturbed, unlike the perpendicular component, and they spiral about the field lines until reaching an attenuating surface, Figure 2.10. This is referred to as the Electron Streaming Effect (ESE) [8]. These important changes in OFD characteristics in MRgRT systems are still relatively new concepts, warranting further investigation.

Note the maximum angle that an electron can be ejected in a Compton interaction, relative to the photon's initial trajectory, is 90.0° [34]. For clarity, backscattered electrons in 0 T are those which have: (a) undergone a multiple scatter event (Figure 2.11(a)), (b) originate from a laterally scattered, or divergent, photon interaction (Figure 2.11(b)), (c) escape a sloped surface at the beam entry (Figure 2.11(c)), or (d) are contaminant electrons within the primary beam (Figure 2.11(d)). With the presence of a transverse magnetic field, the altered trajectory of electrons results in variations to the number of electrons that can escape a sloped surface. For electrons sweeping toward the slope, more will be ejected (Figure 2.11(e)), and the opposite for electrons sweeping away (Figure 2.11(f)). Additionally, with a transverse magnetic field, fewer contaminations electrons are present at the phantom/patient entrance due to the altered trajectory (Figure 2.11(g)).

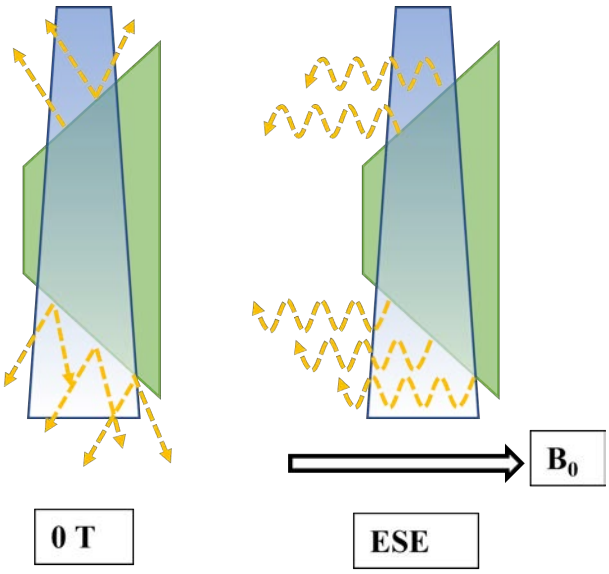

Figure 2.10: A schematic showing the electron streaming effect, recreated from Malkov *et al.* [8]. Electrons (gold) produced during photon (blue) interactions with a sloped phantom, 0 T, travel along a path in approximately the same direction as their exit trajectory. However, with a transverse magnetic field, the perpendicular component of motion is restricted and electrons are able to spiral, miss the surface from which they were ejected and continue along the field lines

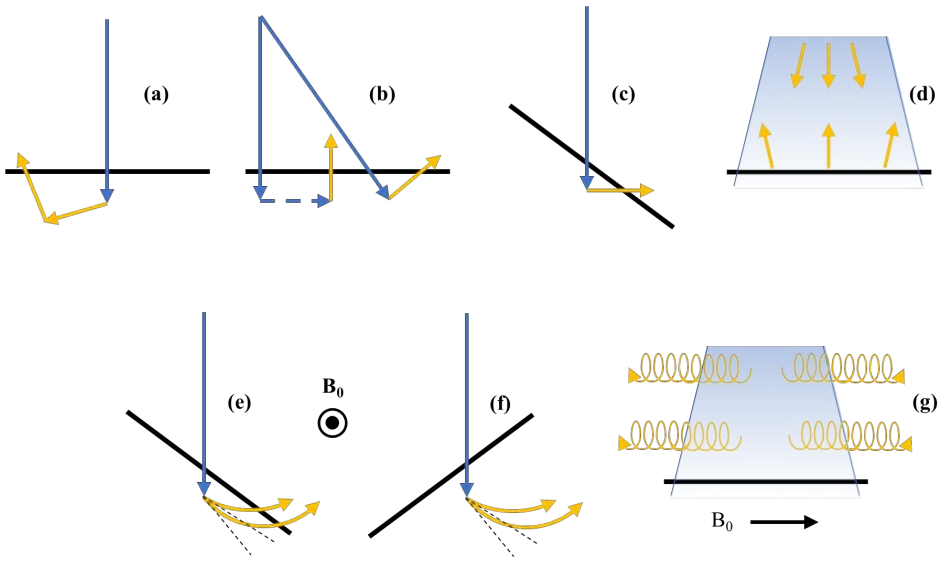

Figure 2.11: Various mechanisms for backscatter electrons (gold) from photon (blue) interactions with a surface (black). Non-magnetic field effects are shown for (a) multiple scatter electrons, (b) electrons from scattered (dashed blue line) and divergent (solid line) photons, (c) electrons escaping a sloped surface, and (d) contaminant electrons scattering off the surface. The effect of a static magnetic field (B_0) on electrons exiting a sloped surface are shown for (e) electrons sweeping toward the surface, increasing backscatter, and (f) electrons sweeping away from the surface, decreasing backscatter. Also with a magnetic field, in (g) electron contamination is decreased as the electrons cannot travel perpendicularly to the field, and this contribution to backscatter is reduced. The magnetic field is in the same direction for (e) and (f), and the black dashed lines indicate the initial trajectory of the electrons in 0 T

2.2 Literature Review

2.2.1 Introduction

The following section provides a literature review for this thesis. An overview of issues clinics may face when commissioning an Elekta Unity MRL is provided first. This is then focused to Mechanical and Safety considerations, and Dosimetric considerations. Commissioning tests specific to these two sections are reviewed, and a discussion of limitations and problems a clinic may want to address, are summarised. Finally, a similar discussion for out-of-field doses on the Unity is presented, with focus on SCE and ESE.

2.2.2 Commissioning Overview

As briefly mentioned above, before being released for clinical use Linear Accelerators first undergo periods of acceptance and commissioning. Traditional acceptance processes consist of verification of machine performance against minimum requirements, often outlined during tender, in purchase contracts with the vendors, or as specified by the manufacturer [4,10]. Acceptance tolerances are typically set to match those of international standards [27,55,56] or published works. Following acceptance is typically the commissioning process, where all possible machine characteristics are determined [4] with the intended clinical use a key consideration. Efficacy of treatment provision can be degraded over the life of the machine due to a variety of reasons, notably electronic malfunctions, component breakdown or gradual operational decline [10]. Hence this commissioning data is used as a baseline, against which routine quality assurance measurements can be compared. Furthermore, components are not entirely consistent between machines, due to a variety of reasons such as manufacturing tolerances and damage during transport. As such, a set single set of commissioning data for a given machine type is not adequate to describe is operation. Finally, it is beneficial to acquire a large suite of commissioning data to assess accuracy of TPS calculations (or even to establish the TPS), to provide guidance on future clinical needs and to determine other previously undiscovered issues with machine behaviour [4, 10]. Typically, commonly available commercial phantoms and equipment are used to gather this baseline data, such that comparisons between machines, or with data from other clinics, can be readily achieved.

The Elekta Unity MRL (Elekta, Stockholm, Sweden) design presents quality assurance challenges not present for conventional systems. Following the on-site construction of the system, Elekta personnel perform device acceptance tests (DAT) that replace conventional linac acceptance tests. Commissioning and beam modelling validation measurements are also performed by Elekta personnel, with Philips staff responsible for MR image quality testing. Following this, a period of internal commissioning and quality assurance occurs during which in-house physicists perform baseline measurements across both MR and MV modalities. Elekta tests incorporate specialised

QA devices and analysis software that are not necessarily commercially available. Furthermore, due to the presence of the magnetic field, conventional equipment available to the clinic may not be compatible with the Unity system. As such, Unity users may encounter challenges performing independent, routine QA tests without further guidance.

Acceptance, commissioning and continuous QA tests, tolerance and frequencies for the Elekta Unity have been described by other authors [19–22]. Recently the work of Roberts *et al.* [22] provides tolerances and frequencies for common QA tests and Woodings *et al.* [21] for acceptance procedures on the linac component. Their findings have been summarised in Tables 2.1 to 2.3. However, due to the complexity and novelty of the machine, the scope of such work is limited. The variety of possible tests also means it is likely that a clinic will not find comparative values for all commissioning work performed locally. Furthermore, since this technology has only recently been clinically introduced in Australia, there is currently no region-specific guidance for implementation and safe use of the MRL, as is the current situation for conventional treatment systems [35]; however, position paper/s are unlikely to vary significantly from the recommendations of the above investigators [22]. Additionally with the novelty of the system, it can be argued that lack of experience or training would be a challenge during commissioning [57]; which can be alleviated in part with clear guidance or methodologies in publications. It is the intention that this work will aid clinics introducing an Elekta Unity and provide some benchmarks for test results to address the highlighted issues.

The significance of this work is in the novel QA methods that describe alternative uses for vendor supplied phantoms and the use of simple, in-house developed phantoms and software. This work aims to provide straightforward methodologies that can be employed by most clinics for performing these tests, as well as comparative baseline results for Unity users. Additionally, alternate methods for independently verifying vendor measurements are provided. Adaptations of an Elekta supplied phantom enabled independent QA of the gantry angle and MV isocentre size. Development of in-house phantoms was required for measurements of beam attenuation, due to the anterior imaging coil, and End-to-End (E2E) testing. Difficulties were encountered with commercial equipment when measuring beam quality and output, and when performing intensity modulated radiation therapy (IMRT) commissioning, that required adaptations to standard methodologies and as such are also presented in this thesis. During installation there was limited time to facilitate customer selected measurements prior to magnet ramp up; although a spontaneous quench and planned ramp down events enabled selected commissioning tests to be performed with B = 0 T. Hence, the following literature review is focused on these aforementioned tests and, for brevity, more common commissioning measurements are not discussed. These include aspects of the mechanical behaviour of the system, relative dosimetry measurements, a thorough investigation of the TPS, commissioning and implementation of independent dose checking techniques [59–61], commissioning of the MR system [62, 63] and MLC

Test	Tolerance	Frequency
Audio-visual/CCTV monitors	Functional	Daily
Intercom system	Functional	Daily
Emergency stop (table)	Functional	Daily/Monthly
Radiation door interlock	Functional	Daily
Radiation monitors and indicators	Functional	Daily
Emergency off (power)	Functional	Weekly
Radiation interlocks (FKP*)	Functional	Weekly/Monthly
MLC and jaw positions	± 1.0 mm / ± 2.0 mm†	Weekly/Monthly†
Gantry angle accuracy	± 0.3°	Monthly
Table position	± 1.0 mm	Monthly
Leaf position accuracy (IMRT)	± 1.0 mm	Monthly
MV isocentre diameter	≤ 1.0 mm	Monthly
Leaf position repeatability	± 0.5 mm	Annually

Table 2.1: Linac Mechanical and Safety QA tests, tolerances and frequencies listed in Roberts *et al.* [22]. These are provided as a summary only and readers are referred to the original publication for the complete list. *Function Key Pad, †variable tolerances are set according to test frequency

Test	Tolerance	Frequency
X-ray output	± 3.0 % / ± 2.0 % / ± 1.0 %*	Daily/Weekly/Annually*
Backup monitor chamber constancy	± 3.0 % / ± 2.0 %	Daily/Weekly
Beam profile constancy	± 2.0 % / ± 1.0 %	Monthly/Annually
X-ray beam quality	± 1.0 %	Monthly/Annually
Beam profile constancy with gantry angle	± 2.0 %	Annually
Output factor constancy	± 2.0 % ($< 4.0 \times 4.0\,cm^2$) ± 1.0 % ($\geq 4.0 \times 4.0\,cm^2$)	Annually
MU linearity	± 5.0 % (2 - 4 MU) ± 2.0 % (≥ 5 MU)	Annually
Dose-rate linearity	± 2.0 % from baseline	Annually
Output with gantry angle	± 2.0 % from baseline	Annually
Off-axis factors with gantry angle	± 2.0 % from baseline	Annually

Table 2.2: Linac Dosimetric QA tests, tolerances and frequencies listed in Roberts *et al.* [22]. These are provided as a summary only and readers are referred to the original publication for the complete list. *variable tolerances are set according to test frequency

Test	Tolerance
Mechanical and Safety	
Radiation inhibits	Functional
Scattered radiation to patient	avg. < 0.1 % of in-field dose
MVI panel rigidity	< 0.3 mm
MVI panel rotation alignment	$< 0.2°$
Pixel scale and isocentre location	Determined
Gantry tilt	$< 0.2°$
Gantry angle accuracy	$< 0.2°$
Beam alignment (with target/focal spot)	< 1.0 mm and $< 0.2°$
MV isocentre diameter	< 1.0 mm
MLC stripe test	< 0.5 mm
MLC transmission	< 0.5 % from baseline/TPS
Jaw stripe test	< 1.0 mm
Gantry angle dependency	< 0.5 mm
Table orthogonality and movement accuracy	$< 1.0°$ and < 2.0 mm
Laser accuracy	< 1.0 mm
MR-to-MV alignment	$< 0.3°$
Dosimetric	
X-ray output	< 1.0 %
Output stability	< 2.0 %
Backup monitor constancy	< 2.0 %
MU linearity	< 2.0 %
Dose-rate linearity	< 2.0 %
Output with gantry angle/Cryostat dependency	< 1.0 % from baseline
Profile constancy	< 1.0 %
Profile constancy with gantry angle	< 1.0 %
MR influence on MV operation	< 2.0 %
End-to-End (Alderson phantom)	> 90.0 % points pass*

Table 2.3: Acceptance tests and their tolerances from Woodings *et al.* [21]. Note that test frequency is omitted as these apply to acceptance procedures, which are performed as part of the MRL implementation/commissioning. These are provided as a summary only and readers are referred to the original publication for the complete list.*using gamma analysis [58] with 5.0 % dose tolerance, 2.0 mm distance-to-agreement and dose suppression below 10.0 %

characterisation [64].

2.2.3 Linear Accelerator Mechanical and Safety Commissioning

Couch and Laser Accuracy

Woodings *et al.* [21] and Roberts *et al.* [22] have previously investigated mechanical couch operation. Simple couch drive accuracy and reproducibility tests were discussed by both, with extended testing on couch drive orthogonality highlighted in Woodings *et al.* [21]. The investigators argued against the need for accurate and reproducible couch positioning for patient set up, as for each day of treatment the adapted plan will be shifted according to the new treatment position. Hence couch position was considered of little relevance. Additionally, for the aforementioned reason, previous investigators did not discuss test methodologies for sagittal laser accuracy [21, 22].

However, a counter argument can be made that consistent set up between patient simulation and treatment will aid with non-standard scenarios, such as the use of bolus shielding against electron streams. The provision of additional lasers would aid treatment staff in positioning of this crucial shielding, as well as reducing setup variability during *in vivo* dosimetry measurements. The lack of additional lasers, or inaccuracies in the sagittal laser, adds increased difficulty for busy clinics when ensuring patient safety from OFD. Hence, the assurance of laser accuracy, and couch positioning, can alleviate the highlighted issues. The need for a QA method of the laser accuracy on the MRL was apparent from the literature, and such a method is provided in an appendix for this work.

Gantry Angle

Due to the construction of the gantry ring, accurate verification of the gantry angle using an inclinometer can only be achieved at two angles, 270.0° and 240.0° [21]. At these angles there is a conveniently located machined flat surface on which an inclinometer can be mounted. As part of routine QA for conventional linacs it is common to determine gantry angle accuracy for multiple positions and to assess the reproducibility of gantry rotation. Previous publications report on the use of spoke films to assess relative beam angles [21, 22]. Additionally, a unique phantom design has been described for gantry angle QA on the Elekta Unity MRL [65]. In that work, the phantom was used to confirm gantry angle accuracy for gantry 0.0° (G0) and G90. In theory the opposing angles could also be imaged and confirmed. Woodings *et al.* [21] discussed the use of a water surface to confirm gantry angles with MVI imaging, which is restricted to lateral angles only (G90 and G270). In the absence of specialized phantoms, a clinic will find difficulties with performing gantry angle confirmation at all desired projections; hence, a method needed to be devised to perform such measurements.

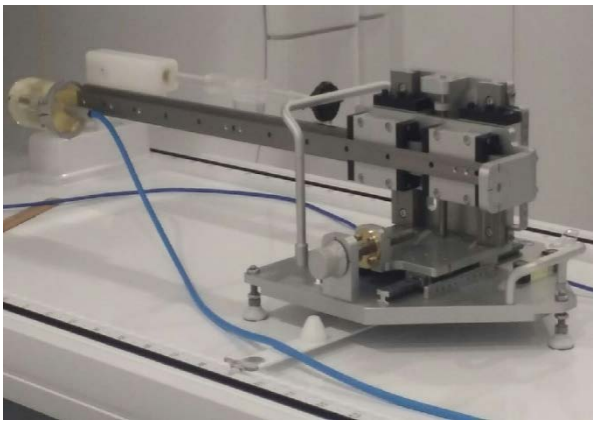

Figure 2.12: The tool used by Elekta, prior to clinical release, for cryostat characterisation and MV isocentre size determination

Cryostat Characterisation

The cryostat characterisation is measured during DAT before clinical release of the machine. It is a measure of cryostat attenuation as a function of gantry angle, relative to gantry 90.0°. It will vary between machines mostly due to differences in construction of the cryostat annulus; however, a small component will be due to differences in cryostat fill [22]. Elekta performs these measurements using the Cryostat Characterisation Tool (CCT), see Figure 2.12. An example cryostat characterisation is provided in Figure 2.13, and readers are referred to previous publications for other examples [19, 20, 59]. In general anterior beams have lower attenuation (higher characterisation values) due to the beam passing through less liquid helium from these projections. Furthermore, angles between ~ 8.0° to 18.0° are avoided due to the presence of the cross-over pipe [22]. The cryostat is modelled in Monaco TPS calculations as a homogeneous structure, with machine specific characterisations accounted for using a 2D lookup table (i.e. the measured cryostat characterisation), to adjust particle weights as they pass through the structure. In 2020 there was a spontaneous quench on the Unity system Townsville Cancer Centre (TCC), where the helium was rapidly exhausted and the magnetic field strength was reduced to approximately 0 T. After the quench, and subsequent magnetic field recovery, the helium fill of the cryostat could not be returned to its pre-quench level. Thus a slight difference in cryostat characterisation was expected, particularly around the top of the cryostat annulus, which could have required further planning system checks. Measurement uncertainty, due to chamber rotational effects or subtle machine output fluctuations (for example), could also contribute to potential variations between characterisations. This testing is included in Appendix A.

MVI Operation

In this work, and by other clinics, the MVI is extensively used in QA procedures for alignment of equipment and localization of the MV isocentre. Woodings *et al.* [21] and Roberts *et al.* [22] have both highlighted the importance of the MVI panel for QA

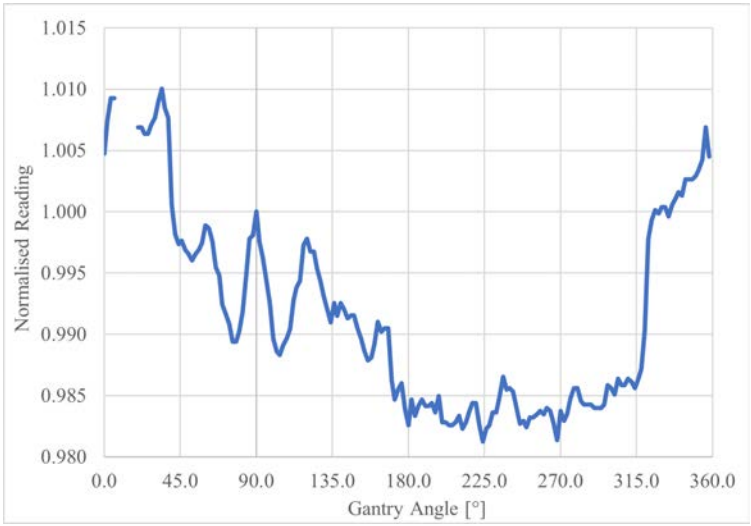

Figure 2.13: An example cryostat characterisation measured on the Elekta Unity at TCC

procedures. In Woodings *et al.* [21] extensive testing of the panel was highlighted and as such there was little scope for improvement in this area. Specifically, panel rigidity with gantry angle, rotation, pixel/image scale accuracy, coincidence of the centre pixel with isocentre and image quality was investigated [21]. It is worth noting for a line pair resolution surrogate test (Modulated Transfer Function, MTF), Woodings *et al.* [21] credits a previous publication [66]. Although there was lack of novelty for these test, given the importance of the panel it was felt that reproduction of some results of previous work [21] and the Elekta procedure was warranted in this work, using alternate methods. These are included in an appendix.

MV Isocentre

Measurement of the MV isocentre size on the MR-linac has been reported by several authors [19, 22, 67]. The method employed by Elekta during device acceptance tests (DAT) involves the irradiation of a ballbearing attached to the Elekta supplied Cryostat Characterisation Tool (CCT), see Figure 2.12. Images of the ballbearing projected onto the MVI panel are obtained at gantry angles 45.0°, 135.0°, 225.0° and 315.0° using four 5.7 × 5.0 cm^2 fields. These images are then forwarded to Elekta for analysis using the Radiation Isocentre Tool (RIT) software v6.6.64 (Radiological Imaging Technologies, Colorado Springs, Colorado, USA). During the in-house physics validation measurements, spoke shot films were obtained with Gafchromic^{TM} RTQA2 (Ashland ISP Advanced Materials, NJ, USA) film following the methodology proposed by previous groups wherein copper rings are introduced [22, 68]. The spoke shot dose distribution under the rings is less influenced by the interaction of electrons with the magnetic field, improving the precision of the isocentre determination in the X-Z plane.

The use of the MV alignment phantom (see Figure 2.14(a)) for measuring the MV isocentre size has been previously outlined by Snyder *et al.* [19]. In their study, MVI images of the central ballbearing were obtained using a 3.0 × 3.0 cm^2 field at gantry

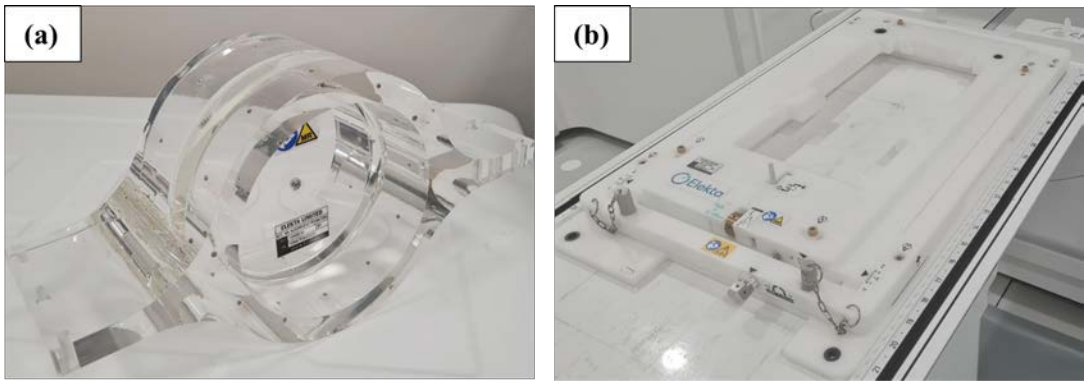

Figure 2.14: The Elekta supplied (a) MV alignment phantom and (b) QA platform used during MRL commissioning

angles of G0, G25, G40, G140, G160, G215, G225, G315 and G330. These images were analysed using the RIT v6.7.64 3D Stereotactic Analysis application [19]. Snyder *et al.* [19] avoided gantry angles of 60.0°-120.0° and 240.0°-300.0° due to issues with field edge detection in RIT, from distortion created by the mounting stands for the phantom [19]. Angles between 5.0° and 20.0° were avoided due to the cryostat cross-over pipe. This method is consistent with that recommended by Elekta during the physics validation stage of Unity commissioning.

Another option available to users for performing the MV isocentre size measurement on the Unity is with the Elekta supplied AQUA^{TM} software. Licences for this software are often provided with purchase of the Unity system; although, the use of this software suffers from the same angle restriction as that of Snyder *et al.* [19].

Unfortunately, the CCT may not necessarily be available to a clinic when MV isocentre measurements are required. Even with access to the tool, on-site access to compatible commercial software to analyse images may not be available. Having to send images off-site for analysis by Elekta is not ideal and common approaches using more readily available equipment, like the spoke shot, do not provide information about the MV isocentre in 3 dimensions. Utilising previously published methods requires a restriction of gantry angles, and ultimately may not represent the true isocentre size. Thus, there was a need for an in-house method to determine the MV isocentre size and location in 3 dimensions using the MV alignment phantom (Figure 2.14(a)) and QA platform (Figure 2.14(b)).

MR-to-MV Isocentre

The MR-to-MV Isocentre offset is measured during Set-to-Work (STW), and is routinely performed over the life of the machine [22]. The Elekta supplied MR-to-MV phantom (Figure 2.15) contains several ballbearings embedded in plastic rods filled with copper sulphate solution. The phantom can be simultaneously imaged with MR and the MVI from multiple gantry angles [19, 22]. The offset between ballbearing centres between the two imaging modalities is determined in the supplied QA Alignment software to give the MR-to-MV alignment offset. The offset is stored on the MOSAIQ sequencer

Figure 2.15: The Elekta supplied MR-to-MV phantom

and used during the fusion stage in the clinical workflow [19]; hence, it is important to check if these stored values will be applied correctly for a treatment. Moreover, the Elekta supplied phantom is approximately 22.0 cm in diameter. Due to the geometric distortion associated with MR imaging [37, 62, 69], the localization of ballbearings at the phantom peripheries could be susceptible to large errors. For this reason, and as an independent check on Elekta values, a method was needed to confirm the stored MR-to-MV isocentre offsets using a novel, smaller, in-house phantom, which is included in an appendix.

In-Bore Radiation Survey

When designing linear accelerators, manufacturers often have to meet specific tolerances, described in International Electrotechnical Commission Reports, for machine performance and basic safety. An example of such is the requirement for linac head shielding to reduce the beam to an acceptable level outside the primary area of irradiation. Given that MRgRT platforms have only recently been introduced in Australia, no region-specific standard is available for important characteristics such as radiation head leakage. However, Australian and New Zealand Standards (AS/NZS) are based heavily on such IEC reports [55, 56], and as such are not expected to vary significantly from the recommendations of the IEC [27].

Currently, only Woodings *et al.* [21] and Wang *et al.* [63] have reported on an in-bore radiation survey in a manner as discussed in IEC 60601-2-1 [27]. For the former [21], no data was presented for the survey; however, it was stated that results were within the IEC tolerances. Additionally, it is assumed that the survey was performed in a 1.5 T environment as no statement was made to the contrary. The presence of the magnetic field will change charged particle motion, and potentially detector response [5, 70], interfering with radiation survey results. It also assumed that only IEC 60601-2-1 test 201.10.101.3.3 [27] was performed by Woodings *et al.* [21] since results were quoted relative to these tolerances.

Wang *et al.* [63] performed head leakage and scatter measurements on the Unity in 0 T and 1.5 T environments. In their investigation, they used a large volume ionisation chamber to measure scattered radiation at several locations around the machine. Solid water was placed at the isocentre to simulate patient scatter. Furthermore, they investigated head leakage at 1.0 m from the linac head, in the direction of the maximum leakage as indicated from a film wrap. The effect of the magnetic field on the head leakage was less than 5.0 % [63]; however, significant changes to scatter dose were noted between 0 T and 1.5 T measurements. Wang *et al.* [63] only measured scatter and leakage readings at discrete locations, and a comprehensive investigation in the patient plane was not discussed. Furthermore, only a single dosimeter was used (an ionisation chamber) with other common survey devices, like film, not investigated.

Hence, it is clear that an in-bore radiation survey on the Elekta Unity warrants further investigation, following the IEC recommendations for BLD shielding (IEC test 201.10.101.3.2.1) in addition to that performed in Woodings *et al.* [21] and Wang *et al.* [63]. Comprehensive survey data, in 0 T and 1.5 T, is also needed against which other centres or governing bodies can compare. A published methodology for performing these tests is also needed.

2.2.4 Linear Accelerator Dosimetric Commissioning

Output with Gantry Angle and Anterior Coil Attenuation

During DAT, the cryostat characterisation is performed to determine the gantry angular dependent attenuation from this component [21, 22]. However, for this test the couch and bridge components are removed, inconsistent with the patient irradiation conditions. Therefore, it is advised that clinics perform their own determination of angular dependent output, consistent with treatment irradiation conditions (i.e. all attenuating components included in the measurement). With the higher density components of the couch, some beam attenuation could be expected when irradiating from gantry angles between 120.0° to 240.0°. Additionally, for all treatments on the Unity the anterior imaging coil is present above the patient and should be fully characterised in terms of it is dosimetric impact on treatment beams [20, 21]. This is not routinely performed by Elekta during DAT for individual installations, with a factory default for the RED applied in the TPS to model attenuation. A comparison of calculated and measured attenuation should be considered by other clinics implementing this machine. Although guidance has been suggested to perform these tests [21, 22], no methodology or data have been provided. To date, no known published data exists regarding the attenuation effect of the anterior coil for a variety of gantry angles; however, the magnitude of the effect is known by Elekta and other Unity users. Thus, the use of an in-house phantom to determine coil attenuation for a selection of gantry angles is described in this work, with results provided. Output with gantry angle was also determined with this phantom, and results are provided in an appendix.

Beam Quality

The beam quality specifier for the Elekta Unity MRL is the $TPR_{20,10}$ [5, 20, 29, 48], consistent with the recommendations of the TRS-398 protocol, and because of its insensitivity to the magnetic field and the extended SSD [5, 20, 48]. Due to the difficulties with measuring PDDs, a direct measurement of $TPR_{20,10}$ is preferred and with the presence of the cryostat, slight angular dependence of beam quality could be expected. With the quality dependent factors for reference output, a determination of this angular dependence should be evaluated with measurements.

Furthermore, profile shape is known to be more sensitive to beam quality changes than TPR or PDD metrics. Profiles are generally acquired in water, using a 3D scanning water tank: however, such a device is not available to all Unity clinics and, even if available is cumbersome for routine use. MR compatible profilers overcome these issues, and some groups have published on their use with the Unity [21, 71]. As well as can be determined, the use of the PTW Octavius 1500^{MR} array (PTW, Freiburg, Germany) for Unity profile measurements has yet to be published.

Beam Shape with Gantry Angle

The photon beam shape is measured during DAT with an Elekta supplied and maintained IC PROFILER-MR^{TM} (Sun Nuclear Corporation, Melbourne, Florida, USA) [21]. To accurately measure the beam shape at cardinal gantry angles requires the couch and bridge to be removed, and the Elekta supplied rotating platform to be inserted into the bore. The profiler is then inserted into the platform and measurements can be performed with the detector array perpendicular to beam delivery for all gantry angles, in addition to removing the effect of beam attenuation from the couch components. Not all clinics will be supplied with the rotating platform and furthermore, the removal of the couch and bridge, as well as handling of the platform, can be cumbersome. As such, for routine measurements this is undesirable and a need for another method to determine beam shape with gantry angles was apparent. This was addressed in this work using the Octavius 1500^{MR} array, and results are provided in an appendix.

Output Calibration

During DAT, on the recommendation of Elekta, the MRL was calibrated to give 1.000 Gy per 100 MU to isocentre, at 5.0 cm depth in water, for a 10.0×10.0 cm^2, G90, field. Measuring from G90 is the preferred methodology due to the constancy of the helium fill at this angle compared to acute anterior angles, like G0, where the output may vary depending on the level of helium. The choice of calibration depth was based on advice provided by Elekta to extend magnetron life; however, other users report a calibration depth of 10.0 cm to optimize output [19] thereby reducing treatment times.

For the TCC, the PTW 1D water tank (PTW, Freiburg, Germany) was used for output determination following a modification of the formalism proposed by van

Asselen *et al.* [5], discussed below. The use of this equipment, in combination with the van Asselen *et al.* [5] dosimetry protocol and calibration conditions (at 5.0 cm) is unique. Hence, no other researchers have presented on this technique and a clear gap in the literature was apparent.

Magnetic Field Correction Factors

There are currently two protocols in common use for reference dosimetry on the Elekta Unity MRL, that of O'Brien *et al.* [48] and van Asselen *et al.* [5]. They are similar, however separately discuss adaptions of the widely used TG-51 protocol [36] and TRS-398 [29] protocols, respectively, to account for magnetic field effects on dose determination. In either case, there are two physical factors in magnetic field dosimetry which vary from conventional (i.e. no magnetic field) protocols: the change in local dose deposition, due to the Lorentz force on secondary particles, and; the change in dosimeter reading, through alteration of the electron path length through the chamber and the change of electron flux entering the chamber cavity [5]. These factors are dependent on beam quality Q, magnetic field strength, chamber design and orientation with the magnetic field. The O'Brien *et al.* [48] formalism uses a single correction factor to account for these effects ($k^{Q}_{\vec{B}}$), where the magnetic field is shown as a vector to denote directional dependence with the chamber. Chamber correction factors were determined using Monte Carlo methods, for different chamber-field orientations (parallel $\parallel$, clockwise perpendicular and counter-clockwise perpendicular). In the van Asselen *et al.* [5] formalism the TRS-398 protocol is adapted with a dose conversion factor $c_{\tilde{B}}$ to account for the difference in local dose deposition, and a detector dependent magnetic field correction factor, $k_{\tilde{B},M,Q}$, accounting for the variation in chamber response. Note M denotes the chamber corrected charge reading, and the combination of the two factors reduces to that in O'Brien *et al.* [48]. For their work, $c_{\tilde{B}}$ was determined through simulations with the GPUMCD algorithm ($c_{\tilde{B}} = \frac{D^{\tilde{B}}_{w,Q}}{D_{w,Q}}$) and $k_{\tilde{B},M,Q}$ with measurements in 0 T and 1.5 T ($k_{\tilde{B},M,Q} = \frac{M_Q}{M^{\tilde{B}}_Q}$). Both groups investigated several chambers, including the PTW 30013 Farmer type chamber used in this work.

On the Elekta Unity, beam irradiation occurs perpendicularly to the magnetic flux and is often convenient to align chambers along this direction. Due to the direction of the Lorentz force, chamber factors for this orientation are typically smaller [5, 48]. Since the van Asselen formalism [5] is used in this work, the factors of interest were $k_{B_\parallel,M,Q}$ and $c_{\tilde{B}}$. O'Brien *et al.* [48] showed that the change in local dose deposition due to the magnetic field is constant from depths ranging from 5.0 cm to 25.0 cm. Both groups [5,48] showed that this factor was of the order of 0.5 %, or a correction 0.995 (i.e. the magnetic field decreased the local dose deposition). These factors were determined for the more common reference dosimetry conditions (isocentre at 10.0 cm depth or SSD of 133.5 cm). Although not expected to vary significantly, the determination of $c_{\tilde{B}}$ for use at a 5.0 cm calibration point (SSD = 138.5 cm) is warranted.

It is common for beam quality to be determined from G0 and reference dosimetry from G90. Some uncertainty in $k_{B_\parallel,M,Q}$ could be expected if the change in beam quality

between the gantry angles is not considered. Pojtinger *et al.* [72] has showed, with Monte Carlo modelling, that there is little change in such a factor with beam quality; however, measurements to confirm this may be warranted given inherent variabilities in such modelling [72, 73]. Again, with the variation in depth between this work and those of previously published users [5, 48], arguments against the use of the published $k_{B_\parallel,M,Q}$ value for calibration at 5.0 cm depth can be made. O'Brien *et al.* [70] has previously showed that ionisation chamber responses typically only vary with depth for small fields (below 2.0×2.0 cm^2). It was also shown that in a 10.0×10.0 cm^2 field the depth dependence of the PTW 30013 chamber, in a magnetic field, did not vary significantly from a nominal solid-state detector. Nonetheless, it was still determined prudent in this work to investigate any depth dependence of the $k_{B_\parallel,M,Q}$ factor for the specific PTW 30013 chambers used at TCC.

MR Interference on Linac of an Elekta Unity

The presence of the MR system introduces potential sources of error in the linear accelerator behaviour. With the strong magnetic field, and the complicated electrical subsystems of the linac, interference from the MR system could be expected. Woodings *et al.* [21] discussed several tests which could be performed to highlight this interference. In their work, output and profiles were acquired with and without operation of a variety of MR sequences. Film was used to determine profiles for a rectangular field (field size not stated) from G0, with the MVI used to capture profiles for an 18.0×7.0 cm^2 field at cardinal gantry angles. The maximum reported difference was 1.1 %, for film, and was quoted to be within film and beam delivery uncertainty. Ion chamber readings were also acquired (field settings omitted) and were reported to vary 0.13 % between MR operational states. Although a comprehensive set of tests were performed, little information was provided for the methodology and equipment used. Information on film analysis and calibration was not provided. Furthermore, assurance of MLC segmentation with MR operation was not performed. Thus the need to repeat these measurements was apparent, with and without the MR operation, with comparison to the work of Woodings *et al.* [21].

IMRT Commissioning

Typically, as part of the Elekta beam validation procedure, nine vendor IMRT plans based on AAPM TG-119 [74] guidance are imported to the Monaco TPS and delivered on the Unity system. Elekta recommended gamma criteria [58] of 3.0 % (global/max dose), 3.0 mm distance-to-agreement (DTA) during beam validation with the ArcCheck®-MR device (Sun Nuclear, Melbourne, FL, USA). The Elekta Unity is capable of stereotactic delivery, and this functionality needed to be tested as it was to be used clinically. None of the nine supplied plans focused on stereotactic deliveries for QA, a noticeable deficit in process. Additionally, the gamma tolerance suggested during validation was not considered adequate and varied from departmental tolerances (2.0 % local dose, 2.0 mm DTA, 10.0 % dose threshold, pass rate $>$ 95.0 %)

and international guidance (3.0 % global dose, 2.0 mm DTA) [75]. Furthermore, the ArcCheck®-MR device was not available during commissioning at TCC, which may be common when other clinics are implementing this machine, requiring alternate methods to be developed. For these reasons, the Elekta provided methods, tolerances and expected pass rates were not applicable during IMRT commissioning at TCC, warranting further investigation.

Gamma results of the TG119 plans delivered to the ArcCheck®-MR device have been reported by previous investigators for 2.0 % (global dose), 2.0 mm DTA [76] and 3.0 % (global dose), 2.0 mm DTA [19, 57, 76], for which average gammas were above 95.0 %, compared to TPS calculations. These criterion are less strict than that proposed in this work. Alternative devices which have been investigated in magnetic fields are radiosensitive film [16, 77–80] and the Octavius 1500$^{\text{MR}}$ array [81]. Both of these were available to TCC at the time of commissioning.

Wen *et al.* [80] used film for IMRT QA procedures on the ViewRay system, with a clear methodology stated; however, specific for the Unity MRL are the works of Werensteijn-Honingh *et al.* [79] and Raaymakers *et al.* [16]. In the former [79], the feasibility of pelvic stereotactic treatments on the Unity was of focus, and their discussion of patient specific QA procedures was limited. Gamma results against the TPS, at 5.0 % (global dose), 2.0 mm DTA and 10.0 % threshold, had average pass rates of 99.9 % for thirty plan deliveries. Similarly, Raaymakers *et al.* [16] omitted specific methodologies for film QA procedures; however, it is assumed from their results that coronal planes were acquired in a polystyrene block. For their work [16], the mean gamma pass rate for twenty commissioning plans was 98.8 % at 3.0 % (global dose), 3.0 mm DTA, with a minimum value of 92.2 %.

In Mönnich *et al.* [81], IMRT QA procedures were performed with beams delivered to the 1500$^{\text{MR}}$ array inside an octagonal prism phantom. In that work, patient beams were delivered to the array rotated to cardinal angles, with choice of orientation dependent on planned gantry angle. Deliveries were assessed, against TPS calculations, with 3.0 % (local), 3.0 mm DTA gamma criteria and pass rates were mostly above 90.0 %, with the lowest reported average pass being 88.6 %. It is highlighted that this criteria is also less strict than that currently employed locally.

As stated, changes to the Elekta beam validation process were required for TCC, with alternate equipment. In-house developed stereotactic plans were developed for commissioning of IMRT plans, in addition to Elekta supplied plans. The departmental criteria of 2.0 %, 2.0 mm was employed instead of the Elekta suggested 3.0 %, 3.0 mm or other reported values [16, 19, 75, 76, 79, 81]. Furthermore, in absence of the ArcCheck®-MR, the Octavius 1500$^{\text{MR}}$ array and Gafchromic$^{\text{TM}}$ EBT3/EBT-XD film (Ashland ISP Advanced Materials, NJ, USA) were utilized. The literature review suggested passing rates below 90.0 % at 3.0 % (local), 3.0 mm DTA could be expected for the former [81] and below 95.0 % (3.0 % global, 3.0 mm DTA) for the latter [16]. However, the use of these dosimeters, with the methodologies proposed in this work, had yet to be published on for the Unity MRL.

End-to-End

Elekta provides phantoms for End-to-End (E2E) testing on the Unity during the Physics Validation stage; however, a clinic may want to perform their own measurements for routine QA and, for example, during treatment site commissioning. Purchasing specific phantoms for individual site development can be expensive and furthermore, a centre may not have ready access to commercial phantoms for adaptive radiotherapy E2E testing.

Commercial phantoms for E2E purposes on MRgRT platforms have been presented by several groups [19,82–85]. Chen *et al.* [82] discussed daily adaptive E2E procedures for the Unity using the Elekta supplied MR-to-MV phantom, to confirm connectivity and performance of the Unity and associated computer systems. The phantom was simulated (online) and an adapted plan created and delivered; however, dosimetric accuracy of the delivery was confirmed using the MVI panel (attached to the MRL), instead of with an independent dosimeter. Although adequate for daily E2E procedures, and potentially easy to implement given the availability of equipment, this process was felt insufficient as part of a commissioning procedure.

In Pappas *et al.* [83], 2D and 3D E2E dosimetry was performed on the Unity with commercial, 3D-printed, head phantoms [86] and film (2D) and radiosensitive gel (3D) [87,88]. Gamma analysis was used for both 2D and 3D methods, and plan metrics (i.e. homogeneity index, target coverage etc.) were directly measured with the 3D gel and compared to TPS values. Although more informative than 2D methods, gel dosimetry is not available at TCC. Nonetheless, gamma results for their 2D film measurements were above 90.0 % at 2.0 %, 2.0 mm DTA, 20.0 % dose threshold for both original and an ATP created plan. Results for gamma analysis using a 3.0 %, 3.0 mm DTA criteria were approximately 98.0 %, for both plans.

Snyder *et al.* [19] presented E2E results on a commercial thorax phantom (CIRS, Norfolk, VA, USA) and a Head and Neck phantom provided by Imaging and Radiation Oncology Core (IROC, Houston, TX, USA). The former is the phantom provided by Elekta during validation; however, was not available to TCC for routine measurements. With the IROC phantom, Snyder *et al.* [19] performed measurements with film and thermoluminescent devices (TLDs), and compared to TPS simulations. Interestingly, pass rates of 98.0 % on two films were reported (for a single ATS created plan) at 7.0 % (global), 4.0 mm DTA. This is clearly a less strict criteria than other publications using film [83, 89]; however, the authors did highlight it was consistent with IROC credentialing standards [19]. TLD measurements were within 1.0 % of TPS calculations for most points, with one outlier at 4.0 %. Although, the uncertainty quoted for such measurements was 5.0 % [19]; larger than that known for the film dosimetry process at TCC (approximately 2.0 %).

Alternatives to commercial phantoms have been successfully developed and employed in-house by several groups [80,84,89,90]. The work of Bernchou *et al.* [89], was of interest for this investigation. In that study [89], EBT3 film was set inside a 3D printed, MR visible, E2E phantom. ATP and ATS plans were created and delivered

to the phantom in E2E workflows, and the geometric accuracy of the delivery was assessed against the TPS. This was performed using MATLAB® code (MathWorks, Natick, MA, USA), with an in-built function to determine the mutual information similarity metric. Geometric accuracy of ATP and ATS deliveries was better than 1.0 mm [89]. However, Bernchou *et al.* [89] discussed a limitation of their work being that the phantom had no adaptive components, like those of other groups [84, 85, 90].

3D-printing can be a comparatively cheap option for the production of in-house phantoms, to alleviate the issues discussed above with commercial phantoms, and is readily available at TCC. 3D printed materials have been extensively used in conventional radiotherapy applications [91–93] and their use in MR-guided radiotherapy (MRgRT) systems has seen much development [83,89,94,95]. For these reasons a novel, in-house designed phantom, with 3D printed components was used for E2E measurements for future baseline comparisons. The results of previous investigators [83, 89] indicated that film dosimetry could be utilized for this endeavour. Although TLDs were available, they have increased uncertainty compared to film [19] and as such were not used in this work. Successful implementation of in-house developed E2E phantoms by other groups [89, 90] suggested the process was feasible for the TCC.

2.2.5 Out-of-Field Doses

Spiralling Contaminant Electrons

With the orientation of the static magnetic field to the beam direction of the Elekta Unity, the effect of the Lorentz interaction on dose deposition in tissue and at planar tissue-air interfaces has been investigated [42, 44]. For such interfaces the situation in which electrons generated in tissue enter air orthogonal to the interface has been reported. In the case of the Elekta Unity 7 MV FFF beam, these electrons have an average energy of 500.0 keV and follow a circular path, radius approximately 2.2 mm, and return to the tissue surface [42]. Due to this electron return effect, dose at and within the exit surface is increased significantly and this has implications for skin dose in MRgRT [42].

In general, secondary electrons exiting a tissue-air interface or contaminant electrons in the primary photon beam have directions of motion that result in more complex trajectories relative to B_0. The interaction of contaminant electrons associated with the Elekta Unity beam has been investigated [9]. In that work a 10.0×10.0 cm^2 field, gantry zero, was used to determine dose 5.0 cm beyond each field edge in the isocentric plane. EBT3 film aligned to capture profiles in that plane was used to measure dose parallel to each field edge at depths 0.0 – 6.5 mm in a solid water phantom. The observed variation of dose with depth exhibited an elevated surface dose relative to that below approximately 3.0 mm for films orientated perpendicular to B_0. Based on this observation it was suggested that contaminant electrons in the primary beam had spiralled parallel and antiparallel to B_0 producing a surface dose around 5.5 % of D_{max} [9].

Monte Carlo simulations modelling the same experimental setup on a Unity linac have been used to investigate out-of-field dose (OFD) due to these spiralling contaminant electrons [96]. Such simulations, using the EGSnrc Monte Carlo package [97], show that surface dose is approximately 1.0 % of D_{max} with 0 T and approximately 4.0 % of D_{max}, in the direction of SCE, with 1.5 T. The work of Malkov *et al.* [96] also addressed the effect of the magnetic field strength on SCE doses. Based on measured and simulated surface dose it has been suggested that SCE is a source of OFD on the Unity and other systems involving x-ray beams with transverse magnetic fields should exhibit SCE dose. SCE dose would contribute to OFD to the chin and neck from chest treatment fields and should be reviewed as part of treatment plan quality assurance [9].

Notably with previous work [9, 96], there is a lack of measured data available for 0 T measurements. The Monte Carlo simulations of Malkov *et al.* [96], whilst comprehensive and benchmarked against 1.5 T measured data, could be susceptible to error. The phase space files upon which these calculations are based were initially only developed with 1.5 T considerations and, given the drastic change in charged particle motion, may not be suitable for use in a 0 T simulation. This was attempted to be addressed by this work.

Furthermore, to date no modelling of this effect has been performed using the Monaco TPS. In-field characteristics of the Monaco GPUMCD have been benchmarked against Geant4 simulations [6], and directly against linac measurements [46]. However, treatment planning systems typically have to use approximations for computational efficiency and this could have significant impacts on out-of-field dose characteristics. Monaco is the primary tool which clinicians will use to assess patient doses when using the Unity, hence it is important to confirm accurate dose calculation to all areas. Comparison of Monaco calculated OFD, in 0 T and 1.5 T, against measured data was therefore investigated.

Electron Streaming Effect

The Electron Streaming Effect (ESE) has previously been shown to be a larger effect than SCE [8,23–26,98]; however, there is currently little available ESE work specific to the Elekta Unity MRL design [8,24,25]. Park *et al.* [23] reported on out-of-field doses to the jaw and ipsilateral shoulder approaching 16.0 % of the treatment prescription dose during accelerated partial breast irradiation (APBI) on an MRIdian system. Such large doses were attributed to secondary electrons escaping breast tissue when the treated lesion is in proximity (within 5.0 mm) to the breast surface. Electrons entering air in APBI experience a transverse magnetic field and spiral superiorly, creating an electron stream, as well as contributing to skin dose through ERE [23].

Nachbar *et al.* [24] investigated similarly to Park *et al.* [23] for a partial breast irradiation (PBI) treatment on the Elekta Unity. A dose of 6.5 % (of the prescription dose) to the chin was predicted from Monaco TPS calculations for a 40.05 Gy in 15 fraction treatment, to a lesion within the patient breast (~ 5.0 mm depth). The cause of this dose was as above with electrons entering air and spiralling along the field lines

to reach the chin. Nachbar *et al.* [24] report on efficacy of 1.0 cm bolus to shield this dose, as discussed previously by others [8, 23, 26].

Zhang *et al.* [25] also measured OFD on an anthropomorphic phantom with an MR system (Unity) and a conventional system (VitalBeam, Varian Medical Systems, Palo Alto, CA, USA). Additionally they performed measurements on solid water around square fields of various sizes. For the latter measurements, dose was measured in the X-Y plane (isocentre height) nominally along these axes. They used optically stimulated luminescent devices (OSLDs), and compared against Monaco TPS calculations. For the treatment regions (head, thorax and pelvis), measured versus TPS doses disagreed between - 35.0 % (TPS underestimating measurements) to 270.0 %. This was for doses between 2.0 % to 5.0 % of the prescription dose 20.0 Gy. For their work [25], OAR doses (internal) and surface doses were considered; however, a clear distinction was not made between these as to where the TPS either under or overestimated dose. Measurements highlighted an increase in OFD on surfaces, due to the magnetic field, of up to 21.0 %; however, the authors did highlight differences in machine designs could have contributed to some of this discrepancy [25]. For the simple phantom geometry, doses up to approximately 5.0 % were observed for OFD around a 10.0 × 10.0 cm^2 field, consistent with that reported for SCE. This was for both X and Y directions, in contrast to above researchers [9] where this magnitude was only apparent in the direction of SCE (± Y). However, given the measurement geometry differences, this discrepancy is unsurprising.

Malkov *et al.* [8] performed Monte Carlo simulations of the electron streaming effect for the Elekta Unity MRL design. In their work, trapeziform water phantoms were simulated with different magnetic fields (0 T, 0.35 T and 1.5 T) orientated orthogonally to primary beam direction. Dose from electron streams, from the beam entry and exit through the sloped surfaces of the phantom, was determined for these magnetic fields. Further simulations were performed to assess how OFD changes with field size (10.0 × 10.0 cm^2 and 2.0 × 2.0 cm^2 fields), distance from beam entry/exit, phantom thickness and angle of phantom surface to the beam (10.0°, 30.0° and 45.0°). OFD between 15.0 % and 40.0 % of D_{max} were predicted, dependent on the above.

Liu *et al.* [26] investigated doses to the chin and neck for oesophageal radiation therapy on the Unity. In their investigation, three plans for an oesophagus treatment were investigated in Monaco (with magnetic field, similarly with bolus and a plan without magnetic field). They found increased doses to the chin (up to 5.0 % of the prescription dose 40.0 Gy) and neck (up to 10.0 %) due to the magnetic field causing ESE. Additionally, they found the use of 1.0 cm of bolus to shield ESE doses produced results comparable to that of the non-magnetic field scenario [26]. Unfortunately, this work is focused on clinical scenarios and no direct measurements of ESE dose on the Unity were performed.

From the literature review it was clear that there is a lack of a systematic determination of measured ESE doses for simple geometries on the Elekta Unity MRL. Comparisons between 0 T and 1.5 T data have been made using Monte Carlo methods,

susceptible to errors in simulation conditions, and whose use in 0 T on the Unity has yet to be validated with measurements. Assessments of Monaco TPS calculations of ESE have been attempted by investigators, yet have been focused primarily on clinical cases with a systematic study using simple fields and beam/phantom geometries (like those for previous Monte Carlo investigations [8]) lacking. In this work, a systematic comparison of measured and TPS simulated ESE is presented, to address these issues. Clinical cases of OFD due to ESE (and SCE) were also investigated in this work; however, are provided in an appendix.

2.3 Summary

In summary, medical linear accelerators are clearly intricate and complex machines whose operation must first be verified before clinical use. This is particularly important for MRgRT systems, where the presence of the MR can interfere with machine operation and radiation characteristics. Commissioning work is lacking in terms of variety of test methodologies and equipment, as well as available data against which other clinics can benchmark their systems. Additionally, investigations of OFD on the Elekta Unity are lacking, and there is a lack of available 0 T data against which SCE and ESE doses can be compared. Finally, a systematic evaluation of the accuracy of Monaco OFD modelling (0 T and 1.5 T) is warranted.

3

Mechanical and Safety Commissioning

This chapter contains material which was published in the following article:

[1] Marcus Powers, John Baines, Robert Crane, Chantelle Fisher, Stephen Gibson, Linda Marsh, Bronwyn Oar, Ariadne Shoobridge, Emily Simpson, Page Marchant, and Van Der Walt Glenn. Commissioning measurements on an Elekta Unity MR-Linac. *Physical and Engineering Sciences in Medicine*, **Online** (2022). doi:10.1007/s13246-022-01113-7

Additionally, some material in this chapter is intended to be submitted with John Baines as co-author:

- Marcus Powers and John Baines. In-bore radiation survey performed on the Elekta Unity MRL. Target journal: Physical and Engineering Sciences in Medicine. *(In draft)*

Some data presented below was acquired with Jason Arts of Elekta, using Elekta supplied equipment. Robert Crane developed the MATLAB® analysis code for MV isocentre analysis. All other work described in this chapter is my own unless otherwise stated.

3.1 Introduction

In this chapter, the commissioning tests performed on the mechanical and safety components of a clinical Elekta Unity MRL are presented. Previous investigators have published on similar data [19, 21, 22]; however, the methods for such tests can vary

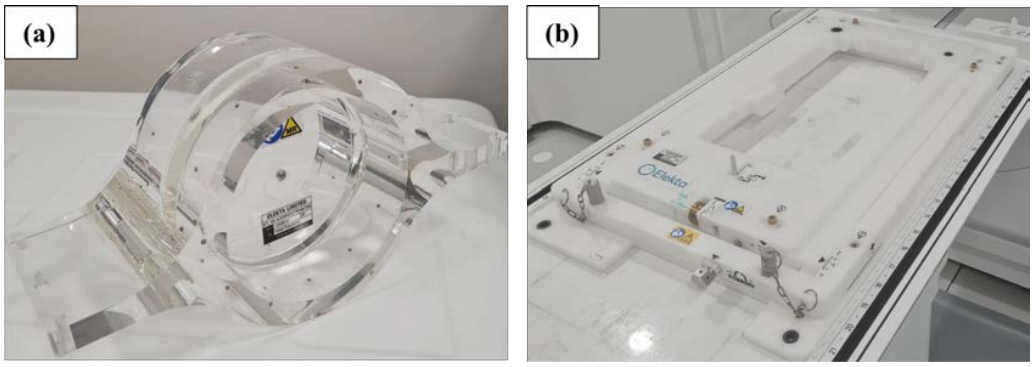

Figure 3.1: The Elekta supplied (a) MV alignment phantom and (b) QA platform

between clinics. Hence, the novelty of this work is in the methodology and analysis of test results. Less novel results are provided in Appendix A.

Unique adaptations of vendor supplied phantoms are presented which facilitated independent verification of common commissioning measurements, for example gantry angle accuracy and MV isocentre determination. The use of in-house phantoms reduced costs, and in some cases, mitigated the lack of a commercial alternative. Other clinics can reference this work for guidance. Radiation survey results have been presented by other authors [21, 63]; however, comprehensive data was not provided. With a ramp down event, a radiation survey in 0 T was able to be attempted with equipment that is not MR-safe/conditional. It is hoped the following work can be used by clinics when performing mechanical and safety commissioning tests on an Elekta Unity MRL.

3.2 Methods

3.2.1 Gantry Angle

The vendor supplied phantom shown in Figure 3.1(a) facilitates determination of several machine mechanical characteristics. This cylindrical, acrylic phantom contains a centrally located 10.0 mm diameter ballbearing. At each end are two arrays of twelve 4.0 mm ballbearings, radially arranged at 30.0° intervals, offset from the centre by ± 3.5 cm in the Y direction. With this phantom positioned on the Elekta supplied QA platform (see Figure 3.1(b)) images of the phantom on the mega-voltage imager (MVI) were obtained at the cardinal gantry angles using 20.0×9.5 cm^2 fields, 20 MU. Images were analysed using vendor supplied software to determine the offset of the phantom from the radiation isocentre (translations and rotations). These offsets were used to reposition phantom using the QA platform with X, Y and Z vernier adjustments. Additional MVI images were used to re-assess the phantom position until the offsets were less than 0.2 mm and 0.2° in all directions. The phantom was then shifted ± 3.5 cm in the Y direction, so that the centre of a given array of ballbearings was nominally at the isocentre.

MVI images of the phantom were obtained with the gantry angle varying from 0.0° (G0) to 360.0° in 30.0° increments using a 10.0×10.0 cm^2 field, 50 MU. Each image

showed diametrically opposed ballbearings at the centre, as well as projections of off axis ballbearings at the peripheries. A self-levelling laser was used to verify that ballbearings at twelve and six o'clock were aligned vertically within the phantom. Visual inspection of the images from each angle was performed to confirm that diametrically opposed ballbearings were eclipsed, producing an image of a single ballbearing. For all measured angles, the separation between ballbearings at the image peripheries was also assessed for consistency between rotations. MVI images were obtained with the gantry rotated 1.0° in both directions from vertical, in increments of 0.1°, to assess the resolution of the central and peripheral ballbearings. For these projections, gantry angle change was measured with a digital Clinotronic PLUS inclinometer (Wyler AG, Winterthur, Switzerland) between each rotation to confirm the relative shift from G0. The inclinometer was placed at a fixed position on a convenient surface of the gantry ring.

In addition to visual inspection of the images, pixel value profiles were extracted using ImageJ v1.53a (NIH, Bethesda, MD, USA) [99]. Profiles through the centre of all ballbearings, in each MVI image, were obtained for all delivered gantry angles and compared to that for the G0 image. For the deliberate misalignment of the gantry from the vertical, it would be expected that pixel profiles shapes would vary from that of the G0 image. Additionally, as a first-order approach, profiles taken through the images at 30.0° increments could be assessed against those with the deliberate sub-degree offsets to confirm rotational accuracy within published tolerances [21, 22].

3.2.2 MV Isocentre Diameter

For the determination of the MV isocentre size, the MV alignment phantom (Figure 3.1(a)) was mounted on the QA Platform and aligned to the isocentre using the methodology described above. Note that the vendor alignment software for positioning the phantom at isocentre does not report an isocentre size. With the centre of the phantom at isocentre, the central ballbearing was projected onto the MVI using 5.0×5.7 cm^2, 50 MU, fields every 10.0° for gantry angles ranging from 0.0° - 360.0°. In contrast to the methodology used by Snyder *et al.* [19] and Elekta, gantry angles of 10.0° and 20.0° were avoided (due to the presence of the cryostat cross-over pipe that provides electrical connection between the split coils), as well as angles of 60.0° and 300.0° (due to image distortion resulting from beam transmission through couch edges). Images with the gantry rotating in both directions were obtained in a single sequence, for a total of sixty-nine projections. The images were exported from the MVI computer and analysed with in-house MATLAB® code (MathWorks, Natick, MA, USA). Vertical and horizontal pixel intensity profiles were extracted from each MVI image to determine the ballbearing position.

When imaging from 130.0° to 50.0° and 310.0° to 230.0°, the phantom, QA platform and couch edges created distortion in the images. To minimize this effect, horizontal background pixel profiles just above and below the ballbearing were acquired for a given projection, averaged, and then subtracted from the horizontal profile through

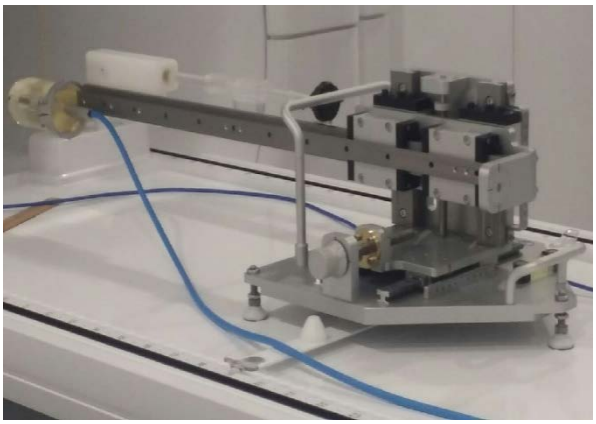

Figure 3.2: An image of the cryostat characterisation tool (CCT) with the Farmer chamber and build-up cap attached

the ballbearing. The full-width, half-max (FWHM) of the ballbearing profile was then more accurately determined from the resulting profile. The centre pixel of the FWHM peak was compared against the MVI central pixel, at each projection, to determine the MV isocentre size. Note that coincidence of the MVI central pixel with the isocentre was performed by Elekta prior to DAT, the method for which is outside the scope of this work. Routine use of this technique requires accurate and consistent alignment of the beam line with the beam limiting device (BLD) and MVI panel (at multiple angles), and this should be ensured by clinics before adopting this method. However, this is not expected to vary significantly once established [21, 67]. For context, on the TCC Unity system the maximum variation of the central pixel (from G0) since commissioning is less than 0.7 pixels, where 1.0 pixel is approximately 0.22 mm.

To compare with Elekta results acquired during DAT, measurement of the isocentre size using the in-house method was also performed with the Elekta supplied cryostat characterisation tool (CCT), Figure 3.2. Furthermore, the method of Snyder *et al.* [19]was replicated with the MV alignment phantom. Isocentre sizes were compared between phantoms, beam sequences and magnetic field environments. During the in-house physics validation measurements, spoke shot films were obtained with Gafchromic^{TM} RTQA2 (Ashland ISP Advanced Materials, NJ, USA) film following the methodology proposed by previous researchers, wherein copper rings are introduced [22, 68]. The spoke shot expsoure under the rings is less influenced by the interaction of electrons with the magnetic field, improving the precision of the isocentre determination in the X-Z plane. These results are also provided for comparison.

3.2.3 In-Bore Radiation Survey

During a ramp down event in 2021, a radiation survey in the isocentric plane was performed. Measurements were made using EBT3 film (Ashland ISP Advanced Materials, NJ, USA), Optically Stimulated Luminescent Devices (OSLD, LANDAUER®, Glenwood, IL, USA) and a PTW 30013 Farmer chamber (PTW, Freiburg, Germany). EBT3 film and OSLD measurements were acquired concurrently. Dosimeters were

Figure 3.3: Experimental setup for in-bore radiation survey, with positive X and Y axes shown. The survey metre displayed in the image was not used for measurements

placed atop several stacks of solid water, $30.0 \times 30.0 \times 14.0$ cm^3, placed along the length of the couch (~ 2.0 m). Multiple film strips of 2.0×25.0 cm^2 were placed, end to end, extending to $\pm$ 100.0 cm from isocentre along the Y-axis. Due to the size restrictions of the bore, film could only be positioned up to $\pm$ 30.0 cm along the X-axis. OSLDs were placed at isocentre, and in $\pm$ 10.0 cm steps from here to $\pm$ 100.0 cm, along the Y-axis. In the X-axis, OSLDs were located only at $\pm$ 10.0 cm and $\pm$ 30.0 cm, due to a limited supply. 10.0×10.0 cm^2 fields were delivered from G0 to the experimental setup. 2000 MU was delivered to the dosimeters within $\pm$ 10.0 cm of isocentre, and 10,000 MU elsewhere to (a) avoid saturation of the central dosimeters and (b) obtain measurable at large off-axis distances. An image of the setup is shown in Figure 3.3.

For film calibration, several 2.0×5.0 cm^2 strips of film were placed atop 14.0 cm of solid water aligned to isocentre using MVI images. 5.0 cm of solid water was added as build-up and a 10.0×10.0 cm^2, G0 field was delivered to individual film pieces for 5, 10, 30, 60, 125, 250, 500, 1000 and 2000 MU. Film was processed using an Epson 12000XL Expression flatbed scanner (75.0 dpi), FilmQA™ Pro v5.0 software (Ashland ISP Advanced Materials, NJ, USA) and triple channel analysis [100]. Corrections were applied to account for the lateral response of the scanner [101]. A central 1.0×1.0 cm^2 region of interest (ROI) on each calibration film was used to determine mean pixel values for the exposures. Along each film strip, a 0.3×25.0 cm^2 ROI was used to determine the dose delivered to the film. These doses were normalised (and weighted by MU) to the dose derived for a 1.0×1.0 cm^2 ROI at the isocentre, to determine out-of-field dose. OSLDs were processed using a microSTAR®ii Dosimetry Reader (LANDAUER®, Glenwood, IL, USA), with count response multiplied by the individual sensitivities of the devices. Note that OSLD calibration was performed using a generic, pre-determined sensitivity value for each device. Similarly to film, OSLD readings out-of-field were normalised (and weighted by MU) to the central axis reading.

For chamber readings, the device was placed atop a solid water stack such that the chamber reference point was at isocentre height. The Farmer chamber was initially positioned with its long axis perpendicular to the Y-axis, to limit volume averaging

in this direction. Using MVI images from G0 and G90, the chamber reference point was aligned to isocentre. A 10.0 × 10.0 cm^2, 100 MU field was delivered and the charge reading was recorded. Using the couch drive, the chamber was shifted off-axis in 10.0 cm increments up to ± 100.0 cm and readings were obtained for the same field geometry; however, MU was varied between shifts to improve chamber response. For all readings, the chamber build up cap was on. The chamber was then rotated such that the long axis was parallel to the magnetic field direction, and realigned to isocentre using MVI images. Readings were acquired at the same locations as that above for the OSLDs along the X-axis. To offset the chamber the required X distances, the solid water upon which the device was mounted was shifted laterally on the couch. All chamber readings were normalised to that at the central axis, and weighted by MU, as described previously for film and OSLD measurements.

Since it was possible for metal blocks to be used on the machine in the 0 T environment, the measurements were repeated with some modifications. Metal alloy blocks were placed on the couch at isocentre in the X-Y plane to reduce the radiation through the residual field in a manner similar to that recommended in IEC 60601-2-1 [27]. The chamber was positioned as previous for the Y-axis measurements, this time atop 14.0 cm thick alloy blocks instead of solid water. Measurements were repeated for + 10.0 cm, + 30.0 cm and + 50.0 cm from isocentre with the same field as previous; however, due to the difficulties with stabilization of the metal blocks, all readings were acquired from G180, instead of G0. Readings were also acquired from G180 to the Farmer chamber at isocentre, suspended over the edge of a solid water stack, and the alloy blocks removed. Initially, this reading was to be used for normalisation; however, the couch attenuates the beam when irradiating from G180 and a G0 reading is better suited. Hence, this G180 reading was corrected for couch attenuation (Appendix A.5) and cryostat differences (Appendix A.5). This gave an approximate, unattenuated G0 reading to which remaining G180 readings could be normalised.

IEC 60601-2-1 recommends that absorbed dose be used for leakage radiation calculations, with normalisation to the reference absorbed dose [27]. In an attempt to replicate these conditions, for all devices, an additional normalisation procedure was employed. Doses recorded by film and OSLDs were normalised to the nominal D_{max} dose to water, for a 10.0 × 10.0 cm^2 field, delivered from G0 with 2000 MU, at an SSD of 142.2 cm and in a B = 1.5 T environment. Chamber readings were normalised to the nominal charge that the chamber would have received for that same field, through application of a previously determined tissue maximum ratio (TMR).

3.3 Results

3.3.1 Gantry Angle

Representative MVI images of the gantry angle measurements are shown in Figure 3.4. Images have been auto enhanced within MVI to highlight pixel value gradients. With a set gantry angle of 270.0° the inclinometer measured an angle of 270.02° and the set

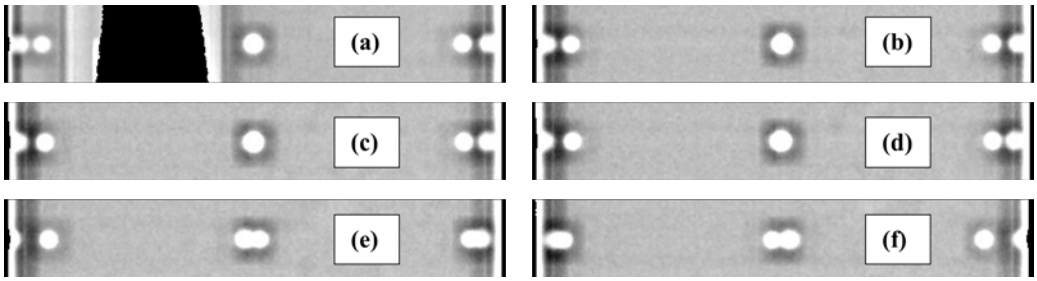

Figure 3.4: MVI images of the superior outer ring of ballbearings on the MV alignment phantom, for gantry angle testing. Gantry angles of (a) 270°, (b) 0.0°, (c) 0.2°, (d) 0.3°, (e) 1.0° and (f) 359.0° are presented

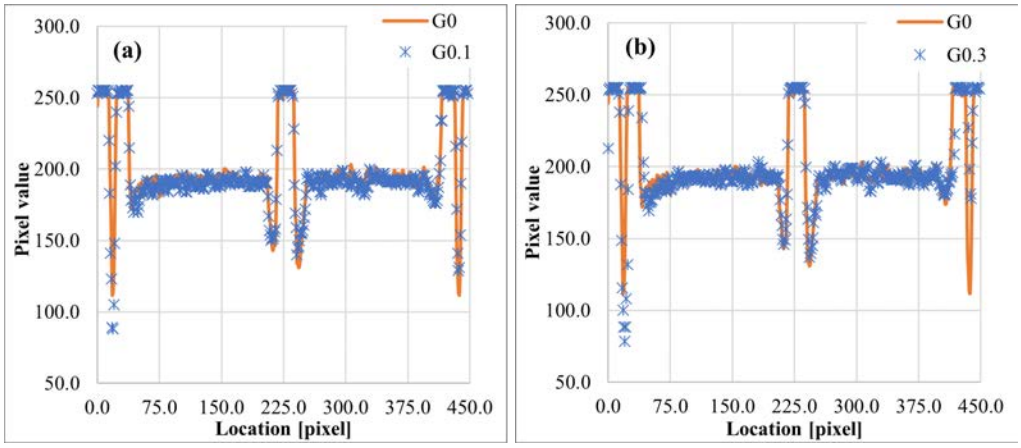

Figure 3.5: Comparison of profiles, for gantry angle tests, taken left to right from MVI images for the ballbearings at (a) G0 and G0.1 and (b) G0 and G0.3

angular shifts from 0.0° were also confirmed to be within ± 0.02°. The attenuation effect of the acrylic phantom is apparent in the 270.0° image (Figure 3.4(a)). Images every 30.0° from gantry zero were indiscernible from the G0 image, Figure 3.4(b), except for G270 and G90 where the thicker acrylic component of the phantom was being imaged (see Figure 3.1(a)). Diametrically opposite ballbearings were eclipsed for those images. Additionally, pixel intensity profiles for three angles are given in Figure 3.5 (G0, G0.1 and G0.3).

3.3.2 MV Isocentre Diameter

Results for the various isocentre measurement techniques are presented in Table 3.1. All techniques showed that the isocentre was within tolerance ($\leq$ 1.00 [mm] [22]). Note that uncertainty values for RIT and spoke shot techniques could not be determined due to limited measurements.

3.3.3 In-Bore Radiation Survey

Results for the radiation survey within the treatment bore are provided in Figure 3.6. For both X and Y directions there is clearly large variations between the measurement devices, notably closer toward the isocentre, with film showing the largest doses. For

Equipment and Method	Magnetic Field [T]	Isocentre Diameter [mm]
CCT + RIT	1.5	0.45
MV Alignment + RIT	1.5	0.42
CCT + In-house	1.5	0.34 ± 0.04
MV Alignment + In-house	1.5	0.38 ± 0.04
MV Alignment + In-house	0	0.32 ± 0.04
Spoke shot with copper ring	1.5	0.36
Spoke shot with copper ring	0	0.24
Spoke shot without copper ring	0	0.28

Table 3.1: MV isocentre results for the various methodologies, analyses and magnetic field environments. The isocentre size is determined by Elekta, with the RIT software, during DAT with the CCT and during physics validation with the MV alignment phantom. The latter is consistent with that discussed by Snyder *et al.* [19]

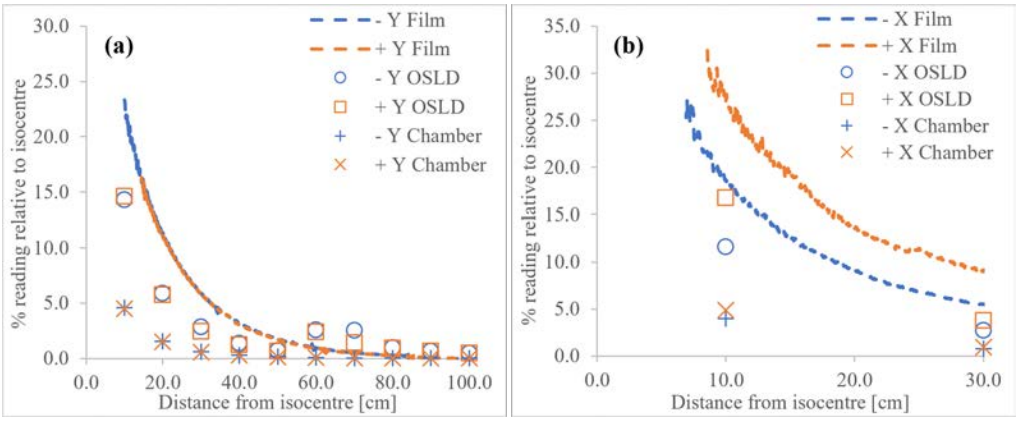

Figure 3.6: Survey results for film, OSLDs and chamber readings taken along the (a) Y-axis and (b) X-axis. Note the variation in scales, on both axes, between Y and X plots for visualization

the Y direction, Figure 3.6(a), the dose for all devices tend asymptotically toward 0.0 % as the distance from isocentre is increased, with the lowest measured value being 0.02 % of that at the centre (chamber). A noticeable increase in the OSLD readings, around 60.0 cm for both ± Y, is present which is not observed with the other dosimeters. For the X direction, there is difference observed between opposing sides which is not observed in the data for the Y direction.

Chamber readings with the residual field shielded are presented in Table 3.2, and very little change in reading is noted between the two normalisation techniques. In Figure 3.7, the data has been normalised to the nominal D_{max} dose to water for a 10.0× 10.0 cm^2 field, SSD of 142.2 cm. Better agreement between all measurements, than that in Figure 3.6, devices can be observed; although, the results are still significantly varied between ± X directions.

Y distance from isocentre [cm]	% relative to isocentre	% relative to D_{max} charge
0.0 (Open)	100.0	100.3
0.0 (Shielded)	1.16	1.16
10.0	0.21	0.21
30.0	0.12	0.12
50.0	0.03	0.03

Table 3.2: Results for the chamber readings during the radiation survey, taken with the residual field shielded with alloy blocks. Values are normalised to an open (unshielded) G0 reading at isocentre or the D_{max} charge produced for a 10.0×10.0 cm^2 field at 142.2 cm SSD

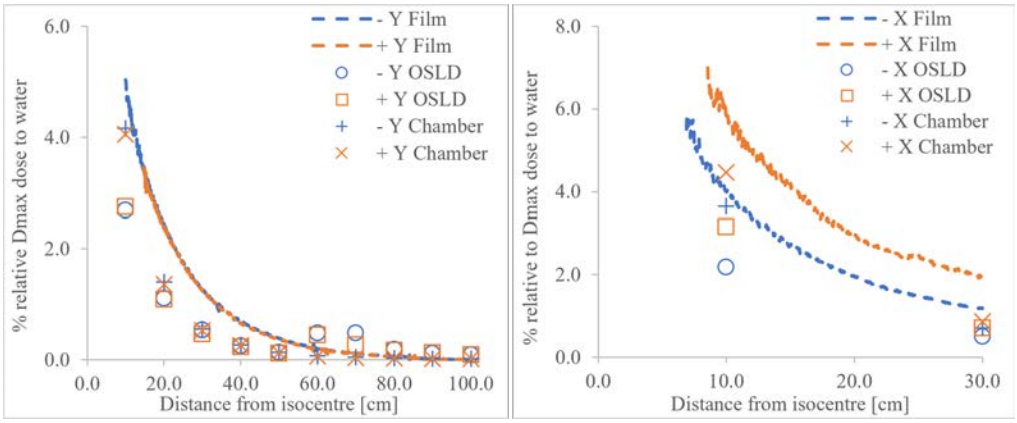

Figure 3.7: Survey data normalised to the nominal D_{max} dose to water, for readings taken along the (a) Y-axis and (b) X-axis. Note the variation in scales, on both axes, between Y and X plots for visualization

3.4 Discussion

3.4.1 Gantry Angle

The results for the gantry angle measurement, as well as the MVI images in Figure 3.4, highlight the accuracy of the gantry angle positioning of the Unity system. Imaging the MV alignment phantom from G270 introduced image distortions, hence G0 was chosen as the baseline image for gantry angle reproducibility with this method. The ballbearing positions on the G0 image appear to coincide with those on the G270 image. The MVI images show that gantry angle offsets of $\geq 0.3°$ (Figure 3.4(d)) from the nominal angle can be easily resolved, particularly when observing the ballbearings at image peripheries. With offsets $\leq 0.2°$ (Figure 3.4(c)) images are not readily discernible from the nominal (no angular offset) image without further analysis of pixel intensity profiles. Obviously, visual inspection cannot be used to determine the absolute gantry angle; however, it is useful for determining if set positions are within the tolerance specified by Roberts *et al.* [22] ($\pm$ 0.3°). Note that the more recent publication of Woodings *et al.* [21] suggests a specification of $< 0.2°$ for gantry angle, which cannot be achieved with visual inspection. For all projections at the 30.0° intervals, the actual

gantry angle appeared to match the set position within 0.3°, further highlighting the accuracy of the gantry rotation system.

From Figure 3.5, symmetry in the G0 profiles, particularly for the regions between ballbearings at image peripheries, was apparent. This symmetry was also seen for profiles taken from the images at the 30.0° gantry angle intervals, excluding G90 and G270 where image distortion interfered with the analysis. In comparison, the profiles for G0.1 (Figure 3.5(a)) show asymmetry at the peripheries, which highlights the deliberate angular offset in image acquisition. This was magnified for the G0.3 image (Figure 3.5(b)), which is the gantry angle tolerance [22]. Notably, the comparison of profiles for the different gantry angles does not result in an absolute gantry angle, but rather a confirmation of reproducible position for routine QA. However, these results indicate a proof-of-concept for the use of this phantom, supplied to all Unity sites, for gantry angle QA.

Further work is needed to assess how phantom set up affects results, with attention given to positional reproducibility and subsequent misalignment effects. Additionally, the process could be improved by imaging with the 3.5 cm longitudinal offset removed and confirming alignment of diametrically opposed ballbearings along the Y-axis on MVI images. An absolute gantry angle offset may also be able to be determined from the offset of ballbearing centres from the lateral pixel centre on the panel; however, correct rotational alignment of the MVI would need to be confirmed, such as that discussed by Woodings *et al.* [21].

3.4.2 MV Isocentre Diameter

The results presented in Table 3.1 highlight the benefit of the Unity's gantry slip-ring over conventional C-arm systems for reducing the isocentre size [19]. The isocentre diameter as measured using the CCT with the commercially available RIT software was 0.45 mm. This is larger than other reported values [19] however still within vendor tolerance (1.00 mm). The isocentre as measured with the MV alignment phantom and recommended methodology was similar in magnitude. Using the in-house method with the CCT and the MV alignment phantom, isocentre diameters were 0.34 mm and 0.38 mm, respectively. These are again slightly larger than that reported by Snyder *et al.* [19], although are still within tolerance, with differences most likely due to variations in machine construction. Consistency between isocentre values reported in Table 3.1 indicates that in-house techniques, such as that presented in this work, can be used by other clinics for this test. This alleviates the issues discussed above, such as with sending images to Elekta for analysis or access to commercial software.

In the 1.5 T environment, the spoke shot with copper technique, as mentioned in Roberts *et al.* [22], suggested an isocentre size in the X-Z plane comparable in magnitude to the 3D methods. The magnetic field had a limited effect on the isocentre measurements, the largest difference observed in the spoke shots between 1.5 T and 0 T (approximately 0.1 mm). It is worth noting, the removal of the background noise,

from profiles where distortion interfered with ballbearing edges, produced FWHM size comparable to images which did not suffer from distortion.

3.4.3 In-Bore Radiation Survey

From the survey results in Figure 3.6, there are significant differences between dosimeters. Along ± Y, the measured film dose (normalised to centre, Figure 3.6(a)) is greater than the other devices, and falls below the IEC primary collimator leakage tolerance of 0.1 % [27] around 60.0 cm from the field centre. For OSLDs, the out-of-field dose does not fall below 0.1 % of the isocentre at any distance; however, appears to match the film marginally better than chamber readings, excepting an increase at ~ 60.0 cm. A shift of approximately 7.0 cm is required to bring these two datasets into agreement; however, given this magnitude is unlikely to have occurred. A potential source of difference between readings may be due to the effective point of measurement (EPOM) depth of each device. The depth of the active layer of the film is approximately 0.13 mm, whereas an OSLD is closer to 1.0 mm [102]. Hence, one may expect the OSLDs to report lower doses (compared to film) closer to the field edge where electron contamination from the primary field could be significant. At greater distances from isocentre, divergence and attenuation would cause the electron component of the measured dose to be decreased. Therefore, at these regions the extra thickness of the OSLD would act as build up for the scattered and leakage photons and increased doses could be expected. The difference in effective atomic number between dosimeters, and the subsequent sensitivity to low energy photons, could also be a factor [25, 103]. Angular dependence of the OSLDs, particularly for lower energy photons [102], could also influence the readings which would not be a factor for film.

The increase in OSLD readings at ± 60.0 cm is not seen in the film, which was measured concurrently with the OSLDs, suggesting that an error during the experiment did not occur. Additionally, the increase in OSLD dose at this location is observed for ± Y, suggesting that individual OSLDs were not defective. A positional offset of greater than 15.0 cm is required for this data to match film, yet is again unlikely to have occurred. Currently, the reason for this notable dose increase compared to film is unknown.

Chamber readings in ± Y fall below 0.1 % of the central reading at ~ 60.0 cm, similar to film. However, closer to the field, readings are approximately 6.0 times lower than film. At this position, electron contamination from the primary field will be a larger consideration, and measuring with the chamber cap on would serve to reduce the device's sensitivity to these particles. This would not be the case with the remaining two dosimeters.

For film in the ± X directions, there is a difference of approximately 8.0 % (relative to the centre reading) between directions, and doses for the Y directions are between these values (i.e. + X is ~ 4.0 % higher than the Y directions, and inversely for - X). A similar pattern is observed for the other devices, however the difference is reduced. Asymmetry in profile shape for the X direction could explain the discrepancy. Note

that a differences in leakage doses of 8.0 % would not manifest in the in-field shape to the same magnitude, as the absolute dose is low out of field and sensitive to subtle symmetry changes. Additionally, the radiation contributing to these distal regions would pass through high density BLD components, and subtle differences between opposing sides may be exacerbated. Similarly to the Y direction, an offset of 7.0 cm between film and OSLD data would result in better agreement and the consistency between the four directions is noteworthy, further suggesting that it may be due to physical operation of the devices. It is noteworthy that an 8.0 % error (between ± X) is of the order with that previously reported for film scanning orientation effects [100], and may explain the asymmetry between positive and negative X directions. Note that currently, there is no comparative published data for the tests described above.

Attempting to replicate IEC 60601-2-1 conditions, measurements with the Farmer chamber were repeated with the residual field opening shielded. These results are presented in Table 3.2. With the available metal alloy block and couch attenuation, the reading was reduced to 1.2 % of the open field, slightly above that recommended by the IEC [27]. Leakage radiation dose fell below 0.1 %, of either normalisation value, at > 30.0 cm from the isocentre, and was 0.21 % at the most proximal measured point to the field. Both of these are below IEC tolerances [27] for similar conditions[1]. Interestingly, the corrected charge reading at isocentre was not significantly different to the nominal charge from G0 for the D_{max} dose to water at 142.2 cm SSD. However, for readings shown in Figures 3.6 and 3.7, the nominal charge reading was approximately 9.4 % greater than the raw, G0 reading at isocentre. Differences in amount of backscatter, temperature and pressure, and machine output between measurements taken for the shielded measurements and the data in Figures 3.6 and 3.7 would have contributed to this variation; however, may not be enough to explain it in entirety, therefore warranting additional measurements.

Dosimeter values normalised to the nominal D_{max} dose are shown in Figure 3.7, where better agreement between devices is observed. Additionally, this data agrees with similar measurements shown later in Chapter 5. The change in normalisation affected film and OSLD readings more than the chamber, as seen in Figure 3.7 and Table 3.2. This can be attributed to the presence of the build up cap for chamber readings, meaning the effective measurement depth was closer to the depth of maximum dose than the other dosimeters. Although IEC measurement recommendations [27] were attempted to be followed, the exact procedure was not followed. Firstly, the collimating components in the head were not closed for leakage measurements [21, 27, 63]. Secondly, open field measurements were not made at the recommended field size of 20.0 × 20.0 cm^2, against which the out-of-field data is meant to be normalised. Unfortunately, the magnet ramp down/up procedure prohibits easy repeat of the tests.

Due to the variability of dose between film, OSLDs and chamber readings, further investigation of radiation survey data in a 0 T environment is warranted. However,

[1] < 1.0 % anywhere in an area at isocentre corresponding to the projection of the primary collimator and excluding the residual field, for equipment making use of IMRT techniques. Additionally, the average leakage dose in that area should be < 0.38 % when IMRT techniques are used.

these were performed on a clinical machine and ramp down/up processes are costly in terms of time, money and interruptions of patient treatments. Care should be taken with OSLD readings to query the dose increase around 60.0 cm along the Y-axis, as well as dosimeter placement for ± X to reduce setup uncertainty. Additionally, it would be beneficial to repeat Farmer chamber measurements with the build-up cap removed to observe its effect in attenuating scattered electrons. Film readings for the shielded set up would also be of benefit. For completeness, and comparison of the change in doses due to the magnetic field, a repeat of these measurements in 1.5 T is also recommended. The methodologies proposed in IEC, where the collimating components are fully closed and residual openings are shielded, should be implemented in both 0 T and 1.5 T. However should IEC techniques be attempted in 1.5 T, the material required to shield the residual field should be considered carefully with MR-safety of importance.

3.5 Conclusion

This chapter provides novel mechanical and safety commissioning tests performed on a clinical Elekta Unity MRL. Adaptions of Elekta supplied phantoms were presented to measure gantry angle and MV isocentre. Also, a comprehensive radiation survey performed in 0 T on an Elekta Unity was presented.

The results above indicated that the machine was operating consistent with available published data and where no data exists, the results in this work can be used by other clinics for baseline comparison. The MV alignment phantom can be used for gantry angle confirmation at angles other than 270.0°, and visual confirmation of the set angle can be achieved within tolerance (0.3°) using MVI images of the phantom. This phantom, and in-house methods can be used to determine an isocentre size comparable to vendor recommended techniques. Radiation survey results were varied between different dosimeters utilized and directions (X and Y); however, tended to match IEC recommendations when conditions were matched.

Further work is warranted to develop the gantry angle measurement technique, with the MV alignment phantom, to potentially determine an absolute gantry angle at multiple positions. Finally, the radiation survey measurements should be repeated in 0 T and 1.5 T to address the discrepancies between dosimeters used in this work. IEC recommended methodologies should be used, where appropriate, with MR safety of concern. Additional work related to this chapter can be found in Appendix A.

4

Dosimetric Commissioning

This chapter contains material which was published in the following article:

[1] Marcus Powers, John Baines, Robert Crane, Chantelle Fisher, Stephen Gibson, Linda Marsh, Bronwyn Oar, Ariadne Shoobridge, Emily Simpson, Page Marchant, and Van Der Walt Glenn. Commissioning measurements on an Elekta Unity MR-Linac. *Physical and Engineering Sciences in Medicine*, **Online** (2022). doi:10.1007/s13246-022-01113-7

Furthermore, material in this chapter has been presented at the following:

- A dosimetric investigation of Elekta Unity based adaptive planning with Monaco 5.4. How to Develop Research/Validation Programmes when Implementing New Technology? Edition 1: MRI Linac. Marcus Powers. ESTRO, Madrid 2019.
- Treatment plan quality assurance review for the first cohort of patients treated using the Elekta Unity MR linac in Australia. John Baines, Marcus Powers, Ariadne Brodmann. Elekta Users Meeting, Noosa, 2020.
- Plan QA and Independent MU Verification at the Townsville Cancer Centre. Marcus Powers, John Baines. 15th Elekta MR-Linac Consortium Meeting, Virtual 2020.
- Physics considerations for Unity. Marcus Powers, Ariadne Shoobridge. Elekta Asia Pacific Unity User Collaborative, Virtual, December 2020.
- Energy measurements on the Elekta Unity following the 2UNI2 upgrade. Marcus Powers, John Baines. 16th Elekta MR-Linac Consortium Meeting, Virtual 2021. (Poster Presentation)

Additionally, some material in this chapter is intended for publication with John Baines, Stephen Gibson and Glenn de Vine as co-authors:

- Stephen Gibson, Marcus Powers, John Baines and Glenn de Vine. Mutual Interference of the MR and MV systems on the Elekta Unity. Target journal: Journal of Medical Imaging and Radiation Oncology. (Est date of submission: May 2022). *(In draft)*

All other work described in this work is my own unless otherwise stated.

4.1 Introduction

The commissioning of dosimetry components of the Elekta Unity MR-Linac is discussed in this chapter. Beam characteristics of this machine [20] and dosimetric commissioning work [19] have been published previously. Guidance and tolerances for some tests have also been discussed [21, 22]. Not every clinic will have access to the equipment specified in these references and comparative values of locally performed tests may not be available. The novelty of the work discussed is in the methodology and equipment used. Test results reported in this chapter, determined with the use of alternate equipment, are compared to those provided by Elekta and previous groups [19, 21, 22], where applicable.

In the work below, in-house developed phantoms enabled an assessment of anterior coil attenuation and End-to-End (E2E) measurements. Difficulties were encountered with commercial equipment when determining beam quality and machine output, that required adaptions of standard methodologies. A ramp down event in 2021 enabled measurement of chamber correction factors, and repetition of some tests in a 0 T environment. Unique methods were proposed to assess MR interference on linac operation, with comparisons made to previous reported work [21]. Furthermore, adaptions to standard methods for intensity modulated radiation therapy (IMRT) commissioning are reported. It is hoped this work will aid other clinics when performing commissioning work and assigning tolerances. Additional commissioning work relating to linac dosimetry can be found in Appendix A.

4.2 Methods

4.2.1 Anterior Coil Attenuation

Attenuation of the anterior imaging coil, as function of gantry angle, was determined with a PTW 30013 Farmer chamber within an in-house, cylindrical, water-filled phantom of diameter 6.0 cm and length 15.0 cm. The long axis of the chamber was coincident with the central axis of the cylinder, see Figure 4.1, with the Farmer threaded section and tapped cylindrical hole providing a waterproof seal. The cylindrical section of the phantom is free to rotate on two height-adjustable stands and a scale at one

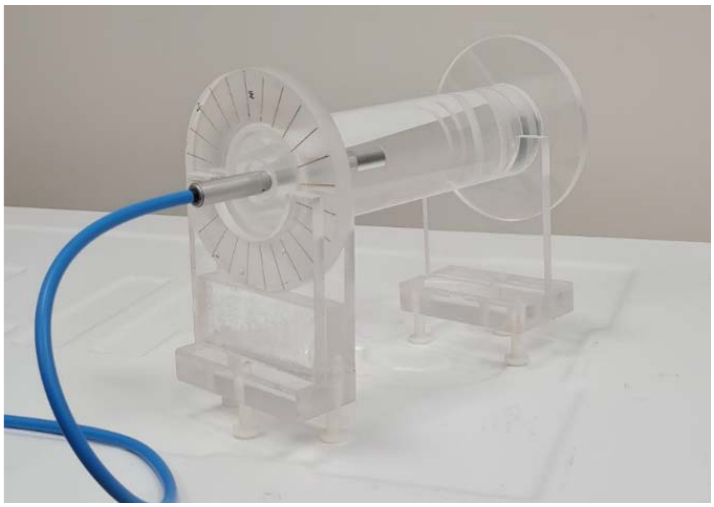

Figure 4.1: Cylindrical water phantom, with chamber inserted, used for output with gantry angle and anterior coil attenuation measurements

end facilitates angular positioning in 15.0° increments. This phantom was also used for output with gantry angle testing, provided in Appendix A.

The phantom was positioned in the bore with the chamber reference point positioned at the isocentre. To realise this, A-P and L-R MVI images were used to determine necessary lateral and height adjustments. Chamber readings were obtained using a 5.0×5.0 cm^{2}field, 100 MU, at 15.0° gantry angle increments from 75.0° to 285.0° with and without the coil present. For each gantry angle, the cylindrical phantom was also rotated to maintain the same orientation of the chamber with respect to the beam. Readings, with and without the coil, were compared to determine attenuation at each angle.

The experimental arrangement was simulated in Monaco using a 6.0 cm diameter, 15.0 cm long, cylindrical structure for the phantom, which was assigned a forced relative electron density (RED) of 1.000. Isocentre position for calculations was centred in the X-Z plane of this structure, using virtual couch shifts, and longitudinally adjusted to match the position of the chamber reference point. For measurement and calculation, the coil height was set such that the bottom of the coil was 26.0 cm above the couch. A 0.1 cm dose grid, statistical uncertainty of 0.25 % per control point and the Patient lookup table were used in Monaco to calculate the dose-to-medium.

4.2.2 Beam Quality

For $TPR_{20,10}$ beam quality measurements the previously mentioned Farmer chamber was inserted in the PTW 1D water tank (PTW, Freiburg, Germany), Figure 4.2. The chamber was aligned parallel to the Y-axis, with the reference point at the isocentre in the X-Y plane using A-P/L-R MVI images. Due to the size of the water tank, the chamber was lowered 4.0 cm below isocentre (SCD 147.5 cm) to facilitate measurements at a depth of 20.0 cm in water. Measurements at 10.0 cm (SSD 137.5 cm) and 20.0 cm depths (SSD 127.5 cm) were obtained using a 9.7×9.7 cm^2 (10.0×10.0 cm^2 at the

Figure 4.2: The PTW 1D water tank with Farmer chamber inserted

depth of the chamber), 100 MU field, G0. $TPR_{20,10}$ was derived from the ratio of the average readings (n = 3) for each depth. Measurements were performed in 0 T and 1.5 T.

To investigate the impact of the cryostat on beam quality, $TPR_{20,10}$ measurements were also performed from G90 using a 10.0×10.0 $cm^2$100 MU field, with the chamber at isocentre. The acrylic tank wall was measured to have a water equivalent thickness of 1.2 cm, therefore for these measurements the chamber was set 8.8 cm and 18.8 cm from the inner surface of the wall. This was achieved using a 3D-printed 8.8 cm indexer (confirmed to be the correct length with a calliper) to position the chamber reference point at 10.0 cm of water equivalent depth. A-P/L-R images were used to determine required shifts to position the water tank such that the chamber was at isocentre. For readings at 20.0 cm, A-P images were used to shift the chamber 10.0 cm laterally (-X) and reposition the tank, so the chamber remained at isocentre.

For dose map measurements, the QA Platform (Elekta, Stockholm, Sweden) was placed on the Unity couch with the patient foam mattress removed. Using four in-house 3D-printed holders, 6.5 cm depth of solid water (RW3, PTW, Freiburg, Germany) was positioned centrally on the QA Platform. Printing material used was poly-lactic acid (PLA). With the 1500^{MR} array on top of the solid water, see Figure 4.3, the effective plane of measurement of the array was at isocentric height. The orientation of the array with respect to isocentre was checked using a 22.0×22.0 cm^2 G0 MVI image, with an in-house aluminium "ruler" aligned on the X-axis of the array. The ruler is 2.5 cm wide and 30.0 cm in length, with thirteen machined 3.0 mm holes spaced 2.0 cm apart along its length. Misalignment of the ruler/array with the centre of the MVI image was determined using the MVI measurement tool, and array rotation was assessed using the horizontal markers on the ruler against the 1.0 cm MVI digital grid. Necessary position adjustments were identified and applied using the X and Y verniers on the QA Platform. Following adjustments, additional MVI images were obtained

Figure 4.3: 1500^{MR} array setup for dose map measurements on the Elekta supplied QA Platform. The in-house developed 3D printed holders (orange) aid with positioning

to confirm array offsets, and rotations, from isocentre were negligible. With the array correctly aligned, the ruler was removed and 4.2 cm of solid water was added (0.8 cm intrinsic build up), so that the detector plane was at the calibration depth of 5.0 cm. The array was then calibrated with a 10.0×10.0 cm^2 field, 100 MU, delivered from G0. Finally, a 22.0×22.0 cm^2, G0 field with 100 MU was delivered to the array to determine dose maps at 5.0 cm depth.

During an upgrade to the linac control system, control values for the gun-grid voltage were erroneously raised (from 34.0 V to 50.0 V). resulting in more electrons entering the accelerating waveguide. With more electrons per RF-pulse, the average energy of the beam was reduced and energy metrics were expected to change. As such, the measurements described above were repeated when the grid voltage was raised (energy lowered).

The two measurement geometries described above were simulated in the Monaco v5.40 TPS. For the $\mathrm{TPR}_{20,10}$ simulations, two separate datasets were used where heights of the external contours produced the SSDs of the measurement geometries (137.5 cm and 127.5 cm). Remaining dimensions of the contours were set to 20.0 cm to decrease calculation time whilst maintaining full scatter conditions. For calculations, a $30.0 \times 30.0 \times 19.0$ cm^3 region was contoured and set as the external structure. All three external structures were assigned an RED of 1.000. TPS calculations were performed with a 0.2 cm dose grid, 0.1 % statistical uncertainty per control point, the phantom look-up table and dose deposition to medium. With these settings, the statistical uncertainty at the regions of interest was less than 0.15 %. To calculate the TPS $\mathrm{TPR}_{20,10,}$mean dose to a 0.3 cm radius interest point 4.0 cm below isocentre was acquired for each geometry, and the ratio taken. For maps, extracted from 5.0 cm depth in the TPS, gamma analysis between calculated and measured dose maps was performed with 2.0 % local dose, 2.0 mm distance-to-agreement (DTA), with dose suppression below 10.0 %, as per routine clinical practice. For comparisons of measured

maps at the two grid voltages, a gamma criteria of 1.0 % local dose, 1.0 mm DTA was used.

4.2.3 Reference Dosimetry

Other investigators calibrate the Elekta Unity MRL to deliver 1.000 Gy per 100 MU for a 10.0×10.0 cm^2 field from G90 to an isocentre depth of 10.0 cm in water. Linac calibration in this work was performed with the isocentre at 5.0 cm depth in water, based on advice from Elekta to extend the life of the magnetron. When using the PTW 1D tank, Figure 4.2, a direct measurement of the output at isocentre for a chamber depth of 5.0 cm in water cannot be achieved from G90. This arises since the lateral shift for the tank, required to accommodate such a chamber position, is incompatible with the size of the bore. Thus the G90 output at 5.0 cm depth, cannot be determined by direct measurement in the water tank. However, a measurement at 10.0 cm can be performed from this angle and corrected to 5.0 cm using a $\text{TPR}_{10,5}$. Calibration in plastic water phantoms is avoided due to variation in response of the chamber due to the presence of air gaps generating and the electron return effect (ERE) [48, 53].

For reference dosimetry measurements on this system, a PTW 30013 Farmer chamber was placed in the PTW 1D water tank, Figure 4.2, with the chamber reference point positioned at isocentre using MVI images. Readings were acquired using 10.0×10.0 cm^2, 100 MU, G0 fields, with the chamber reference point at 5.0 cm (SSD 138.5 cm) and 10.0 cm (SSD 133.5 cm) depths, to derive a $\text{TPR}_{10,5}$. Next, to determine the output from G90 (5.0 cm depth) required the tank to be shifted 6.2 cm laterally (- X direction) so the chamber was at isocentre, 10.0 cm depth, whilst accounting for the water equivalent thickness of the tank wall (1.2 cm). Chamber readings with the same field, now delivered from G90, were acquired and corrected to 5.0 cm, using the G0 $\text{TPR}_{10,5}$, to give the machine output.

Chamber influence quantities for temperature and pressure, polarity and recombination, and a published magnetic field correction factor, $k_{B_{\parallel},Q}$ of 0.992 [5] were applied to the readings at 10.0 cm depth, G90. A non-uniformity correction factor [28] for the FFF beam was not applied given the relative flatness of the profiles at 10.0 cm depth over the dimensions of the chamber sensitive region [48]. Routinely, measuring the output from G90 using the methodology described above can be cumbersome. It is known from the cryostat attenuation that the output at isocentre for G0 is 0.5 % higher than from G90 for a 10.0×10.0 cm^2 field. Hence for routine quality assurance (QA), and as an independent check on the methodology adopted above, the output of the machine from G0 was determined where a direct measurement at isocentre beneath 5.0 cm of water was readily achieved. With the ramp down event, measurements were repeated in a 0 T environment, to determine an output. Magnetic field correction factors were not applied to these readings.

4.2.4 Determination of Magnetic Field Correction Factors

Following a ramp down event, $k_{B_{\parallel},M,Q}$ factors for two PTW 30013 chambers (S/N 10765 and 11298) were determined following the formalism of van Asselen *et al.* [5], at the two calibration depths. The experimental arrangement described in section 4.2.3 was repeated. Readings were acquired in the 0 T environment with a 10.0 × 10.0 cm^2 field, G0, at depths 5.0 cm and 10.0 cm, to investigate depth dependence of the magnetic field chamber factors. Since this work was performed to confirm applicability of using published factors (10.0 cm) at a depth of 5.0 cm, no reference chamber was used for these measurement [47], increasing the uncertainty in the determined factors.

In the formalisms of van Asselen *et al.* [5] and O'Brien *et al.* [48], the dose correction factor $c_{\tilde{B}}$ is given at an SSD of 133.5 cm. Output calibration in this work is performed at an SSD of 138.5 cm, for an isocentre depth of 5.0 cm. The dose conversion factor has been shown to be constant at depths ranging from 5.0 cm to 25.0 cm [48]; however, explicit SSD dependence has not been discussed, thus $c_{\tilde{B}}$ needed to be calculated at an SSD of 138.5 cm. Using Monaco v5.40 TPS, doses were calculated in a 30.0 × 30.0 × 19.0 cm^3 phantom for a 10.0 × 10.0 cm^2,100 MU, G0 field. The SSD was set to 138.5 cm, and calculations run using the clinical 1.5 T beam model and with an additional 0 T model. The 0 T model is a direct copy of the clinical model with the exception that the magnetic field strength is set to zero. Five calculations were performed for each beam model and using a 0.2 cm dose grid, 0.25 % statistical uncertainty per control point and the Phantom look-up table. For each calculation, the mean dose to an interest point at isocentre (5.0 cm depth) with radius 0.3 cm was taken and then averaged across the five simulations. The ratio of the mean values for 1.5 T and 0 T were used to calculate $c_{\tilde{B}}$. Additionally, to compare uncertainty with van Asselen *et al.* [5], the standard error of the mean (SEM) was calculated.

4.2.5 MR Interference on Linac Operation

To investigate the effect of MR imaging on beam delivery, several tests were performed. The effect of MR imaging on simple beam dosimetry, with a square field, was tested first. The cylindrical phantom and chamber described previous, Section 4.2.1, were used. Chamber reference point was positioned at the isocentre using MVI images as previous. With no MR imaging operating, a 10.0 × 10.0 cm^2 G0 field, with 1000 MU, was delivered and chamber reading recorded. The Motion Monitoring (MM) sequence was then initiated from the MR Philips software. This sequence was chosen due its planned use during treatments. With the sequence running, the same beam described above was delivered. The charge readings with and without MM were compared. This process was repeated for the same beam at other cardinal angles.

Additional tests were also performed to check for difference in multileaf collimator (MLC) shaping, gantry angle and overall plan delivery whilst MR imaging. Using a simple 5.0 × 5.0 cm^2, 100 MU field, the MVI panel was irradiated several times to capture the MLC shapes with and without MR imaging. Three deliveries were captured prior to any MR imaging to determine the reproducibility of the MLC shape on the

images. Following this, the MM sequence was run, and the panel irradiated again with the same field. After MR acquisition, the panel was irradiated twice more; however, for the final acquisition the MLCs and Jaws were exercised. This was performed to determine differences in MVI images due to Leaf/Jaw positioning. All images were exported in DICOM format and analysed using ImageJ [99]. MLC positions on the panel were compared, for MM and non-MM deliveries, against the initial, reference 5.0×5.0 cm^2 image (without MR imaging). Pixel value subtraction between images was performed, and the results were normalised to the reference image, to highlight differences in MLC positions.

Two Elekta supplied plans were delivered to EBT3 film in a solid water stack – a Head and Neck plan and a Lung plan. The methodology for the film delivery and calibration is described later as part of IMRT commissioning, Section 4.2.6. The plans were delivered twice without MR imaging (to determine machine reproducibility), and once with MM running (to determine the effect of the MR imaging). Deliveries to film with and without MR were compared with gamma analysis: criteria of 1.0 % global dose difference, 1.0 mm DTA and dose suppression below 10.0 %.

Treatment Record Files (TRFs) were also acquired during the time of film irradiation, with two non-MR deliveries and one MR delivery for each plan. These files were used to determine if errors in MLC shaping and gantry angle accuracy were within nominal limits. From each file, the positional errors of each leaf, over each delivery, were extracted and binned in 0.1 mm widths. The percentage of leaf positional errors for the MR plans (two plans) were compared to the non-MR deliveries with histograms.

4.2.6 IMRT Commissioning

Planning System Calculation

A $30.0 \times 30.0 \times 19.0$ cm^2 solid water stack was scanned on a Toshiba Aquilion CT using 1.0 mm slices. The CT data set was imported into the QA clinic in Monaco and contoured as an external patient structure. The RED of the structure was forced to 1.000 and the MRL couch structures were added, excluding the 1.0 cm foam mattress. All plans were calculated on this QA dataset.

Following clinical practice, TPS calculations for Elekta plans used a statistical uncertainty of 3.0 % per control point and a 0.3 cm dose grid. For stereotactic IMRT plans, a 0.2 cm dose grid and 3.0 % statistical uncertainty per control point were used. For both, the overall calculated dose uncertainty was 1.0 % or lower. The phantom look-up table, with dose deposition to the local medium, was selected. For all plans, calculation times were less than 2.0 minutes.

Simple Segment Shape Check

To confirm correct MLC shaping, the segments of each stereotactic plan were delivered to the MVI panel at their respective planned gantry angles. Due to the restricted imaging area of the panel (22.0×9.5 cm^2), this was not performed with the Elekta

plans. The size, shape and position of the individual segments were visually compared to corresponding Monaco segments.

Perpendicular Delivery

At Townsville Cancer Centre (TCC), film is considered the gold-standard for IMRT patient specific quality assurance (PSQA) of treatment plans on conventional linacs, with other detectors like the Octavius 1500^{MR} array being benchmarked against film during commissioning. To this end, the nine vendor IMRT plans and two in-house developed stereotactic plans were delivered at G0 to both film (Gafchromic EBT3 or EBT-XD, Ashland ISP Advanced Materials, NJ, USA) and the array. Figure 4.3 shows the setup of the Octavius 1500^{MR} array on the QA Platform for IMRT plan verification measurements. Array setup and calibration was performed with the same methodology as described above with dose map measurements. Fields for the eleven IMRT plans were delivered perpendicularly to the array, beam-by-beam, and resulting dose maps were recorded. Comparisons of beam-by-beam dose maps and a composite dose map were made to those from the TPS. Gamma analysis was performed with Verisoft v7.2 software (PTW, Freiburg, Germany) and criteria of 2.0 % of local dose, 2.0 mm DTA and dose suppression below 10.0 %.

Choice of film for measurements depended on dose per fraction; EBT3 film was used for doses less than approximately 8.0 Gy and EBT-XD was used above 8.0 Gy. The suitability of these film types at these dose levels has been investigated previously [104]. For film dosimetry the QA Platform was placed on the couch with the foam mattress removed and 30.0 × 30.0 × 8.0 cm^3 of solid water was placed on top with 3D-printed supports (Figure 4.3) that nominally centre the solid water at isocentre in the X-Y plane. With this setup, the upper surface of the solid water was at isocentre height. Crosslines marked through the centre of the solid water were used to position the aluminium ruler and aid with aligning the phantom and QA Platform to isocentre using the methodology described previously. After phantom alignment, film calibration was performed on the Unity using a geometric dose progression with five 4.0×2.0 cm^2 strips of film, to encompass the maximum delivered dose for all plans [100]. The calibration was performed using 10.0 × 10.0 cm^2 G0 fields, film at 5.0 cm depth. For plan QA, films were centred on the solid water stack at 5.0 cm depth, cross lines on the solid water, indicating X and Y axes, were used to mark the film orientation. Fields for all plans were delivered compositely from G0 to individual films. Films were scanned using an Epson 10000XL scanner at 72.0 dpi and scanner corrections were applied for the Lateral Response Artefact [101]. Comparisons to the planning system were made using FilmQA^{TM} Pro v5.0 software (Ashland ISP Advanced Materials, NJ, USA) and triple channel analysis [100]. Comparison of TPS and measured dose distributions was performed using gamma analysis with 2.0 % of global dose, 2.0 mm DTA and dose suppression below 10.0 %.

True Composite Delivery

Delivering plans perpendicularly from G0 obviously does not simulate the treatment geometry. Consequently, all plans were delivered, with planned gantry angles, to individual coronal films within a solid water block. Again, depending on dose level, EBT3 or EBT-XD films were used. Prior to measurement, optimal plan dependent depth for the film was identified using Monaco. Choice of depth primarily depended on beam geometry, beam weighting and the resulting dose distribution; however, typically a coronal slice was chosen through the centre of beam convergence and steep dose gradients were avoided. Film dosimetry was performed using a solid water phantom $30.0 \times 30.0 \times 19.0$ cm^3, placed on the couch (mattress removed) and aligned to the X and Y axes using the aluminium bar and MVI images as outlined above. The anterior coil was excluded during measurements, and the posterior coil was included to replicate the TPS calculations. Film calibration and analysis were performed as discussed previously. To investigate the potential effect of the electron return effect (ERE) on the film dose, due to the presence of air gaps between the film and solid water, measurements were repeated with the calibration and plan delivery films sprayed with water [9].

4.2.7 End-to-End Test

End-to-End (E2E) testing on the Unity was performed using an in-house designed phantom, with components 3D-printed by researchers at the Royal Brisbane and Women's Hospital, Australia. The phantom comprised of a hollow acrylic cylinder (20.0 cm length, 22.0 cm diameter) containing a 3D-printed frame and a platform on which 3D-printed tumour surrogates (see Figure 4.4(a)) could be mounted (see Figure 4.4(b) for the assembled phantom). All printing material was PLA and had a nominal RED of 1.050. Surrogates were hollow, hemi-spherical and half-cylindrical shells with known internal radii and shell thickness. Two hemispheres or half-cylinders could be secured together with film in-between to facilitate dosimetric measurements and were printed with holes for filling the hollow sections with MR-visible material. The platform had multiple points in which the surrogates could be inserted at known offsets for testing of either adapt-to-position (ATP) or adapt-to-shape (ATS) workflows. A thorough characterisation of the phantom and printing materials was performed on the system; however, is not reported in this work.

The E2E water-filled phantom containing a 2.5 cm radius spherical 3D-printed surrogate was scanned on a Toshiba Aquilion CT with 2.0 mm slices and the image dataset was imported into Monaco. Contours of the phantom and its components were defined and forced REDs were applied to the respective mean values as calculated by the TPS. Calculated REDs agreed within 0.6 % of the nominal value for the 3D-printed components. The water filled sections of the hemispheres were contoured together, designated as the target and set to enable automatic deformable registration. A margin expansion of 1.5 mm was applied to the target, to generate a contour for the outer surface of the spherical shell. Dose-to-medium within the phantom was calculated using a seven beam Step-and-Shoot IMRT (SSIMRT) plan. A 0.3 cm dose grid and

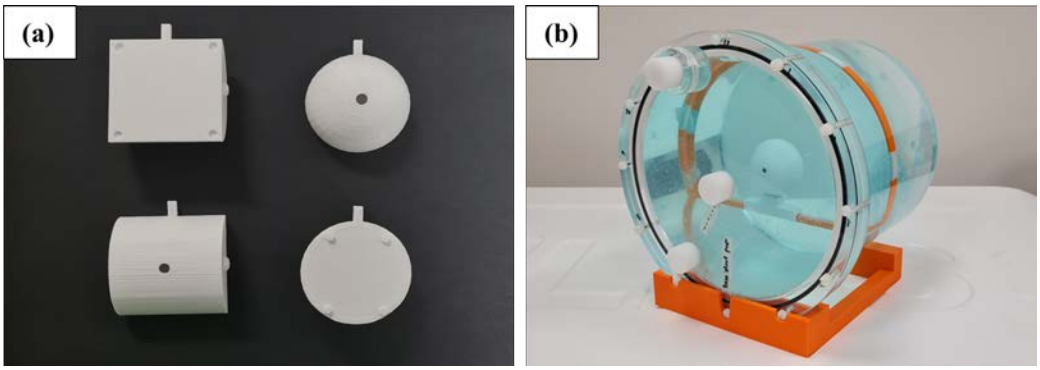

Figure 4.4: The phantom used for End-to-End testing. In (a) the tumour surrogates are shown and (b) shows the assembled phantom filled with copper sulphate solution

3.0 % statistical uncertainty per control point was used for calculations. Inclusion of the anterior coil in the E2E workflow required the use of the Patient lookup table, and as such phantom components were mapped to tissue materials. With these parameters, the statistical uncertainty was less than 0.8 % at the film location and the optimization time was 140.9 s.

For delivery, the phantom was positioned on the Unity couch with 3D-printed frames attached to an accessory fixation lock-bar to locate the phantom. The spherical surrogate was inserted in the platform, offset from the centre (0.5 cm X and 1.0 cm Y), with a piece of Gafchromic EBT3 film set between the hemispheres. A 2.0 min, T2-weighted MR-image was acquired, registered to the CT dataset and an ATP plan was calculated using segment shape optimization (SSO) and segment weight optimization (SWO), with the aim of reproducing goal dose [18]. Objective function parameters were not altered from their default values and the resulting recalculation time for the ATP plan was 47.8 seconds. The newly generated plan was then delivered to the phantom.

Following this the spherical surrogate was replaced with a cylindrical one, at the same offset as above, of internal radius 2.5 cm, length of 5.0 cm. A film strip was set between the two half-cylinders. Again, a 2.0 min T2-weighted MR scan was acquired and registered to the CT dataset; however, now the ATS workflow was used. The auto-deformed target contour was visually checked for accuracy and manually adjusted as necessary, following clinical workflow. The ATS plan was generated from fluence with five iterations, as per the clinical default. With these settings, and the same calculation settings as for the reference plan, optimization time for the ATS plan was 149.9 seconds. Each film was compared to the planning system using FilmQA^{TM} pro and gamma analysis with 2.0 % global dose, 2.0 mm DTA and dose suppression below 10.0 %.

Gantry Angle [°]	Measured Attenuation [%]	Calculated Attenuation [%]
75.0	0.0	0.0
60.0	0.6	0.8
45.0	0.6	0.9
30.0	0.5	1.0
0.0	0.5	0.7
345.0	0.4	0.8
330.0	0.7	0.9
315.0	0.6	0.8
300.0	0.6	0.7
285.0	0.0	0.0

Table 4.1: Measured and calculated anterior coil attenuation as a function of gantry angle

4.3 Results

4.3.1 Anterior Coil Attenuation

For the range of angles investigated, measured and calculated attenuation values as a function of gantry angle are shown in Table 4.1. The average measured attenuation was (0.6 ± 0.1) %, compared to the calculated average (0.8 ± 0.1) %.

4.3.2 Beam Quality

The measured $TPR_{20,10}$ in the B = 1.5 T environment was 0.705 ± 0.001 (n = 4) and for the original magnetron with B = 0 T, it was 0.703 (n = 1). Planning system $TPR_{20,10}$ was calculated as 0.702 and following a magnetron replacement, the $TPR_{20,10}$ was measured as 0.703 ± 0.001 (n = 5). With the replacement magnetron the $TPR_{20,10}$ from G90 was 0.703 (n = 1) and when the grid voltage was erroneously raised, the metric from G0 was 0.696 ± 0.001 (n = 4).

A dose map comparison of the measured beam with the original $TPR_{20,10}$ to the TPS is shown in Figure 4.5(a) (95.3 % gamma pass rate, at 2.0 %, 2.0 mm criteria) and similarly for the new magnetron/$TPR_{20,10}$ in Figure 4.5(b) (99.6 % gamma pass rate). Dose maps with the raised grid voltage are compared to the TPS in Figure 4.6(a), and to a dose map taken with the correct voltage (same magnetron) in Figure 4.6(b)). Significant degradation in gamma pass rates, 60.8 % and 35.2 % respectively, can be observed. From these figures, the dose maps are less peaked with the grid voltage raised, hence the relative dose off-axis is failing hot compared to reference data.

4.3.3 Reference Dosimetry

From G0, measured output at isocentre was 1.002 ± 0.004 Gy per 100 MU (n = 7) at depth 5.0 cm in water, and $TPR_{10,5}$ was 0.858 ± 0.001 (n = 5). From G90, output was 1.000 ± 0.002 Gy per 100 MU (n = 7) at the isocentre at 5.0 cm, and similarly in

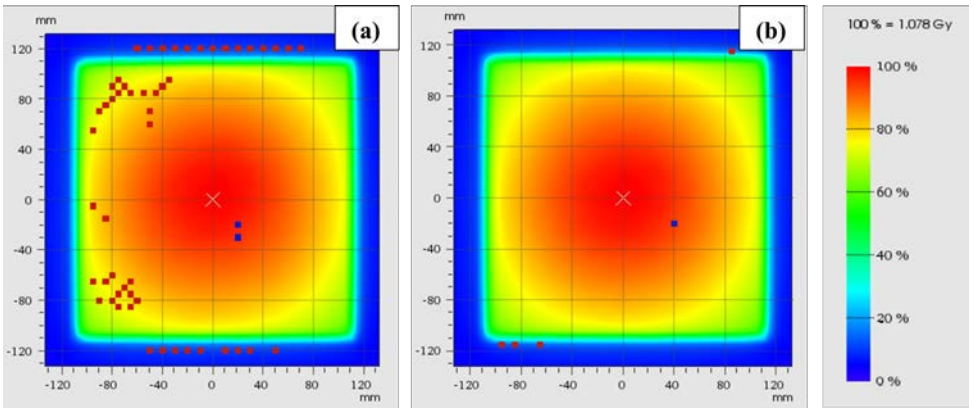

Figure 4.5: Dose maps for 22.0 × 22.0 cm^2 fields measured on the Octavius 1500^{MR} array and compared to TPS calculations using gamma analysis at 2.0 % (local dose), 2.0 mm criteria for (a) the original commissioning data and (b) a dose map obtained with the new magnetron. Regions of hot/cold failure are indicated by the red/blue dots respectively

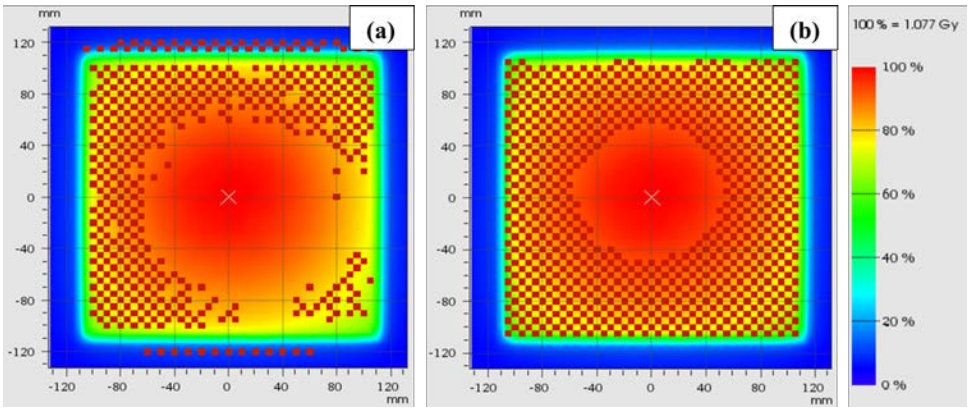

Figure 4.6: Dose maps for the 22.0 × 22.0 cm^2 field measured with a raised grid voltage compared to (a) the TPS at 2.0 % (local dose), 2.0 mm, and (b) a measurement with the correct voltage and same magnetron, at 1.0 % (local dose), 1.0 mm. Regions of hot/cold failure are indicated by the red/blue dots respectively

the B = 0 T environment, the output at G0 was measured as 1.020 Gy per 100 MU (n = 2).

4.3.4 Determination of Magnetic Field Correction Factors

At 5.0 cm depth, G0, the detector magnetic field correction factors, $k_{B_{\parallel},M,Q}$, were 0.995 (S/N 10765) and 0.996 (S/N 11298) for n = 1. Similarly, with the chambers at 10.0 cm depth, $k_{B_{\parallel},M,Q}$ factors were 0.999 for both. After applying the published dose conversion factor (0.9949) [5], the values for the combined magnetic field correction factors $k_{B_{\parallel},Q}$ were 0.990 (S/N 10765) and 0.991 (S/N 11298) at 5.0 cm and 0.994 for both chambers at 10.0 cm. As too few measurements were taken in the 0 T environment (due to clinical requirements of the machine) no uncertainty of the values could be determined. The independently calculated $c_{\tilde{B}}$ factor was 0.9948 ± 0.0005 (1 SEM, dose decrease of 0.52 % in 1.5 T with a 0.05 % error).

Gantry Angle [°]	Output Difference [%]
0.0	-0.04
90.0	-0.05
180.0	0.03
270.0	-0.03

Table 4.2: 10.0×10.0 cm^2 output differences, between MR operational states, at the cardinal gantry angles. Negative values indicate the reading with MR operation is lower

Delivery	Lung pass rate [%]	H&N pass rate [%]
Without MR operation	98.0	98.6
With MR operation	97.8	98.6

Table 4.3: Gamma comparisons for two Elekta provided plans between deliveries with and without MR operation. Measurements were compared to a separate delivery whilst no MR imaging was occurring

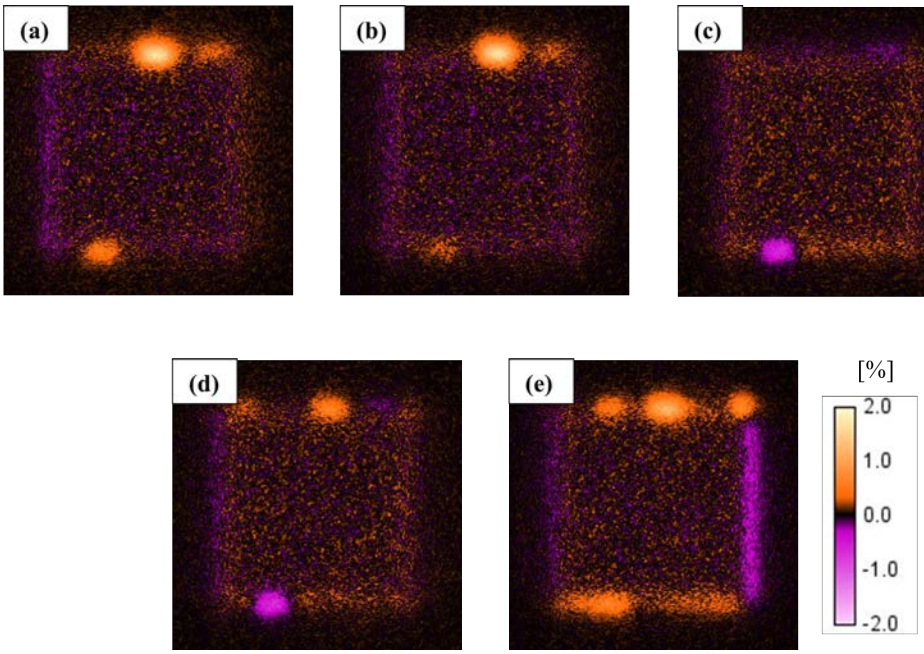

Figure 4.7: Percentage difference maps for MVI images of a 5.0×5.0 cm^2 field. (a), (b) and (c) show differences between deliveries without any MR sequence running, whereas (d) shows differences with and without MR imaging. (e) highlights differences due to reshaping the 5.0×5.0 cm^2 field. All fields are compared to a separate 5.0×5.0 cm^2 image acquired without MR imaging

4.3.5 MR Interference on Linac Operation

The dosimetric measurements for the MR interference on linac operation are shown in Table 4.2 and Table 4.3. No adverse effect from the MM scan was noted for either. The interference on MLC shaping is shown in Figure 4.7. Histograms generated from the treatment record files for the lung and head and neck (H&N) deliveries with and without the MM scan running are shown in Figure 4.8.

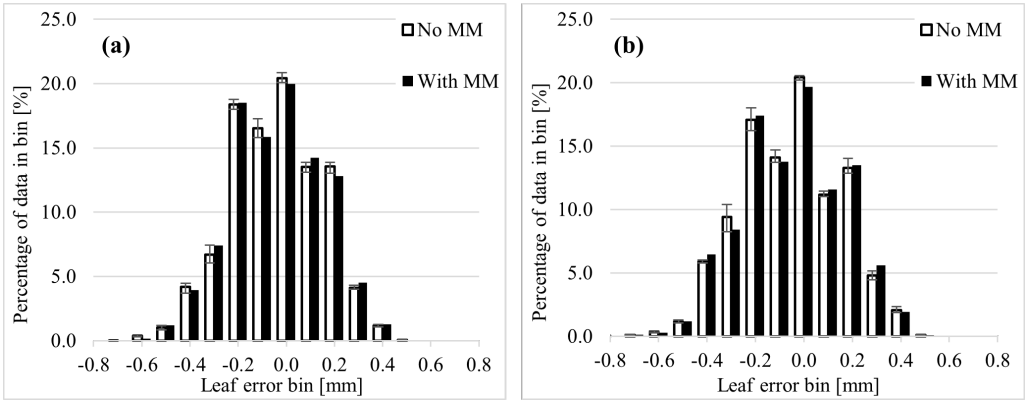

Figure 4.8: Histograms of leaf position errors for the Elekta supplied (a) Lung and (b) Head and Neck plans. For each, columns on the left (white) correspond to leaf errors while no MR was operating and columns on the right (black) are for errors while a Motion Monitoring (MM) scan was running

Plan	Pre-Fix		Post-Fix	
	2.0 %, 2.0 mm	3.0 %, 3.0 mm	2.0 %, 2.0 mm	3.0 %, 3.0 mm
Abdomen	99.2	100.0	97.9	100.0
Head and Neck	94.2	100.0	95.8	100.0
Lung	96.4	100.0	96.1	100.0
Multi-Target	77.8	96.2	95.6	99.8
Prostate	97.4	100.0	97.8	100.0
Prostate_2	84.8	93.1	99.6	100.0
Prostate_7fld	88.4	94.8	100.0	100.0
Prostate_9fld	90.9	98.2	99.5	100.0
Prostate_11fld	96.5	100.0	100.0	100.0
Stereo 1	94.0	98.5	100.0	100.0
Stereo 2	71.2	82.0	98.6	100.0

Table 4.4: Gamma results for perpendicular deliveries to the 1500^{MR} array of the Elekta supplied TG119 plans and the two in-house developed stereotactic plans

4.3.6 IMRT Commissioning

A representative segment from one of the in-house stereotactic plans delivered to the MVI panel is shown in Figure 4.9. Comparison of this MVI image (and similar) to the TPS segment, Figure 4.9(c), revealed a discrepancy between delivered MLC shapes and those calculated in the planning system, which ultimately was caused by erroneous guard leaf behaviour.

Results from IMRT commissioning are shown in Tables 4.4 - 4.6 for both pre- and post- guard leaf fix. Values in the tables are for dry film; however, when the patient and calibration films were sprayed with water, no statistically significant variation in the gamma results were noted. This was confirmed for multiple deliveries (n = 11) across several film batches.

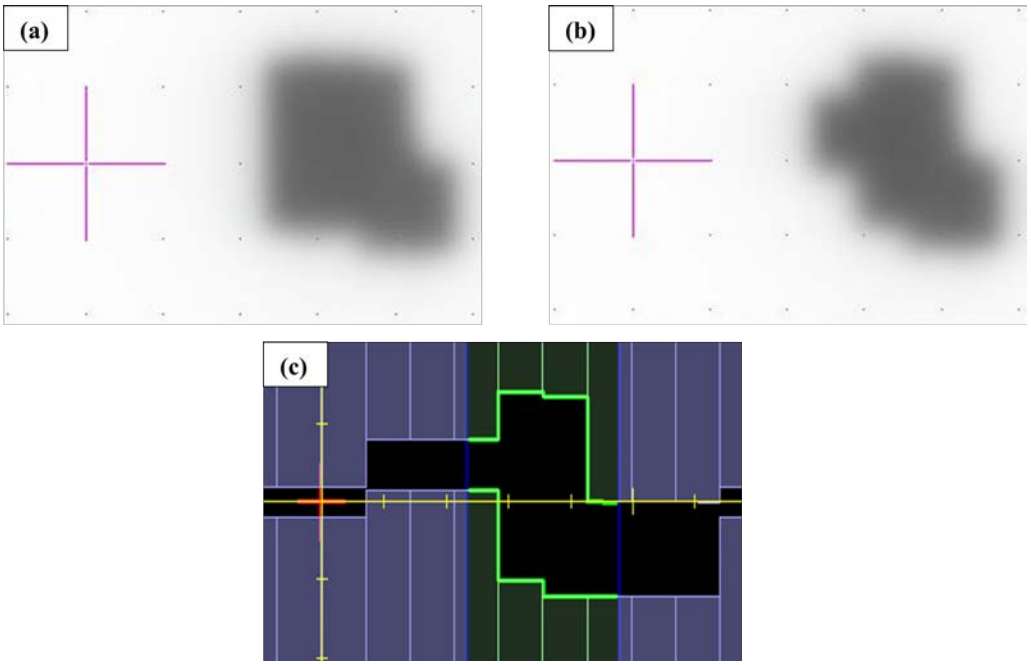

Figure 4.9: Images of two segments for one of the in-house developed stereo plans. (a) shows one delivered segment with the guard leaf error present and (b) shows the same segment with the error removed, matching that which was planned as indicated by (c) the beams-eye-view from Monaco TPS. All scales are in centimetres

Plan	Pre-Fix		Post-Fix	
	2.0 %, 2.0 mm	3.0 %, 3.0 mm	2.0 %, 2.0 mm	3.0 %, 3.0 mm
Abdomen	96.2	99.8	96.0	99.7
Head and Neck	91.7	95.7	99.7	100.0
Lung	68.8	86.0	99.9	100.0
Multi-Target	77.4	92.9	98.0	99.9
Prostate	97.0	99.9	99.2	100.0
Prostate_2	75.7	90.5	97.6	99.7
Prostate_7fld	92.7	96.1	95.7	99.8
Prostate_9fld	95.2	99.3	97.0	100.0
Prostate_11fld	98.9	100.0	98.2	99.8
Stereo 1	70.2	92.1	97.3	99.3
Stereo 2	NA		95.2	95.2

Table 4.5: Gamma results for perpendicular deliveries to film of the Elekta supplied TG119 plans and the two in-house developed stereotactic plans

Plan	Pre-Fix		Post-Fix	
	2.0 %, 2.0 mm	3.0 %, 3.0 mm	2.0 %, 2.0 mm	3.0 %, 3.0 mm
Abdomen	74.5	94.7	96.5	99.7
Head and Neck	92.3	99.1	97.4	99.8
Lung	80.4	97.4	98.0	100.0
Multi-Target	79.1	94.8	97.3	99.8
Prostate	97.9	99.9	95.5	99.5
Prostate_2	87.4	97.1	96.9	99.9
Prostate_7fld	NA		95.1	99.3
Prostate_9fld	98.0	100.0	98.8	100.0
Prostate_11fld	NA		99.5	100.0
Stereo 1	81.2	96.3	97.8	99.6
Stereo 2	NA		96.0	98.7

Table 4.6: Gamma results for composite deliveries to film of the Elekta supplied TG119 plans and the two in-house developed stereotactic plans

4.3.7 End-to-End Test

The ATP created plan, for an adaptation of the reference CT to a daily MR with the tumour surrogate shifted, passed with an average of 99.3 % across the film RGB colour channels (2.0 % global dose, 2.0 mm DTA gamma criteria, dose suppression below 10.0 %). The ATS created plan, with an adaptation of the reference CT to a daily MR of a cylindrical surrogate, passed with an average of 97.5 % across the three RGB colour channels.

4.4 Discussion

4.4.1 Anterior Coil Attenuation

Anterior coil attenuation for various gantry angles is shown in Table 4.1. Attenuation was measured as approximately 0.6 % from G0 and ranged between 0.4 % to 0.7 % for listed gantry angles. For the TPS, the G0 attenuation was 0.8 % and ranged between 0.7 % to 1.0 % across the gantry angles investigated. Measured and calculated attenuation were consistent to within 0.5 %, with the largest discrepancy occurring at G30. It appears that the TPS determined coil attenuation is more varied across the investigated gantry angles, causing increased discrepancies compared to measured data. The TPS values would be susceptible to calculation uncertainties which may have contributed to such discrepancies. Note that inaccuracies in the TPS model of the cryostat characterisation, due to the spontaneous quench recovery/differing helium fill (see Appendix A), are unlikely to have significantly affected the beam spectrum to manifest in the coil attenuation. Whilst the attenuation of the beam due to the anterior coil is small, the effect this has on out-of-field doses is not [2] (Chapter 6 for more information). During patient treatments on the Unity system, where multiple gantry angles would be used, the effect of the anterior coil attenuation on the delivered dose would be negligible; however, the potential ESE should be investigated, and

appropriate patient shielding should be provided [2]. Note that the water equivalent thickness of the acrylic phantom was negligible for the TPS simulations.

4.4.2 Beam Quality

X-ray beam quality measurements showed that at commissioning the beam energy, according to the $TPR_{20,10}$, matched the TPS within 0.5 %. The measured $TPR_{20,10}$ value (0.705 ± 0.001) was slightly higher than those reported by Snyder *et al.* (0.704) [19], Woodings *et al.* (0.701) [20] and van Asselen *et al.* (0.701 ± 0.002) [5]; however, was within 0.6 %. Interestingly, dose map comparison at this beam quality to the TPS, 4.5(a) highlight the opposite where the measured dose map appeared slightly less peaked than the calculated. The differences presented here were consistent for several deliveries, suggesting that measurement uncertainty was not the cause. However, given the subtlety of the difference, with gamma results above 95.0 %, and the difficulties associated with attempting to improve results, no changes to the beam were made. Although, with the introduction of a new magnetron, the $TPR_{20,10}$ decreased approximately 0.4 % (0.703 ± 0.001) and better agreement was achieved with the TPS, Figure 4.5(b), and other reported values [5, 19, 20].

Note for consistency with the TRS398 protocol [29], a 10.0 × 10.0 cm^2 field at an SCD of 147.5 cm required set field of 9.7 × 9.7 cm^2 at isocentre; however, when a 10.0 × 10.0 cm^2 field at isocentre was set, the change in measured $TPR_{20,10}$ was negligible. $TPR_{20,10}$ was insensitive to the change in magnetic field strength, consistent with the work of previous investigators [5,20,48]. For the same magnetron the $TPR_{20,10}$ from G0 and G90 were equal within the measured standard deviation of the G0 measurements. The beam hardening effect of the tank wall was assumed to be negligible compared to that of the aluminium cryostat for these measurements; however, would still introduce uncertainty in the measurement.

When the grid voltage parameter was raised to 50.0 V the $TPR_{20,10}$ from G0 was 0.696 ± 0.001, which is a decrease of ~ 1.0 % from the nominal value (0.703 ± 0.001). As a side note, for this change of $TPR_{20,10}$ the chamber beam quality correction factor, used in reference dosimetry (k_{Q,Q_0} [29]), changed by less than 0.1 %. Although the reduction in $TPR_{20,10}$ was minimal, the degradation in beam shape was significant (Figure 4.6), with higher relative doses measured away from the centre. This was not unexpected as a lower average energy per pulse, in the accelerating waveguide, will cause the resulting bremsstrahlung distribution from the target to be less forward peaked, and have increased intensity off-axis. When doses are normalised to the centre reading, the relative dose off-axis is therefore greater compared to a dose map with the correct energy (34.0 V). Additionally, comparison of the direct charge readings taken at 10.0 cm G0 (as part of $TPR_{20,10}$), between grid voltages suggested an output decrease of up to 5.0 %, with the energy lowered.

These results highlight the relative insensitivity of $TPR_{20,10}$ to beam quality changes which significantly impact radiation characteristics. Roberts *et al.* [22] suggested a tolerance of ± 1.0 % to be used for routine $TPR_{20,10}$ measurements. However, such a

value may not be strict enough, or perhaps should be used in conjunction with an additional energy measurement technique (i.e. a determination of beam shape, with comparison to baseline measurements or TPS simulations), which is more sensitive to aforementioned changes. Further investigation is warranted to observe how grid voltage changes the beam quality, and subsequent machine behaviour. For example, an intentional voltage change to create a 0.5 % alteration to $TPR_{20,10}$ may cause a significant dose change (greater than ± 3.0 %). A study such as this would also help guide investigators when assigning tolerances to such tests.

4.4.3 Reference Dosimetry

Reference dosimetry as performed from G90 using the $TPR_{10,5}$ was reproducible, with a coefficient of variation (COV) of 0.3 %, and consistent with the nominal value of 1.000 Gy per 100 MU. This method can therefore be argued to be suitable for determination of machine reference output. The use of the $TPR_{10,5}$ reading from G0 to determine a 5.0 cm, G90 dose assumes comparable beam quality between the two angles, which may not be the case due to variations in cryostat construction. However, it can be assumed from the consistency of $TPR_{20,10}$ from G0 and G90 that a change in $TPR_{10,5}$ would also be negligible. Output measurements from G0 showed larger differences from the nominal value of 1.005 Gy per 100 MU and were more varied (COV = 0.5 %) compared to the G90 technique; however, were still deemed adequate as a routine check.

4.4.4 Determination of Magnetic Field Correction Factors

Measured correction factors for the two identical Farmer type chambers, at depths 5.0 cm and 10.0 cm, were consistent with values reported by other investigators for the same chamber type (0.997 ± 0.002) [5]. After applying the published dose conversion factor $c_{\tilde{B}}$ of 0.995 [5], the combined correction factors ($k_{B_\parallel,Q}$) were consistent with the work of O'Brien *et al.* (0.994 ± 0.001) [48] and van Asselen *et al.* (0.992 ± 0.002) [5]. The results for the $c_{\tilde{B}}$ factor showed the validity of applying published value for the calibration conditions in this work, since it was determined to be independent of SSD.

Although the $k_{B_\parallel,Q}$ correction factors for the two depths differ by 0.5 %, they agree with published values at 10.0 cm within the measurement uncertainty of van Asselen *et al.* [5]. This suggests the magnetic field correction factor $k_{B_\parallel,Q}$ is independent of depth and supports the use of published values at either calibration depth. This is not surprising given the previous work of O'Brien *et al.* [70], where the dose-response of ionization chambers in a magnetic field environment tended to be depth dependent only for small fields. The lack of a reference chamber used in the determination of factors here will increase uncertainty [47], as consistent machine output between 0 T and 1.5 T measurements cannot be guaranteed. However, this should not interfere with an assessment of depth dependence of the factors, as readings at the depths were acquired consecutively and output fluctuations were minimal on a given day.

Strictly speaking for Unity users calibrating machines in a similar manner to that in this work, magnetic field correction factors at 10.0 cm depth should be used, due to the measurement setup requirements. Ideally, reference dosimetry should be performed directly at isocentre from G90 and should this be achievable at 5.0 cm depth (with future vendor-designed 1D tanks) the corresponding correction factors should be correctly determined [47] and applied. The consistency of $TPR_{20,10}$ between G0 and G90 supports measuring these factors from G0, in agreement with previous Monte Carlo simulations [72].

4.4.5 MR Interference on Linac Operation

The operation of the MR had little effect on the linac behaviour, as is evident from the results in Tables 4.2 and 4.3. The output at the cardinal gantry angles while the MM scan was running was at worst 0.05 % from the non-MM state. The plan deliveries whilst the MM scan was operational were statistically the same as their non-MM counterparts as measured with EBT3 film, Table 4.3. Slight variation in leaf positions during multiple deliveries of the 5.0×5.0 cm^2 field, in Figure 4.7, is attributed to slight leaf movements between irradiations. The effect of the MM scan on the MVI panel/MLC behaviour was negligible, Figure 4.7(d), and results were statistically less than those observed in the difference map when the MLCs/jaws were exercised Figure 4.7(e). This was also apparent from the error histogram from the treatment record files Figure 4.8, where leaf errors as reported by the system whilst the MR was operational were within the reproducibility of the non-MR deliveries. These results agree with previous investigations [21].

4.4.6 IMRT Commissioning

Initial commissioning of the Elekta supplied TG119 IMRT plans failed the departmental criteria of 2.0 %, 2.0 mm (Tables 4.4 - 4.6) with average pass rates of 91.7 ± 7.0 %, 88.2 ± 11.1 % and 87.1 ± 9.4 % for the Octavius perpendicular (composite comparison), film perpendicular and film composite measurements, respectively. Of note were the poor results for the Multi-Target plan and the Prostate_2 plan for the three QA techniques. At 3.0 %, 3.0 mm gamma (as recommended during physics validation) results were initially considered acceptable with average rates above 95.0 % for the three methods, consistent with previous investigators reporting with the same devices and criteria [16, 81]. Similar gamma results with criteria of 3.0 %, 2.0 mm, as per AAPM TG-218 [75], were observed. The in-house stereotactic plans also failed the departmental tolerance of 2.0 %, 2.0 mm and even highlighted beam delivery issues at 3.0 %, 3.0 mm. During segment-by-segment delivery of the stereotactic plans to the MVI panel, Figure 4.9, an issue in the MOSAIQ sequencer was discovered, wherein it was applying an additional guard leaf rule to what was already set by the TPS. This occurred in part due to variation in leaf thickness at isocentre of the Unity MLCs (approximately 7.0 mm) from that for conventional systems (5.0 mm). Once rectified, all plans passed above 95.0 % at 2.0 %, 2.0 mm gamma criteria, with average passes

of 98.3 ± 1.8 %, 97.6 ± 1.6 % and 97.2 ± 1.3 % for the Octavius perpendicular, film perpendicular and film composite deliveries, respectively. These values compare well to other investigators using the 1500^{MR} array [81], ArcCheck®-MR device [19,57] and film [16]; however, for those works a less strict criteria was reported. For array beam-by-beam analysis, the beams for all plans had pass rates greater than 94.5 % at 2.0 % (local dose), 2.0 mm gamma criteria.

These results show that the PSQA techniques above can be used to determine issues with plan delivery. Small field stereotactic-type plans were clearly more sensitive to the guard leaf error. These small-field plans would also be expected to be more sensitive to other beam shaping issues. As such it would be beneficial for new sites to perform their own measurements of such plans, as well as the Elekta TG119 plans, during commissioning. Segment-by-segment delivery of these stereotactic plans, to the MVI, would also be useful to help discern issues with field shapes, as shown above. Note that an alternate method for detecting such issues would be through analysis of the auto-generated TRFs [105,106]. Comparison of set leaf positions in the TPS could be compared against delivered position in TRFs, to highlight the errors discovered in this work.

For the PSQA procedures, dose is calculated in the planning system to a homogeneous water phantom. Previous investigators alluded that this may be inadequate to highlight modelling issues [107]. Additionally, the audit process by the Australian Clinical Dosimetry Service (ACDS) requires unforced densities for their phantom when performing similar measurements. For the PSQA procedures above, the use of unforced densities in the TPS could potentially add uncertainty, due to day-to-day variations in setup which would not be present in the reference scan. Furthermore, forcing the RED of the solid water contour to 1.000 is more convenient for routine practice, is accounted for during the film calibration and was determined to be acceptable through comparison of a measured water PDD to that of the solid water under the same conditions. Finally, comparisons between film and TPS dose, with and without water sprayed on the film, revealed no statistically significant differences in gamma results between the two when following the QA methodology above.

4.4.7 End-to-End Test

End-to-end results for both ATP and ATS plans had pass rates > 97.0 % at 2.0 % local dose and 2.0 mm DTA. Snyder *et al.* [19], using a commercial thorax E2E phantom with film, reported a pass rate of 98.0 % for an ATS plan at 7.0 % dose difference and 4.0 mm DTA. At 2.0 %, 2.0 mm, Pappas *et al.* [83] reported a film pass rate of 93.1 % for a 3D-printed head phantom. Due to the resolution of the 3D printer, the tumour surrogates housing the film were not able to be constructed water-tight. This may have been of benefit as it meant that the copper sulphate solution was able to surround the film, thereby reducing uncertainties due to air gaps generating increased ERE dose.

The tumour surrogates used in this demonstrate the use of 3D printed phantoms for independent dosimetric assessment of the ATP and ATS workflows. This is consistent with the work of previous investigators [83, 86, 89]. Potential improvements can be made to the phantom to incorporate MR visible avoidance structures, in order to more closely match a clinical setting. Furthermore, as systems develop, the use of MR visible 3D printing materials could be investigated for phantom components.

4.5 Conclusion

In this chapter, the dosimetry commissioning work on the Elekta Unity MRL was discussed. Previous commissioning work was limited in terms of scope of potential tests a clinic may want to perform. Additionally, for centres that may not have access to specialised equipment, adaptions of commercial equipment, and development of phantoms in-house, facilitated measurement and reproduction of results for common vendor tests.

With the use of an in-house phantom, the attenuation due to the anterior imaging coil was determined to be negligible and measured values agree with TPS calculations. Beam quality, with correct grid voltage setting, agreed with published values and TPS calculations. The commonly used $TPR_{20,10}$ metric was found to be insensitive to changes in beam quality that significantly affected dosimetry. However, further investigation is warranted, with focus on how quantifying the grid voltage parameter affects this metric.

When vendors are designing commercial 1D water tanks, the requirements of different clinics should be considered, specifically linac calibration depths. However, even with equipment limitations, output calibration performed at 5.0 cm depth can still be achieved. Gafchromic film and the Octavius 1500^{MR} array can be used to highlight issues with plan deliverability, when appropriate gamma criteria are set, and commissioning of small field plans should be considered by clinics to help highlight differences between measurements and TPS calculations. The use of 3D printing materials and in-house phantoms can be of benefit when performing E2E tests on the Unity, and further development of MR visible 3D printing materials is worth pursuing. Additional commissioning work on the dosimetry of this system can be found in Appendix A.

5

Spiralling Contaminant Electrons

This chapter contains material that was published in the following publications and presentations:

[2] John Baines, Marcus Powers, and Glen Newman. Sources of out-of-field dose in MRgRT: an inter-comparison of measured and Monaco treatment planning system doses for the Elekta Unity MR-linac. *Physical and Engineering Sciences in Medicine* (2021). doi:10.1007/s13246-021-01039-6

- Out of field dose due to electrons generated in-field on an Elekta Unity MR linac. John Baines, Marcus Powers. Engineers and Physical Sciences in Medicine Conference, Brisbane, 2020
- Measured and calculated electron streaming on the Elekta Unity MRL. Marcus Powers, John Baines. Engineers and Physical Sciences in Medicine Conference, Brisbane, 2021

Additionally, material in this chapter is intended for publication with John Baines as co-author:

- Marcus Powers and John Baines. Sources of out-of-field dose in MRgRT: a systematic investigation of measured and calculated phantom electron streaming doses on the Elekta Unity MRL. Target journal: Physics in Medicine and Biology. (Est date of submission: March 2022). *(In draft)*

For this chapter, I performed the measurements on the Unity and the simulations described below. The simulation toolkit is a commercial product developed and provided by Elekta for patient radiation treatment planning calculations. Comparative measurements and calculations were performed by researchers at the Olivia Newton-John

Cancer Wellness and Research Centre. All other work described in this chapter is my own unless otherwise stated.

5.1 Introduction

In this chapter, measured and calculated out-of-field dose (OFD) on the 1.5 T Elekta Unity MRL at the Townsville Cancer Centre (TCC) is reported. Measured spiralling contaminant electron (SCE) dose was determined with EBT3 film in a similar set up to that of Hackett *et al.* [9]. However, in order to differentiate film dose due to head leakage and photon scatter from SCE dose, film was exposed in both 0 T and 1.5 T environments thus extending previous work. As an independent check on the 0 T data, additional measurements were performed at another Unity facility, namely the Olivia Newton John Cancer Wellness and Research Centre (ONJ), prior to magnet ramp up. Monaco v5.40.01 (Elekta, Stockholm, Sweden) treatment planning system calculations (TPS), with both 0 T and 1.5 T, were performed and enabled an inter-comparison of measured and computed OFD across both facilities. An assessment of Monaco's simulation of SCE had yet to be performed by researchers and the work below also aimed to address this gap in current knowledge.

5.2 Methods

5.2.1 SCE Measurements

To facilitate positioning of solid water, RW3 (PTW, Freiburg, Germany) and Solid Water® HE (Gammex Inc – A Sun Nuclear Company, Middleton, WI, USA), RTQA2 film (Ashland ISP Advanced Materials, NJ, USA) was located on the patient positioning system (PPS) so that it could be exposed to a 500 MU, $10.0 \times 10.0\,\mathrm{cm}^2$ field.

The exposed $11.0 \times 11.0\,\mathrm{cm}^2$ region on the RTQA film was used to position a solid water block 4.5 cm from each field edge and as such, the front surface of each block was 10.0 cm from the isocentre. Pairs of blocks were either parallel (Para) or perpendicular (Perp) to B_0. Figure 5.1 shows the block orientation according to the IEC 61217 coordinate system, with the notation of Hackett *et al.* [9], namely Para +ve, Para –ve, Perp +ve and Perp –ve included for comparison. OFD was determined using EBT3 film (Ashland ISP Advanced Materials, NJ, USA). For each position of the solid water blocks, a $10.0 \times 10.0\,\mathrm{cm}^2$ field, 4000 MU, gantry zero, was delivered orthogonal to the X-Y plane (- Z direction) following the work of Hackett *et al.* [9]. The corresponding D_{max} dose to water, 133.5 cm SSD, was used to normalize film dose. Film strips (batch number 06201903) $22.0 \times 2.0\,\mathrm{cm}^2$ were located on the surface, and at nominal depths of 1.0 mm, 3.0 mm and 5.0 mm into each block, centred around isocentre height. An annotated photograph of the experimental arrangement with the solid water block at X = + 10.0 cm is shown in Figure 5.2.

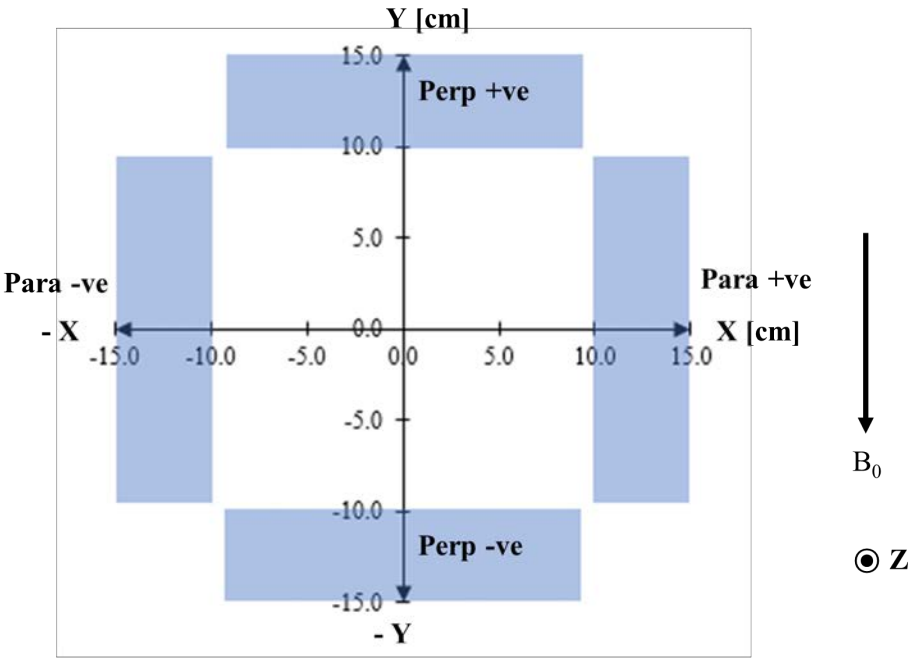

Figure 5.1: Beams-eye-view schematic at the isocentric plane showing the solid water block orientations relative to the IEC and Hackett *et al.* [9]coordinate systems and B_0

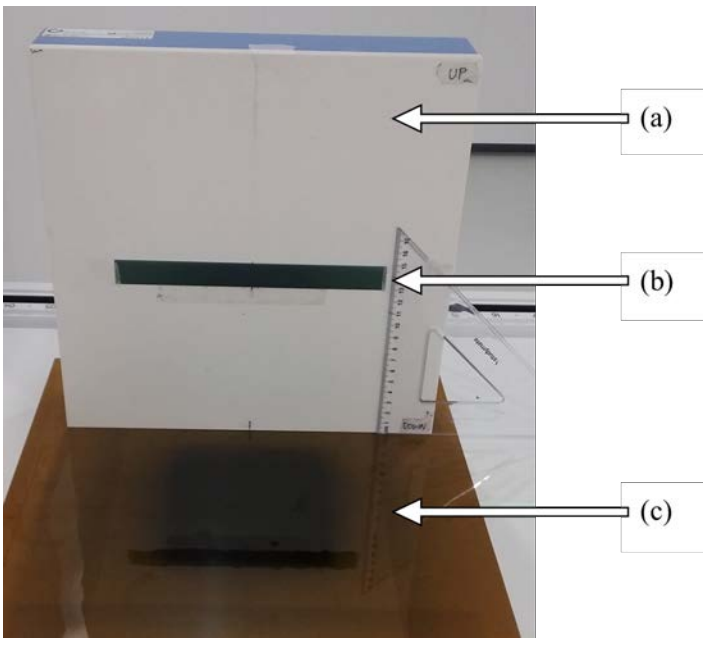

Figure 5.2: Annotated photograph showing the set up for a block at X = 10.0 cm. In the figure, (a) shows the solid water, (b) shows the placement of the EBT3 film (14.0 cm above the couch) and (c) shows the projection of the $10.0 \times 10.0\,cm^2$ field onto RTQA film which was used for localization

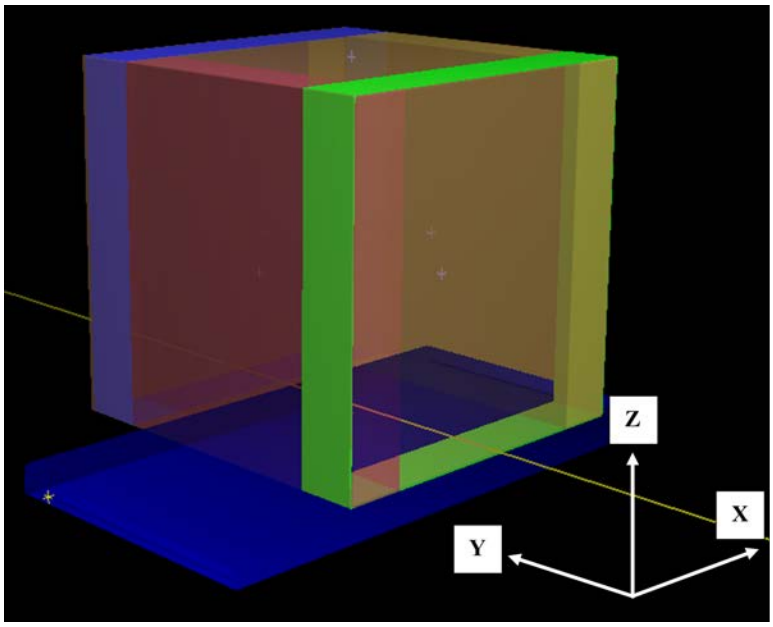

Figure 5.3: Geometry simulated in Monaco for SCE determination with the IEC 61217 coordinate system shown. In the figure, the beam is orientated along the - Z-axis

Given the thickness of EBT3 (0.27 mm) and central active layer depth (0.13 mm) the actual measurement depths were 1.1 mm, 3.4 mm and 5.7 mm. Film calibration was performed as described previously, in Section 4.2.6, for 0, 60, 125, 250 and 500 MU exposures with a $10.0 \times 10.0\,\text{cm}^2$ field. Film was processed as described previously (Section 4.2.6) with triple channel analysis and accounting for the Lateral Response Artefact [100, 101]. Using the $22.0 \times 2.0\,\text{cm}^2$ strips, mean doses within a $1.0 \times 1.0\,\text{cm}^2$ region of interest (ROI) centred on the films were determined for each depth and magnetic field environment. Profiles at $\pm$ X and Y, and both 0 T and 1.5 T environments, were derived using $20.0 \times 0.3\ \text{cm}^2$ ROIs. Using the same methodology, out-of-field doses and profiles were determined at ONJ for 0 T. Also by way of comparison, OFD for an Elekta Infinity linac (Agility head) was determined for the same block set up (IEC 61217 – X, collimator = 0.0°).

5.2.2 SCE Simulations

To simulate the measurement geometry, the Monaco treatment planning system was utilised. The physics and operation of the simulation toolkit has been discussed previously in this work (Section 2.1.2) and further information can be found in other publications [6, 46]. For the SCE computations, a CT scan of air with 1.0 mm slices was imported into the Monaco treatment planning system. A cube of $30.0 \times 30.0 \times 30.0\text{cm}^3$ was contoured and set as the external structure. Within this volume, $30.0 \times 30.0 \times 5.0\,\text{cm}^3$ block structures were contoured to simulate the experimental arrangement shown in Figure 5.1. Contours of $1.0 \times 1.0 \times 0.1\ \text{cm}^3$ were created at 1.0 mm intervals from 0.5 – 5.5 mm depths within each block and centred at isocentre height. The geometry created for the simulations is shown in Figure 5.3.

Due to increased uncertainty arising from dose grid voxelization near a contour edge, dose at 0.5 mm will be referred to as surface dose in this work. Block structures had a forced relative electron density (RED) of 1.000 and were layered above the external (air) structure. The air structure initially had a forced RED of 0.010 (the minimum forced RED that can be assigned). Additional computations were performed without forcing the air RED, such that the individual voxel RED values approached 0.001. Couch structures were added and the anterior coil was excluded for calculations. A $10.0 \times 10.0 \text{cm}^2$, 4000 MU, gantry zero beam was added. Calculations were performed using a 0.1 cm dose grid and a statistical uncertainty of 0.1 % per control point. With these settings, the statistical uncertainty within the block structures was less than 1.0 %. Dose calculations were performed with deposition to the local medium, using the phantom look-up table, and calculation time was approximately 8.0 hours. Monaco calculations were performed with a clinical 1.5 T model and a 0 T model which contains the TCC facility's cryostat characterization. Using the DVH Statistics tab, the mean dose to each of the $1.0 \times 1.0 \times 0.1$ cm^3 contours embedded in each block structure was determined. Doses were normalised to the nominal D_{max} dose for a water phantom at 133.5 cm SSD, with the same beam geometry as simulated, and field strength of 1.5 T. These simulations were also performed independently at ONJ.

5.3 Results

5.3.1 SCE Measurements

The variations of out-of-field depth-dose for the four block positions, 0 T and 1.5 T, are shown in Figure 5.4. For 0 T, Figure 5.4(a), measured depth-dose are comparable for all directions and there is agreement with ONJ data. The variation of depth-dose for a 6 MV FF Elekta Infinity beam (Agility head) is similar to that observed for the Unity with 0 T. With 1.5 T, Figure 5.4(b), the variation of depth-dose within the solid water at ± Y are alike, marginally less than with 0 T, and clearly different to that observed at ± X. In all directions for 0 T, surface dose is approximately 4.4 % of D_{max} and at a depth of 1.1 mm, the dose decreases to approximately 2.5 % of D_{max}. In comparison, with 1.5 T surface dose is approximately 3.8 % of D_{max} for the blocks at ± Y and for each direction the dose decreases to approximately 2.0 % of D_{max} at a depth of 1.1 mm. At 5.7 mm depth in solid water, dose for all directions is approximately 1.5 % of D_{max} and 1.3 % of D_{max} for 0 T and 1.5 T, respectively.

In the absence of a magnetic field, dose profiles at a given depth in each direction are comparable and representative examples are shown in Figure 5.5. These profiles do not exhibit a penumbral region and are symmetric. In contrast, 1.5 T profiles at Y = ± 10.0 cm from isocentre are distinctly different to those at X = ± 10.0 cm as shown in Figure 5.6. For the solid water at ± Y, profiles at a given depth are the same and surface profiles exhibit distinct penumbral regions as reported previously [9]. In this region of the profile surface dose is less than that for other depths, which appear equal. In addition, dose in this region is not zero, consistent with other investigators [9].

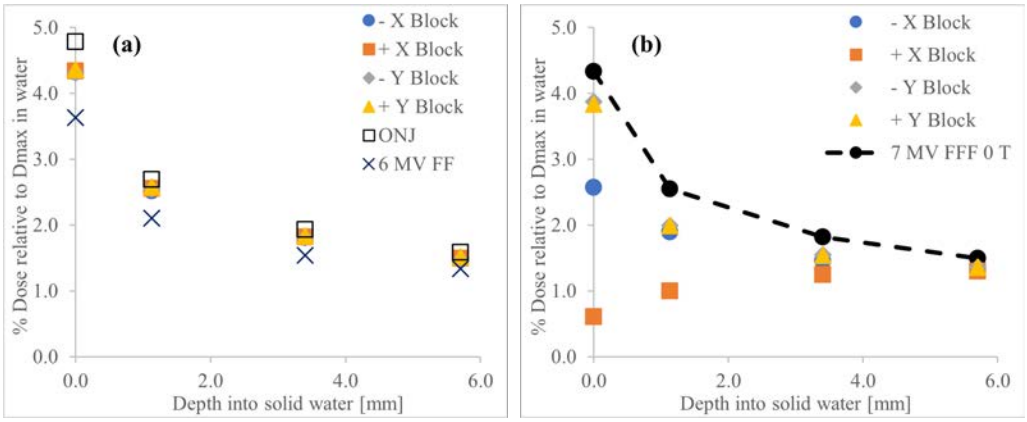

Figure 5.4: Comparison of measured out-of-field dose variation with depth within each block for (a) 0 T, and (b) 1.5 T (0 T average depth-dose shown for comparison)

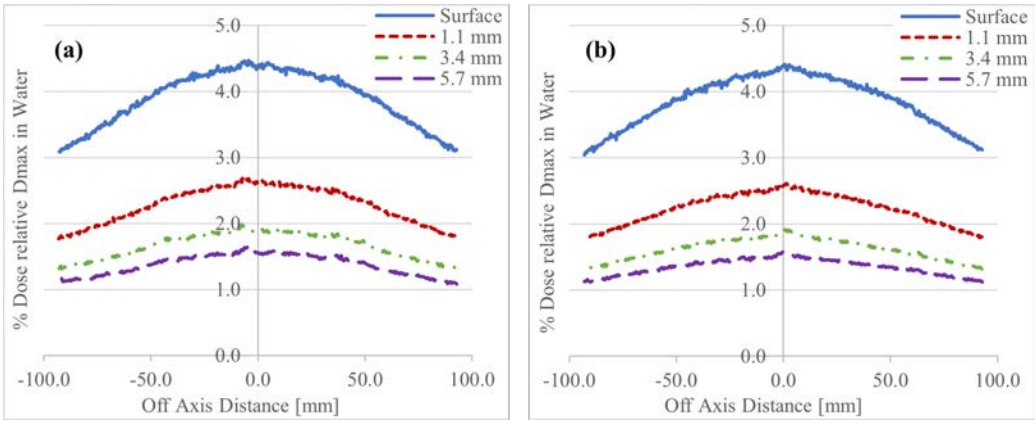

Figure 5.5: Measured out-of-field dose profiles for 0 T at depth into solid water blocks at (a) Y = 10.0 cm and (b) X = 10.0 cm from isocentre

Profiles within the solid water at ± X, 1.5 T, are symmetric and there appears to be a peak in the dose at an off-axis distance (OAD) of 0.0 mm, most evident at increasing depth and consistent with other experimental data [96].

5.3.2 SCE Simulations

Figure 5.7 shows a comparison of TPS calculated and measured out-of-field depth-dose for all directions and both magnetic field strengths, with calculations performed using a forced RED of 0.010. The variation in TPS depth-dose for 0 T is in general agreement with measured data for all directions. The maximum difference between measured and TPS dose occurs at the surface (depth = 0.5 mm) and is approximately 1.0 %. In the solid water blocks at ± Y, 1.5 T, the TPS overestimates dose for RED = 0.010, most notably near the surface (Figure 5.7(c)); however, the variation in depth-dose is consistent with measured data. Further, the dose is consistent between ± Y directions and the maximum calculated value is approximately 9.7 % of the D_{max} dose. TPS depth-doses into the solid water at X = ± 10.0 cm agree with and follow the same trends as the measured data, see Figure 5.7(d).

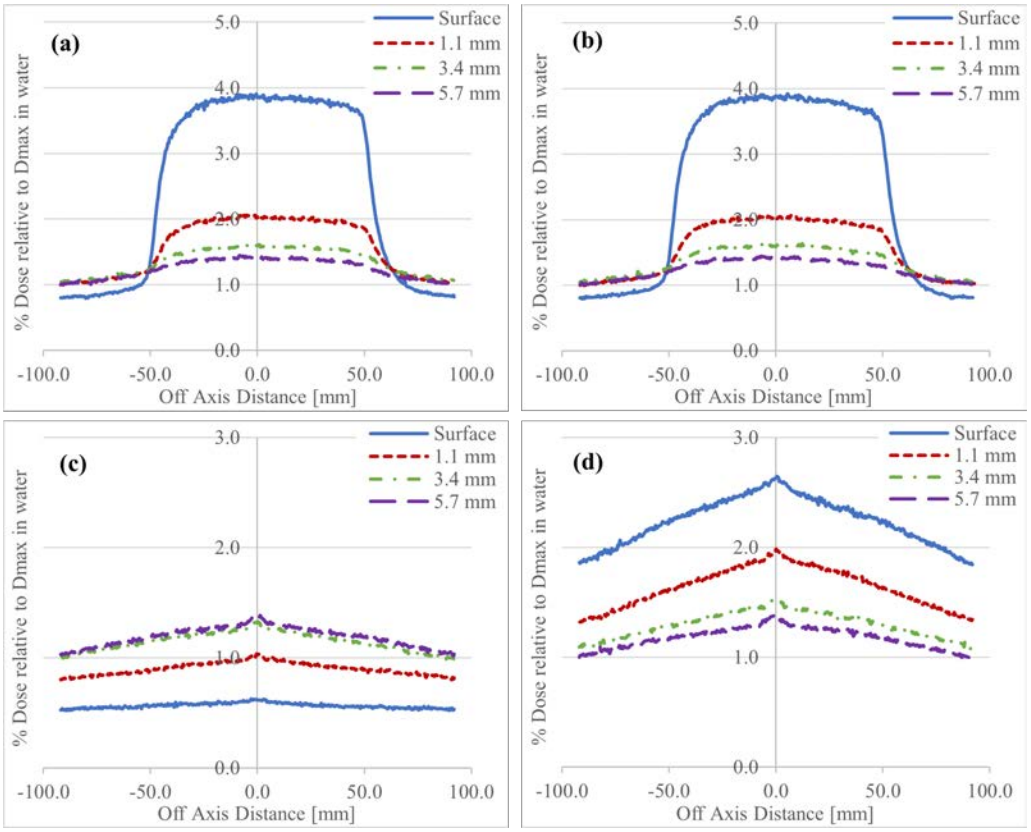

Figure 5.6: Measured out-of-field dose profiles for 1.5 T at the given depths into solid water at (a) Y = 10.0 cm, (b) Y = – 10.0 cm, (c) X = 10.0 cm and (d) X = – 10.0 cm, from isocentre

Figure 5.8 shows the TPS calculations for air with unforced RED. These are compared to measured data and forced RED calculations, for all directions and both magnetic field strengths. In 0 T, there is a difference in depth-dose behaviour between the forced and unforced calculations, and a maximum difference of approximately 1.0 % near surface is observed. Unforced calculated data does not agree with film measurements, and the largest difference occurs near surface (2.7 %). For 1.5 T, ± Y, the magnitude and variation of depth-doses without forcing the air RED shows agreement with experimental data, and doses are significantly lower than forced RED calculations. The maximum calculated dose occurs near the surface and is approximately 3.5 % of the D_{max} dose. At the same field strength, ± X, there is little variation between forced and unforced calculations.

5.4 Discussion

5.4.1 SCE Measurements

For 0 T, the variation of out-of-field depth-dose is isotropic, Figure 5.4(a). This dose arises from the background photon fluence associated with leakage and scatter (collimator and air) and the electrons set in motion by such photons. The average energy

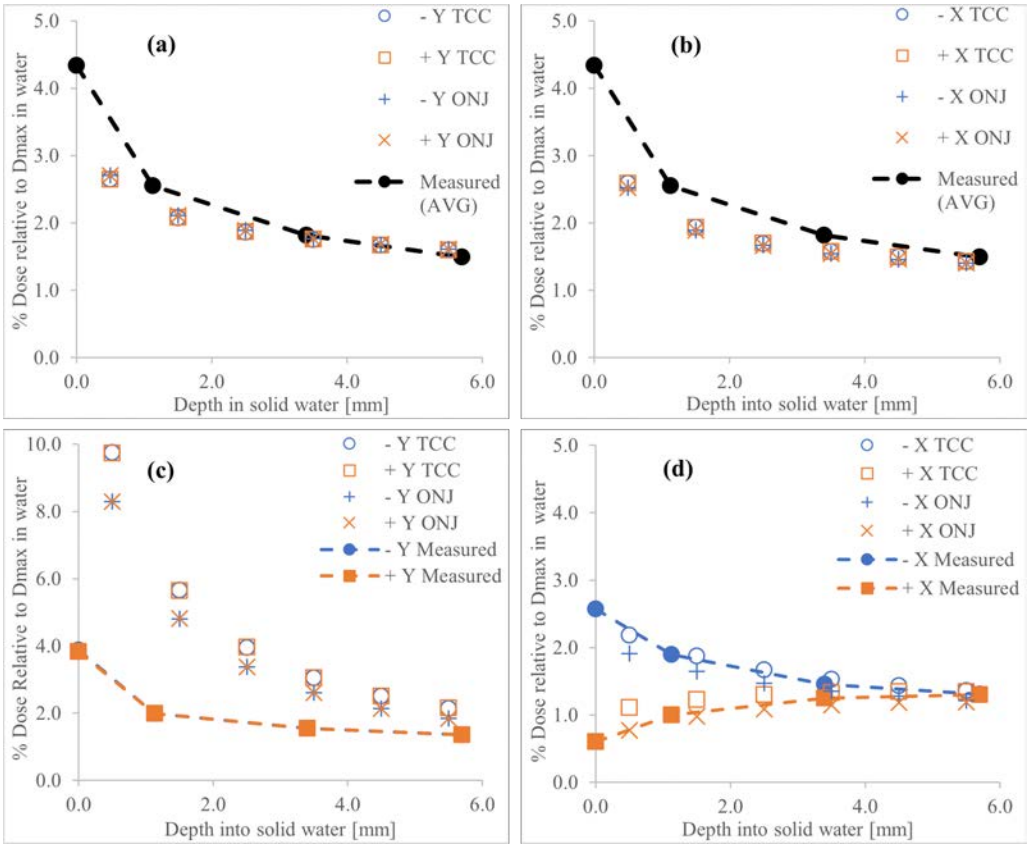

Figure 5.7: Calculated (RED = 0.010) and measured out-of-field dose for 0 T within blocks at (a) Y = ± 10.0 cm, and (b) X = ± 10.0 cm, from isocentre. Similarly, for 1.5 T within blocks at (c) Y = ± 10.0 cm and (d) X = ± 10.0 cm from isocentre. For 0 T, measured data is the average for all four blocks

of these electrons is approximately 500.0 keV, and the continuous slowing down approximation (CSDA) ranges of such electrons in tissue and air are approximately 2.0 mm and 1.5 m, respectively [42, 108]. The observed decrease in dose within 3.0 mm of the block surface is consistent with the attenuation of in-air generated electrons. Furthermore, it is reasonable to assume that the dose around 5.7 mm is predominantly due to local interactions of the photon fluence within each block.

With 1.5 T, out-of-field depth-dose in the solid water at X = ± 10.0 cm exhibits a decrease in surface dose relative to 0 T. As there is no SCE dose in these directions, the influence of the magnetic field on electrons set in motion by background photons is a determinant factor in the observed depth-dose behaviour. For example, at the – X solid water block, forward scattered electrons in front of the surface film are swept away from it by the Lorentz force, whilst electrons set in motion within the solid water are swept towards that film. On the contrary at the + X solid water block, electrons in front of the surface film are swept towards it and those behind the film within the solid water are swept away. This asymmetry in the trajectory of electrons at – X and + X blocks has been discussed previously [42, 43].

For mechanical safety, the MLCs are not able to fully close so as to avoid collisions and damage to linac components. As such, the closest the leaves can be is 0.5 cm,

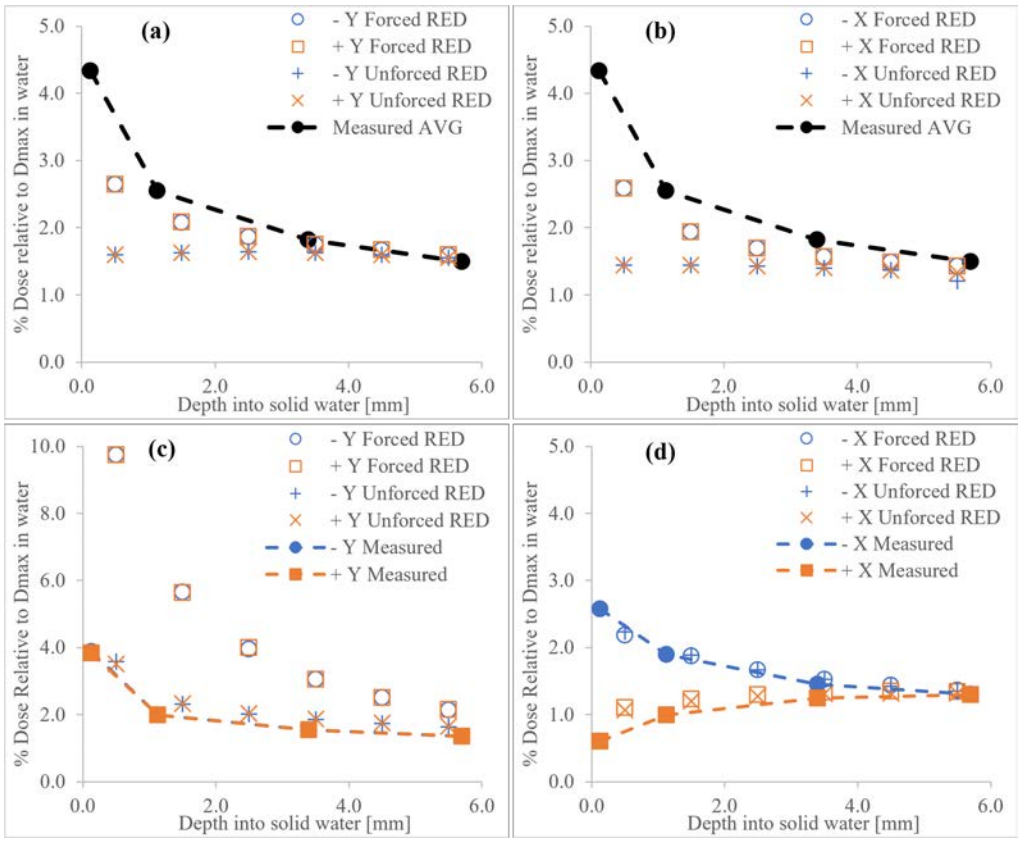

Figure 5.8: Calculated (forced and unforced RED) and measured out-of-field dose for 0 T within blocks at (a) Y = ± 10.0 cm, and (b) X = ± 10.0 cm, from isocentre. Similarly, for 1.5 T within blocks at (c) Y = ± 10.0 cm and (d) X = ± 10.0 cm from isocentre. For 0 T, measured data is the average for all four blocks

when projected to isocentre, and is referred to as the closed leaf gap. Hence, the peak dose observed at OAD = 0.0 mm in the film profiles from blocks at X = ± 10.0 cm, for 0 T and 1.5 T, can be attributed to radiation transmission through the jaw from this closed leaf gap on axis.

The magnitude and variation of measured depth-dose in 0 T within each solid water block is different to previous reported work [96]. The agreement between independent measurements performed at two centres in Figure 5.4(a) suggests that the published Monte Carlo data [96] may require investigation. Currently, it is unknown the exact source of the discrepancy in the previous Monte Carlo data [96]; however, modelling parameters, simulation setup or currency of the phase space source files should be scrutinized.

In the solid water at Y = ± 10.0 cm, 1.5 T, out-of-field depth-dose variation is the same for both directions, Figure 5.4(b). However, from the surface to around 3.4 mm depth into the solid water, dose is less than that for 0 T. At 5.7 mm depth, the dose for both field strengths is (1.4 ± 0.1) % of D_{max}. Thus, it is reasonable to suggest that at this depth, for 0 T or 1.5 T, dose deposition is dominated by local interactions of background photons. SCE and other in-air generated electrons do not contribute to the dose at or beyond 5.7 mm. Profiles from the blocks at Y = ± 10.0 cm in 1.5 T,

have been associated with the spiralling paths of contaminant electrons along the field direction [9]. The lateral extent of the profiles is correlated with the $10.0 \times 10.0\,cm^2$ field size in the isocentric plane. However, at OAD 80.0 mm, the dose for the profile at 5.7 mm depth in the solid water is greater than that for the surface profile. At depth, 500.0 keV electrons do not contribute to measured dose. Hence, background photons, not SCE, appear to account for penumbral dose at 5.7 mm. At present the relative contributions of SCE and background photons to the dose distributions at and near the surface have not been determined. In future work, Monte Carlo simulations of out-of-field dose should be performed to differentiate the contributions of SCE and background photons to depth-dose in this region.

5.4.2 SCE Simulations

The TPS computed variation of out-of-field depth-dose in 0 T shows the same general behaviour as experimental data when the air RED is forced to 0.010. Similarly, with 1.5 T TPS out-of-field depth-dose in the solid water at X = ± 10.0 cm is also in good agreement with experimental data. Although, forced RED calculations of near surface dose at Y = ± 10.0 cm are slightly underestimated in 0 T, and significantly overestimated in 1.5 T. The largest difference occurs near the surface (approximately 8.0 %). When the air RED remains unforced, simulations in 0 T disagree with the two independently measured experimental datasets presented above; however, they agree with previous Monte Carlo simulations [96]. It can be seen that at around 3.5 mm depth, the two TPS datasets converge (Figures 5.8(a) or 5.8(b)). At this range, dose would begin to be dominated by local photon interactions. Hence, it would seem that the contribution from in-air generated electrons is reduced with the lower (unforced) voxel REDs. In contrast, with 1.5 T, the results in Figure 5.8(c) and Figure 5.8(d) show better agreement between calculations with unforced RED and experimental data.

The disagreement between unforced and forced RED calculations at 0 T, and the differences observed in the three 1.5 T datasets (measured, forced and unforced calculations), can be explained by the simulation conditions. Specifically, it may not be appropriate to use an RED of 0.010 for air in Monaco calculations, with such a value being too high. The higher RED simulates a denser material; therefore, more SCE would be generated and recorded in the ± Y directions. This would also explain why the large discrepancy is not observed for the solid water at X = ± 10.0 cm, 1.5 T, as dose behaviour is dominated by local interactions and there are no SCE contributions. In addition to creating more electrons, the higher RED now means the path these electrons travel would also be more attenuating. The resulting difference, between forced and unforced/film SCE data, would be dictated by these effects and it appears that the generation is more heavily affected than attenuation, as more dose is observed for the higher RED.

This does not explain the discrepancy in measured data compared to Monaco unforced RED calculations in 0 T. Furthermore, the agreement of Monaco 0 T simulations with previous Monte Carlo simulations [96] is also noteworthy. The reason

for disagreement between 0 T measurements and unforced calculations is unknown. However, the same variables as above (modelling parameters, simulation set up etc.) should be scrutinised. Specifically, electron components in each simulation generation file (phase space file for Monte Carlo and the charged particle contamination source in Monaco) could be the genesis of the discrepancies. If the phase space files were created in 1.5 T, generated electrons would not be able to reach the phase space scoring plane, due to the altered trajectory from the Lorentz force [9]. Secondly, a charged particle contamination source would not be needed in 1.5 T Monaco simulations, as again these electrons would not be able to reach the patient plane. Thus, its inclusion in the Monaco modelling would only serve to increase calculation time. Therefore, for both Monte Carlo and Monaco modelling, the contributions of electrons in 0 T OFD would be underestimated (which may be a reason why these datasets agree). The presence of more electrons, would serve to increase out-of-field surface doses and may cause the calculated 0 T data to agree with measured. Independent Monte Carlo modelling, to that already published, is an investigation worth pursuing to address discrepancies between simulations and measurements of OFD in 0 T.

These differences between forced and unforced REDs calculations need to be handled with care in clinical scenarios. When generating radiation treatment plans on MR-only datasets, no electron density information is obtained directly from the image. Possibly the most common method to assign RED information to structures is to force density information, based on an average value obtained from a CT or a literature value. In Monaco, the lowest RED which a voxel can be forced to is 0.010. As such, this would be a typical value to assign to air structures around, and within, a patient. For a treatment plan it is uncommon to assign air around the patient a specific RED, unless visualization of the OFD is required. Thus the clinical implications of the above forced/unforced OFD discrepancy would be minimal. If accurate out-of-field dosimetry is required, whilst being able to visualize electron streams, then a simple solution would be to contour a large region around the patient and assign this as the external structure, thereby treating the patient as internal to this larger contour. This would increase calculation overhead with limited benefit for most patients. Nevertheless, it is a method worth considering in cases where OFD needs to be visualized for shielding considerations (common examples being breast or clavicular treatments). In contrast, difficulties would be encountered for air structures within the patient which are expected to exist on the daily MR scan (e.g. the oesophagus). These structures would need to be forced to the minimum RED, and the modelling of the electron streams (and the dose away from the structure) would be incorrect. SCE contributions to the dose away from these structures will be largely dependent on the cavity and the irradiated field sizes, but would be minimal compared to the contributions from the electron streaming effect (ESE) [8, 23].

Previously it was mentioned that there are uncertainties related to dose voxelization near contour edges. These uncertainties largely arise due to two reasons: (1) Monaco forces contours to align with the centre of CT voxels (meaning contours can be shifted

from where the user defines them), and (2) the dose grid may not overlay exactly with the CT grid (and therefore the contour edges). Positioning of the dose grid to overlay with contour edges is possible in Monaco; however, is restrictive and it is not always possible to directly overlay the two. When a dose grid voxel partially covers multiple structures, Monaco calculates an average RED based on a super-sampling of that voxel (i.e. the original voxel is further sampled by 27 sub-voxels). In such cases, voxel REDs (for those near contour boundaries) in simulations may be less representative of their actual RED. Specific to this work, voxels near the solid water contour edges (RED = 1.000) had reduced RED (either 0.333 or 0.667 depending on the offset of the grid). Higher resolution grids, or more freedom in grid placement, would alleviate this issue which is possible in non-commercial Monte Carlo packages. However, with more resolved grids, statistical noise becomes a significant issue, and calculation times to ensure accurate dose representation can be prohibitively long. Of course, coarsely resolved dose grids suffer from volume averaging effects, hence a balance needs to be found in the grid size to optimize simulated results. It is beyond the scope of this work to suggest such a grid size for SCE simulations; however, this may be possible should further Monte Carlo simulations be performed.

5.5 Conclusion

In this chapter, the SCE contributions to out-of-field dose was assessed with measurements and Monaco simulations for both 0 T and 1.5 T environments. Previously, no measured 0 T data of OFD was available and an assessment of Monaco OFD calculations in 0 T and 1.5 T had not been performed.

With 0 T, it was shown that measured and TPS calculated background scatter and leakage doses are isotropic and consistent between two independent clinics; however, the magnitude and variation of measured doses were inconsistent with previous reported Monte Carlo simulations. Agreement between Monaco calculations with an unforced RED air contour and published Monte Carlo data was obtained; although, differences were observed when the structure was forced to an RED of 0.010. For the latter, agreement with measured data was observed.

In 1.5 T, measured and calculated doses at ± X were consistent with previous measurements and Monte Carlo simulations. For Monaco calculations at ± Y, large differences with measured data were observed, and previous work, when the RED of the air generating the SCE was forced to 0.010. Such differences were not observed when the RED remained unforced. This limitation may have clinical implications for internal air-like structures when planning on MR datasets.

Future work is required for independent Monte Carlo modelling of the 0 T OFD to address the areas of discrepancy between this work and published data. Finally, the contribution of background photons to surface dose, for 1.5 T, in the ± Y directions needs to be quantified.

6

Electron Streaming Effect: Phantom Investigation

This chapter contains material that was presented in the following:

- Measured and calculated electron streaming on the Elekta Unity MRL. Marcus Powers, John Baines. Engineers and Physical Sciences in Medicine Conference, Brisbane, 2021.

Additionally, material in this chapter is intended for publication with John Baines as co-author:

- Marcus Powers and John Baines. Sources of out-of-field dose in MRgRT: a systematic investigation of measured and calculated phantom electron streaming doses on the Elekta Unity MRL. Target journal: Physics in Medicine and Biology. (Est date of submission: March 2022). *(In draft)*

For this chapter, I performed the measurements on the machine and the simulations described below. The simulation toolkit is a commercial product developed and provided by Elekta for patient radiation treatment planning calculations. All other work described in this chapter is my own unless otherwise stated.

6.1 Introduction

The work of Malkov *et al.* [8] and Park *et al.* [23] demonstrated that photon beams entering and exiting oblique surfaces caused the Electron Streaming Effect (ESE). Other investigators [24–26] have published on clinical, or anthropomorphic phantom, cases

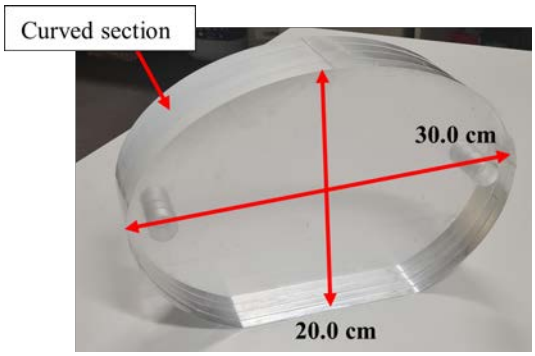

Figure 6.1: The acrylic phantom used for ESE measurements on the Unity. The primary beam was directed, from lateral gantry angles, onto the indicated curved section

with modulated treatment fields. However, to date ESE focused investigations remain limited. Furthermore, a systematic comparison of measured and simulated ESE on the Elekta Unity has yet to be reported. The aim of this work was to perform such a comparison using a phantom and a series of simple fields. Measurements were performed, using film, in a 1.5 T environment on a clinical Elekta Unity MRL. Monaco treatment planning system (TPS) calculations were investigated for the measured phantom geometry. Clinical investigations, like those previously discussed [24–26], are provided in Appendix B.

6.2 Methods

6.2.1 Phantom ESE Measurements

To determine ESE doses on the Elekta Unity, an acrylic curved phantom was used (see Figure 6.1). The phantom consists of several 30.0 cm by 20.0 cm ellipsoidal slabs which are 2.0 cm thick. Hollow channels, inset 2.0 cm from each lateral apex, allow for acrylic rods to be inserted to secure slabs together and minimize air gaps. The phantom was positioned on the Elekta Unity, such that the longer axis (30.0 cm) was aligned parallel to the Y direction, the shorter axis (20.0 cm) was parallel to the X direction and the flat section was at + X. In this way, lateral beams could be directed onto the curve section of the phantom and ESE generated from beam exit and entry through the phantom. Four acrylic slabs were used for a total thickness of 8.0 cm. This was placed on 10.0 cm of solid water so that the centre of the phantom was at isocentre height (14.0 cm above the couch). A connecting rod was inserted to remove the air cavity due to the channel and help align slabs. Gantry 0.0° (G0) images on the mega-voltage imager (MVI) were used to centre the phantom laterally at the isocentre. Longitudinally the phantom was positioned such that the beam edge, for the largest delivered field (5.0×5.0 cm^2), was 5.0 mm from the phantom apex. An example set up of the phantom is shown in Figure 6.2. Note that additional phantom material is shown in this image that was not used during these measurements.

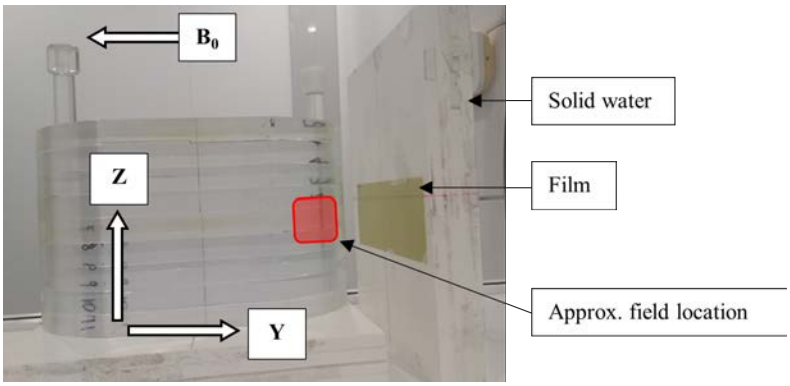

Figure 6.2: Example phantom set up for ESE measurements. The approximate beam location is shown in red, for a 5.0×5.0 cm^2 field, with the beam directed into the page (- X). Additional phantom material is shown which was not used during these measurements

To measure the out-of-field dose (OFD), EBT3 film was used. The measurement film (7.5×25.0 cm^2) was set within a $30.0 \times 30.0 \times 5.0$ cm^3 stack of solid water, beneath a 1.0 mm solid water piece and a "dummy" 0.27 mm EBT3 film (1.4 mm measurement depth). The surface of this solid water slab was set 5.0 cm superior from the phantom apex. Film was aligned parallel to the beam direction and centred at isocentre height. G90, 1000 MU, beams were delivered to the phantom, and separate film pieces were exposed to ESE from 5.0×5.0 cm^2 , 4.0×4.0 cm^2, 3.0×3.0 cm^2, 2.0×2.0 cm^2 and 1.0×1.0 cm^2 fields. A G270 delivery was also performed using a 5.0×5.0 cm^2 field.

To assess the attenuation of water on these streaming electrons, several exposures were obtained for varying film measurement depth. Measurements were performed with a 5.0×5.0 cm^2 G90 beam, 1000 MU. Exposures were determined for film on the surface, as well as with solid water of 1.0 mm, 3.0 mm, 5.0 mm, 7.0 mm and 10.0 mm in front of the dosimeter. For each exposure, the distance of the film plane to the isocentre remained constant.

ESE measurements were also performed with Optically Stimulated Luminescent Devices (OSLDs) [102]. OSLDs were placed on the surface of the solid water stack, and laterally positioned to coincide with the approximate positions of the max ESE doses, entry and exit, from the phantom. Due to the thickness of the device, doses recorded correspond to a depth of 1.0 mm [102].

EBT3 film was processed as described previously (Section 4.2.6), and a calibration using 0, 50, 100, 200 and 400 MU. Profiles through the centre of the dose distribution on the film, parallel to the beam direction (horizontal), were acquired. Profiles perpendicular to the beam direction (vertical) through the exit ESE dose were also determined for the G90 beams. For vertical profiles, "field sizes" were determined where, after normalisation, the distance between the 50.0 % dose levels on either side of the profile were determined.

For OSLDs, calibration was performed in a manner similar to film, where known doses were delivered to a sample of OSLDs, and a device response for this sample determined. OSLDs were read out as previously discussed in Section 3.2.3. All doses,

for both measurement devices, were normalised to the nominal D_{max} dose to water for a 5.0×5.0 cm^2 field, with the same MU, at an SSD of 133.5 cm. The 5.0×5.0 cm^2 (for normalisation) contrasts with the previously used 10.0×10.0 cm^2 (Chapter 5), and more closely matched delivered fields in the current investigation.

For the film attenuation data, raw dose was plotted against depth and values were fit using a double exponential. Using these plots (entry and exit), an approximate ratio for the change in dose between 1.0 mm (OSLD) and 1.4 mm (film) depths was determined. The depth correction was applied to the OSLD readings, and the result compared to film measurements, for all delivered field sizes. A value for the approximate surface dose, which could not be accurately measured with the aforementioned dosimeters, was also determined from the exponential fits. Using this value, attenuation measurements were normalised for entry and exit streams.

6.2.2 Phantom ESE Simulations

The experimental arrangement was simulated in the Monaco TPS. The phantom was set up on the CT, with Unity couch overlay, and scanned with 1.0 mm slices. This dataset was transferred to Monaco, the phantom components were individually contoured, as well as the solid water slab superior to the phantom. The phantom was set as the external contour and its relative electron density (RED) remained unforced, allowing the TPS to assign appropriate values. For the superior solid water slab, the RED was forced to 1.000. Additionally, the air around the phantom was contoured and two RED conditions were assigned. For separate calculations, either: (1) the air contour remained unforced, such that the RED was 0.001, or (2) the air was forced to 0.010, the minimum value that can be assigned (Section 5.2.2). The isocentre location was set to match the experimental arrangement, and simulations were performed for all measured field sizes. A screenshot of the simulation environment is shown in Figure 6.3.

TPS calculations were performed using a 0.1 cm dose grid, 0.2 % per control point statistical uncertainty and the phantom look up table. It was feasible that slight misalignment between simulation and measurements could have occurred. Hence, for the 5.0×5.0 cm^2 field, calculations were repeated with $\pm$ 1.0 mm shifts in the Y location of the plan isocentre. Transverse dose scoring planes 1.5 mm into the solid water were acquired. This was the closest depth that could be obtained from the TPS that matched film measurement depth (1.4 mm). Note that surface measurements on voxelized geometries are difficult, as in Chapter 5, due to grid resolution. Furthermore, in Monaco Unity a process is implemented for electron transport (to reduce calculation time) such that spiralling around the field lines in low density media is ignored, and instead only energy change is modelled along a line [109]. This results in lower calculated doses in air, hence why comparisons to measured data must be taken in dense materials [109]. Dose planes were analysed in Verisoft v7.2 (PTW, Freiburg, Germany) and profiles, horizontal (entry and exit) and vertical (at exit), were extracted for comparison with corresponding film profiles. Doses were normalised to the same value as film. For each

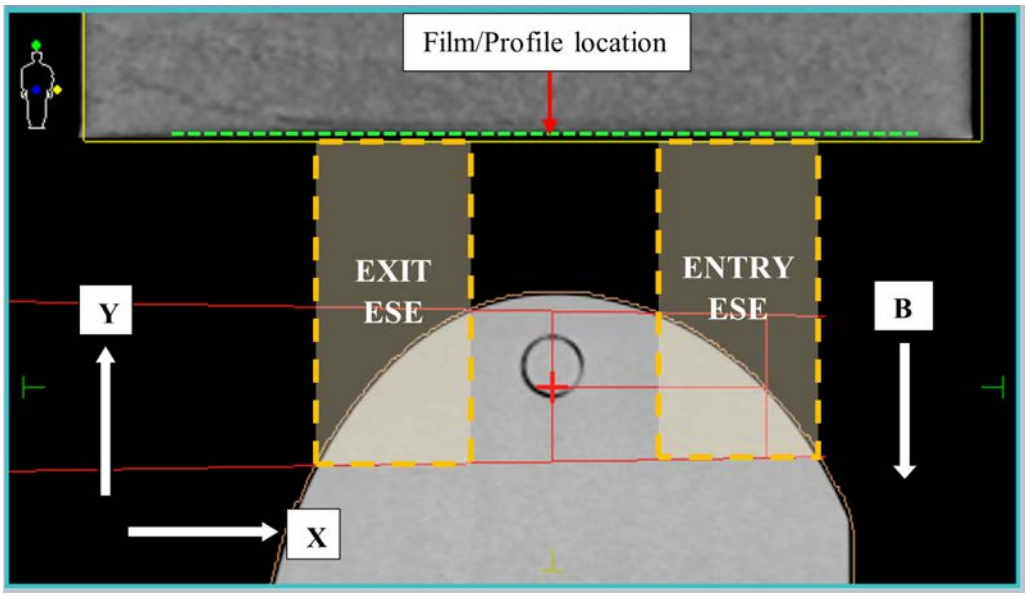

Figure 6.3: The simulation geometry used to determine ESE with the curved phantom. The 5.0×5.0 cm^2 beam from G90 is shown in red, with areas of entry and exit ESE (for this beam direction) also highlighted. The film/profile location is shown, inset 1.5 mm into the solid water. Note that this is 0.1 mm offset from where the film location was for measurements. The positive Z-axis is directed out of the page

field size, film profiles were subtracted from TPS profiles to give difference plots. Field sizes for vertical TPS profiles were determined and compared to measured values.

6.3 Results

6.3.1 Phantom ESE Measurements

Horizontal profiles of the film OFD, for the G90 fields investigated, are shown in Figure 6.4(a). Figure 6.4(b) shows demarcation of specific regions. Comparative OSLD data is presented in Table 6.1. For the latter, values have been corrected using the exponential fit described above. Exit ESE doses for all fields, from forward scattered electrons exiting the phantom, are larger than the entry ESE doses. For the 5.0×5.0 cm^2 G90 field, the largest ESE dose on the film was nearly 20.0 % of the D_{max} dose to water. Entry dose was approximately 6.8 % of the D_{max} dose for the same field. Dose in peripheral regions, outside the peaks of ESE, was about 1.3 % of the D_{max} dose. In the central region (between $\pm$ 20.0 mm), dose was approximately 2.7 % of D_{max}. This is less than adjacent ESE regions; however, was larger than the peripheral regions.

It can be observed, from Figure 6.4 and Table 6.1, that ESE decreases as the field size is reduced. Nevertheless, for the 1.0×1.0 cm^2 field, the peak ESE dose was still 5.0 % of D_{max}. The magnitude of dose in this central regions, for the 4.0×4.0 cm^2 field and below, tends to that observed in the peripheral regions. OSLD readings after correction, Table 6.1, showed similar differences between entry and exit ESE dose as the film; however, the magnitudes differed between the two dosimeters.

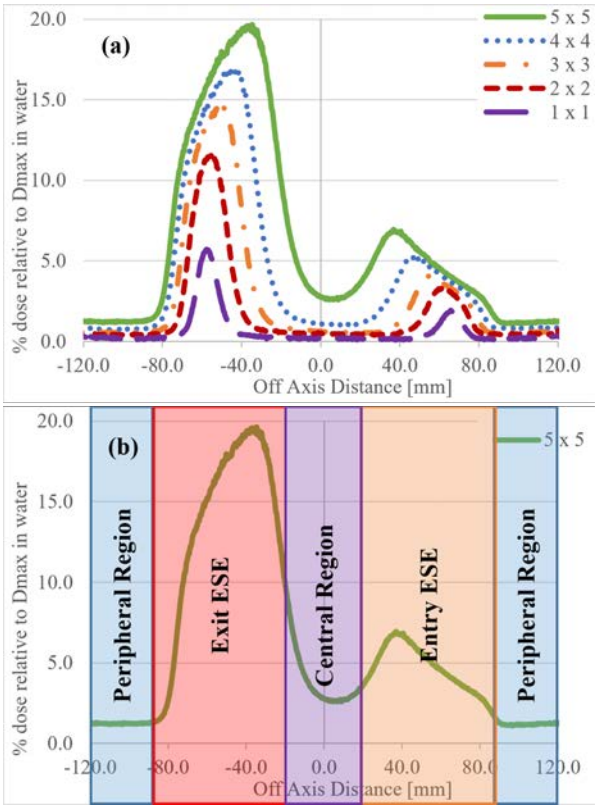

Figure 6.4: Profiles horizontally through the OFD measured on film. (a) shows measured film data for investigated fields, in the (b) approximate demarcated regions. Doses are normalised to the D_{max} dose for a 5.0×5.0 cm^2 field

Field Size [cm^2]	Film dose [%]		OSLD dose [%]	
	Entry	Exit	Entry	Exit
5.0×5.0	6.8	17.1	7.4	20.0
4.0×4.0	5.3	15.7	5.6	19.3
3.0×3.0	4.0	14.4	4.9	18.8
2.0×2.0	3.2	10.4	4.2	13.8
1.0×1.0	1.8	4.7	2.9	7.0
5.0×5.0*	4.9	17.2	6.4	22.6

Table 6.1: Film and OSLD doses for entry and exit ESE doses. Doses are presented as a percentage of the D_{max} dose to water for a 5.0×5.0 cm^2. Film dose reported at the same lateral location as the OSLD. * delivered from G270

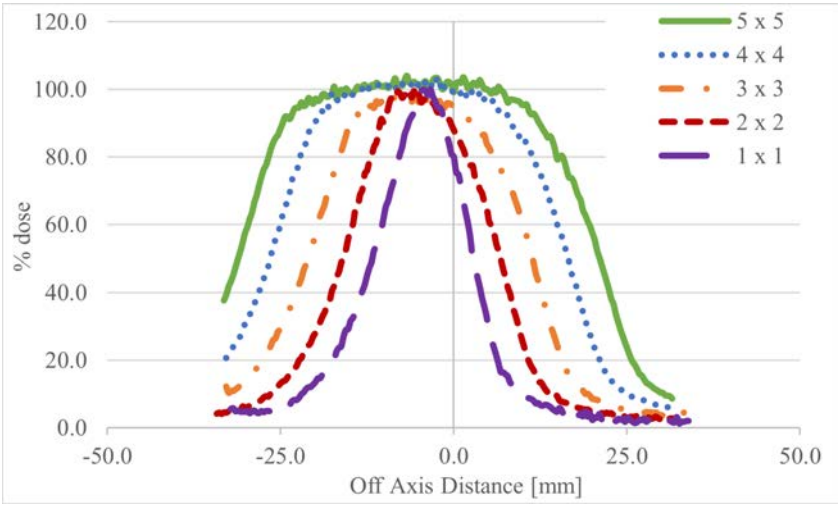

Figure 6.5: Profiles vertically through the OFD measured on the film. Doses are normalised to the D_{max} dose for a 5.0×5.0 cm^2 field

Vertical profiles are provided in Figure 6.5. Note that film markings, used to record film orientation, impinged on exposed regions and consequently some profiles are clipped; however, the necessary information was maintained. Doses have been normalised to the maximum value from the raw dose profile; with the exception of the 5.0×5.0 cm^2 and 4.0×4.0 cm^2 where noise interfered with this procedure. For these larger fields, which are comparatively flat, the dose from the marked centre was used for normalisation. Smaller fields produced narrower ESE regions on the film. However, there is an apparent offset in each profile, indicating ESE doses were deposited asymmetrically around isocentre height. This offset was more pronounced with smaller fields (3.0×3.0 cm^2 and below), and was biased in the direction of the Lorentz force (- Z direction).

The depth dependent attenuation of entry and exit ESE is shown in Figure 6.6. Note that the thickness of the active layer of the film has been taken into account. Using the double exponential plots, depth corrections were 0.770 and 0.809 for entry and exit streams, respectively. Attenuation of the electron streams for entry and exit are slightly different from each other.

6.3.2 Phantom ESE Simulations

Simulation results for the phantom ESE investigation with the various field sizes are provided in Figures 6.7 and 6.8. In each, the film data is provided for comparison, as well as associated difference plots. For the 5.0×5.0 cm^2 field, Figure 6.7, the + Y isocentre shift of 1.0 mm ("Superior") showed improvements in results compared to film; hence, this shift was repeated for the remaining fields. Conversely, simulations of the 5.0×5.0 cm^2 field with the isocentre shifted inferiorly showed increased differences to measured data. For this same field, differences in max ESE doses and peak slopes, between G90 and G270 data, can be observed. Simulations with the air unforced showed better agreement to film data, for all fields, compared to forced RED profiles.

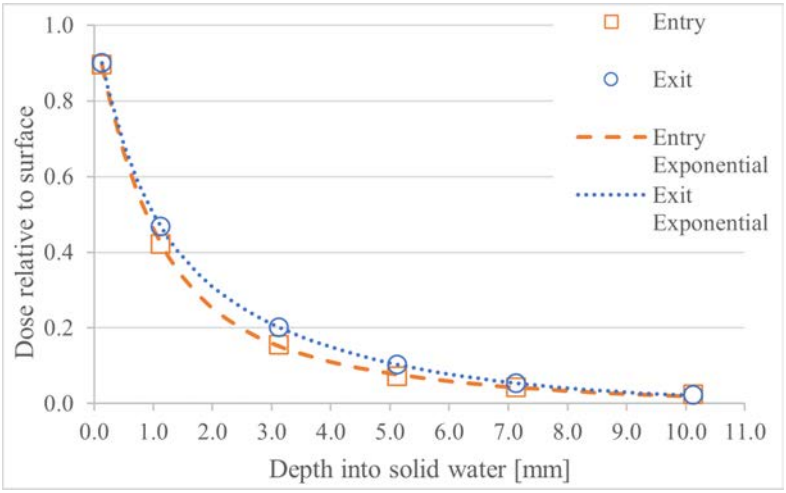

Figure 6.6: Attenuation data for the entry and exit streams. Values have been normalised to the surface dose determined from the exponential fits to raw dose measured on film

Field Size [cm^2]	Entry Differences [%]		Exit Differences [%]	
	Unforced	Forced	Unforced	Forced
5.0 × 5.0	0.3	-1.5	-1.7	-5.1
4.0 × 4.0	0.4	-1.2	-1.0	-3.9
3.0 × 3.0	0.5	-0.9	-0.7	-3.7
2.0 × 2.0	0.4	-0.9	-1.0	-3.3
1.0 × 1.0	0.1	-0.5	-0.4	-2.0
5.0 × 5.0*	0.5	-1.2	-0.9	-3.9

Table 6.2: Calculated versus measured (film) dose differences for ESE peaks. Negative values indicate film measurements were greater than TPS, and percentage expressed relative to the D_{max} dose to water for a 5.0 × 5.0 cm^2 field. * delivered from G270

In the former, the maximum absolute difference was approximately 1.7 % of the D_{max} dose (after correct alignment of the isocentre), occurring for the largest field. In general, with the air unforced, the TPS tended to calculate ESE doses lower than film measurements (see difference plots in Figures 6.7 and 6.8). With the air forced, doses in ESE regions were lower than film and oppositely in the peripheral regions. Absolute differences up to 5.0 % were observed when the air was forced. Table 6.2 provides dose differences between the calculations, with forced and unforced RED (corrected isocentre), compared to film data. Smaller fields can be seen to produce lower differences between TPS and measured data, Figure 6.8 and Table 6.2.

The calculated vertical profiles are shown in Figures 6.9 and 6.10, and have been normalised similarly to film. Similar patterns are observed in TPS calculations as in the film. Differences across the vertical profiles are comparable to those in the horizontal profiles at the same lateral locations. Although, in the smaller fields some lateral constriction of the calculated peak, compared to the film, can be observed. This was most notable for the 1.0 × 1.0 cm^2 field. Field sizes, and vertical offsets of the ESE distributions, compared to film data are in Table 6.3 for the different exposures.

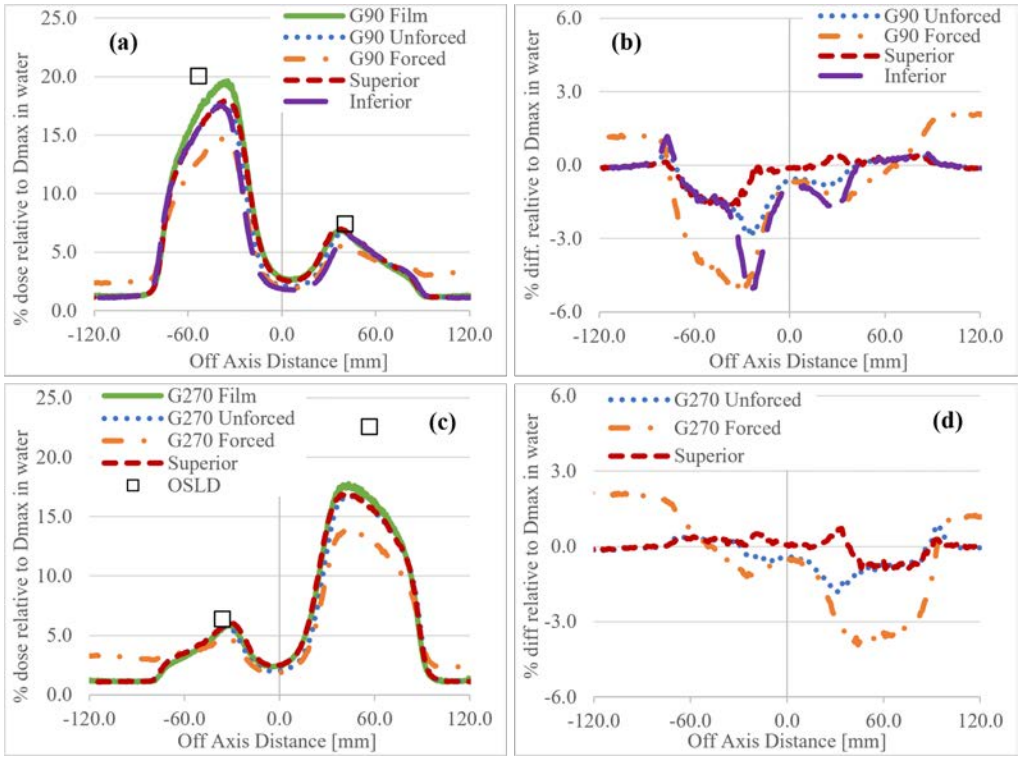

Figure 6.7: Horizontal profiles for the 5.0×5.0 cm^2 fields. (a) shows the G90 data, and (b) associated differences, with (c) showing the G270 data and (d) differences to film. Values are expressed as a percentage of the D_{max} dose to water for a 5.0×5.0 cm^2 field. OSLDs have been corrected

Field Size [cm^2]	Metric	Measured value [mm]		
		Unforced	Forced	Film
5.0×5.0	Field Size	52.35	52.53	52.17
	Offset	-4.0	-7.0	-3.0
4.0×4.0	Field Size	42.08	42.26	42.98
	Offset	-8.0	-9.0	-5.0
3.0×3.0	Field Size	31.78	31.85	32.40
	Offset	-6.0	-8.0	-4.0
2.0×2.0	Field Size	21.75	21.98	22.70
	Offset	-6.0	-7.0	-6.0
1.0×1.0	Field Size	13.30	13.56	14.53
	Offset	-4.0	-4.0	-4.0

Table 6.3: Field sizes and offsets of the ESE dose distributions for G90 calculations and measurements. For the offsets, negative values are in the - Z direction

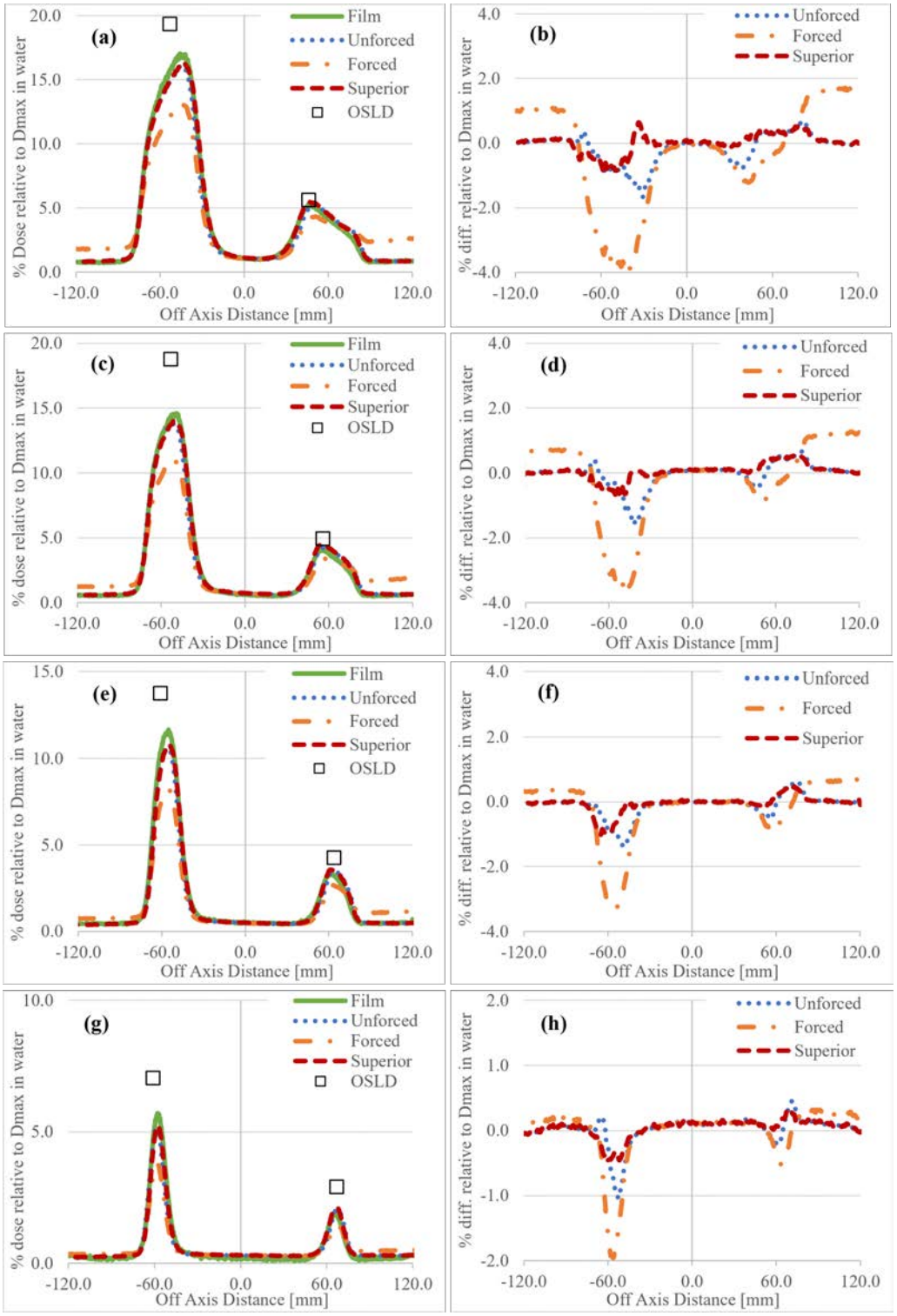

Figure 6.8: Calculated doses for the the phantom ESE compared to film. (a) shows the 4.0×4.0 cm^2 field and (b) the associated difference plot, (c) 3.0×3.0 cm^2 field and (d) differences, (e) 2.0×2.0 cm^2 and (f) differences, and lastly (g) 1.0×1.0 cm^2 and (h) differences. Values are expressed as a percentage relative to the D_{max} dose to water for a 5.0×5.0 cm^2 field, and OSLD readings have been corrected

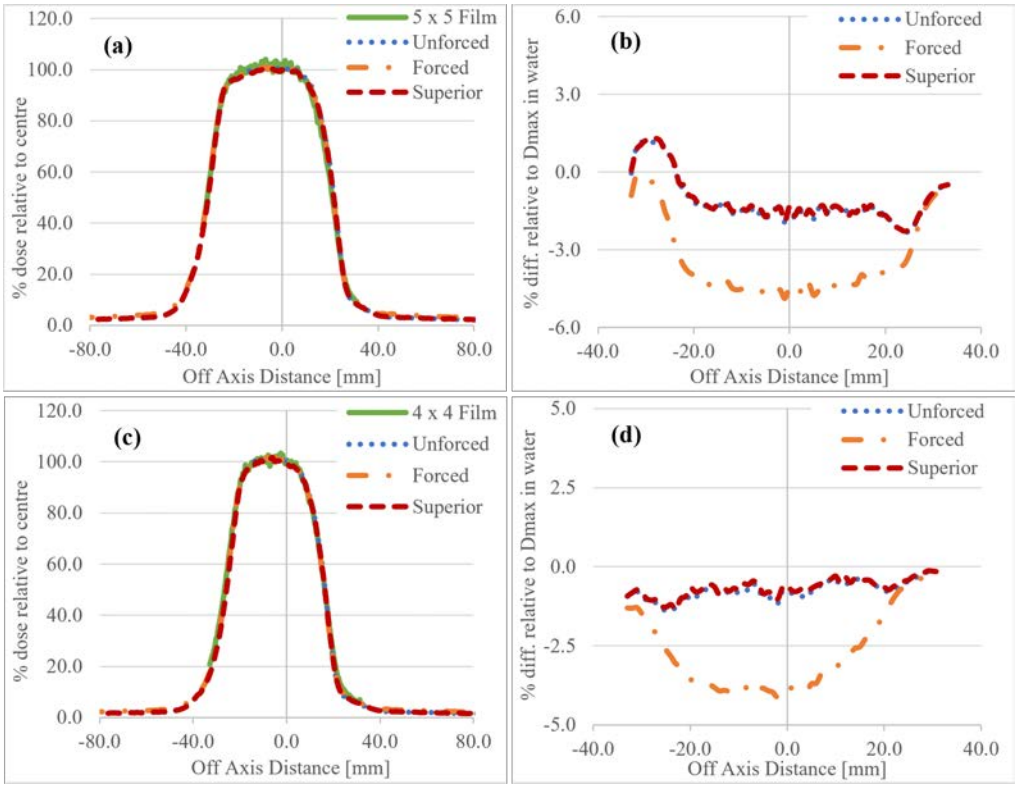

Figure 6.9: Calculated vertical profiles for the (a) 5.0×5.0 cm^2 field with (b) associated differences to film, and (c) the 4.0×4.0 cm^2 field and (d) differences. Profiles in (a) and (c) have been normalised to the central value, and percentage differences in (c) and (d) are relative to the D_{max} dose to water for a 5.0×5.0 cm^2 field

6.4 Discussion

6.4.1 Phantom ESE Measurements

In Figure 6.4 the horizontal film profiles highlight the entry and exit ESE from the phantom. For the investigated gantry angles, the exit ESE was larger than entry, consistent with the work of Malkov *et al.* [8]. ESE dose at the entry and exit decreased as the field size was reduced. However for all fields, doses were significant and clearly greater than those measured for spiralling contaminant electrons (SCE) [2,9]. Previous publications [2, 9] have discussed strategies to mitigate these doses with the use of patient specific shielding. At the peripheries of the profile there is no ESE contribution, hence dose in this regions is due to SCE and background photons, and dose in this region is consistent with previous investigations [2, 9].

Slopes within ESE dose regions can be attributed to the shape of the phantom, in combination with the primary beam and generated electron streams. When the primary beam transits the sloped phantom, there will be differential attenuation across the beam cross section. Therefore, upon exit, the parts of the beam which have transited less material (those closer to the phantom apex) will generate more electrons which will stream to the film, Figure 6.11. Furthermore, due to the curvature, the rate at which the phantom surface falls away from the electron stream changes along the Y-

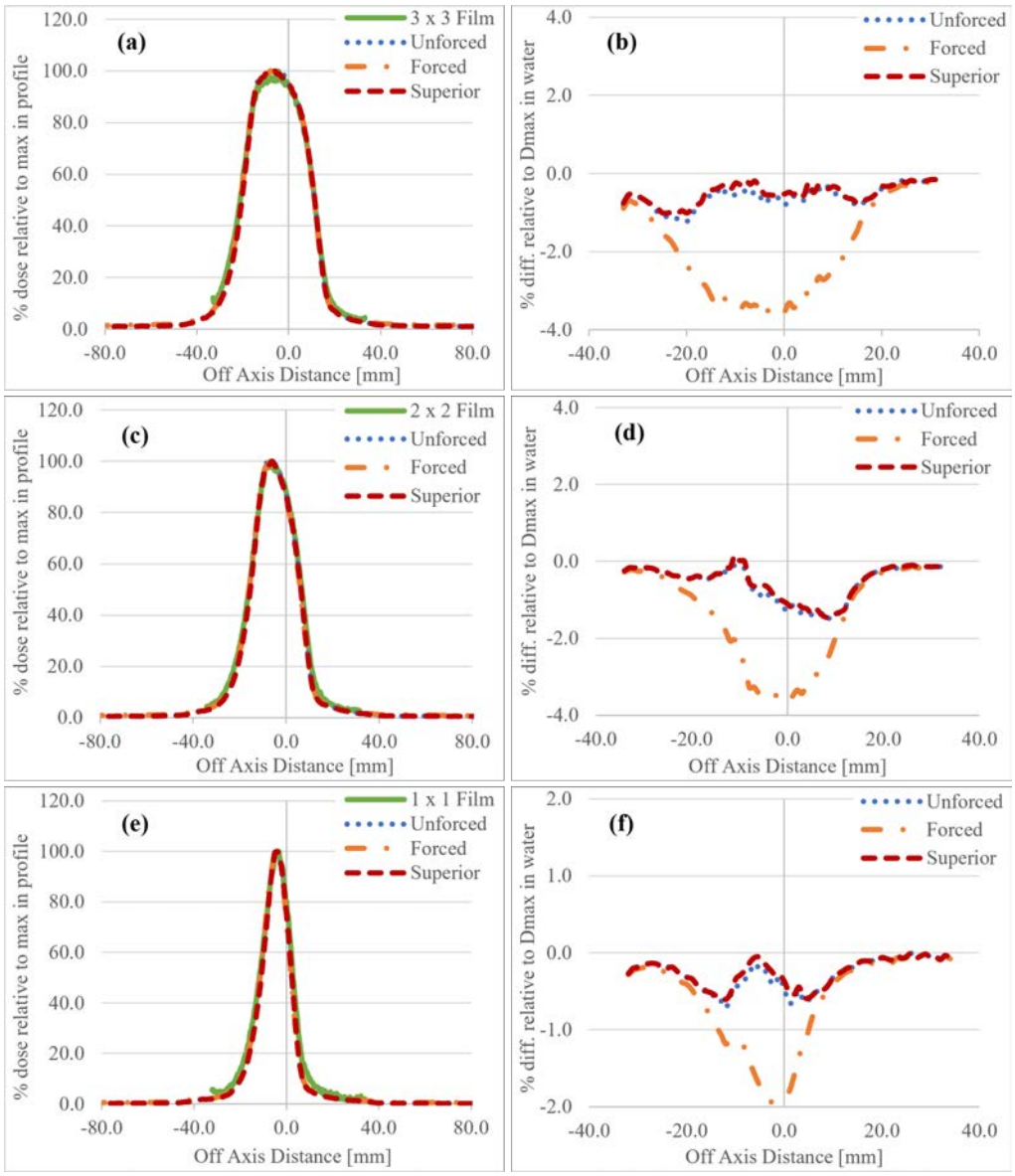

Figure 6.10: Calculated vertical profiles, compared to film, for (a) the 3.0×3.0 cm^2 field with (b) associated differences to film, (c) the 2.0×2.0 cm^2 field and (d) differences, and lastly (e) 1.0×1.0 cm^2 field with (f) differences. Values in (a), (c) and (e) have been normalised to the maximum value in the profile, and differences for (b), (d) and (f) are relative to the D_{max} dose to water for a 5.0×5.0 cm^2 field

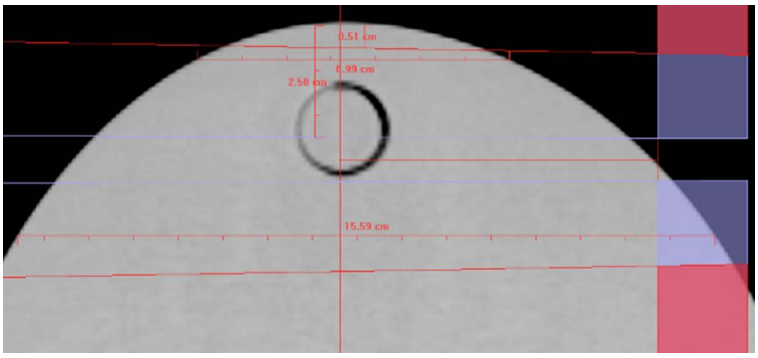

Figure 6.11: An image from the TPS of the curve phantom, with distances marked. One can see that as the field size is reduced from the 5.0×5.0 cm^2 (red) to 1.0×1.0 cm^2 (blue), the distance to the phantom apex is increased. Furthermore, photons which transit the phantom closer to the apex undergo more attenuation than those distal to this point. Hence one would expect more electrons be produced from this former position

axis. In effect, an ejected electron is more likely to be able to spiral and return to a less steep surface (in the 1.5 T environment). Thus, more electrons are able to escape and stream from regions which have greater curvature (i.e. regions closer to the phantom apex), as the distance to the surface is greater than the electron spiral radius Figure 6.11. The variable phantom curvature, between entry and exit, is why the gradients of these corresponding parts of each plot are different. A smaller effect which also contributes, is the variable air attenuation for the electrons escaping from different regions on the phantom. Electrons exiting closer to the phantom apex transit less air, before reaching the solid water, compared to those away. The spiralling electrons have a range of about 1.5 m in air [2], meaning they undergo little air attenuation, hence this effect is a lot smaller than the slope effect.

The above effect also accounts for variation in OFD between G90 and G270 beams. In Figure 6.12, the measured OFD for the two gantry angles are presented together. It can be observed that G270 ESE peak dose is less than G90; however, the profile is broader. A simple numerical integration of each curve, between 0.0 mm to 100.0 mm, suggested that the total exit ESE dose deposited on the G270 film was greater. The variation in phantom slope will account for this, where the G270 beam exiting the phantom interacts with a greater area than the G90 exiting. ESE generated from a less steep slope (relative to the magnetic field) will be concentrated to a smaller area and hence one would expect higher peak doses but a narrower distribution, shown in Figure 6.13. One may think of the changing gradient as compressing or expanding the resultant distribution out of field. Of course, as the gradient is reduced (i.e. the surface becoming parallel with the field lines), less ESE can be generated and the situation tends more to that seen for the electron return effect (ERE). Interestingly, the peak dose for the entry ESE on the G90 is greater than the G270, however the distribution is still broader.

For reducing field size, two effects are occurring which affect the shape of the resulting ESE curve: (1) fewer primary photons are interacting to generate the electrons,

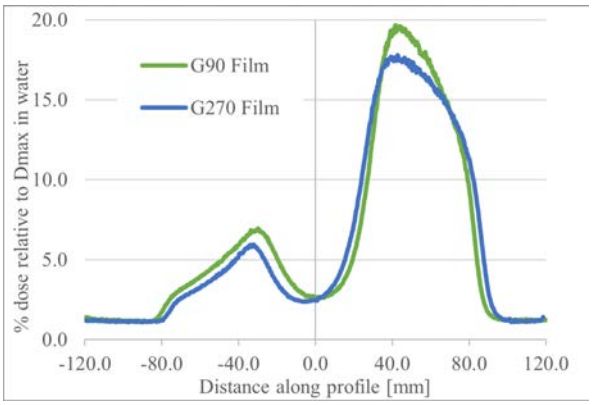

Figure 6.12: G90 and G270 film ESE distributions. Note that the G270 data has been flipped around the Y-axis to aid with visualization

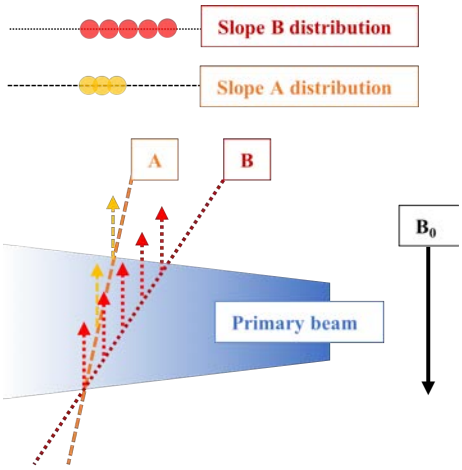

Figure 6.13: Diagram showing how variable slopes can alter ESE distributions. One can see how the lesser slope A creates a more concentrated distribution that is narrower than that for slope B

simply due to reduced collimator opening and (2) the divergence of the primary beam is reduced. For the first point, fewer electrons obviously causes the measured ESE dose to be lower. On the second point, as the photons at the centre diverge less than those at the peripheries, one may expect smaller fields to have more forward directed photons. Electrons generated during these interactions could be expected to be forward directed, causing the electron stream to effectively become more focused (less broad). An additional reason for this "focusing" is also due to reduced curvature across the cross-sectional area of the smaller fields, compared to larger fields.

It can also be observed, for these smaller fields, that the regions of peak ESE doses expand laterally on the horizontal profiles. This can be attributed to the phantom shape as above, where the rate at which the surface falls away varies due to the curvature. With smaller fields, electron streams closer to the phantom apex are not created (as this part of the phantom is not irradiated). Therefore, these contributions to the profile are lost and broadening in the entire profile is observed. Additionally, one can see that the dose in the central region is reduced for smaller fields. With

larger fields, the beam edge is close enough to the phantom apex that electrons and low energy photons are able to escape to contribute dose to the film. As the distance from phantom apex to beam edge is increased, due to reducing field size, the electrons and scattered photons undergo more attenuation. At some field size, the distance the electrons have to travel to escape the phantom is too great and they will not contribute to the measured dose. In this situation, the dose recorded will be due to: photons escaping the phantom; background photons scattered from the air around the phantom and linac components, and; any electrons which are generated in the air between the phantom and the film, at the level of the measuring plane. Such doses, for these small fields, could be expected to be comparable to SCE or head-leakage and scatter (HLS) [2], and differences would be minimal (see Chapter 5).

OSLD readings were greater than film, even after correcting to equivalent measurement depths. This was particularly the case for exit streams, where dose differences to film were up to 5.0 % of the D_{max} dose. For entry streams, better agreement was observed with the largest difference being 1.5 % for the G270 5.0×5.0 cm^2 field. Agreement for entry ESE doses between dosimeters, G90 deliveries, was better than 1.1 %. The use of OSLDs to measure OFD on the Unity has been discussed previously [25]. Therefore, it is supposed here that the disagreement between dosimeters in this work lies in the method used to correct readings. Although empirically a good fit to the film data, the use of the double exponential to describe the attenuation of the electron streams may not be valid. The fundamental quantity which describes electron energy loss as it penetrates a medium is the linear stopping power [33]. The functional form of this quantity is complicated [33], and the application of a simple double exponential to describe this process can be questioned. Electrons in the stream will have a polyenergetic spectrum. Additionally, there will also be "contaminant" photons present, with their own energy spectrum. So to determine the attenuation of just the spiralling electron components cannot be readily determined with measurements, and Monte Carlo methods will need to be considered. Nonetheless, repeat measurements may be of benefit. Specifically, the use of a film at the solid water surface, with a dummy film in front, would produce a measurement depth similar to the depth of the active layer within the OSLD, allowing for easier comparison. Such measurements are currently the subject of future investigations. OSLD positional offsets, relative to the point of comparison on a film profile, may also have increased observed differences between dosimeters.

The vertical film profiles in Figure 6.5 show a clear reduction in ESE doses with field size, consistent with the horizontal profiles. Interestingly, a distinct offset in peak position is apparent, particularly so for the small fields. This skew follows the direction of the Lorentz force, and the projection of the primary beam; however, is more distinct than offsets observed in-field for water profiles [20,70]. This is because the range of the electrons in air, and hence the extent to which the profile is skewed, is larger than in water. It is also for this reason that the penumbras of these profiles are greater than those measured in field for water profiles. The offset could be noteworthy clinically, as

previous investigations have highlighted that OFD directly follows the projection of the primary field [2,9]. It is apparent here that there is some discrepancy between the two, which should be noted when considering shielding for clinical cases. In practice, a user would more than likely search for regions of significant OFD by adjusting isodoses and the above mismatch, between beam "position" through the patient and the subsequent OFD location, may not be an issue.

Attenuation plots in Figure 6.6, show the significant reduction in dose with depth in solid water. The general shapes of the two curves are consistent with previous investigations [2], and indicate that at around 5.0 mm and below, the electron dose is significantly reduced. At 5.0 mm, the dose tends to fall below 10.0 % of the unattenuated "surface" value determined from the exponential fit. At 10.0 mm and below, the corresponding value is < 2.0 %, consistent with the attenuation of 500.0 keV electrons as in previous investigations [2,8,23]. The varying shape between entry and exit curves, particularly at shallower depths above 5.0 mm, suggests that the spectrum of electron energies are different between streams. At depths, these curves begin to coincide possibly suggesting that photon components to the individual streams are of comparable energies. Note that it may be typical to express attenuation curves for photon beams on a logarithmic scale. The application of this to electron beams is arguably not valid, as discussed above, and was not adapted in this work.

6.4.2 Phantom ESE Simulations

TPS simulations of the OFD associated with the phantom, Figures 6.7 and 6.8, show the same trends as recorded on film and OSLDs. Specifically, the entry ESE dose was calculated to be less than exit, for all field sizes, both RED settings and all isocentre positions. Noting the 5.0×5.0 cm^2 field (Figure 6.7(a)), the shape of the original unforced calculation shows some difference to film, notably around the centre of the profile. These differences were exacerbated in the calculations performed with the isocentre shifted 1.0 mm inferiorly, which was observed from the difference plot in Figure 6.7(b). An inferior offset in isocentre position would tend to lower dose in the central region, as the distance from the beam edge to the phantom apex is increased, as reasoned previously. Larger differences for the inferior isocentre shift calculations, compared to film, were observed at the regions of steep dose gradients approaching ESE peaks. Dose here originates from electrons from the primary beam edges, and differences indicated the curvature of the phantom did not match the measurements. After shifting the isocentre superiorly 1.0 mm from the original calculation, differences between film and TPS were reduced at these regions. Discrepancies at the centres of each peak were not affected for either shift, as dose here comes from electrons escaping from the central region of the primary field. This part of the phantom, and as a smaller effect the shape of the primary beam here, would not change significantly with a 1.0 mm offset. Note that a 1.0 mm error in isocentre position between delivery and calculation is small, easy to erroneously introduce and difficult to detect. Given this,

when considering shielding requirements for patients, reproducible set up is important as subtle changes between calculation and delivery can change OFD characteristics.

Similar field size trends were observed in the calculated data as for the film, with less ESE dose at entry and exit being calculated with reducing field size. Agreement between TPS calculations and film improved as the field size was reduced, for all calculation conditions. At fields of 4.0×4.0 cm^2 and below, TPS calculations with the corrected isocentre position matched film within less than 1.0 % of the D_{max} dose. Interestingly, for the larger 5.0×5.0 cm^2 field, the G270 delivery also agreed to film better than 1.0 %, contrasting with the G90 delivery where differences were of the order of 1.3 - 1.5 %. This is still under investigation; however, the current suggestion is that subtle differences in measurement position between the two could have contributed to discrepancies.

From dose difference plots for all fields, it can be observed that calculations with forced RED differ from film and unforced calculations. At ESE peaks, less dose is calculated in forced RED calculations compared to unforced, and measured, and the opposite is seen in peripheral (SCE) regions. The difference between forced and unforced SCE doses has been previously discussed in Chapter 5. Unlike SCE, forcing the air around the phantom will not interfere with ESE generation, as the point of electron generation occurs inside the phantom. However, the air will be more attenuating with the higher forced RED, and electrons transiting this air will deposit less dose at the scoring plane.

Another brief point to note, regarding calculations, is the use of the Phantom look-up table to model the material properties (mass density and Z). The use of this table for modelling the experiment above is valid, given that all the materials used were phantom-like rather than tissue-like. For patient calculations, the Patient look-up table will be used and REDs will be mapped to tissue equivalent materials. This will have limited impact on the high energy Compton events; however, for low energy interactions associated with electrons and scattered photons, the atomic number of the medium becomes important. The effect of look-up table on calculated dose should be investigated, simply by repeating the simulations above with the alternate table, and results compared to measurements. It is also a factor worth considering when performing *in vivo* measurements of OFD on patient datasets.

Calculated vertical profiles are presented in Figures 6.9 and 6.10. Dose differences between calculated and measured data were less than 2.0 % for the largest field, unforced RED calculations, and typically decreased with field size. Note that differences in the 2.0×2.0 cm^2 vertical profiles increased in magnitude, potentially due to a mismatch in film and TPS profile location, discussed below. Additionally, differences were consistent across the vertical profiles as at the same location on the horizontal (i.e. dose differences for a vertical profile, extracted at a given lateral distance, matched that for the horizontal at the same lateral distance). Forced calculations showed increased differences through the vertical, consistent with the horizontal data. The general shapes of the calculated profiles match measurements; however, some lateral constriction was

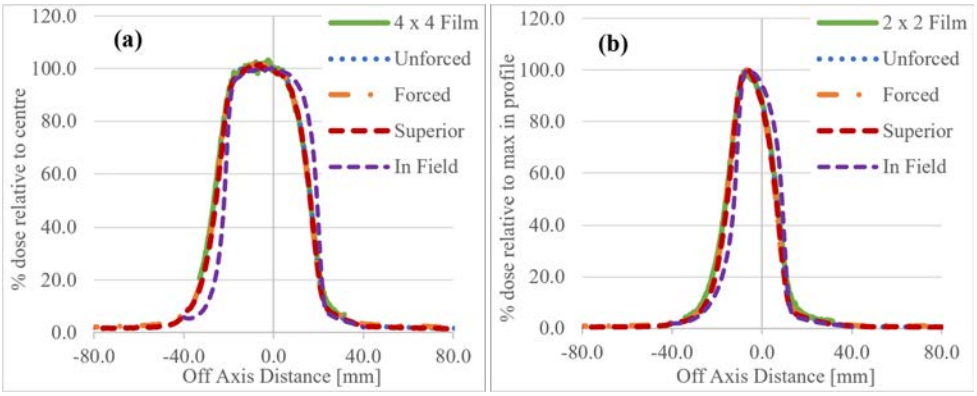

Figure 6.14: Comparison of out-of-field vertical profiles compared to those in-field for the (a) 4.0×4.0 cm^2 and (b) 2.0×2.0 cm^2 fields. In-field profiles were acquired within the acrylic phantom at the same lateral distance from the isocentre as those out-of-field

noted for the smaller fields. This corresponds to narrower dose distributions calculated than what are measured, with differences in the penumbra regions. The grid resolution, incorrect jaw positioning during measurements and uncertainty when extracting the vertical profiles from the datasets, may contribute to this. With decreased fields, sharper ESE dose distributions are created. It may be the case that the calculated grid resolution is too large to accurately model this, notably for steep gradients, whereas the film has improved resolution and can measure without significant volume averaging effects. Furthermore, the jaw drive direction is along the vertical axis for this set up. If jaw positioning during measurements was slightly different to that set in the TPS, then broader (or narrower) distributions could be expected. Lastly, inconsistent location of the vertical profile between the calculated and measured data could contribute to discrepancies. The location of the vertical profiles is through a relatively high-gradient region on the horizontal plots. Differences in lateral location from which vertical profiles are extracted could cause discrepancies, in both shape and magnitude, between datasets.

Total "field size" metrics for the calculated data matched those as measured; however, there is marked differences in the peak offset location between field sizes and calculation settings. This may be due to a number of things, the most likely being noise in the data. For instance, the maximum value in the profile was used to determine the location of the peak position. In Monte Carlo simulations, and film measurements, intra-voxel noise can interfere with this determination. To overcome this TPS and film data could be averaged, say to a 3.0 mm voxel region. Such a method was not originally performed, as it diverges from clinical workflow; however, it is a method worth considering to potentially reduce this discrepancy. Aside from this, the calculated offsets matched the direction of the Lorentz force; although, all are of larger magnitude than those reported for the primary field from other investigators [20, 70], as discussed above. An example of this is shown in Figure 6.14, where offsets and penumbras of profiles calculated in field for the 4.0×4.0 cm^2 and 2.0×2.0 cm^2 fields are different

from those out-of-field.

6.5 Conclusion

In this chapter, measured ESE during irradiation of a phantom with simple field geometries was performed on the Elekta Unity. EBT3 film and OSLDs were used to determine ESE dose 1.4 mm within solid water, from beam entry and exit through a curved phantom. Five square beams were delivered, 5.0×5.0 cm^2 to 1.0×1.0 cm^2. The experimental geometry was simulated in the Monaco TPS. Measured and calculated OFD were compared for each field, using vertical and horizontal profiles. Additionally, attenuation of entry and exit streams were determined.

Film data showed that doses of up to 20.0 % of the D_{max} dose to water could be measured out-of-field for the maximum investigated field size of 5.0×5.0 cm^2. OSLD readings of the ESE dose did not match film, nor TPS, warranting further investigation. The magnitude of ESE doses associated with these fields represents a safety concern for patient shielding, and the necessary bolus shielding should be provided. The attenuation data showed that 10.0 mm of water equivalent material provides the necessary protection. General shapes of ESE profiles have been shown to be influenced by phantom and beam geometry, and it was highlighted that smaller fields resulted in less ESE dose.

TPS data generally agreed with film when the air around the phantom remained unforced. It was highlighted that forcing the air to the minimum assignable value (0.010) will interfere with both SCE and ESE simulated doses. Furthermore, the need for accurate positioning during experiments or clinical treatments, is needed as subtle changes in isocentre position and dose scoring location (profile location) can cause significant differences between measurements and simulations. It was also highlighted that ESE may not necessarily following the projection of the primary field, due to differences in density of irradiated media and the subsequent effect on electron range/radius of curvature.

Finally, further investigation is warranted into the use of OSLD for measuring OFD. Discrepancies between film readings and OSLDs could potentially be eliminated if measurement depth could be consistent between the dosimeters. Monte Carlo simulations of ESE from phantom entry and exit is also an area worth considering. Such calculations would potentially discern how these electrons are attenuated by water, or tissue, in the absence of contributions from background photons.

7

Electron Streaming Effect: Anterior Coil Investigation

This chapter contains material that was published in the following articles and presentation:

[2] John Baines, Marcus Powers, and Glen Newman. Sources of out-of-field dose in MRgRT: an inter-comparison of measured and Monaco treatment planning system doses for the Elekta Unity MR-linac. *Physical and Engineering Sciences in Medicine* (2021). doi:10.1007/s13246-021-01039-6

[3] Marcus Powers and John Baines. Electron Streaming Effect Associated With the Elekta Unity Anterior Imaging. *Frontiers in Physics*, **10** (2022). doi:10.3389/fphy.2022.880121

- Measured and calculated electron streaming on the Elekta Unity MRL. Marcus Powers, John Baines. Engineers and Physical Sciences in Medicine Conference, Brisbane, 2021.

For this chapter, I performed the measurements on the machine and the simulations described below. The simulation toolkit is a commercial product developed and provided by Elekta for patient radiation treatment planning calculations. All other work described in this chapter is my own unless otherwise stated.

7.1 Introduction

The investigation of the electron streaming effect (ESE) by Malkov *et al.* [8] and others [23,25,26] focused primarily on irradiation of patient or phantom materials. Since ESE

can be generated from any attenuating material in the beam path, the transit of such beams through the anterior imaging coil was investigated. The anterior imaging coil is present for all treatments on the Unity, hence should be fully characterised in terms of dosimetric impact to patients [2, 20, 21]. Prior to this work, no publications had focused on this area, hence the first recorded observations of coil induced ESE are reported in this chapter. Out-of-field dose (OFD) was measured, during irradiation of a tilted anterior coil, using EBT3 film. Various coil angulations were investigated. Additionally, Monaco treatment planning system (TPS) calculations for ESE from the tiled coil were performed, using both a CT of the coil and a default coil model within the TPS. Measured and calculated data for a variety of field sizes were compared. Changes in simulated ESE, with varying electron density of the coil, were investigated. A clinical investigation of OFD resulting from irradiation of the tilted coil is provided in Appendix B.

7.2 Methods

7.2.1 Coil ESE Measurements

To investigate ESE associated with the anterior imaging coil, the coil was tilted approximately 7.0° to the horizontal. The superior end was nominally 5.0 cm above the inferior end, and the underside of the superior end was approximately 31.0 cm above the couch. EBT3 film, 15.0 × 15.0 cm^2, was attached approximately 2.0 cm in from each end of the coil. This was achieved by taping the film directly to the coil, ensuring that the distance from the coil edge was approximately consistent along the width of film. Given that these electrons streams are not significantly attenuated in air [2], changes to measured OFD from differences in film-to-isocentre distance, i.e. film not parallel to beam edge, were expected to be negligible.

ESE was measured for 8.0×22.0 cm^2, 5.0×22.0 cm^2, 5.0×5.0 cm^2, 5.0×3.0 cm^2 and 3.0 × 3.0 cm^2, 500 MU, G0 fields, incident on the centre of the coil. Larger rectangular field sizes, 8.0 × 22.0 cm^2 and 5.0 × 22.0 cm^2, were selected to represent head and neck treatment fields, and to exacerbate ESE dose. Smaller fields were selected to represent prostate-type treatments, and to correlate results with the phantom ESE investigations in Chapter 6. Film set below the coil at the superior end, detected streaming electrons from forward scatter exiting the coil. At the inferior end, film placed above the coil detected backscattered streaming electrons. For each delivery, a piece of "dummy" film was taped to the measurement film, to act as build-up material such that measurement depth was 0.4 mm (0.27 mm dummy film, plus 0.13 mm to the active layer of the measurement film). The Y-axis of the primary beam was marked on each film, to localize results. A schematic of the experimental set up is shown in Figure 7.1.

To determine the effect of coil angulation on induced ESE doses, two additional measurements were performed using the 5.0 × 22.0 cm^2 field and coil tilts of 0.0° and ~ 3.5°. Film calibration was performed using the methodology described previously

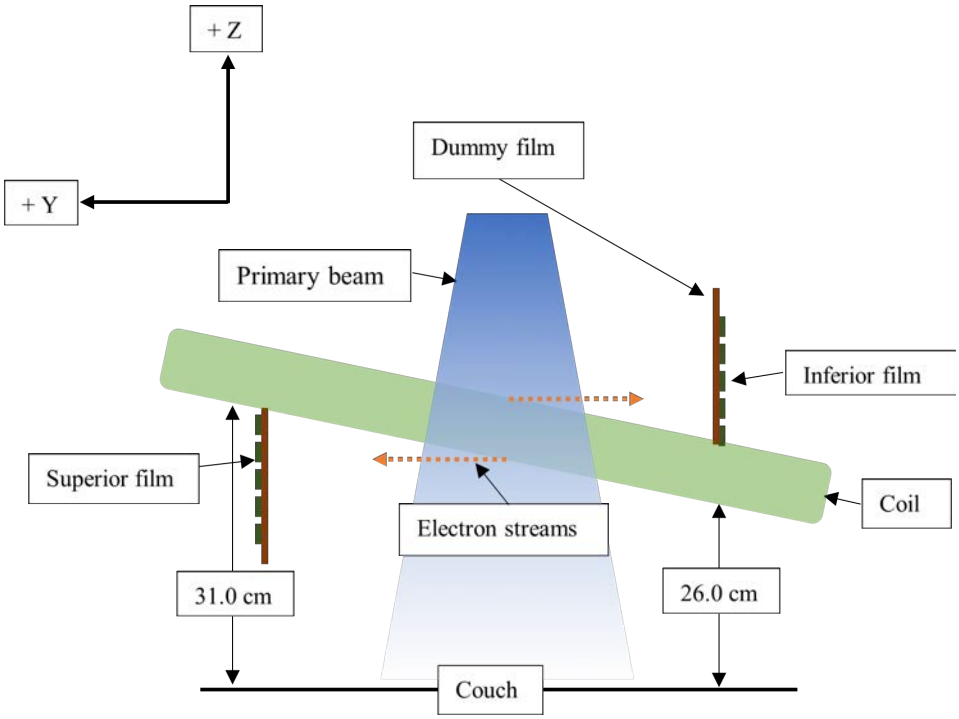

Figure 7.1: Schematic showing the film set up for coil ESE measurements, not to scale. The IEC 61217 positive Y and Z axes are shown and B_0 is in the negative Y direction

(Section 4.2.6) for exposures of 60 MU, 125 MU, 250 MU and 500 MU. Film was processed using the previously described method, Section 4.2.6. For all deliveries, vertical (moving away from the coil) and horizontal profiles were extracted from the ESE distribution on the film, using a 0.3×10.0 cm^2 region of interest (ROI). The ROI was aligned to the film markings for vertical profiles, and taken through the region of peak dose for the horizontal profiles. Doses were normalised to D_{max} to water for a 10.0×10.0 cm^2 , 500 MU, G0 field and 133.5 cm SSD.

7.2.2 Coil ESE Simulations

The experimental coil orientations and exposures were simulated in the Monaco planning system. Firstly, a CT dataset of the coil was acquired with 1.0 mm slices, and the coil tilted as for measurement (7.0°). The coil, air around the coil, and two "scoring planes" at either end of the coil were contoured, corresponding to film positions. Air around the coil was left unforced, so that Monaco converted the air CT number to relative electron density (RED). Scoring planes, $30.0 \times 30.0 \times 0.1$ cm^3 , were assigned a forced RED of 1.000. Simulations were performed with the 8.0×22.0 cm^2 G0, 500 MU, field and different density conditions for the coil: forced to water (RED of 1.000), forced to the mean value as determined by Monaco (RED of 0.075) and remaining unforced.

Secondly, for all investigated field sizes, the Elekta provided coil model (RED of 0.089) was imported onto a CT dataset of air. The height and tilt of the coil were set to match the experimental conditions. Scoring planes were again contoured at both

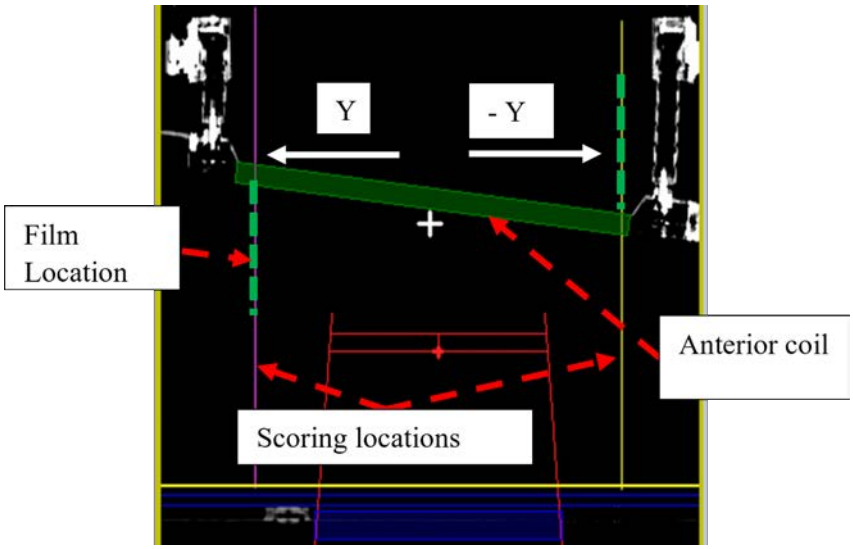

Figure 7.2: A screenshot of the TPS environment for the coil tilt simulations. B_0 is in the - Y direction and the beam (in red) is in the - Z direction

film locations, and the fields were added. In these simulations, the air around the coil model was contoured and originally had an unforced RED. However, to investigate the effect of air RED on ESE doses, simulations were repeated with the air forced to 0.010. For the forced air RED calculations and the 8.0×22.0 cm^2 field, dose at either end of the coil was extracted from the scoring planes. For the remaining fields (5.0×22.0 cm^2 and smaller), only the dose at the superior end was extracted from the TPS for conciseness.

For the 5.0×22.0 cm^2 field, the coil tilt using the Elekta model was halved (3.5°) for one simulation, and removed altogether for another. In both cases, the air around the coil was re-contoured and had unforced RED. For the half tilt simulations, dose at each end of the coil was extracted for analysis. However, for the coil flat simulations, only dose at the superior end was acquired.

In all cases, simulations were performed on a 0.1 cm dose grid, with statistical uncertainty of 0.2 % per control point. With these settings, the statistical uncertainty in the scoring volume was better than 1.0 % for all simulations. The calculations were performed with dose deposition to the local medium. To include the anterior coil in the calculations required the patient look up tables to be utilised. Dose profiles were extracted from transverse dose-planes exported from Monaco, centred on the scoring regions, using Verisoft^{TM} v7.2 (PTW, Freiburg, Germany). An image of the TPS environment for simulations is shown in Figure 7.2.

7.3 Results

7.3.1 Coil ESE Measurements

Vertical profile results for the coil ESE measurements are provided in Figures 7.3 and 7.4. For the 8.0×22.0 cm^2 field, ESE from the 7.0° coil tilt was approximately 23.0

Field Size [cm^2]	Peak Dose Superior [%]	Peak Dose Inferior [%]
8.0×22.0	22.9	22.0
5.0×22.0	20.9	23.1
$5.0 \times 22.0^*$	13.8	16.1
5.0×5.0	10.5	11.8
5.0×3.0	6.8	7.8
3.0×3.0	6.8	7.3

Table 7.1: Measured coil ESE peak doses for the coil tilt irradiations (7.0° and 3.5°). Doses expressed as a percentage of the D_{max} dose to water for a 10.0×10.0 cm^2 field. * coil tilt 3.5°

% of the D_{max} dose in a 10.0×10.0 cm^2 field, at the superior end (below) of the coil. For the inferior end (above), dose was 22.0 % of D_{max}. For all fields, the dose measured from ESE above and below the coil were comparable; although, a maximum differences of 4.2 % of the D_{max} dose was observed for the 5.0×22.0 cm^2 field, within the ESE peak. In general, the measured dose above the coil (backscattered electrons) was greater than dose below (forward scattered electrons). Smaller fields resulted in less ESE dose on the film, with the minimum measured peak value for the 3.0×3.0 cm^2 field being approximately 6.8 % of the D_{max} dose to water.

When the coil tilt was halved, dose for the 5.0×22.0 cm^2 field was 13.8 % of the D_{max} dose superiorly, and 16.1 % inferiorly. Such doses are approximately 7.0 % less than that for the 7.0° tilt. These results are shown in Figure 7.4, and a reduction in peak width can be observed. With the coil horizontal, the measured dose profile was constant at approximately 4.7 % of D_{max} and no peak was observed. Table 7.1 summarises measured peak entry and exit doses for all field sizes and coil tilt orientations. Similarly for dose in the tail regions of the profiles in Table 7.2. For the latter, the average value between 60.0 to 80.0 mm from the coil is reported.

Horizontal film profiles through the 8.0×22.0 cm^2 peak doses, above (inferior) and below (superior) the coil, are presented in Figure 7.5. The film at the superior end shows a consistent shape (width and penumbra skew [20]) to a projection of the primary field; however, a noticeable step can be seen for the inferior profile above the coil. Doses recorded horizontally are consistent with the peak in the vertical profiles, at about 23.0 % of the D_{max} dose to water for a 10.0×10.0 cm^2 field.

7.3.2 Coil ESE Simulations

Figures 7.6 to 7.9 show comparisons of simulated and measured vertical profiles, and differences (simulated - measured) for each field. Corresponding difference plots are also provided. 8.0×22.0 cm^2 simulations with the CT of the coil (Figure 7.6), with coil RED either unforced or forced to a mean value, showed larger differences with measurements than those from the default coil model (Figure 7.7). Doses above and below the coil were comparable for these simulations (Figures 7.7(a) and 7.7(c)), and the maximum absolute difference (compared to film) was approximately 3.5 % of D_{max}.

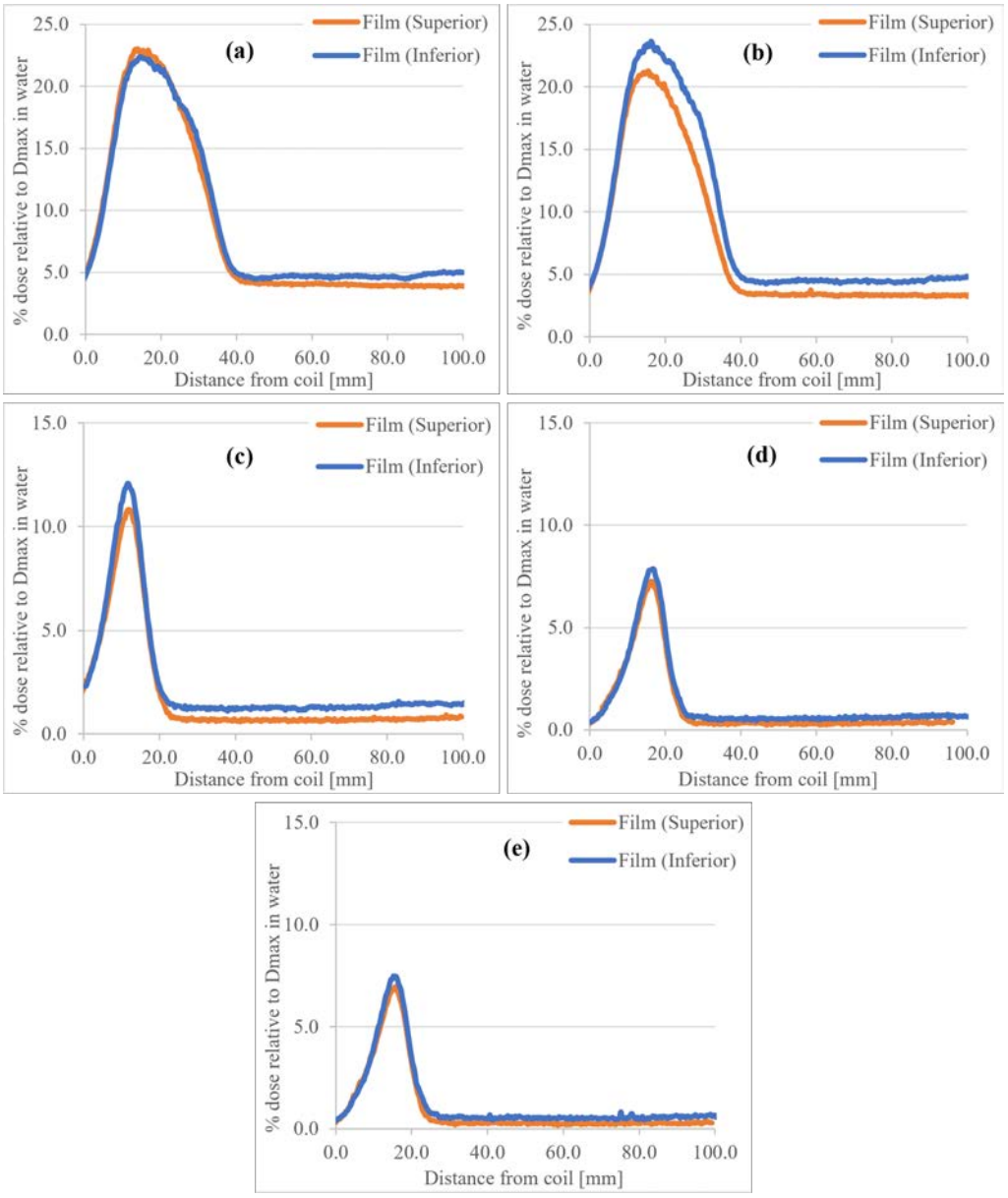

Figure 7.3: Vertical measured coil ESE doses for a 7.0° coil tilt, and the (a) 8.0×22.0 cm^2, (b) 5.0×22.0 cm^2, (c) 5.0×5.0 cm^2, (d) 5.0×3.0 cm^2, and (e) 3.0×3.0 cm^2 fields. Doses are expressed as a percentage of the D_{max} dose to water for a 10.0×10.0 cm^2 field

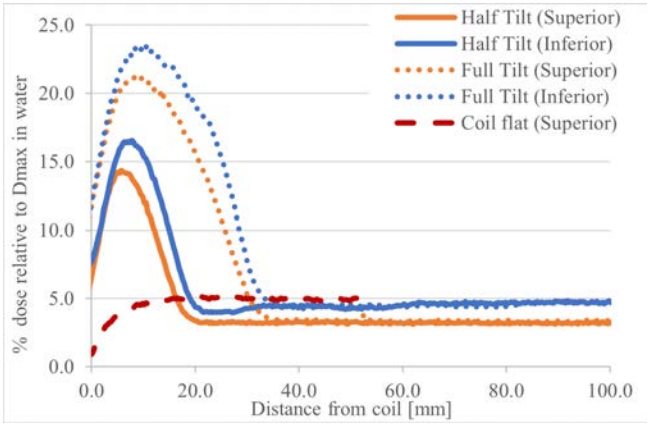

Figure 7.4: Measured doses for various coil tilts and the 5.0 × 22.0 cm^2 field. Plots have been approximately aligned to peak doses, for ease of viewing

Field Size [cm^2]	Tail Dose Superior [%]	Tail Dose Inferior [%]
8.0 × 22.0	3.9	4.6
5.0 × 22.0	3.3	4.5
5.0 × 22.0*	3.3	4.5
5.0 × 22.0†	4.7	NA
5.0 × 5.0	0.7	1.3
5.0 × 3.0	0.5	0.6
3.0 × 3.0	0.4	0.5

Table 7.2: Measured out-of-field doses in the profile tail regions for the coil tilt irradiations (7.0°, half tilt and coil flat). Doses are expressed as a percentage of the D_{max} dose to water for a 10.0 × 10.0 cm^2 field. The average value between 60.0 - 80.0 mm from the coil is reported. * coil tilt 3.5° , † coil flat

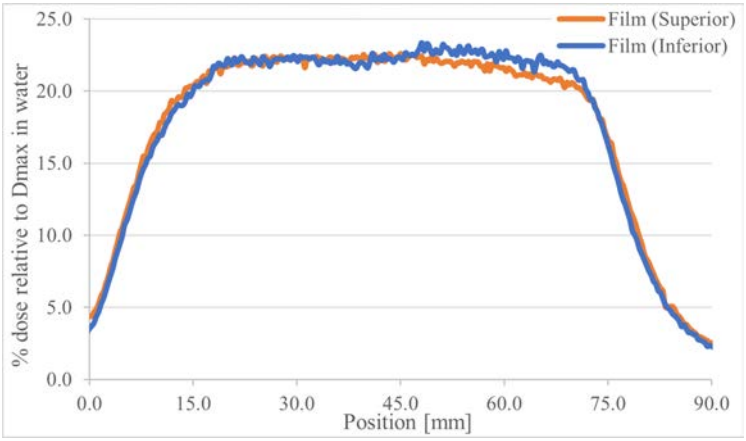

Figure 7.5: Horizontal measured profile, through the peak ESE dose, for the 8.0 × 22.0 cm^2 field

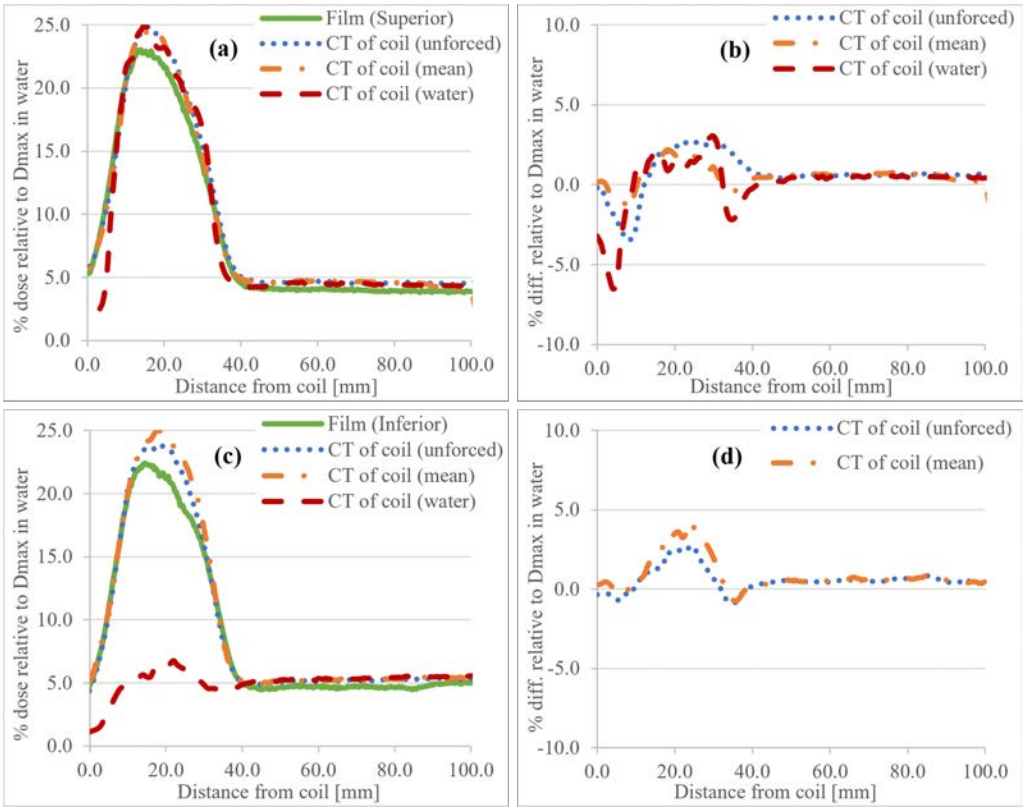

Figure 7.6: Calculated ESE for the 8.0×22.0 cm^2 field with a CT of the coil. Measured and calculated values for (a) the superior end of the coil can be compared using (b) the difference plot. Similarly for (c) the inferior end and (d) associated difference plot. The RED status of the CT contour is provided in parentheses for each simulation

However, for the coil RED set to 1.000 (water), ESE doses above the coil were significantly less than those below, Figure 7.6(c) and were clearly different to film ESE measurements. The difference plot for the inferior dose is omitted due to its obvious mismatch with other data. Peak calculated doses for the 8.0×22.0 cm^2 field are presented in Table 7.3 for the various simulations.

When the air was unforced for the Elekta coil model simulations, Figures 7.7 to 7.9, doses above and below the coil were of comparable magnitude. The latter was calculated slightly larger than the former, contrasting with film measurements. Peak ESE doses for all fields, with air unforced, are in Table 7.4 and noticeably, smaller fields exhibit smaller ESE doses, consistent with measured data (Table 7.1). When forcing the air to an RED of 0.010, smaller doses were calculated in ESE peaks and larger doses in the tail region, compared to measurements.

Figure 7.8 shows calculated and measured OFD for the 5.0×22.0 cm^2 field, for coil tilts of 7.0°, 3.5° and 0.0°. When the tilt was halved, the calculated peak dose was 16.5 %, of the D_{max} dose, at the superior end and 15.4 % at the inferior end. These were 5.6 % and 5.2 % less than corresponding doses calculated with a 7.0° tilt, respectively. For a flat coil, the TPS profile does not exhibit a peak and the dose is approximately 3.8 % of D_{max}, equal to the tail region for the coil tilted data, see Table 7.5.

In the calculated horizontal profiles for the 8.0×22.0 cm^2 field, Figure 7.10, distinct

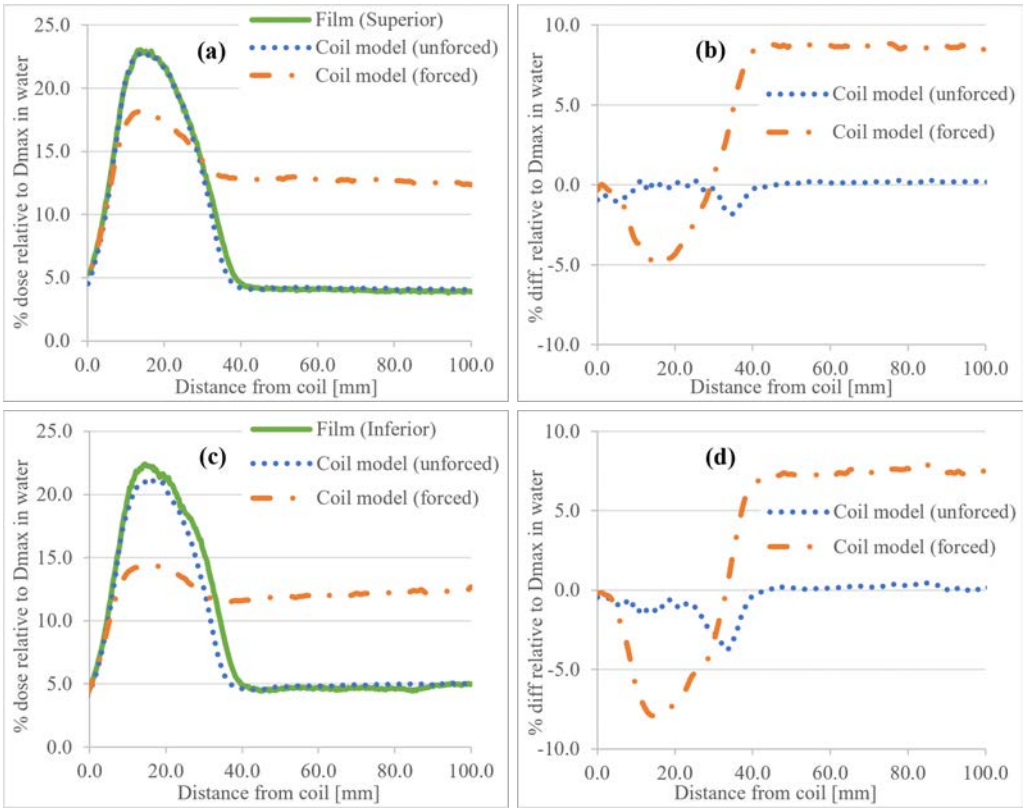

Figure 7.7: Calculated ESE dose for the 8.0×22.0 cm^2 field with the Elekta coil model. Measured and calculated values for (a) + Y (superior) can be compared using (b) the difference plot. Similarly for (c) - Y (inferior) and (d) associated difference plot. The RED status (forced or unforced) of the air around the coil is provided in parentheses for each simulation

Coil Simulation	Superior Peak		Inferior Peak	
	Dose [%]	Difference [%]	Dose [%]	Difference [%]
CT (coil unforced)	24.9	2.0	23.9	1.9
CT (coil mean)	24.6	1.7	25.0	3.0
CT (coil water)	25.0	2.1	6.7	-15.3
Model (air unforced)	22.9	0.0	21.3	-0.7
Model (air forced)	18.2	-4.7	14.5	-7.5

Table 7.3: Peak calculated ESE doses for the 8.0×22.0 cm^2 field simulations. Values are presented as a percentage of the D_{max} dose to water for a 10.0×10.0 cm^2 field, with differences compared to film

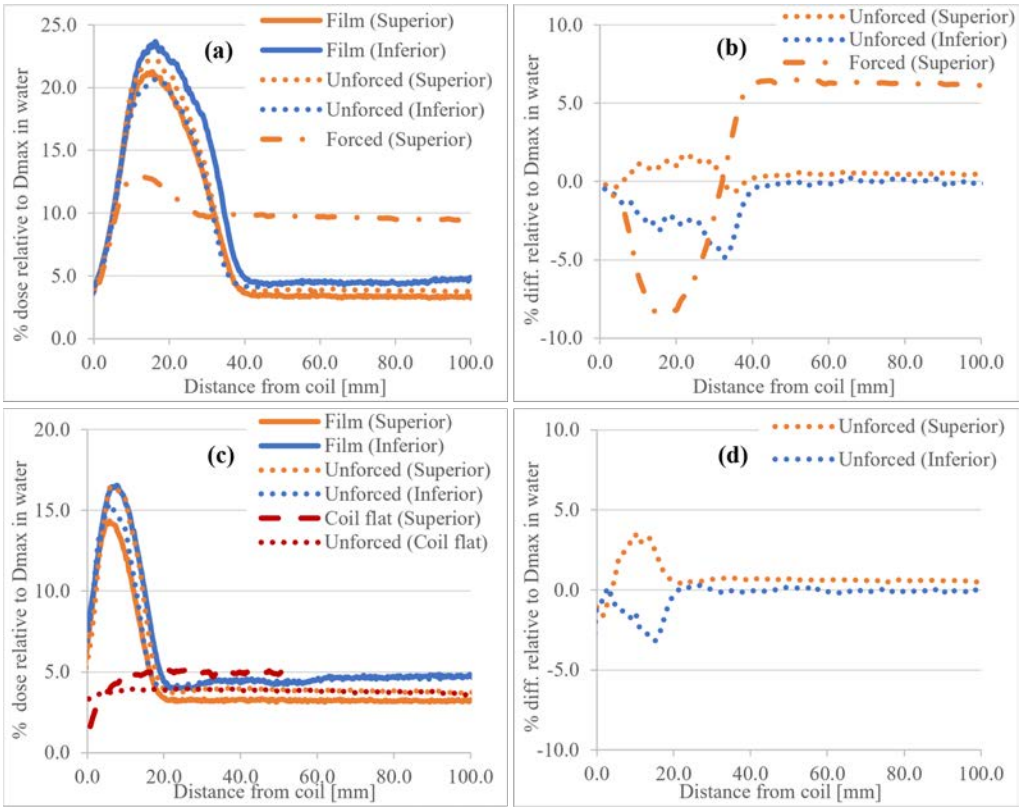

Figure 7.8: Calculated ESE dose for the 5.0×22.0 cm^2 field with the Elekta coil model and various tilts. Results for (a) the 7.0° tilt are provided with (b) difference plots compared to film. In (c) the half and no tilt results are provided with (d) associated difference plots. Dose differences for the coil flat are omitted due to inconsistency between measurement and simulation conditions. All percentages are relative to the D_{max} dose for a 10.0×10.0 cm^2 field

Field Size [cm^2]	Superior Peak		Inferior Peak	
	Dose [%]	Difference [%]	Dose [%]	Difference [%]
8.0×22.0	22.9	0.0	21.3	-0.7
5.0×22.0	22.1	1.2	20.6	-2.5
5.0×22.0*	16.5	2.7	15.4	-0.7
5.0×5.0	11.9	1.4	11.2	-0.6
5.0×3.0	7.8	1.0	7.3	-0.5
3.0×3.0	7.6	0.8	7.1	-0.2

Table 7.4: Peak calculated ESE doses for all fields using the Elekta coil model with air unforced. Values are presented as a percentage of the D_{max} dose to water for a 10.0×10.0 cm^2 field, and differences are compared to film. * coil tilt 3.5°

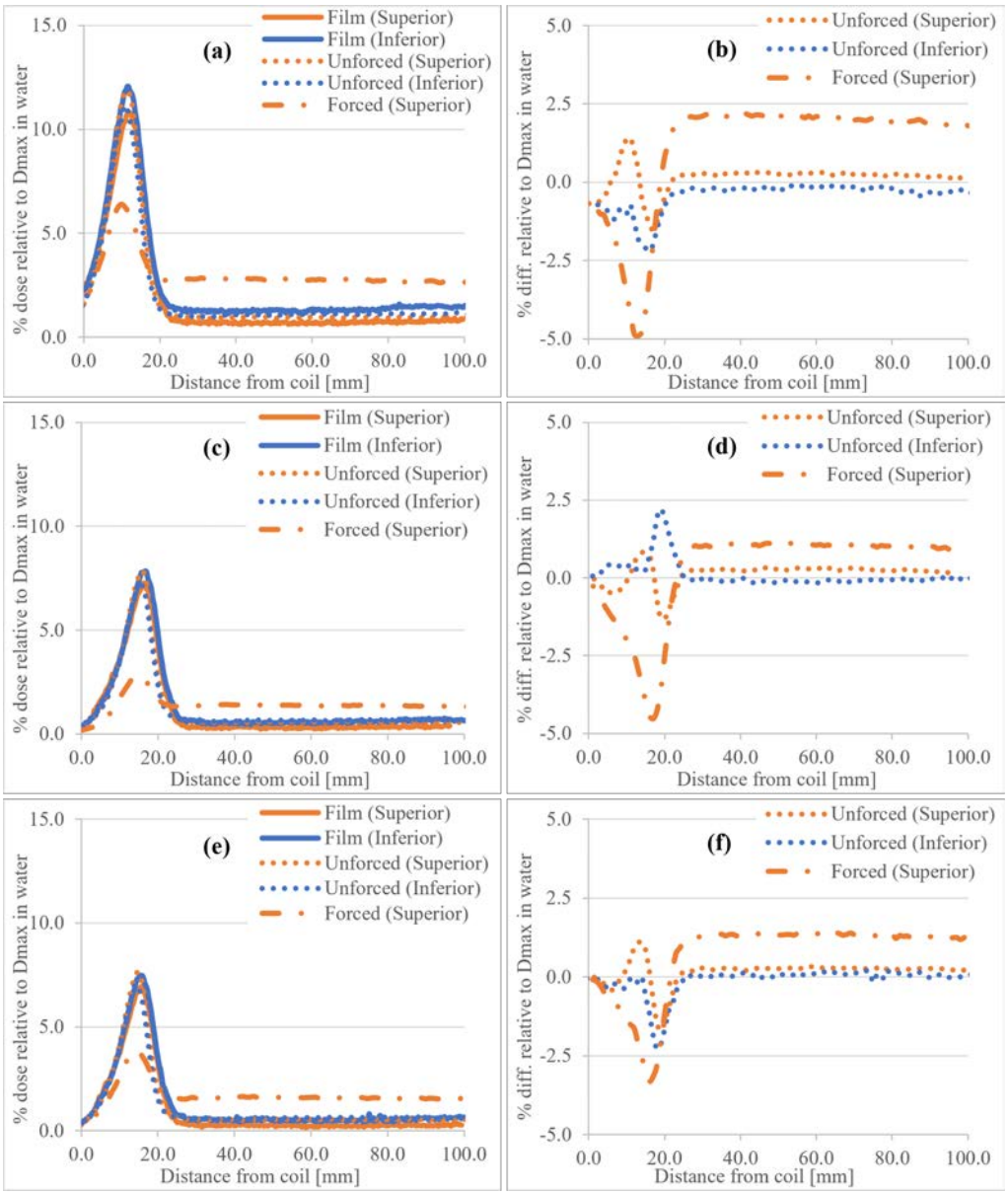

Figure 7.9: Small field coil ESE, calculated and measured, for the (a) 5.0×5.0 cm^2 field, with (b) associated difference plot. In (c) the 5.0×3.0 cm^2 results are shown, with (d) associated plot, and similarly with (e) the 3.0×3.0 cm^2 field and (f) difference plot

Field Size [cm^2]	Superior Tail		Inferior Tail	
	Dose [%]	Difference [%]	Dose [%]	Difference [%]
8.0 × 22.0	4.6	0.7	5.2	0.6
5.0 × 22.0	3.9	0.6	4.4	-0.1
5.0 × 22.0*	3.9	0.6	4.6	0.1
5.0 × 22.0†	3.8	-0.9	NA	
5.0 × 5.0	0.9	0.2	1.1	0.2
5.0 × 3.0	0.6	0.1	0.7	0.1
3.0 × 3.0	0.5	0.1	0.6	0.1

Table 7.5: Calculated dose in the tail region for investigated fields. Values are presented as a percentage of the D_{max} dose to water for a 10.0 × 10.0 cm^2, and differences are compared to film. * coil tilt 3.5° , † coil flat

deviations from profile flatness are observed when using the CT dataset of the coil. This was observed for superior and inferior ends, forced and unforced calculations. Although, the inferior profiles showed greater deviations. When using the coil model, horizontal profiles were in better agreement with film data.

7.4 Discussion

7.4.1 Coil ESE Measurements

The magnitude of the ESE emanating from the coil was significant (Figures 7.3 and 7.4), with nearly 23.0 % of the D_{max} dose to water observed for the 8.0×22.0 cm^2 field. This value is comparable to phantom ESE (Chapter 6); however, will be influenced by field size and coil tilt. In general, it appears that the superior film, below the coil, measured comparable ESE dose to that above the coil, contrasting with results presented in Chapter 6 and those of other investigators [8]. From coil CT images (Figure 7.11), a high density substructure was identified. This structure could tend to restrict electron motion through it, hence increasing the number of backscattered electrons. Subsequently, this may tend to increase ESE dose at the entry. Note that such an effect may not be observed for uniformly dense materials, and is worth investigating with Monte Carlo simulations.

The comparable ESE dose above and below the coil, as well as the magnitude doses, has significant implications for patient safety. Where a coil tilt is required for a patient treatment, to improve MR signal for example, bolus should be considered at both ends of the coil to shield patient surfaces in the path of streaming electrons. The energy of streaming electrons is ~ 500.0 keV, as discussed previously, and 1.0 cm of jelly bolus would provide the necessary shielding [23, 42].

Furthermore, with Figure 7.3, a field size effect can be observed where smaller fields produce less ESE dose. This is to be expected, given that reducing the primary field will: (1) reduce the number of secondary electrons produced within the medium, and; (2) limit the length of the coil which is irradiated in-line with the magnetic field. The latter appears to be the greater effect, as peak ESE doses for the 5.0 × 3.0 cm^2 and

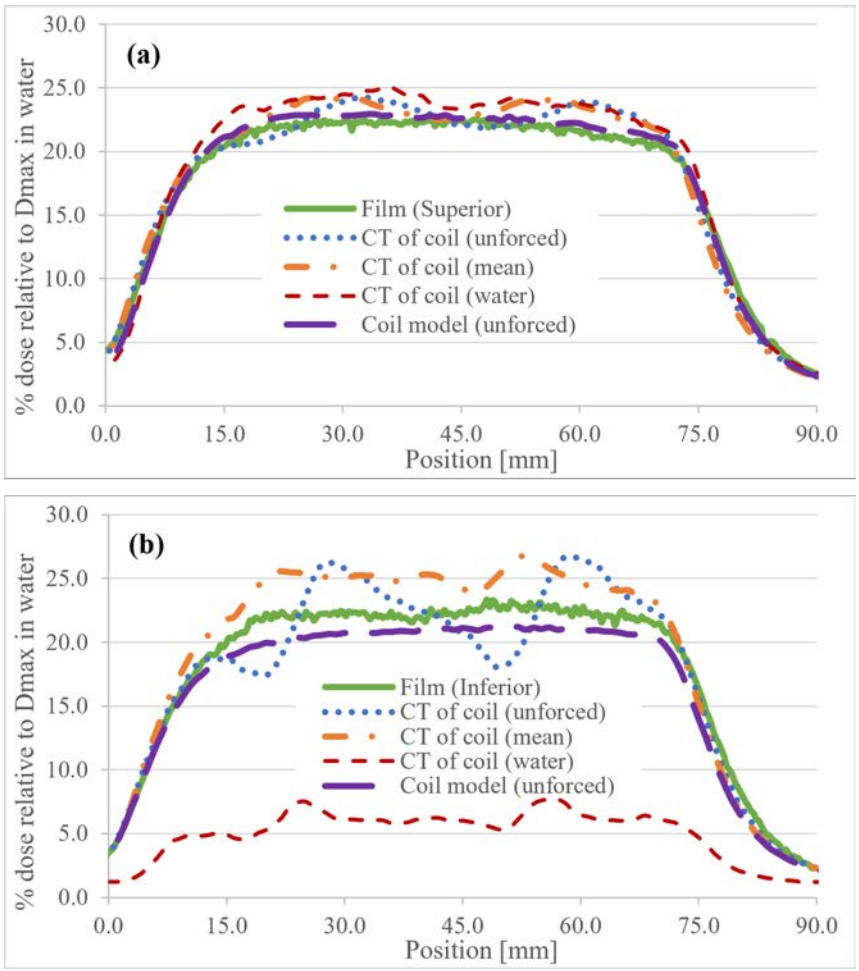

Figure 7.10: Calculated and measured horizontal profiles through the peak ESE for the 8.0×22.0 cm^2 field, at (a) superior and (b) inferior ends of the coil

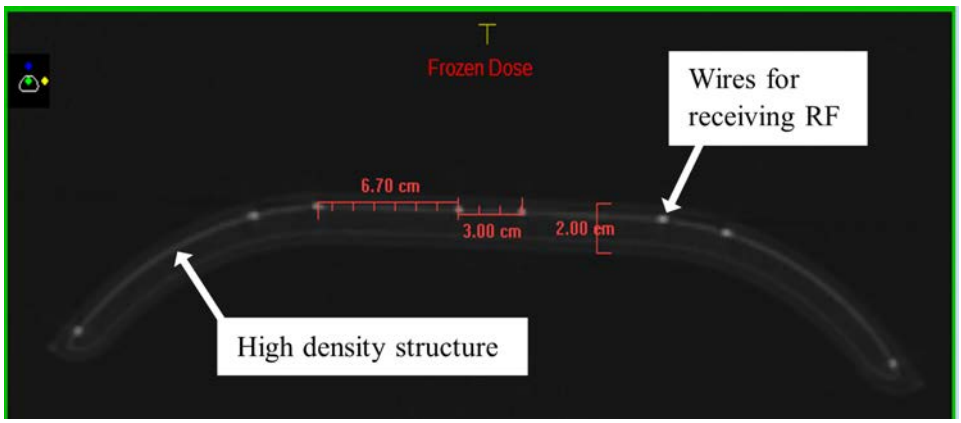

Figure 7.11: A CT of the coil showing the high density substructure housing the RF receiving wires and providing support for the coil. Distances between wires, and the coil thickness, are shown in red

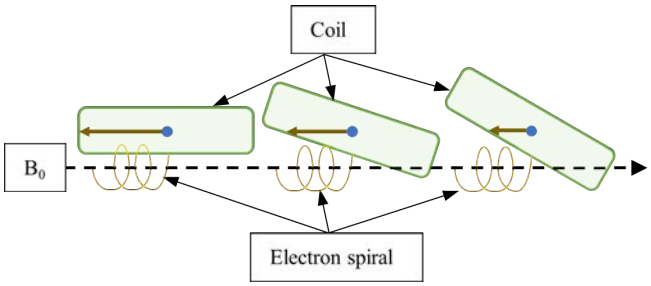

Figure 7.12: Diagram showing how the coil tilt can affect the electron streaming. Larger tilts (middle and right) create increased distance between the electron spiral and the coil surface, as well as reducing the lateral distance electrons have to travel to escape the coil (brown) after initial generation

3.0×3.0 cm^2 (same Y dimension) are similar, whereas those for the 5.0×5.0 cm^2 and 5.0×3.0 cm^2 (same X dimension) are not. Note that the reduction in primary beam can be argued to be approximately the same for both situations (2.0 cm), and that the aforementioned pattern was seen both above and below the coil. This was also observed in the doses for the larger rectangular fields, (Figures 7.3(a) and 7.3(b)), where the Y dimension of the field was consistent between the two.

In the measurements with the coil tilt halved (Figure 7.4), peak dose above and below the coil are reduced by approximately 7.0 % compared to the 7.0° coil tilt. This was not unexpected as the distance from the coil surface to the line about which a secondary electron will spiral, is reduced with lesser coil tilts relative to the horizontal; the result being more returning electrons, rather than spiralling, for the smaller inclinations (see Figure 7.12). For reducing coil tilts the distance which an electron has to travel, along B_0, for it to be able to rotate around the field lines and not intersect with the coil surface is increased. Hence, only the electrons which have larger parallel components of motion are able to stream and not return to the surface (representing the more laterally scattered electrons, as opposed to forward scattered). Secondly, for greater inclinations, the distance which an electron has to travel to exit the coil is reduced for a given generation point. Thus, one could expect more electrons escaping for larger inclinations, and fewer for smaller inclinations. In general, reducing the coil tilt will reduce ESE peak dose and the width of the ESE distribution. Both of these were observed in the coil tilt results in Figure 7.4. Additionally, increasing the coil tilt increases the surface area of the coil irradiated, enabling more electron streams to be produced as previously discussed (Section 6.4.1). The change in ESE dose with phantom angulation has been highlighted by previous investigations [8].

In the tail regions for all measured fields fields, Table 7.2, doses are comparable to previous results for OFD spiralling contaminant electrons (SCE) and background photons [2], with equivalent field sizes. Here, the dose measured above the coil is greater than that below. Since this dose is deposited by SCE and background photons, this result is unsurprising. With increasing distance from the source, the intensity of the primary photon beam is reduced through the inverse square law (ISL). Logically, a reduction in intensity of primary beam will result in fewer generated electrons spiralling

to deposit dose on the film. This is observed in the measured vertical profiles which show tail regions diverging between inferior and superior films, with the latter decreasing with distance from the coil. Another point to highlight is that reducing the coil tilt increases the magnitude of the electron return effect (ERE) [52] in-field, and OFD becomes dominated by SCE and background photons [2, 9]. Note that with the coil flat, measured dose is higher than tail regions in tilted results for the same field size (5.0×22.0 cm^2). For measurements with the coil flat, it was discovered that the dummy film in front of the measured had not been used, therefore increasing recorded dose. Furthermore, this film was not as long others, and only dose up to ~ 50.0 mm away from the coil was measured.

The measured horizontal profiles in Figure 7.5 appear as expected, with the exception of a small step observed for the inferior plot. The cause of the step has yet to be identified; however, the film set up and coil structure are being investigated.

7.4.2 Coil ESE Simulations

In Figure 7.6, the modelling of the coil using a CT dataset showed that dose is typically overestimated by the planning system compared to measured data. Differences between these calculations and measurements were mostly less than $\pm$ 5.0 %. These occurred primarily in the peak dose and steep dose gradient regions. This was the case both superior and inferior and for all simulations, with the exception of inferior dose calculated with contour RED forced to water. Here, lower doses were observed, consistent with the phantom scenario in Chapter 6 and other investigations [8]. The increase in density appears to cause the resulting electron distribution to be more forward directed, for this scenario.

Larger differences, between calculations with the CT of the coil compared to film, could be attributed to a number of factors. However, given the consistency of the Elekta coil model data with the film (Figure 7.7), it seems the contouring accuracy was the primary cause. The contour was consistent between the calculations for Figure 7.6, and a mismatch in contour to experimental (say for example, different angulation or contour thickness) could explain the increase in peak dose. The comparable calculated dose superiorly regardless of scatterer RED is interesting. Compton interactions depend on the electron density of the scattering material, and one would assume that a more electron dense material would create more electron streaming. It is possible that this effect is being countered by the fact that for more dense scattering materials, the path an electron takes to exit said material is now more attenuating. As yet the consistency of peak dose regardless of material RED is unexplained, warranting further investigation with Monte Carlo simulations and phantom measurements.

The length of the calculated ESE peaks for the 8.0×22.0 cm^2 vertical profiles were consistent with measured (superior and inferior), for the CT contour of the coil forced to its mean RED and leaving it unforced. However, when this contour was forced to water, constriction of the superior dose peak was observed. It was supposed from the large disparity between superior and inferior doses in these results, that the

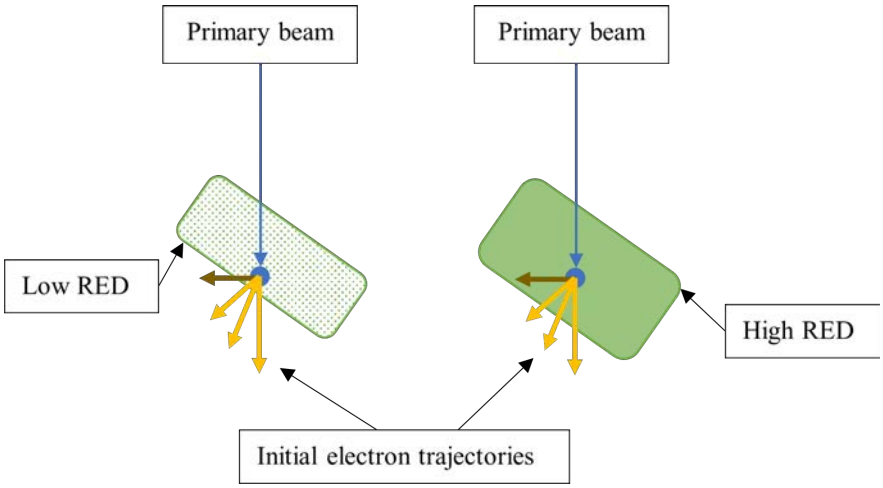

Figure 7.13: Diagram showing how increasing the RED can change resulting ESE doses. One can see that for the higher RED material the water equivalent thickness is increased. Hence laterally scattered electrons (brown) are not energetic enough to escape. Note that the the effect of the magnetic field on the electron paths, and the full electron distribution, are not shown

resulting electron distribution was more forward directed. This would also be reflected as a constriction of the peak. Furthermore, doses around the slopes of the peak are correlated with electrons escaping the coil at the beam peripheries. It is reasonable to suggest that these electrons are more laterally scattered than those in the centre, due to the shape of the primary beam. In Compton interactions, the more laterally scattered electrons have a lower kinetic energy. With a higher RED material (more attenuating), these laterally scattered electrons may not be energetic enough to escape, and constriction of the peak would be observed. This is described schematically in Figure 7.13.

ESE calculations using the Elekta supplied coil model (Figures 7.8 and 7.9) showed comparatively good agreement to film, when the air RED remained unforced. Dose differences, superior and inferior, were less than $\pm$ 5.0 % of D_{max} and again were primarily around steep dose gradients. Notably, the TPS seemed to calculate larger ESE doses emanating below the coil (superior) compared to above, opposite to film data. This may be due to the substrate layer causing more backscattered ESE doses in the measurements, which would not be present in the TPS simulations with the uniform RED of the coil. Furthermore, the agreement of the calculated tail region with film, and correct trends with increasing distance from the coil (increasing dose for inferior, decreasing dose for superior), suggested the issue was not with data handling. This subtle discrepancy between film and TPS simulations is currently being investigated with Monte Carlo methods. From Figure 7.9, reduction in ESE dose with decreasing field size was observed, as well as a reduction in dose differences compared to film for the Elekta coil model data.

When the density of the air was forced to 0.010, similar results as in Chapter 6 were observed where greater differences to film, relative to unforced RED, were

evident. Higher REDs generate more SCE than lower REDs, and a greater dose would be observed in the profile tail. Coil ESE is subjected to increased attenuation with higher air RED, and thus lower dose would be observed for the peak.

For the coil tilt comparison in Figure 7.8, larger differences for calculated dose compared to film were observed for the half tilt than the 7.0° tilt. Additionally, the TPS reduction in dose when reducing the tilt was less significant than measurements. Again, the set up consistency between measurement and TPS will affect contribute to such differences. Profiles computed with and without coil tilts exhibited regions of equal SCE dose; however, there is clear discrepancy between the film and TPS with the coil horizontal. This is due to the difference in measurement depth between the two, as mentioned previously, warranting repeat measurements. Furthermore, OFD with the coil flat was only simulated at the superior end. Consistency of tail regions with the coil tilted and those with the coil flat (Figure 7.8(c)) was obtained, for this end of the coil. Hence, one could conclude that the same would be true for the opposing side. However, differences between superior and inferior doses with the coil flat would exist due to divergence of the primary beam, as discussed above. It may be beneficial to compare calculated and measured doses at both ends of the horizontal coil in a future investigation.

Horizontal profiles through superiorly placed scoring planes, for the Elekta coil model, show good agreement with film. Little lateral constriction was observed. Inferiorly, for the same calculation, there is a constant discrepancy; however, it is less than 2.0 % of the D_{max} dose. Overall, the use of the Elekta coil model predicted OFD in agreement to film measurements, for both superior and inferior doses, horizontally and vertically. For the superior horizontal profiles calculated with the CT of the coil, any RED, the dose was overestimated by the TPS. There is also some evidence of discontinuities for the calculated doses across the central region of the profiles; however, calculated penumbras agree with measured. Inferiorly, there are obvious steps in the profile. Although most significant in the unforced RED calculation, the steps can be observed in the remaining datasets. The horizontal profile at the inferior end of the coil, with the RED of the coil forced to 1.000, is significantly lower than film, consistent with that observed in the vertical profile.

The sharp steps in the inferior horizontal profiles may be caused by the internal structure of the coil. Within the body of the structure there are high density RF receiving wires. With the unforced RED calculation, the location of the discontinuities in the scoring plane is correlated with the location of the wires upstream (see Figure 7.14). Clearly, care must be taken when attempting to calculate ESE dose with a CT of the coil; however, this is outside routine clinical practice and would not be of concern for users.

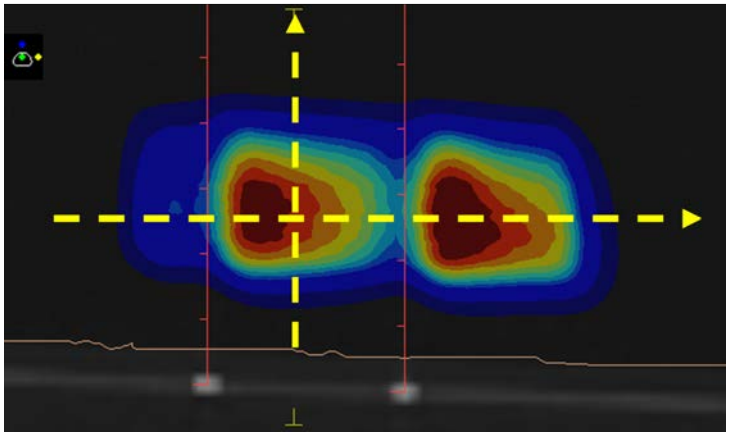

Figure 7.14: Image of the calculated dose distribution (inferior) for the 5.0×22.0 cm^2 field using a CT of the tilted coil. The projection of the wires is marked using red lines, and the location and direction of profiles shown by the dash lines (yellow). Note that no quantitative information is provided as this figure is for illustrative purposes only

7.5 Conclusion

In this chapter out-of-field dose associated with the tilted anterior coil was characterised with film measurements and Monaco TPS calculations. Several G0 fields were delivered to a tilted anterior coil, and dose was measured from ESE emanating above (inferior) and below (superior) the device. The experimental arrangement was replicated in Monaco using different models for the coil. Using a single field, the effect of varying the coil tilt on measured and calculated ESE was also investigated. Additionally, the effect of varying RED on resulting ESE distributions was presented.

ESE doses from the coil were significant, with approximately 23.0 % of the D_{max} dose to water being observed, in measurements and calculations, for an 8.0×22.0 cm^2 field. Streaming dose above the coil was comparable to that below the coil, which will have clinical implications as bolus shielding will be required to protect the patient from both sources. A field size effect was observed for peak ESE doses, with smaller fields producing less dose, consistent with previous investigations. However, it appeared that changing the dimension of the field in the direction of the magnetic field had a larger influence on OFD. Angulation of the coil also affected ESE doses, with smaller tilts corresponding to lower measured and calculated doses, consistent with other investigators. Overall, it was determined that the use of the Elekta supplied coil model within the TPS can accurately predict OFD, as long as the air around the coil remains unforced (within the TPS). The effect of forcing the air contour, on SCE and ESE doses, was observed to be consistent with previous investigations.

Finally, further investigation is warranted into modelling the Compton scattering within the anterior coil. Specifically, the effect of non-uniform RED layers within the coil and the resulting electron distribution, are currently being simulated using Monte Carlo methods. These simulations are expected to reveal why comparable doses

superiorly and inferiorly for low RED materials were observed, in contrast to ESE from higher RED materials. Additionally, this data may also reveal why the superior ESE peak dose distribution did not change when varying the uniform RED of the tilted coil.

8 Conclusion

8.1 Summary of Work Performed and Results

The complexity of MRgRT systems means that gaps in published commissioning work can be significant. As part of this work, commissioning of the linac component of the Elekta Unity MRL was performed for mechanical (Chapter 3) and dosimetric (Chapter 4) behaviour. A vendor supplied phantom was used to confirm gantry rotation and for determining the MV isocentre size. Results for both tests were consistent with published data. Using various dosimeters, an in-bore radiation survey in 0 T was performed for which published comparative data was limited.

Dosimetric measurements were performed on the system and results were presented in Chapter 4. The attenuation of the primary beam due to the anterior imaging coil was determined with an in-house, cylindrical phantom. This effect was small, and simulated results were consistent with measurements. Beam quality was measured with $TPR_{20,10}$ and dose maps. $TPR_{20,10}$ was found to be insensitive to changes in beam quality which significantly altered beam characteristics. Therefore, caution is advised when using $TPR_{20,10}$, and published tolerances, to monitor the beam quality. Dose maps (and therefore dose profiles) were shown to be more sensitive, consistent with that known with conventional linacs. Due to the calibration conditions recommended by the vendor, difficulty was encountered when performing reference dosimetry measurements. An adapted methodology for this procedure was discussed, and machine output measurements with this technique were reproducible. Nevertheless this method is not ideal, and calibration conditions of clinics needs to be considered by third party vendors when designing equipment. Depth dependence of magnetic field correction factors was measured to be negligible, consistent with previous Monte Carlo

simulations. The influence of MR imaging on linac and MVI panel operation was not significant. Film and the PTW Octavius 1500^{MR} array were both found to highlight issues with machine behaviour, during IMRT commissioning, when appropriate gamma criteria were set. With these issues resolved, IMRT results were within internationally recommended tolerances. The use of an in-house, 3D-printed, MR-compatible E2E phantom was presented. E2E results were acceptable and highlighted the potential benefit of using such phantoms on MRgRT systems.

The presence of a strong magnetic field alters charged particle kinetics on the Elekta Unity system. This ultimately leads to larger doses out-of-field than would be present in a non-MR environment. OFD was characterised on the Unity system in Chapters 5-7, with measurements and Monaco TPS simulations. Dose associated with SCE and HLS was determined in 1.5 T (SCE and HLS) and 0 T (HLS only) environments and results are presented in Chapter 5. These doses were found to be comparable. Notably, 0 T OFD was found to be inconsistent with previous Monte Carlo work. TPS calculations were consistent with measurements, in both 0 T and 1.5 T. RED of the simulation environment was found to significantly affect the generation and attenuation of OFD, and implications in clinical situations were highlighted.

Characterisation of ESE on the system was presented in Chapters 6 and 7. In the former, ESE during irradiation of a phantom was investigated. ESE dose was measured using film and OSLDs, and compared to simulations with the Monaco TPS. This source of OFD was found to be clinically significant, greater than that associated with SCE, and consistent with previous investigations. ESE doses were shown to be dependent on phantom and beam geometry, as well as RED settings for air in the TPS. Attenuation of ESE doses was also determined, and it was found that 10.0 mm of water equivalent material will significantly reduce this dose, consistent with previous investigations. Monaco ESE was consistent with film measurements, however, OSLD readings were inconsistent with both.

In Chapter 7, ESE generated during irradiation of the tilted anterior coil was investigated. Measurements of coil ESE were made with film and compared to TPS simulations. Significant OFD was determined, above and below the coil, for the fields and inclinations investigated. Doses were comparable to the phantom investigation in Chapter 6. Coil angulation and field size were found to influence ESE doses, consistent with previous investigations. Different models of the anterior coil were employed in the planning system, and it was found that the use of the default, Elekta supplied model provided agreement between simulated and measured data. It was found that changing the RED of the coil in the TPS did not significantly alter the magnitude of ESE doses below the coil. The effect of forcing the air RED around the coil in simulations was also investigated, and dose differences with measured data were consistent with that observed previously.

8.2 Recommendations for Future Work

During commissioning several areas warranting further investigation were highlighted. The use of the MV alignment phantom for determination of an absolute gantry angle was one such area. In this work, MVI images of the phantom at non zero gantry angles were visually compared to the G0 image. Use of a computational system to automate this process, and extract an absolute position from these images, is warranted. This process could be improved by imaging the phantom centred at isocentre, and confirming that the projection of diametrically opposite ballbearings, within a given array, are aligned along the Y-axis. An offset in gantry angle would manifest as lateral separation between these ballbearings on the MVI images.

The radiation survey results were noticeably varied in the $\pm$ X directions, indicating that there may have been an issue in set up. Repetition of this test is warranted. Unfortunately, to repeat in 0 T is not pragmatic given the costs involved. Measurement in 1.5 T may elucidate errors, but would be susceptible to the magnetic field effects on electron motion. Regardless, the 1.5 T data is warranted as this represents the nature of the machine during treatment and will be beneficial to compare data to the 0 T case.

Changes to beam quality with gun grid voltage is also an area worth investigating. Altering the grid voltage was shown to affect the beam energy; however, the commonly used $TPR_{20,10}$ metric was found to be insensitive to changes. The extent to which this metric can highlight an energy change could be considered. This may be achieved by adjusting the grid voltage (for example in 5.0 V increments) and determining the metric. Additional machine characteristics could be determined at each voltage to highlight significance of the change, for example: beam output, profile shape and MV isocentre size and location.

The use of a 3D-printed phantom for E2E testing of ATP and ATS functionality was discussed in Chapter 4. A single, simple design was given; however, little discussion of MR imaging quality, contouring accuracy or plan generation was provided. Further work on using MR compatible, 3D printed materials for E2E phantom designs is an area worth pursuing, to address these aforementioned issues. The phantom design could also be improved by adding anthropomorphic components.

In 1.5 T, there will be contributions to OFD from low energy photons scattered from the linac components and the air. To quantify the magnitude of SCE dose, and differentiate it from HLS, is therefore difficult; however, this may be possible using Monte Carlo methods. Such calculations are currently under investigation. Monte Carlo simulations in 0 T are also warranted, to highlight the discrepancy between measured and calculated data. The electron component of the primary beam in both the Monaco TPS and the Monte Carlo phase space files should be investigated.

In Chapter 6 the electron streaming effect was investigated with film, TPS simulations and OSLDs. OSLD data varied significantly from other data, potentially due to differences in effective measurement depths between dosimeters and simulations.

As such, measurements with film EPOM depth consistent with that for OSLDs, are required. Monte Carlo modelling of ESE will also be of benefit. Such simulations could be used to determine the attenuation of these spiralling electrons in water/tissue, which is not possible with measurements.

Finally, the above simulations would also be of benefit to address further research needs highlighted in Chapter 7. Compton scattering events associated with varying densities of the tilted anterior coil are to be simulated, to determine the point spread distribution in different materials. These simulations may also reveal why comparable doses above and below the coil were observed. The consistency of ESE dose below the coil, with variations in scatterer RED, could also be addressed.

References

[1] Marcus Powers, John Baines, Robert Crane, Chantelle Fisher, Stephen Gibson, Linda Marsh, Bronwyn Oar, Ariadne Shoobridge, Emily Simpson, Page Marchant, and Van Der Walt Glenn. Commissioning measurements on an Elekta Unity MR-Linac. *Physical and Engineering Sciences in Medicine*, **Online** (2022). doi:10.1007/s13246-022-01113-7.

[2] John Baines, Marcus Powers, and Glen Newman. Sources of out-of-field dose in MRgRT: an inter-comparison of measured and Monaco treatment planning system doses for the Elekta Unity MR-linac. *Physical and Engineering Sciences in Medicine* (2021). doi:10.1007/s13246-021-01039-6.

[3] Marcus Powers and John Baines. Electron Streaming Effect Associated With the Elekta Unity Anterior Imaging. *Frontiers in Physics*, **10** (2022). doi:10.3389/fphy.2022.880121.

[4] P Mayles, A Nahum, and J.C Rosenwald (Editors). *Handbook of Radiotherapy Physics*. CRC Press (2007). ISBN 9780429188251. doi:10.1201/9781420012026.

[5] B. Van Asselen, S. J. Woodings, S. L. Hackett, T. L. Van Soest, J. G.M. Kok, B. W. Raaymakers, and J. W.H. Wolthaus. A formalism for reference dosimetry in photon beams in the presence of a magnetic field. *Physics in Medicine and Biology*, **63** (2018). doi:10.1088/1361-6560/aac70e.

[6] Syed Bilal Ahmad, Arman Sarfehnia, Moti Raj Paudel, Anthony Kim, Sami Hissoiny, Arjun Sahgal, and Brian Keller. Evaluation of a commercial MRI Linac based Monte Carlo dose calculation algorithm with geant 4. *Medical Physics*, **43**, 894 (2016). doi:10.1118/1.4939808.

[7] Jan J.W. Lagendijk, Bas W. Raaymakers, and M. Van Vulpen. Presentation: Past, Present and Future: MRI-guided Radiotherapy from 2005-2025.

[8] Victor N. Malkov, Sara L. Hackett, Jochem W.H. Wolthaus, Bas W. Raaymakers, and Bram Van Asselen. Monte Carlo simulations of out-of-field surface doses due to the electron streaming effect in orthogonal magnetic fields. *Physics in Medicine and Biology*, **64**, 0 (2019). doi:10.1088/1361-6560/ab0aa0.

[9] S. L. Hackett, B. Van Asselen, J. W.H. Wolthaus, J. J. Bluemink, K. Ishakoglu, J. Kok, J. J.W. Lagendijk, and B. W. Raaymakers. Spiraling contaminant electrons increase doses to surfaces outside the photon beam of an MRI-linac with a perpendicular magnetic field. *Physics in Medicine and Biology*, **63** (2018). doi:10.1088/1361-6560/aaba8f.

[10] Jacob Van Dyk (Editor). *The Modern Technology of Radiation Oncology: A Compendium for Medical Physicists and Radiation Oncologists*. Medical Physics Publishing, Madison, WI (1999). ISBN 0-944838-38-3.

[11] C. W. Miller. Travelling-Wave Linear Accelerator for X-Ray Therapy. *Nature*, **171**, 297 (1953). doi:10.1038/171297a0.

[12] Constance A. P. Wood and G. R. Newbery. The Medical Research Council Linear Accelerator and Cyclotron. *Nature*, **173**, 233 (1954). doi:10.1038/173233a0.

[13] Martin J. Murphy, James Balter, Stephen Balter, Jose A. Bencomo, Indra J. Das, Steve B. Jiang, C. M. Ma, Gustavo H. Olivera, Raymond F. Rodebaugh, Kenneth J. Ruchala, Hiroki Shirato, and Fang Fang Yin. The management of imaging dose during image-guided radiotherapy: Report of the AAPM Task Group 75. *Medical Physics*, **34**, 4041 (2007). doi:10.1118/1.2775667.

[14] Parham Alaei and Emiliano Spezi. Imaging dose from cone beam computed tomography in radiation therapy. *Physica Medica*, **31**, 647 (2015). doi:10.1016/j.ejmp.2015.06.003.

[15] Jeffrey Olsen, Olga Green, and Rojano Kashani. World's First Application of MR-Guidance for Radiotherapy. *Missouri Medicine*, **112**, 358 (2015).

[16] B. W. Raaymakers, I. M. Jürgenliemk-Schulz, G. H. Bol, M. Glitzner, A. N.T.J. Kotte, B. Van Asselen, J. C.J. De Boer, J. J. Bluemink, S. L. Hackett, M. A. Moerland, S. J. Woodings, J. W.H. Wolthaus, H. M. Van Zijp, M. E.P. Philippens, R. Tijssen, J. G.M. Kok, E. N. De Groot-Van Breugel, I. Kiekebosch, L. T.C. Meijers, C. N. Nomden, G. G. Sikkes, P. A.H. Doornaert, W. S.C. Eppinga, N. Kasperts, L. G.W. Kerkmeijer, J. H.A. Tersteeg, K. J. Brown, B. Pais, P. Woodhead, and J. J.W. Lagendijk. First patients treated with a 1.5 T MRI-Linac: Clinical proof of concept of a high-precision, high-field MRI guided radiotherapy treatment. *Physics in Medicine and Biology*, **62**, L41 (2017). doi:10.1088/1361-6560/aa9517.

[17] Jan J.W. Lagendijk, Bas W. Raaymakers, and Marco van Vulpen. The Magnetic Resonance Imaging-Linac System. *Seminars in Radiation Oncology*, **24**, 207 (2014). doi:10.1016/j.semradonc.2014.02.009.

[18] Dennis Winkel, Gijsbert H. Bol, Petra S. Kroon, Bram van Asselen, Sara S. Hackett, Anita M. Werensteijn-Honingh, Martijn P.W. Intven, Wietse S.C. Eppinga, Rob H.N. Tijssen, Linda G.W. Kerkmeijer, Hans C.J. de Boer, Stella Mook,

Gert J. Meijer, Jochem Hes, Mirjam Willemsen-Bosman, Eline N. de Groot-van Breugel, Ina M. Jürgenliemk-Schulz, and Bas W. Raaymakers. Adaptive radiotherapy: The Elekta Unity MR-linac concept. *Clinical and Translational Radiation Oncology*, **18**, 54 (2019). doi:10.1016/j.ctro.2019.04.001.

[19] Jeffrey E. Snyder, Joël St-Aubin, Sridhar Yaddanapudi, Amanda Boczkowski, David A.P. Dunkerley, Stephen A. Graves, and Daniel E. Hyer. Commissioning of a 1.5T Elekta Unity MR-linac: A single institution experience. *Journal of Applied Clinical Medical Physics*, **21**, 160 (2020). doi:10.1002/acm2.12902.

[20] S. J. Woodings, J. J. Bluemink, J. H.W. De Vries, Y. Niatsetski, B. Van Veelen, J. Schillings, J. G.M. Kok, J. W.H. Wolthaus, S. L. Hackett, B. Van Asselen, H. M. Van Zijp, S. Pencea, D. A. Roberts, J. J.W. Lagendijk, and B. W. Raaymakers. Beam characterisation of the 1.5 T MRI-linac. *Physics in Medicine and Biology*, **63** (2018). doi:10.1088/1361-6560/aab566.

[21] Simon J. Woodings, J. H.Wilfred de Vries, Jan M.G. Kok, Sara L. Hackett, Bram van Asselen, Johanna J. Bluemink, Helena M. van Zijp, Theo L. van Soest, David A. Roberts, Jan J.W. Lagendijk, Bas W. Raaymakers, and Jochem W.H. Wolthaus. Acceptance procedure for the linear accelerator component of the 1.5 T MRI-linac. *Journal of Applied Clinical Medical Physics*, **22**, 45 (2021). doi:10.1002/acm2.13068.

[22] David A. Roberts, Carlos Sandin, Panu T. Vesanen, Hannah Lee, Ian M. Hanson, Simeon Nill, Thijs Perik, Seng Boh Lim, Sastry Vedam, Jinzhong Yang, Simon W. Woodings, Jochem W.H. Wolthaus, Brian Keller, Geoff Budgell, Xinfeng Chen, and X. Allen Li. Machine QA for the Elekta Unity system: A Report from the Elekta MR-linac consortium. *Medical Physics*, **48**, e67 (2021). doi:10.1002/mp.14764.

[23] Jong Min Park, Kyung Hwan Shin, Jung in Kim, So Yeon Park, Seung Hyuck Jeon, Noorie Choi, Jin Ho Kim, and Hong Gyun Wu. Air–electron stream interactions during magnetic resonance IGRT: Skin irradiation outside the treatment field during accelerated partial breast irradiation. *Strahlentherapie und Onkologie*, **194**, 50 (2018). doi:10.1007/s00066-017-1212-z.

[24] Marcel Nachbar, David Mönnich, Simon Boeke, Cihan Gani, Nicola Weidner, Vanessa Heinrich, Monica lo Russo, Lorenzo Livi, Jasmin Winter, Savas Tsitsekidis, Oliver Dohm, Daniela Thorwarth, Daniel Zips, and Chiara De-Colle. Partial breast irradiation with the 1.5 T MR-Linac: First patient treatment and analysis of electron return and stream effects. *Radiotherapy and Oncology*, **145**, 30 (2020). doi:10.1016/j.radonc.2019.11.025.

[25] Yan Zhang, Shaojie Yan, Zhen Cui, Yungang Wang, Zhenjiang Li, Yong Yin, Baosheng Li, Hong Quan, and Jian Zhu. Out-of-field dose assessment for a 1.5 T

MR-Linac with optically stimulated luminescence dosimeters. *Medical Physics*, **48**, 4027 (2021). doi:10.1002/mp.14839.

[26] Hongdong Liu, Shouliang Ding, Bin Wang, Yongbao Li, Ying Sun, and Xiaoyan Huang. In-Air Electron Streaming Effect for Esophageal Cancer Radiotherapy With a 1.5 T Perpendicular Magnetic Field: A Treatment Planning Study. *Frontiers in Oncology*, **10**, 1 (2020). doi:10.3389/fonc.2020.607061.

[27] International Electrotechnical Comission. *IEC 60601-2-1 Medical Electrical Equipment – Part 2-1: Particular requirements for the basic safety and essential performance of electron accelerators in the range 1 MeV to 50 MeV*. Geneva, fourth edition (2020). ISBN 2831886376.

[28] Geoff Budgell, Kirstie Brown, Jason Cashmore, Simon Duane, John Frame, Mark Hardy, David Paynter, and Russell Thomas. IPEM topical report 1: Guidance on implementing flattening filter free (FFF) radiotherapy. *Physics in Medicine and Biology*, **61**, 8360 (2016). doi:10.1088/0031-9155/61/23/8360.

[29] Pedro Andreo, David T Burns, Klaus Hohlfeld, M Saiful Huq, Tatsuaki Kanai, Fedele Laitano, Vere Smyth, and Stefaan Vynckier. IAEA TRS 398: Absorbed Dose Determination in External Beam Radiotherapy: An International Code of Practice for Dosimetry based on Standards of Absorbed Dose to Water. Technical Report June, International Atomic Energy Agency, Vienna (2006).

[30] Michael Joiner and Albert van der Kogel (Editors). *Basic Clinical Radiobiology*. CRC Press, Boca Raton, Fl (2009). ISBN 978-0-340-92966-7.

[31] Matthias Guckenberger, Wolfgang W. Baus, Oliver Blanck, Stephanie E. Combs, Jürgen Debus, Rita Engenhart-Cabillic, Tobias Gauer, Anca L. Grosu, Daniela Schmitt, Stephanie Tanadini-Lang, and Christos Moustakis. Definition and quality requirements for stereotactic radiotherapy: consensus statement from the DEGRO/DGMP Working Group Stereotactic Radiotherapy and Radiosurgery. *Strahlentherapie und Onkologie*, **196**, 417 (2020). doi:10.1007/s00066-020-01603-1.

[32] Eric E. Klein, Joseph Hanley, John Bayouth, Fang Fang Yin, William Simon, Sean Dresser, Christopher Serago, Francisco Aguirre, Lijun Ma, Bijan Arjomandy, Chihray Liu, Carlos Sandin, and Todd Holmes. Task group 142 report: Quality assurance of medical acceleratorsa. *Medical Physics*, **36**, 4197 (2009). doi:10.1118/1.3190392.

[33] Ervin B. Podgorsak (Editor). *Radiation Oncology Physics: A Handbook for Teachers and Students*. International Atomic Energy Agency, Vienna, Austria (2005). doi:10.1118/1.2201870.

[34] Faiz M. Khan (Editor). *The Physics of Radiation Therapy*. Lippincott Williams and Wilkins, a Wolters Kluwer business, Baltimore, fourth edi edition (2010).

[35] ACPSEM. Recommendations for the safe use of external beams and sealed brachytherapy sources in radiation oncology. *Australasian College of Physical and Engineering Sciences in Medicine*, **20**, 1 (1997).

[36] Peter R. Almond, Peter J. Biggs, B. M. Coursey, W. F. Hanson, M. Saiful Huq, Ravinder Nath, and D. W. O. Rogers. AAPM's TG-51 protocol for clinical reference dosimetry of high-energy photon and electron beams. *Medical Physics*, **26**, 1847 (1999). doi:10.1118/1.598691.

[37] B. W. Raaymakers, J. J.W. Lagendijk, J. Overweg, J. G.M. Kok, A. J.E. Raaijmakers, E. M. Kerkhof, R. W. Van Der Put, I. Meijsing, S. P.M. Crijns, F. Benedosso, M. Van Vulpen, C. H.W. De Graaff, J. Allen, and K. J. Brown. Integrating a 1.5 T MRI scanner with a 6 MV accelerator: Proof of concept. *Physics in Medicine and Biology*, **54** (2009). doi:10.1088/0031-9155/54/12/N01.

[38] Sasa Mutic and James F. Dempsey. The ViewRay System: Magnetic Resonance-Guided and Controlled Radiotherapy. *Seminars in Radiation Oncology*, **24**, 196 (2014). doi:10.1016/j.semradonc.2014.02.008.

[39] Urszula Jelen, Bin Dong, Jarrad Begg, Natalia Roberts, Brendan Whelan, Paul Keall, and Gary Liney. Dosimetric Optimization and Commissioning of a High Field Inline MRI-Linac. *Frontiers in Oncology*, **10**, 1 (2020). doi:10.3389/fonc.2020.00136.

[40] Paul J. Keall, Michael Barton, and Stuart Crozier. The Australian Magnetic Resonance Imaging-Linac Program. *Seminars in Radiation Oncology*, **24**, 203 (2014). doi:10.1016/j.semradonc.2014.02.015.

[41] Sebastian Klüter. Technical design and concept of a 0.35 T MR-Linac. *Clinical and Translational Radiation Oncology*, **18**, 98 (2019). doi:10.1016/j.ctro.2019.04.007.

[42] A J E Raaijmakers, B W Raaymakers, and J J W Lagendijk. Integrating a MRI scanner with a 6 MV radiotherapy accelerator: dose increase at tissue–air interfaces in a lateral magnetic field due to returning electrons. *Physics in Medicine and Biology*, **50**, 1363 (2005). doi:10.1088/0031-9155/50/7/002.

[43] A J E Raaijmakers, B W Raaymakers, S van der Meer, and J J W Lagendijk. Integrating a MRI scanner with a 6 MV radiotherapy accelerator: impact of the surface orientation on the entrance and exit dose due to the transverse magnetic field. *Physics in Medicine and Biology*, **52**, 929 (2007). doi:10.1088/0031-9155/52/4/005.

[44] B W Raaymakers, A J E Raaijmakers, A N T J Kotte, D Jette, and J J W Lagendijk. Integrating a MRI scanner with a 6 MV radiotherapy accelerator: dose deposition in a transverse magnetic field. *Physics in Medicine and Biology*, **49**, 4109 (2004). doi:10.1088/0031-9155/49/17/019.

[45] Bas W. Raaymakers, Jan J.W. Lagendijk, Uulke A. van der Heide, J. Overweg, Kevin J. Brown, R. Topolnjak, H. Dehnad, I.M. Jurgenliemk-Schulz, J. Welleweerd, and C. J.G. Bakker. Integrating a MRI scanner with a radiotherapy accelerator: a new concept of precise on line radiotherapy guidance and treatment monitoring. In *14th International Conference on the use of Computers in Radiation Therapy*, 89–92. Seoul, South Korea (2004).

[46] S. Hissoiny, A. J.E. Raaijmakers, B. Ozell, P. Després, and B. W. Raaymakers. Fast dose calculation in magnetic fields with GPUMCD. *Physics in Medicine and Biology*, **56**, 5119 (2011). doi:10.1088/0031-9155/56/16/003.

[47] K. Smit, B. Van Asselen, J. G.M. Kok, A. H.L. Aalbers, J. J.W. Lagendijk, and B. W. Raaymakers. Towards reference dosimetry for the MR-linac: Magnetic field correction of the ionization chamber reading. *Physics in Medicine and Biology*, **58**, 5945 (2013). doi:10.1088/0031-9155/58/17/5945.

[48] D. J. O'Brien, D. A. Roberts, G. S. Ibbott, and G. O. Sawakuchi. Reference dosimetry in magnetic fields: formalism and ionization chamber correction factors. *Medical Physics*, **43**, 4915 (2016). doi:10.1118/1.4959785.

[49] A Hunt, V N Hansen, U Oelfke, S Nill, and S Hafeez. Adaptive Radiotherapy Enabled by MRI Guidance. *Clinical Oncology*, **30**, 711 (2019). doi:10.1016/j.clon.2018.08.001.

[50] Di Yan, Frank Vicini, John Wong, and Alvaro Martinez. Adaptive radiation therapy. *Phys. Med. Biol*, **42**, 123 (1997). doi:10.1088/0031-9155/42/1/008.

[51] Eric Ford, Leigh Conroy, Lei Dong, Luis Fong de Los Santos, Anne Greener, Grace Gwe-ya Kim, Jennifer Johnson, Perry Johnson, James G. Mechalakos, Brian Napolitano, Stephanie Parker, Deborah Schofield, Koren Smith, Ellen Yorke, and Michelle Wells. Strategies for effective physics plan and chart review in radiation therapy : Report of AAPM Task Group 275. *Medical Physics*, **47**, e236 (2020). doi:10.1002/mp.14030.

[52] A. J.E. Raaijmakers, B. W. Raaymakers, and J. J.W. Lagendijk. Magnetic-field-induced dose effects in MR-guided radiotherapy systems: Dependence on the magnetic field strength. *Physics in Medicine and Biology*, **53**, 909 (2008). doi:10.1088/0031-9155/53/4/006.

[53] S. L. Hackett, B. Van Asselen, J. W.H. Wolthaus, J. G.M. Kok, S. J. Woodings, J. J.W. Lagendijk, and B. W. Raaymakers. Consequences of air around an ionization chamber: Are existing solid phantoms suitable for reference dosimetry on an MR-linac? *Medical Physics*, **43**, 3961 (2016). doi:10.1118/1.4952727.

[54] Paola Godoy Scripes, Ergys Subashi, Sarah Burleson, Jiayi Liang, Paul Romesser, Christopher Crane, James Mechalakos, Margie Hunt, and Neelam Tyagi. Impact of varying air cavity on planning dosimetry for rectum patients

treated on a 1.5 T hybrid MR-linac system. *Journal of Applied Clinical Medical Physics*, **21**, 144 (2020). doi:10.1002/acm2.12903.

[55] International Electrotechnical Comission. *IEC 60976 - Australian / New Zealand Standard ® 4434.1:1996 Medical electrical equipment — Medical electron accelerators Part 1: Functional performance characteristics* (1996).

[56] International Electrotechnical Comission. *IEC 60977 - Australian / New Zealand Standard ® 4434.2:1996 Medical electrical equipment — Medical electron accelerators Part 2: Periodic function performance testing* (1996).

[57] Jeremiah de Leon, David Crawford, Zoë Moutrie, Stacy Alvares, Louise Hogan, Claire Pagulayan, Urszula Jelen, Conrad Loo, Jack D. Aylward, Kieran Condon, Nicolle Dunkerley, Monique Y. Heinke, Sandy Sampaio, Kathy Simon, Tania Twentyman, and Michael G. Jameson. Early experience with MR-guided adaptive radiotherapy using a 1.5 T MR-Linac: First 6 months of operation using adapt to shape workflow. *Journal of Medical Imaging and Radiation Oncology*, 1–8 (2021). doi:10.1111/1754-9485.13336.

[58] William B. Harms, Daniel A. Low, John W. Wong, and James A. Purdy. A software tool for the quantitative evaluation of 3D dose calculation algorithms. *Medical Physics*, **25**, 1830 (1998). doi:10.1118/1.598363.

[59] John Baines and Ariadne Shoobridge. Evaluation of MU2net as an Online Secondary Dose Check for MR Guided Radiation Therapy with the Elekta Unity MR Linac. *Physical and Engineering Sciences in Medicine*, **Online** (2021). doi:10.21203/rs.3.rs-368526/v1.

[60] Stephen A. Graves, Jeffrey E. Snyder, Amanda Boczkowski, Joël St-Aubin, Dongxu Wang, Sridhar Yaddanapudi, and Daniel E. Hyer. Commissioning and performance evaluation of RadCalc for the Elekta unity MRI-linac. *Journal of Applied Clinical Medical Physics*, **20**, 54 (2019). doi:10.1002/acm2.12760.

[61] S Hackett, B van Asselen, G Feist, S Pencea, H Akhiat, J Wolthaus, A Kotte, G Bol, J Lagendijk, and B Raaymakers. SU-F-J-148: A Collapsed Cone Algorithm Can Be Used for Quality Assurance for Monaco Treatment Plans for the MR-Linac. *Medical Physics*, **43**, 3441 (2016). doi:10.1118/1.4956056.

[62] Rob H.N. Tijssen, Marielle E.P. Philippens, Eric S. Paulson, Markus Glitzner, Brige Chugh, Andreas Wetscherek, Michael Dubec, Jihong Wang, and Uulke A. van der Heide. MRI commissioning of 1.5T MR-linac systems – a multi-institutional study. *Radiotherapy and Oncology*, **132**, 114 (2019). doi:10.1016/j.radonc.2018.12.011.

[63] Jihong Wang, Joshua Yung, Mo Kadbi, Ken Hwang, Yao Ding, and Geoffrey S. Ibbott. Assessment of image quality and scatter and leakage radiation of an integrated MR-LINAC system:. *Medical Physics*, **45**, 1204 (2018). doi:10.1002/mp.12767.

[64] Ke Zhang, Yuan Tian, Minghui Li, Kuo Men, and Jianrong Dai. Performance of a multileaf collimator system for a 1.5T MR-linac. *Medical Physics*, **48**, 546 (2021). doi:10.1002/mp.14608.

[65] I. Hanson, J. Sullivan, S. Nill, and U. Oelfke. OC-0079: A new multi-purpose QA phantom for use on the Elekta MR-Linac. *Radiotherapy and Oncology*, **127**, S38 (2018). doi:10.1016/S0167-8140(18)30389-X.

[66] B. W. Raaymakers, J. C.J. De Boer, C. Knox, S. P.M. Crijns, K. Smit, M. K. Stam, M. R.Van Den Bosch, J. G.M. Kok, and J. J.W. Lagendijk. Integrated megavoltage portal imaging with a 1.5 T MRI linac. *Physics in Medicine and Biology*, **56** (2011). doi:10.1088/0031-9155/56/19/N01.

[67] James R Hunt, Martin A Ebert, Pejman Rowshanfarzad, and Hans L Riis. Variation in isocentre location of an Elekta Unity MR-linac through full gantry rotation Variation in isocentre location of an Elekta Unity MR-linac through full gantry rotation. *Physics and Imaging in Radiation Oncology*, **67** (2022).

[68] H. M. Van Zijp, B. Van Asselen, J. W.H. Wolthaus, J. M.G. Kok, J. H.W. De Vries, K. Ishakoglu, E. Beld, J. J.W. Lagendijk, and B. W. Raaymakers. Minimizing the magnetic field effect in MR-linac specific QA-tests: The use of electron dense materials. *Physics in Medicine and Biology*, **61**, N50 (2016). doi:10.1088/0031-9155/61/3/N50.

[69] M. A. Moerland, R. Beersma, R. Bhagwandien, H. K. Wijrdeman, and C. J.G. Bakker. Analysis and correction of geometric distortions in 1.5 T magnetic resonance images for use in radiotherapy treatment planning. *Physics in Medicine and Biology*, **40**, 1651 (1995). doi:10.1088/0031-9155/40/10/007.

[70] Daniel J. O'Brien, James Dolan, Stefan Pencea, Nicholas Schupp, and Gabriel O. Sawakuchi. Relative dosimetry with an MR-linac: Response of ion chambers, diamond, and diode detectors for off-axis, depth dose, and output factor measurements: Response. *Medical Physics*, **45**, 884 (2018). doi:10.1002/mp.12699.

[71] K. Smit, J. G.M. Kok, J. J.W. Lagendijk, and B. W. Raaymakers. Performance of a multi-axis ionization chamber array in a 1.5 T magnetic field. *Physics in Medicine and Biology*, **59**, 1845 (2014). doi:10.1088/0031-9155/59/7/1845.

[72] Stefan Pojtinger, Marcel Nachbar, Ralf Peter Kapsch, and Daniela Thorwarth. Influence of beam quality on reference dosimetry correction factors in magnetic resonance guided radiation therapy. *Physics and Imaging in Radiation Oncology*, **16**, 95 (2020). doi:10.1016/j.phro.2020.10.005.

[73] M. Friedel, M. Nachbar, D. Mönnich, O. Dohm, and D. Thorwarth. Development and validation of a 1.5 T MR-Linac full accelerator head and cryostat model for Monte Carlo dose simulations. *Medical Physics*, **46**, 5304 (2019). doi:10.1002/mp.13829.

[74] Gary A. Ezzell, Jay W. Burmeister, Nesrin Dogan, Thomas J. Losasso, James G. Mechalakos, Dimitris Mihailidis, Andrea Molineu, Jatinder R. Palta, Chester R. Ramsey, Bill J. Salter, Jie Shi, Ping Xia, Ning J. Yue, and Ying Xiao. IMRT commissioning: Multiple institution planning and dosimetry comparisons, a report from AAPM Task Group 119. *Medical Physics*, **36**, 5359 (2009). doi:10.1118/1.3238104.

[75] Moyed Miften, Arthur Olch, Dimitris Mihailidis, Jean Moran, Todd Pawlicki, Andrea Molineu, Harold Li, Krishni Wijesooriya, Jie Shi, Ping Xia, Nikos Papanikolaou, and Daniel A. Low. Tolerance limits and methodologies for IMRT measurement-based verification QA: Recommendations of AAPM Task Group No. 218. *Medical Physics*, **45**, e53 (2018). doi:10.1002/mp.12810.

[76] B. Yang, Y. S. Wong, W. W. Lam, H. Geng, C. Y. Huang, K. K. Tang, W. K. Law, C. C. Ho, P. H. Nam, K. Y. Cheung, and S. K. Yu. Initial clinical experience of patient-specific QA of treatment delivery in online adaptive radiotherapy using a 1.5 T MR-Linac. *Biomedical Physics and Engineering Express*, **7** (2021). doi:10.1088/2057-1976/abfa80.

[77] Björn Delfs, Andreas A. Schoenfeld, Daniela Poppinga, Ralf Peter Kapsch, Ping Jiang, Dietrich Harder, Björn Poppe, and Hui Khee Looe. Magnetic fields are causing small, but significant changes of the radiochromic EBT3 film response to 6 MV photons. *Physics in Medicine and Biology*, **63**, 0 (2018). doi:10.1088/1361-6560/aa9bd5.

[78] Ilias Billas, Hugo Bouchard, Uwe Oelfke, and Simon Duane. The effect of magnetic field strength on the response of Gafchromic EBT-3 film. *Physics in Medicine and Biology*, **64**, 0 (2019). doi:10.1088/1361-6560/ab0503.

[79] Anita M. Werensteijn-Honingh, Petra S. Kroon, Dennis Winkel, Ellart M. Aalbers, Bram van Asselen, Gijsbert H. Bol, Kevin J. Brown, Wietse S.C. Eppinga, Corine A. van Es, Markus Glitzner, Eline N. de Groot-van Breugel, Sara L. Hackett, Martijn Intven, Jan G.M. Kok, Charis Kontaxis, Alexis N. Kotte, Jan J.W. Lagendijk, Mariëlle E.P. Philippens, Rob H.N. Tijssen, Jochem W.H. Wolthaus, Simon J. Woodings, Bas W. Raaymakers, and Ina M. Jürgenliemk-Schulz. Feasibility of stereotactic radiotherapy using a 1.5 T MR-linac: Multi-fraction treatment of pelvic lymph node oligometastases. *Radiotherapy and Oncology*, **134**, 50 (2019). doi:10.1016/j.radonc.2019.01.024.

[80] Ning Wen, Joshua Kim, Anthony Doemer, Carri Glide-Hurst, Indrin J. Chetty, Chang Liu, Eric Laugeman, Ilma Xhaferllari, Akila Kumarasiri, James Victoria, Maria Bellon, Steve Kalkanis, M. Salim Siddiqui, and Benjamin Movsas. Evaluation of a magnetic resonance guided linear accelerator for stereotactic radiosurgery treatment. *Radiotherapy and Oncology*, **127**, 460 (2018). doi:10.1016/j.radonc.2018.04.034.

[81] David Mönnich, Jasmin Winter, Marcel Nachbar, Luise Künzel, Simon Boeke, Cihan Gani, Oliver Dohm, Daniel Zips, and Daniela Thorwarth. Quality assurance of IMRT treatment plans for a 1.5 T MR-linac using a 2D ionization chamber array and a static solid phantom. *Physics in Medicine and Biology*, **65**, 0 (2020). doi:10.1088/1361-6560/aba5ec.

[82] Xinfeng Chen, Ergun Ahunbay, Eric S. Paulson, Guangpei Chen, and X. Allen Li. A daily end-to-end quality assurance workflow for MR-guided online adaptive radiation therapy on MR-Linac. *Journal of Applied Clinical Medical Physics*, **21**, 205 (2020). doi:10.1002/acm2.12786.

[83] E. Pappas, G. Kalaitzakis, T. Boursianis, E. Zoros, K. Zourari, E. P. Pappas, D. Makris, I. Seimenis, E. Efstathopoulos, and T. G. Maris. Dosimetric performance of the Elekta Unity MR-linac system: 2D and 3D dosimetry in anthropomorphic inhomogeneous geometry. *Physics in Medicine and Biology*, **64**, 0 (2019). doi:10.1088/1361-6560/ab52ce.

[84] A. Elter, S. Dorsch, P. Mann, A. Runz, W. Johnen, C. K. Spindeldreier, S. Klüter, and C. P. Karger. End-to-end test of an online adaptive treatment procedure in MR-guided radiotherapy using a phantom with anthropomorphic structures. *Physics in Medicine and Biology*, **64**, 0 (2019). doi:10.1088/1361-6560/ab4d8e.

[85] A. Steinmann, P. Alvarez, H. Lee, L. Court, R. Stafford, G. Sawakuchi, Z. Wen, C. Fuller, and D. Followill. MRIgRT dynamic lung motion thorax anthropomorphic QA phantom: Design, development, reproducibility, and feasibility study. *Medical Physics*, **46**, 5124 (2019). doi:10.1002/mp.13757.

[86] D. N. Makris, E. P. Pappas, E. Zoros, N. Papanikolaou, D. L. Saenz, G. Kalaitzakis, K. Zourari, E. Efstathopoulos, T. G. Maris, and E. Pappas. Characterization of a novel 3D printed patient specific phantom for quality assurance in cranial stereotactic radiosurgery applications. *Physics in Medicine and Biology*, **64**, 0 (2019). doi:10.1088/1361-6560/ab1758.

[87] C. Baldock, Y. De Deene, S. Doran, G. Ibbott, A. Jirasek, M. Lepage, K. B. McAuley, M. Oldham, and L. J. Schreiner. Topical Review: Polymer gel dosimetry. *Physics in Medicine and Biology*, **55**, 1 (2010). doi:10.1088/0031-9155/55/5/R01.

[88] L. J. Schreiner, T. Olding, and K. B. McAuley. Polymer gel dosimetry. *Journal of Physics: Conference Series*, **250**, 64 (2010). doi:10.1088/1742-6596/250/1/012014.

[89] Uffe Bernchou, Rasmus L. Christiansen, Anders Bertelsen, David Tilly, Hans L. Riis, Henrik R. Jensen, Faisal Mahmood, Christian R. Hansen, Vibeke N. Hansen, Tine Schytte, and Carsten Brink. End-to-end validation of the geometric dose delivery performance of MR linac adaptive radiotherapy. *Physics in Medicine and Biology*, **66**, 0 (2021). doi:10.1088/1361-6560/abd3ed.

[90] N. I. Niebuhr, W. Johnen, G. Echner, A. Runz, M. Bach, M. Stoll, K. Giske, S. Greilich, and A. Pfaffenberger. The ADAM-pelvis phantom - An anthropomorphic, deformable and multimodal phantom for MRgRT. *Physics in Medicine and Biology*, **64** (2019). doi:10.1088/1361-6560/aafd5f.

[91] Marchant Van der Walt, Tim Crabtree, and Christine Albantow. PLA as a suitable 3D printing thermoplastic for use in external beam radiotherapy. *Australasian Physical and Engineering Sciences in Medicine*, **42**, 1165 (2019). doi:10.1007/s13246-019-00818-6.

[92] O. L. Dancewicz, S. R. Sylvander, T. S. Markwell, S. B. Crowe, and J. V. Trapp. Radiological properties of 3D printed materials in kilovoltage and megavoltage photon beams. *Physica Medica*, **38**, 111 (2017). doi:10.1016/j.ejmp.2017.05.051.

[93] T Kairn, S B Crowe, and T Markwell. Use of 3D Printed Materials as Tissue-Equivalent Phantoms. *IFMBE Proceedings*, **51**, 3 (2015). doi:10.1007/978-3-319-19387-8.

[94] Nina I. Niebuhr, Wibke Johnen, Timur Güldaglar, Armin Runz, Gernot Echner, Philipp Mann, Christian Möhler, Asja Pfaffenberger, Oliver Jäkel, and Steffen Greilich. Technical Note: Radiological properties of tissue surrogates used in a multimodality deformable pelvic phantom for MR-guided radiotherapy. *Medical Physics*, **43**, 908 (2016). doi:10.1118/1.4939874.

[95] Robba Rai, Yu Feng Wang, David Manton, Bin Dong, Shrikant Deshpande, and Gary P. Liney. Development of multi-purpose 3D printed phantoms for MRI. *Physics in Medicine and Biology*, **64**, 0 (2019). doi:10.1088/1361-6560/ab0b49.

[96] Victor N. Malkov, Sara L. Hackett, Bram van Asselen, Bas W. Raaymakers, and Jochem W.H. Wolthaus. Monte Carlo simulations of out-of-field skin dose due to spiralling contaminant electrons in a perpendicular magnetic field. *Medical Physics*, **46**, 1467 (2019). doi:10.1002/mp.13392.

[97] National Research Council of Canada. Metrology Research Centre. Ionizing Radiation Standards. EGSnrc: software for Monte Carlo simulation of ionizing radiation (2000).

[98] Y. M. Yang, M. Geurts, J. B. Smilowitz, E. Sterpin, and B. P. Bednarz. Monte Carlo simulations of patient dose perturbations in rotational-type radiotherapy due to a transverse magnetic field: A tomotherapy investigation. *Medical Physics*, **42**, 715 (2015). doi:10.1118/1.4905168.

[99] Caroline A Schneider, Wayne S Rasband, and Kevin W Eliceiri. NIH Image to ImageJ: 25 years of image analysis. *Nature Methods*, **9**, 671 (2012). doi:10.1038/nmeth.2089.

[100] David Lewis, Andre Micke, Xiang Yu, and Maria F. Chan. An efficient protocol for radiochromic film dosimetry combining calibration and measurement in a single scan. *Medical Physics*, **39**, 6339 (2012). doi:10.1118/1.4754797.

[101] David Lewis and Maria F. Chan. Correcting lateral response artifacts from flatbed scanners for radiochromic film dosimetry. *Medical Physics*, **42**, 416 (2015). doi:10.1118/1.4903758.

[102] Stephen F. Kry, Paola Alvarez, Joanna E. Cygler, Larry A. DeWerd, Rebecca M. Howell, Sanford Meeks, Jennifer O'Daniel, Chester Reft, Gabriel Sawakuchi, Eduardo G. Yukihara, and Dimitris Mihailidis. AAPM TG 191: Clinical use of luminescent dosimeters: TLDs and OSLDs. *Medical Physics*, **47**, e19 (2020). doi:10.1002/mp.13839.

[103] Elsa Y. León Marroquin, José A. Herrera González, Miguel A. Camacho López, José E. Villarreal Barajas, and Olivia A. García-Garduño. Evaluation of the uncertainty in an EBT3 film dosimetry system utilizing net optical density. *Journal of Applied Clinical Medical Physics*, **17**, 466 (2016). doi:10.1120/jacmp.v17i5.6262.

[104] Antony L. Palmer, Alexis Dimitriadis, Andrew Nisbet, and Catharine H. Clark. Evaluation of Gafchromic EBT-XD film, with comparison to EBT3 film, and application in high dose radiotherapy verification. *Physics in Medicine and Biology*, **60**, 8741 (2015). doi:10.1088/0031-9155/60/22/8741.

[105] Christopher N. Kabat, Dewayne L. Defoor, Pamela Myers, Neil Kirby, Karl Rasmussen, Daniel L. Saenz, Panayiotis Mavroidis, Niko Papanikolaou, and Sotirios Stathakis. Evaluation of the Elekta Agility MLC performance using high-resolution log files. *Medical Physics*, **46**, 1397 (2019). doi:10.1002/mp.13374.

[106] Seng Boh Lim, Paola Godoy Scripes, Mary Napolitano, Ergys Subashi, Neelam Tyagi, Laura Cervino Arriba, and Dale Michael Lovelock. An investigation of using log-file analysis for automated patient-specific quality assurance in MRgRT. *Journal of Applied Clinical Medical Physics*, **22**, 183 (2021). doi:10.1002/acm2.13361.

[107] Jessica Lye, Stephen Kry, Maddison Shaw, Francis Gibbons, Stephanie Keehan, Joerg Lehmann, Tomas Kron, David Followill, and Ivan Williams. A comparison of IROC and ACDS on-site audits of reference and non-reference dosimetry. *Medical Physics*, **46**, 5878 (2019). doi:10.1002/mp.13800.

[108] M. J. Berger, J. S. Coursey, M.A. Zucker, and J. Chang. Stopping-Power and Range Tables for Electrons, Protons, and Helium Ions (2017). doi:https://dx.doi.org/10.18434/T4NC7P.

[109] Elekta. GPUCMD Physics for Photon External Beam Reference Manual: LRM-MON0010 (2018).

[110] Ergun E. Ahunbay, Cheng Peng, Guang Pei Chen, Sreeram Narayanan, Cedric Yu, Colleen Lawton, and X. Allen Li. An on-line replanning scheme for inter-fractional variations. *Medical Physics*, **35**, 3607 (2008). doi:10.1118/1.2952443.

A

Additional Commissioning Tests

This appendix contains information pertaining to additional commissioning tests. These were omitted from the thesis body as they are not currently under consideration for publication; however, this may change in future.

For this appendix, I performed measurements on the machine and the simulations described below, with assistance from physicists at the Townsville Cancer Centre.

A.1 Introduction

Similar to previous sections, in-house equipment and simple techniques were employed to determine a variety of common mechanical commissioning measurements. Mega-voltage imager (MVI) panel operation testing and confirmation measurements of magnetic resonance to mega-voltage (MR-to-MV) isocentre offsets was performed with aforementioned bespoke phantoms. Previous investigators [21] have published on common couch operation checks such as couch absolute position accuracy, drive linearity and orthogonality of movement to the gantry plane of rotation. A simple method to measure couch drive orthogonality to the gantry plane is presented. The methodology makes use of commonly available equipment and has not been previously reported on, for this machine. Due to a spontaneous quench on the Elekta Unity, a unique opportunity was afforded to measure a cryostat characterisation differences pre- and post- quench to observe differences. For additional dosimetric commissioning work performed, alternate methods to measure beam output and shape with gantry angle are provided.

A.2 Methods

A.2.1 Couch Operation and Sagittal Laser Accuracy

Using a solid water stack of 14.0 cm height, an MV visible ballbearing was placed at isocentre height, aligned to the sagittal laser. This ballbearing was driven to the approximate isocentre position, and imaged on the MVI using a 10×10 cm^2, 50 MU, field from gantry 0.0° (G0), G90 and G270. The lateral offset of the ballbearing from the MVI isocentre was measured on the G0 image, and solid water height was assessed for coincidence with isocentre on the G90 and G270 images. The table position was recorded and an additional 14.0 cm solid water stack was placed ~ 160.0 cm inferiorly on the table, with another ballbearing atop. This ballbearing was aligned to the sagittal laser as before, however with care taken to ensure this was performed at the same distance from the bore as the first. In this way, any laser rotation did not interfere with results. The couch was driven in 160.0 cm, so that the second ballbearing was nominally at isocentre, and MVI images taken as previous. Lateral and height offset of this setup to the isocentre were compared to those from the first images to determine the couch drive orthogonality to the gantry rotation plane.

A sagittal laser is provided with the Elekta Unity MR-Linac (MRL); however, its use is limited [21, 22]. Direct measurement of the offset, rotation and skew (laser offset change with height) was made. Four ballbearings were set atop individual solid water stacks of 14.0 cm height, spaced approximately 60.0 cm apart along the length of the patient position system (PPS). Each ballbearing was imaged at isocentre using the MVI (several couch longitudinal positions) using the G0 field above, and lateral shifts were made to position the ballbearings along the Y-axis. A self-levelling laser (CXR880, RedBack^{TM} lasers, Geelong, VIC), was then aligned to each ballbearing, with the couch fully withdrawn from the bore. The laser was placed away from the bore, where the magnetic field strength was less than 0.5 mT. After aligning to the ballbearings, and therefore the Y-axis, the self-levelling laser was compared to the sagittal laser at multiple positions.

A.2.2 Cryostat Characterisation

To measure the cryostat characterisation, the couch and bridge components were removed from the bore. The cryostat characterisation tool (CCT, Figure A.1), with a PTW 30013 Farmer chamber (PTW, Freiburg, Germany) inserted in the 56.5 mm diameter build-up cap, was mounted within the bore parallel to the static field. Chamber readings were acquired using a 10.0×10.0 cm^2, 100 MU field delivered to the chamber at 2.0° intervals between G50 and G310, and at 10.0° intervals elsewhere. Gantry angles of 8.0° - 18.0° were avoided due to the cryostat pipe. The chamber was rotated 180.0° about its longitudinal axis and the above measurements were repeated. Corresponding chamber readings were averaged, to minimize chamber directional dependence, and normalised to the averaged G90 reading. Cryostat characterisation determined after

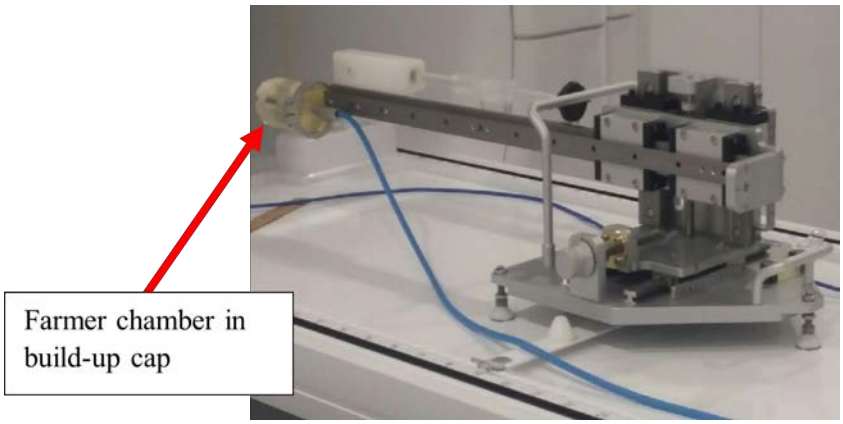

Figure A.1: An image of the cryostat characterisation tool (CCT) with the Farmer chamber and build-up cap attached

the spontaneous quench was compared to that acquired during device acceptance tests (DAT).

A.2.3 MVI Operation

The MVI panel is not used clinically, hence tests presented here focus primarily on those required for quality assurance (QA) purposes. Geometric accuracy of the panel was considered of importance, since most QA equipment uses the panel to set up and align with the machine isocentre. Image scale accuracy and central pixel location were performed independently of Elekta DAT. Panel alignment was performed by Elekta during DAT, and is not presented in this work.

For MVI image scale accuracy, an in-house designed aluminium "ruler" was used. The ruler is 2.5 cm wide, 30.0 cm in length and 0.3 cm thick, and has thirteen machined 3.0 mm holes spaced 2.0 cm apart along its length. The ruler was placed atop 13.9 cm of solid water on the couch, aligned parallel to the X-axis, such that the centre of the device was within 0.05 cm of the isocentre. A 22.0×22.0 cm^2, 50 MU, field from G0 was delivered. From the image, hole separation was measured using the MVI ruler tool and compared to nominal values, to determine the accuracy of the image scaling in this direction. The process was repeated with the aluminium ruler rotated parallel to the Y-axis.

The MVI central pixel is often used as a surrogate for the machine isocentre when aligning equipment, and as such its position with respect to the true isocentre is important. To determine the central pixel location, a process similar to that employed by Elekta is used. As part of this, 1.0×22.0 cm^2 fields, centred at $\pm$ 21.0 cm, were delivered to the MVI panel with 50 MU from G0. With these fields, the back ends of each jaw are projected onto the panel at $\pm$ 4.0 cm. The jaw is machined such that the vertex of the V aligns with the centre of the jaw along the Y-axis, Figure A.2. On each image, the Y (vertical) and X (horizontal) location of the vertex were determined. The average locations, between the two images (two jaws), was taken as the central pixel from G0. This was repeated for G90. The true centre pixel was taken as the

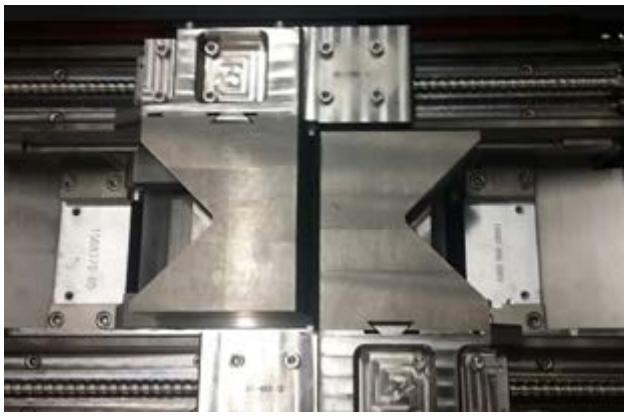

Figure A.2: Image of the jaws in the Elekta Unity beam limiting device (BLD)

average values, for vertical and horizontal pixels, from the two gantry angles. This contrasts with the Elekta method, where only the vertical pixel is determined in this manner [21].

A.2.4 MR-to-MV Isocentre Confirmation

To confirm the MR-to-MV alignment offset, an acrylic, water-filled cylindrical phantom was used (Figure A.3). A 0.6 cm diameter, 11.0 cm acrylic rod, with a 1.5 cm diameter sphere at one end, was attached to the phantom. The phantom was scanned using computed tomography (CT), with 1.0 mm slices, and contoured in Monaco. An arbitrary plan was added and the plan isocentre was set to coincide with the centre of the 1.5 cm sphere using virtual couch shifts. The phantom was then placed at the same position on the Unity couch as for the CT scan.

The phantom was imaged using six-minute, T1-weighted transverse and coronal magnetic resonance (MR) scans, to improve the resolution in stack offset adjustments. Sphere centre to MR isocentre was measured using the Marlin software by adjusting the stack offset to coincide with the centre of the sphere. This can be found in the "Off/Ang" tab in the Planning workflow on the MR system. The transverse scan was transferred to Online Monaco, and registered to the CT image according to the centre of the 1.5 cm sphere. MR-CT image fusion isocentre offsets were recorded from Online Monaco. Stack offset values from the MR isocentre were subtracted from the fusion values and the result was compared to the values for the MR-to-MV isocentre shift obtained from the Elekta supplied phantom (Figure A.4) and software. The process of aligning the stack offset to the centre of the sphere and performing the image registration was performed by several physicists and radiation therapists to investigate inter-observer variations. Two set ups were performed to determine reproducibility.

A.2.5 Output with Gantry Angle

For output variation with gantry angle, the phantom and setup described previously in Chapter 4 for anterior coil attenuation, was used (Figure A.5).

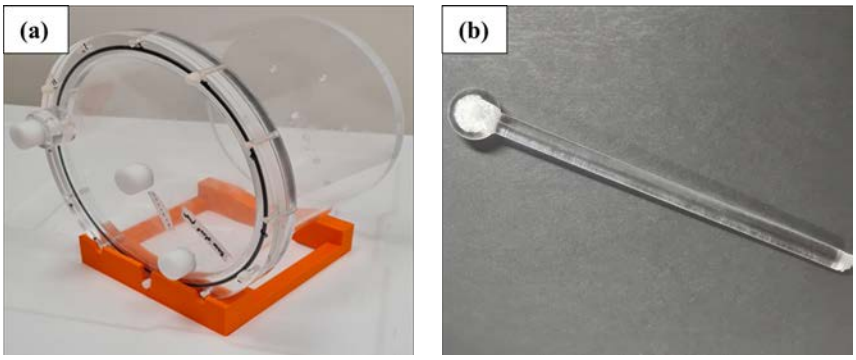

Figure A.3: The (a) acrylic cylindrical phantom for MR-to-MV isocentre confirmation, and (b) the sphere/rod that can be placed within the phantom

Figure A.4: The Elekta supplied MR-to-MV phantom

A 5.0×5.0 cm^2 100 MU field was delivered to the chamber for 15.0° gantry angle increments, between 0.0° - 345.0°. For each gantry angle, the cylindrical phantom was also rotated to maintain the same orientation of the chamber with respect to the beam. A gantry angle of 15.0° was avoided due to the cryostat pipe as previously described. Results were normalised to the reading at gantry 90.0°. Measurements were performed in 0 T and 1.5 T environments.

The measurement geometry was simulated in the planning system, noting the water equivalent thickness of the acrylic was negligible. A 0.1 cm dose grid, statistical uncertainty of 0.25 % per control point and the phantom lookup table were used for calculations.

A.2.6 Beam Shape at Cardinal Gantry Angles

Beam profiles were measured at the cardinal gantry angles using the PTW Octavius 1500^{MR} array (PTW, Freiburg, Germany) and solid water. For each angle, the array was imaged with the previously described aluminium ruler (Section A.2.3), to align with the isocentre. After alignment, 0.5 cm of solid water was added to achieve an effective point of measurement (EPOM) of 1.3 cm (approximate depth of maximum

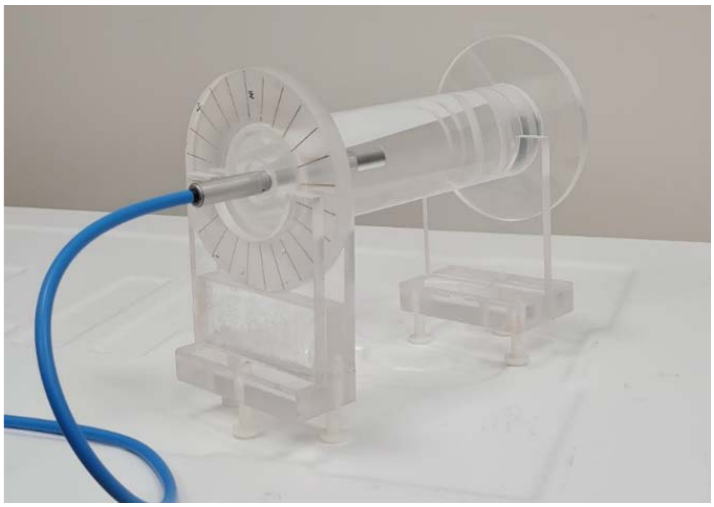

Figure A.5: Cylindrical water phantom and with chamber inserted used for output with gantry angle and anterior coil attenuation measurements

Ballbearing Index	Distance [cm]	Offset [mm]
00	0.0	+ 1.50
15	60.0	+ 1.25
30	120.0	+ 1.00
45	180.0	+ 0.75

Table A.1: Laser alignment results. Offset values are reported relative to the self-levelling laser, with positive values indicating a shift towards + X IEC 61217

dose). 10.0 cm of solid water was used as backscatter. For each delivery, the front surface of the array directly faced the beam. Therefore, for the lateral deliveries, the central chamber of the array was 15.0 cm above the couch, 1.0 cm above isocentre. For the G180 delivery, the array and solid water was set above the couch using additional solid water as stands. Hence, the couch and bridge were present for this measurement. A 22.0×22.0 cm^2 100 MU field was delivered at each angle, and inplane and crossplane profiles through isocentre were determined. The dose, relative to the centre, at several equidistant positions from the central axis were compared to assess beam shape. Symmetry was determined as per IEC 60976 (maximum dose ratio) [55, 56].

A.3 Results

A.3.1 Couch Operation and Sagittal Laser Accuracy

The couch drive orthogonality in the X-Y plane was measured to vary 0.025 cm over 160.0 cm travel, or $\sim 0.01°$. The top of the solid water was coincident with the MVI isocentre at both longitudinal table positions, and both lateral gantry angles, indicating that the couch drive was also orthogonal for the X-Z and Y-Z planes. The sagittal laser accuracy results in Table A.1 were consistent from the top of the couch to $\sim$ 40.0 cm above this point, indicating there was little skew in the laser.

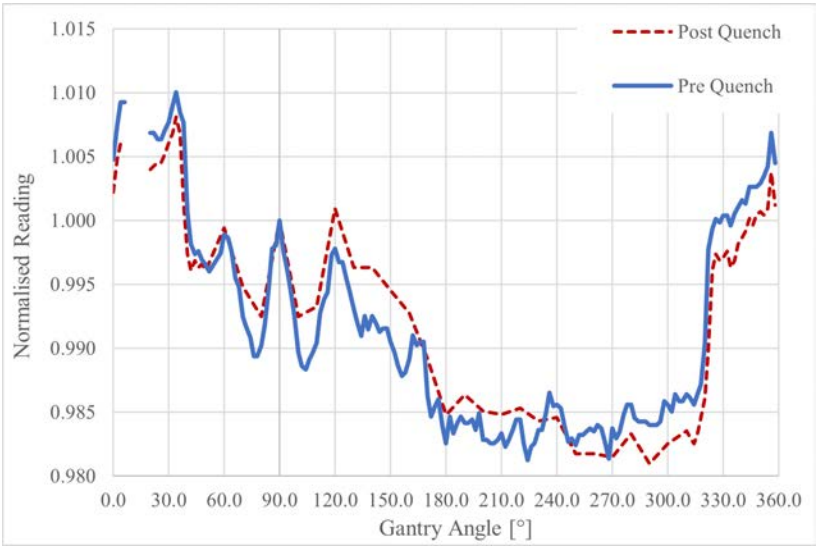

Figure A.6: Cryostat characterisation for pre- and post-quench states

Direction	Measured [mm]	Nominal [mm]
Y	80.32	80.00
X	200.15	200.00

Table A.2: MVI image scale results. Distances are reported between the most distal holes on the images

Gantry Angle	Vertical pixel	Horizontal pixel
G0	654.72	511.52
G90	654.85	512.11
Average	654.78	511.82

Table A.3: Central pixel results. The Elekta determined values were (655.18, 511.63) for vertical and horizontal pixels, respectively

A.3.2 Cryostat Characterisation

The cryostat characterisation for the post quench recovery environment is shown in Figure A.6. The original cryostat characterisation is also displayed to highlight differences.

A.3.3 MVI Operation

The MVI image scale results are presented in Table A.2 and the central pixel data is presented in Table A.3. The Elekta determined central pixel locations were 655.18 and 511.63 for vertical and horizontal, respectively.

A.3.4 MR-to-MV Isocentre Confirmation

MR-to-MV isocentre confirmation results are presented in Tables A.4 and A.5. The stored isocentre offset values, as determined by Elekta, were $(0.23, -1.03, 0.14)$ for (x, y, z).

Observer	x [mm]	y [mm]	z [mm]
1	1.1	0.6	0.0
2	0.5	0.6	0.1
3	0.5	0.6	0.0
4	0.2	0.7	0.1
5	1.2	1.0	2.3
6	0.3	0.8	0.9
Avg.	0.6	0.7	0.6
St.Dev	0.4	0.2	0.9

Table A.4: First set of MR-to-MV isocentre offset results for an initial attempt. Average (Avg.) and standard deviation (St.Dev) of the results between the 6 observers are presented

Observer	x [mm]	y [mm]	z [mm]
1	0.1	1.0	0.6
2	-0.5	1.0	0.9
3	-0.3	0.8	1.3
4	-0.4	0.7	0.8
5	0.2	0.4	1.1
6	-0.2	0.7	0.9
Avg.	-0.2	0.8	0.9
St.Dev	0.3	0.2	0.2

Table A.5: Additional set of MR-to-MV isocentre offset results for a second attempt. Average (Avg.) and standard deviation (St.Dev) of the results between the 6 observers are presented

A.3.5 Output with Gantry Angle

The output with gantry angle is presented in Figure A.7. The couch attenuation was significant, reducing the output by as much as 22.0 % at G240, as compared to the G90 output.

A.3.6 Beam Shape at Cardinal Gantry Angles

The beam shapes at cardinal gantry angles are shown in Figure A.8, along with their corresponding metrics in Table A.6. Only the dose (relative to the central axis) at 80.0 % of the field width (FW), 8.8 cm in all four directions (IEC 61217), is provided for conciseness.

A.4 Discussion

A.4.1 Couch Operation and Sagittal Laser Accuracy

Couch drive orthogonality deviations less than 0.03 cm over 160.0 cm of movement were observed. The method proposed in this work for couch drive orthogonality is currently being implemented at TCC for routine monthly QA.

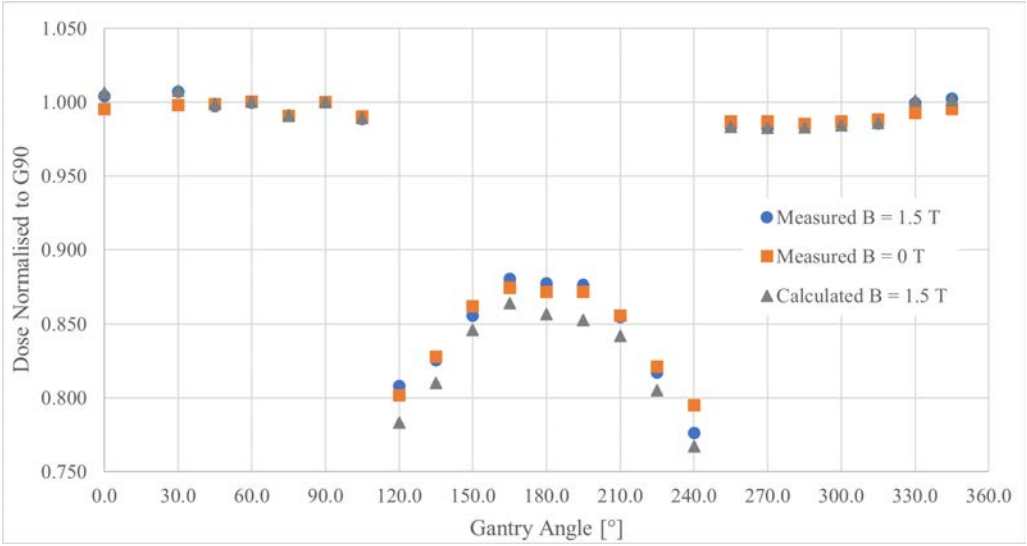

Figure A.7: Output with gantry angle. Values are normalised to the output at G90

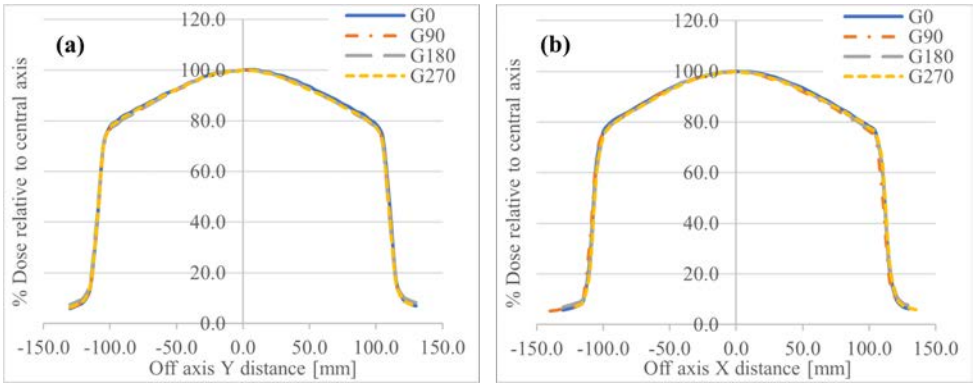

Figure A.8: Profiles obtained on the 1500^{MR} array at the cardinal gantry angles and normalised to the central axis dose for (a) IEC Y direction and (b) IEC X direction

Axis	Gantry Angle [°]	- 0.8 FW Relative dose [%]	+ 0.8 FW Relative dose [%]	Symmetry [%]
Y	0.0	82.4	83.1	101.1
	90.0	81.5	81.7	100.8
	180.0	81.2	81.8	101.0
	270.0	82.0	82.1	100.4
X	0.0	82.0	82.4	100.8
	90.0	81.4	80.7	101.4
	180.0	81.1	81.5	101.0
	270.0	81.0	81.9	102.3

Table A.6: Beam profile metrics for a 22.0 × 22.0 cm^2 delivery at the cardinal gantry angles. The relative dose at 0.8 times the field width (FW) for both directions can be compared for beam shape and the IEC method is used for beam symmetry

Results in Table A.1 show that the laser is rotated ~ 0.75 mm over a longitudinal distance of 180.0 cm, at isocentre height. To determine a laser offset result would require a reference position to be set, and such a location specific for this test has not been suggested previously. In absence of a previously published location, the following is suggested: a reference position of 14.0 cm above a point centred laterally on the 22.0 index on the couch withdrawn from the bore. The index location of 22.0 is commonly used for other QA tests and is approximately centred longitudinally on the couch. At this point, the laser was offset 1.0 mm to + X.

For the Unity system, the daily plan will be adapted for the new patient position [18]. Hence, reproducibility of daily patient positioning and alignment with reference simulation is not needed, and the laser accuracy is not overly important [21, 22]. It is provided primarily to aid with minimizing rotational misalignment. There is an argument that accurate laser positioning can be of benefit for some QA tests. However, the laser system itself is attached to the Faraday cage meaning that vibrations and excursions of the system are common (for example, the laser shakes each time the cage door is shut).

For the above reason, the method proposed for laser accuracy is not suitable for routine use since it is time consuming. A second, far quicker, method can be used to assess the laser at isocentre height. The four ballbearings can be placed on the PPS as before; however, now aligned to the sagittal laser at their respective distances from the bore. This contrasts with previous positioning where ballbearings were aligned to isocentre using MVI images. After alignment to the laser, ballbearings can be imaged on MVI at their longitudinal isocentre positions as before, and their lateral offsets from the Y-axis recorded. Comparison of offset values will determine sagittal laser offset and rotation, at isocentre height only, over the length of most distal ballbearings. This technique incorporates any deviation of couch drive orthogonality into the result; however, from the work above, this would be minimal. Additionally, determining the laser accuracy in this way imitates the clinical setup and would provide insight on potential systematic patient misalignments.

A.4.2 Cryostat Characterisation

Figure A.6 shows the original DAT cryostat characterisation as well as that post magnet ramp up, following the quench. Obviously, during a quench most of the liquid helium is rapidly exhausted. Post quench the cryostat is filled with helium above a minimum operational level (> 66.0 %); however, this will not necessarily coincide with the pre quench level. Regardless, the trend of the two characterisations are consistent. Variations less than 0.5 % were present throughout due to inherent uncertainties in the measurements. As differences between the characterisations were small, the TPS cryostat model was not updated.

A.4.3 MVI Operation

MVI image scale was verified to match nominal values within 0.32 mm over 80.0 mm measured for the Y direction, and within 0.15 mm for the 200.0 mm in the X. Average central pixel values in Table A.3 agree with those determined by Elekta within 0.4 pixels. A single pixel on the panel corresponds to ~ 0.22 mm, hence the independently measured centre was offset < 0.1 mm from the Elekta determined value. The effect of gravity is apparent in the G90 X pixel values, which increased ~ 0.6 pixels compared to that for G0. In this method, it is inherently assumed that the jaw positioning is accurate since the average position of the vertex, at the rear of the jaw, in the X direction is used for the horizontal centre pixel. Jaw offset and gain errors would lead to increased uncertainty for both gantry angles, as well as the effect of gravity on the panel.

A.4.4 MR-to-MV Isocentre Confirmation

Confirmation of the MR-to-MV isocentre offset using the technique described was inconclusive (Tables A.4 and A.5). Results varied between observers, with standard deviations of comparable magnitudes to the offsets being measured. The most likely source of uncertainty in this would be human error in positioning the stack offset within the Marlin system, and the manual registration within online Monaco. For example, in the first attempt there was a significant variation (0.8 mm) between observers when determining the registration in the Z-axis. Analysis of the MR images using in-house code would alleviate this issue and specifically allow for a more accurate determination of the sphere offset relative to the MR isocentre. Additionally, fixation devices could be 3D printed that would ensure the exact phantom position is maintained between CT simulation and MR scan, which would aid with registration accuracy between these two datasets.

The method above was intended to confirm the stored isocentre offsets in MOSAIQ, instead of determining values independently to Elekta techniques. This was the preferred option given that the Elekta values are applied during registration of daily MR images to planning scans for each patient. If one wanted to directly measure the MR-to-MV isocentre offset separately from Elekta, then irradiation of the phantom described above onto the MVI panel would be required. Software analysis of both MR and MV image sets could be performed, to independently determine an isocentre offset. For this, contrast between the acrylic sphere and water would be important and other materials may need to be considered. Additionally, analysis of a single sphere will not provide information on rotations between the datasets, which can be obtained with the Elekta tool. However, with the in-house phantom above, distortion in the MR image would be less of a concern since the region of interest in the centre of the static field [62].

A.4.5 Output with Gantry Angle

The output with gantry angle is shown in Figure A.7. The effect of the couch attenuation can be seen clearly through gantry angles of 120.0° to 240.0°, and particularly at the couch edges. The TPS appears to overestimate this attenuation, by as much as 3.0 %. This discrepancy is well known by users (Elekta private communication); however, data has yet to be published. Measured angular output in 0 T is consistent with the 1.5 T environment, except for one point at G240. Here there is a discrepancy between the two measurements of approximately 2.4 %, which was reproducible across several measurements in 0 T and 1.5 T. The reason for this difference, which is not observed at other angles, is not known. Incorrect set up in either environment does not appear to be the cause, given the reproducibility of the difference. Further, the repeat measurements in 0 T were performed during a ramp down (cryostat filled) and a quench (cryostat empty); hence, the variable helium fill cannot be the cause. This is still under investigation; however this difference is not significant clinically, as treatments are delivered in the 1.5 T environment.

A.4.6 Beam Shape at Cardinal Gantry Angles

The results in Figure A.8 and Table A.6. show some changes in beam shape as the gantry rotates. Specifically, it appears that the beam becomes slightly more forward peaked indicating minor beam hardening. This could potentially be due to variation in attenuation of the cryostat annulus at G90 and G270, compared to G0, and because of the couch components that the beam passes through from G180. The maximum variation between relative doses at the cardinal angles for both directions was 1.7 %, comparable to that measured by Elekta (1.6 %), with commercial profiler and rotating platform. Beam symmetry at all angles were within the IEC tolerance of 103.0 % [56] and values at non-zero angles were within 0.7 % from G0, except for the X direction from G270 which was 1.4 % from G0. The exact reason for this is not known. It is suspected that setup uncertainties and detector resolution may have contributed, as this larger asymmetry occurred at a more distal region from the centre (at X = ± 9.5 cm). Aside from this outlier, the symmetry metrics measured in this work agreed to those measured by Elekta during DAT to within 0.4 %. These results indicate that other clinics can use the 1500^{MR} array to reproduce DAT beam shape metrics at gantry angle on a routine basis, in the absence of specialized Elekta equipment.

A.5 Conclusion

In this section, additional commissioning work was presented, which was omitted from the thesis body. Novel measurement techniques were provided for laser accuracy and couch and MVI panel operation. and cryostat characterisation following the first ever spontaneous quench on a Unity was also presented. An in-house developed phantom was used to attempt to confirm stored MR-to-MV isocentre results, and an additional

phantom was designed to determine output with gantry angle. Independent techniques, to those of the vendor, were discussed to determine beam shape with gantry angles.

Couch orthogonality and laser accuracy were both within acceptable tolerances, as determined using common equipment available to a clinic. Little change was noted in cryostat characterisation following a quench with differences attributed to experimental uncertainty; however, the constancy of helium fill post quench will have contributed. Geometric accuracy of the MVI panel was nominal for image scaling and central pixel location. The developed in-house method for MR-to-MV isocentre was not successful and warrants further investigation, with software analysis under investigation.

Couch attenuation was significant, particularly through couch edges, in both 1.5 T and 0 T environments. Finally, beam shape at cardinal angles using a commercial array matched that with Elekta supplied equipment.

B

Clinical Cases of Out-of-Field Doses

This appendix contains material that was published in the following articles and presentation:

[2] John Baines, Marcus Powers, and Glen Newman. Sources of out-of-field dose in MRgRT: an inter-comparison of measured and Monaco treatment planning system doses for the Elekta Unity MR-linac. *Physical and Engineering Sciences in Medicine* (2021). doi:10.1007/s13246-021-01039-6

[3] Marcus Powers and John Baines. Electron Streaming Effect Associated With the Elekta Unity Anterior Imaging. *Frontiers in Physics*, **10** (2022). doi:10.3389/fphy.2022.880121

- Out of field dose due to electrons generated in-field on an Elekta Unity MR linac. John Baines, Marcus Powers. Engineers and Physical Sciences in Medicine Conference, Brisbane, 2020.

For this appendix, I performed the measurements on the machine and the simulations described below, with the exception of the radiation treatment plans which were developed by Glen Newman. The simulation toolkit is a commercial product developed and provided by Elekta for patient radiation treatment planning calculations. All other work described in this chapter is my own unless otherwise stated. Patient consent was acquired for the use of data in this chapter.

B.1 Introduction

The following appendix presents work on out-of-field doses for clinical cases treated at Townsville Cancer Centre (TCC). The work is provided to give a real-world context for

previous, non-clinical chapters. For the treatments, the presence of the magnetic field, as well as the particular geometry of the irradiated areas, resulted in clinically significant doses out-of-field. Three cases are investigated: a right-sided supra-clavicular fossa (SCF) nodal disease (case 1), a right ankle (case 2) and a left acromion lesion (case 3). For cases 1 and 2, *in vivo* film dosimetry was performed for treatments. Case 1 focused on how the treatment planning system (TPS) simulates the electron streaming effect (ESE) from a patient. The efficacy of bolus shielding was highlighted. In addition to that listed for case 1, case 2 addresses how ESE from the anterior coil can be clinically significant. Finally, case 3 shows how changing the relative electron density (RED) of air around the patient can change out-of-field dose (OFD) in a clinical treatment plan.

B.2 Methods

B.2.1 Case 1 - SCF

In case 1, a right-side SCF lesion, the patient CT dataset was imported into Monaco and a 7 field step-and-shoot, intensity modulated radiation therapy (SSIMRT) pre-treatment reference plan was generated. The prescription was 36.0 Gy in 4 fractions (Fx). On each day of treatment, a magnetic resonance (MR) image of the patient was registered with the reference CT image in the first stage of an adaptive planning workflow. For the patient investigated, the Adapt to Position (ATP) replanning option was utilized for all fractions. All fractions were re-optimized to reproduce the prescription target dose and this changed the MU and segment shape for each beam [18, 110].

It was anticipated that streaming electrons could potentially deposit dose superior to the right shoulder [8, 23]. Consequently, for each adapted treatment, a nominal 2.0 cm slab of tissue equivalent jelly bolus was used to shield the right ear. Bolus was positioned adjacent to the ear defender, abutting the patient's neck and approximately 6.0 cm from the shoulder. A 3.0×1.0 cm^2 strip of EBT3 film was positioned on superior and inferior sides of the bolus at the level of the ear lobe for each adapted plan. The mean dose per fraction on each film was determined using a nominal 1.0×1.0 cm^2 region of interest (ROI).

For TPS calculations, the bolus was included for each adapted plan. The mean entry and exit bolus dose over the course of the treatment, for each beam, was computed for a 1.0×1.0 cm^2 ROI. Estimates for ear dose due to each beam in the absence of bolus were compared to measured values for bolus entrance dose. To visualize potential electron streams from the shoulder region to the ear, a volume of interest (RED = 0.010) surrounding the patient contour was created. This work was performed after the discrepancy between measurements and forced RED simulations was discovered (Sections 5.4.2 and 6.4.1), and could not be repeated due to clinical limitations of the machine. TPS computations were performed in 0 T and 1.5 T, on a 0.2 cm dose grid, with a statistical uncertainty of 3.0 % per control point and the Patient look-up table. These calculation settings, excluding the 0 T field, were consistent with clinical workflow.

B.2.2 Case 2 - Right Ankle

For this case, a lesion in the right ankle, a 5 field SSIMRT plan was generated on the reference CT dataset. The prescription was 30.0 Gy in 3 fractions. The ATP workflow was utilized for each daily treatment, with the intent of reproducing target dose. A vacuum bag immobilization device was used to aid with positioning, and reduce inter-fractional patient motion. Note for this treatment the patient was Feet First Supine (FFS), meaning inferior corresponds to the + Y direction. For this treatment, the orientation of the patient's feet required the anterior imaging coil to be tilted, with the superior end (- Y) lower than the inferior.

Relative positions of the contralateral foot and the anterior coil meant that slight misalignment could result in unintended irradiation of the foot, due to ESE from the tilted coil. Electrons ejected from the right ankle were also expected to spiral superiorly and inferiorly and deposit dose along the patient right leg and foot, respectively. Furthermore, with the coil tilt, electron streams above the coil were expected to be directed toward the patient head. As such, 2.0 cm of jelly bolus was used during treatment to shield patient regions. Bolus was placed at the superior end of the coil (- Y, to protect the patient head), and on the right foot and leg, 2.0 cm beyond the edges of the treatment field. Shielding was not used for the left foot, which was instead rotated laterally to avoid ESE. EBT3 film was used to assess the efficacy of the bolus, and to report the mean dose (per fraction) to each investigated location. Film and bolus were also attached to the inferior end of the anterior coil (+ Y) for the final fraction.

Using the TPS the OFD was assessed for each foot, the right leg and each end of the tilted coil. Air around the patient was contoured, assigned as the external contour and had an unforced RED. The anterior coil was avoided by this air structure. Planning system settings for the calculation matched the clinical workflow (Section B.2.1). A 0.25 cm radius interest point (IP), in the TPS, was placed at the at the approximate location of the film during treatment and in direct path of the electron streams. Mean IP dose was determined for each fraction, then averaged across the fractions to compare with film data.

Due to restrictions of the CT scan length, IPs at the longitudinal ends of the coil did not match the film locations during treatment. Instead they were placed at the most distal longitudinal positions possible on the CT dataset, such that the inferior IP was ~ 13.0 cm from the coil end and the superior IP was ~ 4.0 cm. The effect of air attenuation on the electron streams was expected to influence results [2,9] and needed to be taken into account. To get an approximate correction factor, IPs interrogating streams from the coil were shifted (+ Y was shifted - 3.0 cm, and - Y was shifted + 3.0 cm). Dose change per centimetre was assessed over this distance. Using this gradient the average IP values, across the three fractions, were linearly extrapolated to get an approximate mean dose matching the film locations.

B.2.3 Case 3 - Left Acromion

In this case, a lesion in the left acromion (shoulder), a 5 field SSIMRT pre-treatment reference plan was on the patient CT dataset. The prescription was 30.0 Gy in 3 fractions. For each treatment the ATS workflow was utilised; hence, a new plan was generated, on the daily MR scan, using reference plan constraints. The treatment area was very lateral; hence OFD, due to spiralling contaminant electrons (SCE) and ESE, was not expected to impact the patient. As such, no bolus shielding was required and *in vivo* measurements were not performed.

For a TPS assessment of the OFD, the air around the patient was again contoured and assigned an RED of 0.010. The patient plan, originally generated without the air contour, was calculated with clinical settings (Section B.2.1). Additional calculations were performed with an unforced RED for the air contour. For both REDs, only the 1.5 T clinical model was used. Using Monaco, differences between plans were assessed through dose subtraction, where the unforced RED simulation was the subtrahend. Furthermore, a 0.25 cm IP was placed 5.0 cm superiorly to the patient shoulder, in-line with the centre of the lesion.

B.3 Results

B.3.1 Case 1 - SCF

Table B.1 shows the mean bolus entrance dose computed for each beam over the course of the treatment. The RPO-247, RPO-210, RAO-300 and LPO-160 beams were the dominant contributors to bolus dose. The mean TPS bolus entrance dose for the entire treatment was 11.6 ± 0.9 Gy and the mean dose per fraction was 2.9 ± 0.2 Gy. In the pre-treatment reference plan, corresponding values were 9.7 ± 0.4 Gy and 2.4 ± 0.1 Gy, respectively. TPS unshielded mean ear dose of 9.9 ± 0.7 Gy and bolus entrance dose from the reference plan were comparable. The average measured film dose per fraction (in front of bolus) was 3.5 ± 0.7 Gy, within 1 standard deviation (SD) of the average TPS dose. TPS estimates of ear doses using bolus shielding of either 2.0 cm or 1.0 cm thickness were 0.18 Gy and 0.24 Gy, respectively. Mean exit dose measured with film (behind bolus) was 0.1 Gy for the 2.0 cm shielding used during treatment.

Visualization of the effect of streaming electrons in the air between the shoulder and the bolus, for beam RPO-247, is provided in Figure B.1(a). Using the Monaco TPS with 0 T, air dose is evident for this beam and there is no dose incident on the bolus (Figure B.1(b)). The 3D render in Figure B.2 demonstrates an absence of streaming electrons anteriorly and evidence of such electrons posteriorly.

B.3.2 Case 2 - Ankle

In Table B.2 the measured and calculated doses per fraction are given for each investigated location. Film measurements at the inferior end of the coil were only taken on the final fraction. For film measurements, doses are the maximum recorded value, to

Beam	Site Dose [Gy]	
	Bolus entrance (TPS)	Max ear dose (TPS)
LPO-160	0.87 ± 0.23	1.21 ± 0.21
LAO-50	0.33 ± 0.02	0.38 ± 0.05
A-0	0.14 ± 0.02	0.13 ± 0.02
RAO-330	0.31 ± 0.01	0.32 ± 0.05
RAO-300	1.19 ± 0.19	1.24 ± 0.18
RPO-247	3.29 ± 0.25	3.51 ± 0.39
RPO-210	3.61 ± 0.19	3.87 ± 0.43

Table B.1: Mean ± 1SD TPS bolus entry dose and estimated maximum mean ± 1SD ear dose per beam for the treatment course, as simulated in the reference plan

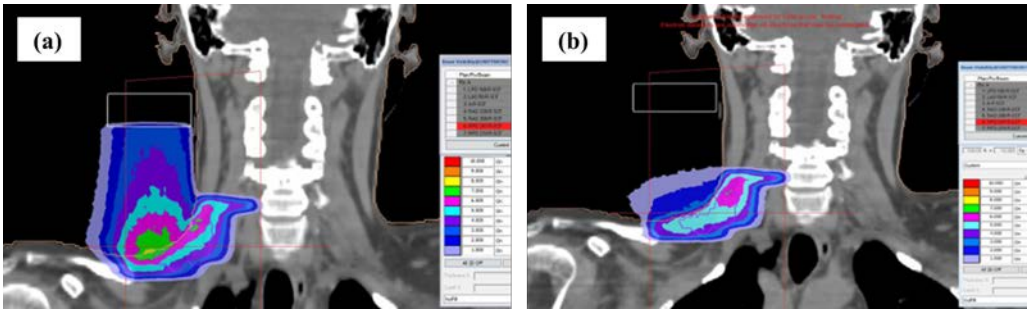

Figure B.1: Coronal view showing Right Post Oblique-247 beam and position of bolus (white rectangle) for (a) 1.5 T and (b) 0 T. In (a) the electron stream from radiation exiting the patient shoulder/neck is observed whilst in (b) some dose is evident outside the patient, but no electron stream can be observed

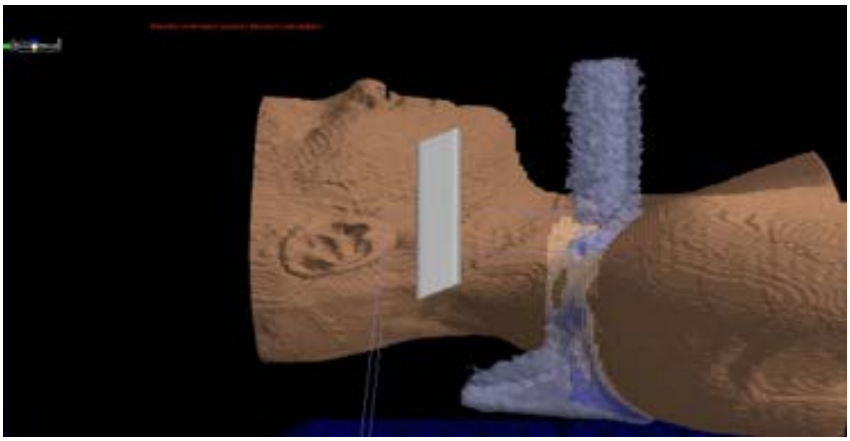

Figure B.2: Anterior-0 beam exiting the patient produces streaming electrons moving parallel to the magnetic field

Site	Dataset	Fraction dose [Gy]			Average Dose [Gy]	SD [Gy]
		Fx 1	Fx 2	Fx 3		
Coil Inferior	Film	NA	NA	0.34	0.34	NA
	TPS	0.49	0.52	0.48	0.50	0.03
Coil Superior	Film	0.15	0.20	0.21	0.19	0.03
	TPS	0.48	0.54	0.59	0.54	0.05
Right Leg	Film	1.25	1.10	1.45	1.27	0.20
	TPS	0.97	0.96	0.98	0.97	0.01
Right Foot	Film	0.10	1.10	0.50	0.57	0.50
	TPS	0.73	0.75	0.71	0.73	0.02
Left Foot	Film	0.02	0.03	0.03	0.03	0.01
	TPS	0.02	0.02	0.02	0.02	0.00

Table B.2: Mean doses per fraction for each location measured in case 2 from film and TPS calculations, uncorrected. Averages and standard deviation (SD) were taken across the three fractions

indicate the potential exposure that could have occurred without appropriate shielding. The largest measured OFD occurred in Fx 3, with a dose of nearly 1.5 Gy reaching the film along the right leg. Large variation can be seen on the films on the right foot and leg. For films behind bolus, average doses per fraction were 0.00 ± 0.00 Gy, 0.04 ± 0.02 Gy and 0.08 ± 0.03 Gy for the superior end of the coil, the right leg and right foot, respectively.

TPS doses were distinctly less varied between fractions compared to film doses. For patient ESE locations (left/right foot, right leg) TPS data is within 2SD of measured data. Visualization of the streams is provided in Figures B.3 and B.4. Note the electron streams emanating from above and below the coil, Figure B.3(a). Figure B.4(a) shows streams travelling superior along the patient right leg, and coil ESE is also highlighted in Figure B.4(b). Additionally, it can be seen that the vacuum bag produces electron streams, Figure B.4(c). The approximate dose change per centimetre, used to correct coil IPs, was 0.03 Gy/cm. After accounting for this, calculated mean doses per fraction were 0.40 ± 0.02 Gy and 0.37 Gy ± 0.05, for the coil inferior and superior ends, respectively.

B.3.3 Case 3 - Left Acromion

Figure B.5 shows the extent of the streaming effect for case 3, with forced and unforced RED calculations. It can be seen that doses as high as 16.7 % of the prescription dose occur external to the patient. Also, from Figure B.6, it can be seen that differences of up to 3.0 Gy (10.0 % of the prescription dose) occur between the two RED calculations. Different coronal slices are displayed in Figure B.5 and Figure B.6(c), to highlight the discrepancy across multiple locations.

In this treatment, the largest contributor to the dose out-of-field was G50-L-SH (see Table B.3). The OFD contribution to the IP from this beam was 2.20 ± 0.04 Gy for the forced RED calculations and 2.14 ± 0.17 Gy for the unforced. These correspond to 7.3 % and 7.1 % of the prescription dose, respectively. For all beams, the cumulative

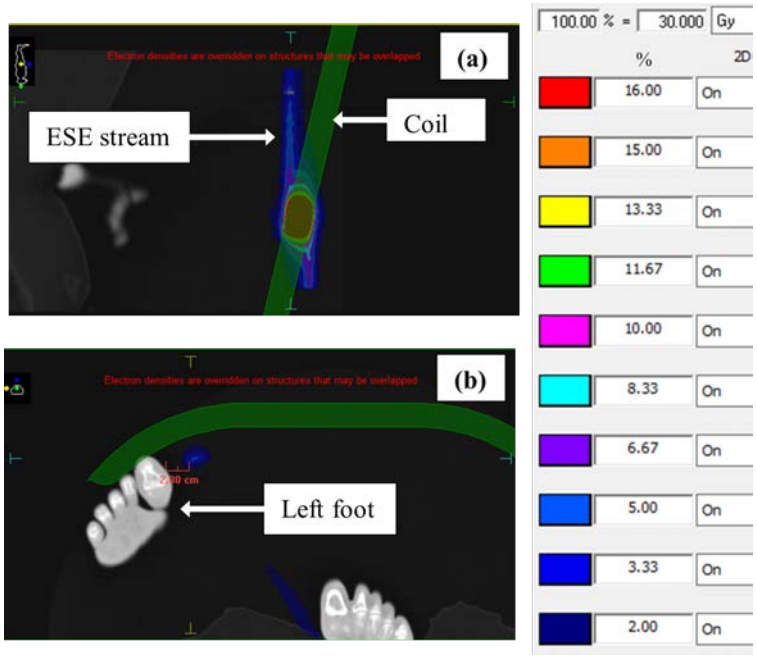

Figure B.3: TPS images showing a single beam irradiating the coil and (a) electron streams travelling inferiorly and superiorly from the tilted coil. (b) shows the proximity of the patient's left foot to the stream, at the time of patient simulation. The yellow dot in the orientation icon in the top left of each image indicates patient-left

Beam	MU	Calculated Dose [Gy]	
		Forced RED	Unforced RED
G210-L-SH	325.9	0.65 ± 0.06	0.54 ± 0.04
G110-L-SH	399.5	0.26 ± 0.05	0.25 ± 0.09
G90-L-SH	247.6	0.44 ± 0.05	0.41 ± 0.06
G50-L-SH	512.8	2.20 ± 0.04	2.14 ± 0.17
G0-L-SH	453.3	0.87 ± 0.03	0.89 ± 0.16

Table B.3: Mean ± 1SD TPS calculated doses for the interest point located 5.0 cm from the patient surface with the RED of the air around the patient forced or unforced

doses to the IP for forced and unforced RED calculations were 4.41 ± 0.14 Gy and 4.21 ± 0.46 Gy, respectively.

B.4 Discussion

B.4.1 Case 1 - SCF

For case 1, TPS unshielded ear dose of 9.9 ± 0.7 Gy is greater than an upper estimate of 1.4 Gy (3.8 % of the prescription dose) for the ear dose due to SCE and background photons. With 2.0 cm bolus, TPS ear dose and measured bolus exit dose are comparable. The magnitude of shielded ear dose is acceptable and is consistent with the attenuation reported for 500.0 keV streaming electrons [23]. Within the volume of interest superior to the right sided SCF treatment region (Figure B.1), dose deposition

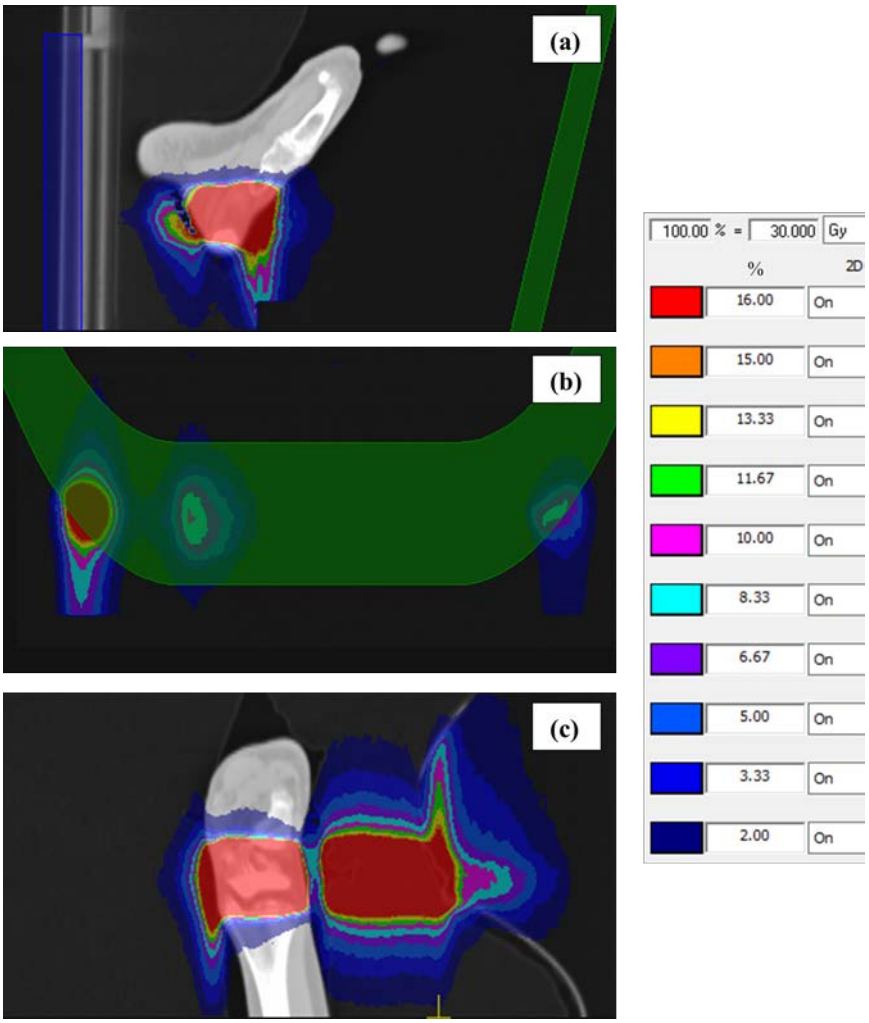

Figure B.4: TPS images of the electron streams, for all beams, from (a) a sagittal slice through the patient's right foot, (b) a coronal slice through the tilted anterior coil, and (c) a coronal slice through the patient's right ankle and the vacuum bag immobilization device. The magnetic field is directed down the page for each image

is evident in the coronal plane at the level of the ear. That dose is dominated by streaming electrons associated with four of seven beams.

Out-of-field dose due to streaming electrons is significantly greater than SCE dose. However, due to the parity of electron energies involved in both processes 2.0 cm of bolus provides effective patient shielding. Other authors have reported on the suitability of 1.0 cm water equivalent bolus attenuation [23]. With appropriate selection of isodose display in the TPS (less than approximately 30.0 % of the prescribed dose) patient regions outside the primary field that require shielding can be identified.

B.4.2 Case 2 - Ankle

In case 2, the TPS dose estimates for the coil ends were consistent inferiorly and superiorly, with calculated average fractional doses of 0.50 ± 0.03 Gy and 0.54 ± 0.05 Gy, respectively. Note that ESE doses for the IPs only had contributions from a single beam (G325). At the superior end, doses above the coil were the result of streaming,

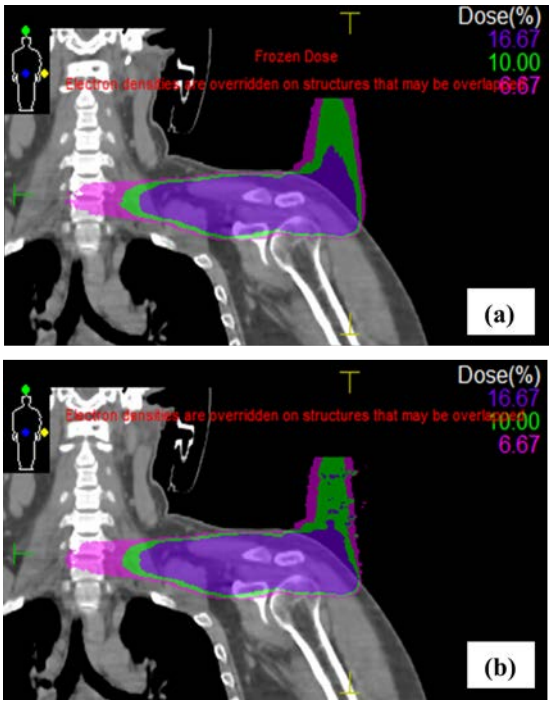

Figure B.5: Coronal view of case 3 showing the electron streams for (a) the forced RED calculation and (b) for the unforced. Isodoses are displayed as a percentage of the prescription dose (30.0 Gy)

backscattered electrons. This is consistent with the data from previous investigations (Chapter 7). TPS average fractional doses were larger than measurements, the latter being 0.34 Gy inferiorly and 0.19 ± 0.03 Gy superiorly. This was still the case after applying an approximate correction for the air attenuation; however, closer agreement was observed. Furthermore, for the investigated locations, 2.0 cm of jelly bolus was sufficient at reducing the OFD to an acceptable level

From Table B.2, measured coil inferior doses (below) were larger than superior (above), in contrast with previous work (Chapter 7). Where the beams transited the anterior coil was biased in the + Y direction, and thus the electron streams travelling inferiorly experienced less air attenuation. This was not observed in the TPS data, as IPs could only be selected at roughly the same distance from the beam axis. However, one can see from the corrected TPS results that the dose superiorly was reduced more than that inferiorly (see Section B.3.2). This was due to the differing distances from isocentre, and therefore different air attenuation. Note that differences between measured superior and inferior doses were consistent with the 0.03 Gy/cm dose fall off, within 1SD.

For patient ESE sites, TPS doses agreed within 2SD to measured data. Measured average fractional dose of 1.27 ± 0.20 Gy was observed along the leg surface, superior to the disease site and in front of the bolus shielding. For a 3 fraction treatment, this corresponds to a skin dose ~ 3.8 Gy (12.7 % of the prescription dose) in the absence of shielding. The TPS appeared to underestimate dose in this region; however, set up variations for measurements would have contributed to discrepancies. Measured and

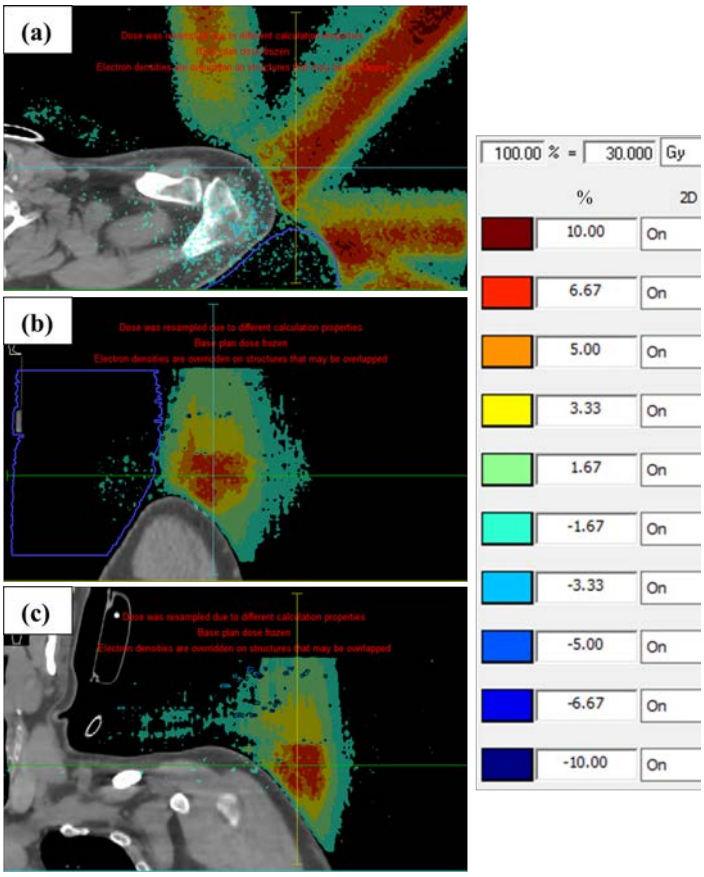

Figure B.6: Dose differences between forced and unforced RED for case 3, as calculated in Monaco, where (a) shows a transverse slice (b) a sagittal and (c) coronal. Positive values indicate that doses in the forced RED calculation are larger and values are normalised to the prescription dose (30.0 Gy)

calculated fractional average doses (0.57 ± 0.50 Gy and 0.73 ± 0.02 Gy, respectively) for the right foot were lower than that for the leg. Again, film set up will contribute to differences between measurement and simulation, discussed below.

Film measurements were significantly varied, particularly for the film/bolus on the right foot, which is largely attributed to positional variations between treatment sessions. Inconsistent film setup, and a mismatch in TPS IP location to film location during treatment, will contribute to the discrepancies between measured and calculated doses. Note that fractional variations in TPS IP values are associated with changes between adapted plans.

In Figure B.4(c), electrons streams from the vacuum bag can be observed. This is an area not yet investigated and warrants further study. Emphasis should be on *in vivo* measurements to characterise this source of OFD for simple beam geometries. Any attenuating material in the path of the beam will generate ESE, and clearly the TPS is predicting some OFD due to such streams emanating from the bag. ESE doses as high as 4.0 Gy (13.33 % of the prescription dose) for the entire treatment were calculated. The geometry of the patient, vacuum bag and planned beams should be scrutinized when using this immobilization device and appropriate shielding provided.

B.4.3 Case 3 - Left Acromion

For case 3, TPS calculations between forced and unforced calculations showed differences in OFD. Dose to the IP on the reference plan, forced RED, was 4.41 ± 0.14 Gy for the entire treatment course. Corresponding unforced RED dose was 4.21 ± 0.46 Gy. From these values, those in Table B.3 and the doses in Figure B.5, it can be seen that TPS calculations with unforced RED were more varied. This was expected, given the inter-voxel variation in CT number (and consequently RED for the calculation) which is not a factor with the single, forced RED value.

Beam G50-L-SH was the largest contributor to OFD, due to beam and patient geometries. Additionally, this beam had the largest MU for the investigated plan. However, comparison of MU for beams 4 and 5, and the corresponding calculated doses, indicates that beam/patient geometry tends to affect OFD more than beam weight.

The difference plot in Figure B.6 highlights regions where the forced RED doses are significantly different than unforced REDs. Differences > 5.0 % of the prescription dose tended to occur in regions where SCE was the dominant contributor to OFD. Variations of approximately 5.0 % were still seen in ESE regions; however, were smaller than those seen in SCE, which were as large as 10.0 %. This is most likely due to the method of OFD production for these regions, as discussed previously where forced RED calculations raise SCE and lower ESE (Sections 5.4.2 and 6.4.1). Interestingly, around the IP location (5.0 cm superior to patient shoulder) forced RED doses were greater than unforced. This is surprising as this point would have contributions from ESE doses from the patient B.5, and higher forced doses contrasts with previous data (Section 6.4.1). However, given the patient geometry at coronal plane of the IP (Figure B.6(c)), there may be some significant SCE dose to this point. This is still under investigation.

On a side note, the change in RED of the air around the patient made very little difference for doses inside the patient. Dose Volume Histogram (DVH) statistics showed that target coverage and several organ doses changed by less than 0.5 % between the forced and unforced settings, which was well within the calculation statistical uncertainty.

B.5 Conclusion

Clinical cases of out-of-field doses were discussed in this appendix, for three different patients treated at TCC. For case 1, a treatment of a supra-clavicular fossa nodal disease, *in vivo* dosimetry agreed with the TPS within 1SD. TPS calculations showed that ESE contributed more than SCE to OFD.

Similar results were observed for patient ESE doses in case 2, a treatment of a lesion in the right ankle. Furthermore, for this second case, coil ESE was investigated and the TPS tended to overestimate OFD compared to measurements. Dose above and below the coil were consistent in TPS calculations; however, this was not observed in

measurements. The importance of reproducible positioning during *in vivo* dosimetry, when comparing to the TPS, was also highlighted. Both cases 1 and 2 showed, for the sources of OFD investigated, 2.0 cm of water equivalent bolus provides the necessary patient shielding.

Case 3 highlighted that forcing the RED appeared to affect SCE doses more than ESE, in addition to highlighting how OFD is more varied for unforced calculations. Furthermore, the effect of forcing the air RED to 0.010 on dose deposition within the patient was statistically negligible.

Finally, further work is needed to characterise OFD generated from vacuum bags, and other patient immobilization devices, such as that shown in Case 2. Specifically, work focusing on *in vivo* measurements is an area worth investigating.